Study of the effect of RF synthesis parameters on the superinsulating properties of xerogel composite blankets

Mohammed Ghith Mussa Abduljalil

Thesis submitted to the University of Strathclyde for the degree of
Doctor of Philosophy

Department of Chemical and Process Engineering
University of Strathclyde

2020

This thesis is the result of the author's original research. It has been composed by the author and has not been previously submitted for examination which has led to the award of a degree.

Signed:

Dated:

Acknowledgements

The path toward this thesis has been tortuous. Its completion is thanks to the contribution of exceptional individuals who challenged, supported and believed with me along the way.

I submit my heartiest gratitude to my supervisor, Dr Ashleigh Fletcher. Here sincere guidance, encouragement, support, help and patient have impressed me to tackle the issues and gain invaluable experience throughout my PhD.

I would like to thank Dr Liu Yang and Dr Fiona Sillars for sharing knowledge and providing technical support in the use of HFM, LFA, and STA facilities within the Advanced Materials Research Laboratory.

Also, great acknowledgement extended to the technical and administrative staff within the Department of Chemical and Process Engineering. Thanks go to Ian Airdrie in particular, for his entire assistant with surface area, porosity and thermal analyses measurements.

To all of my colleagues and friends within the department, with a special mention to Dr Stewart Taylor (previous PhD student) for his help and guidance. Special thanks to Lady Eileen McDonalds for her contribution towards received award from the EU & International Student Discretionary Fund.

I am highly indebted to Cultural Attaché of Libyan Embassy in London for their support and help, as well as for providing necessary information about the scholarship criteria.

Finally, most especially is to my parents, my wonderful family; the melody of my life, brothers and sisters for their support, encouragement and patient.

Abstract

Materials produced from the synthesis of resorcinol-formaldehyde (RF) gels, can be used in a wide range of applications, from contact lenses to water filtration media. As a result of their versatility, there is a need to control the properties of these materials to optimise their performance in such applications; this study investigates the effects of synthetic conditions on the final thermal conductivity of RF gel materials for use in insulation applications.

Novel RF xerogel blankets, for use in insulation applications, were synthesised and studied. The xerogel blankets were fabricated by moulding a base-catalysed mixture of resorcinol-formaldehyde into a polyethylene terephthalate (PET) unwoven fibrous mat. The similar process was employed in the preparation of the parent RF xerogels, utilising identical processing conditions. Altering the formulation of the sol could significantly impact the nanoscale structure, and density of the resulting materials, therefore, their final properties, including thermal conductivity.

Thermal conductivity measurements on the xerogel blankets were performed using a heat flow meter (HFM) assembly. The obtained results specify that the thermal conductivity of the composite blankets tends to decrease with increasing average pore size, towards a critical value, which is less than the mean free path of air. There is good evidence that the average pore size increases as the R/C ratio increases. Within the sample series examined, the bulk density of the materials is inversely proportional to thermal conductivity. However, when the density is below 280 kg/m^3, the thermal conductivity tends to increase. It was observed that the bulk density of the blankets decreases when the percentage of solids content decreases, and the molar R/C ratio increases. Altering the catalyst used in the synthetic process also resulted in slight changes in the textural characteristics, and thermal conductivities of the blankets. The RF xerogel blanket obtained using an R/C of 600, and a solids content of 30%, shows the lowest thermal conductivity (23.47 mW/m.K) among, those obtained using other conditions.

In the case of subcritical dried RF organic gels (xerogel), the thermal conductivity measurements of both monolithic and powdered gels were performed using thermal

analysis methods. The findings indicate that thermal conductivity decreases with decreasing density; however, limitations in the results obtained demonstrate the potential difficulties in obtaining a correlation between porous structure and thermal conductivity.

Studies of the thermal behaviour of RF xerogels and their blankets indicates that these materials are thermally stable up to 300 °C (573 K). Thermal decomposition profiles reveal traces of moisture, released between 100-200 °C (373-473 K); which requires further treatment of the final products.

The results obtained, which focus on the processing steps that can be used to tailor the texture of RF blankets by modifying the composition of the parent sol, demonstrate the potential of such routes to controlling and optimising the thermal conductivity of composite blankets for use as insulating materials.

Table of Contents

List of Figures

List of tables

List of schemes

1 Introduction

Nanostructured materials (NM) are highly versatile, which has led to various novel applications throughout different historical development. Studies show that the multi-walled carbon nanotubes were used to fabricate ancient swords manufactured with Damascus steel (AD 500), their existence within the smoke of the early human-made's fire, and the paint of stained glass. Although NM had been employed in some practical applications far back in human history, it is only recently that has been possible to manufacture these materials under controlled conditions [1]. Aerogels, synthesised via sol-gel chemistry, are a model of these structures, as they exhibit fascinating physical properties including low densities, microstructures, as well as high porosities and surface areas [2].

1.1 History and background of sol-gels

In early thirtieth of the 19th century, the first inorganic gel was accidentally formed during the exposure of a silane (tetraethoxysilane) to the atmosphere, when Ebelmen reacted silicon tetrachloride ($SiCl_4$) with ethanol (C_2H_5OH) to prepare tetraethoxysilane (TEOS) [3]. The so-discovered TEOS was hydrolysed under acid conditions to form silica dioxide (SiO_2), as a silicate solution, from which the fibres could be drawn. Since this invention, many different gels have been synthesised [4]. The term "sol-gel" was first introduced by Thomas Graham(1861-1864) during his studies on colloidal substances [5, 6].

Sol and gel are the two main phases encountered during the process. The sol is a colloidal suspension in which nanoparticles (~1-100 nm) scatter throughout a liquid (Figure 1a); these particles can be crystalline or amorphous [7]. The colloidal particles exhibit solid-like behaviour resulting from a continuous three-dimensional network enclosed by the liquid phase, namely a gel [8]. The gel point or gelation time is defined as the time for which the sol takes to form a gel that can support stress elastically [4]. At the gelation point, the sol phase will contain many clusters, and further condensation reactions continue to occur [3]. With time, inter-cluster bonds become connected to the network (aggregation), extending the crosslinking polymeric structure. The continuous formation process of inter-cluster connections constituents

the curing stage [9]. The particle growth process followed by aggregation and completed gelation is shown in Figure 1b.

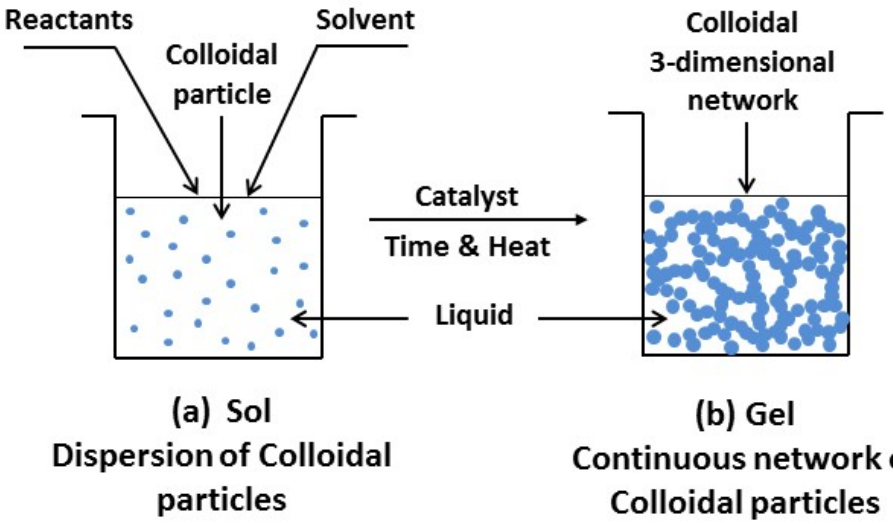

Figure 1: Sol-gel process [8, 10].

1.2 Evolution of aerogels

Aerogels are obtained when the liquid phase entrained within the gel material is extracted through supercritical drying. This process involves extreme conditions (carried out above the critical temperature and pressure) [11, 12]. Samuel Kistler developed the first inorganic aerogel in 1931. The wet SiO_2 gel was obtained from the reaction of an aqueous solution of sodium silicate (water-glass) and hydrochloric acid (Reaction1). To exchange the liquid in gels for air, the formed NaCl had to be removed using multiple washing cycles, with the remaining water exchanged with an appropriate solvent to allow for supercritical drying [8, 13].

$$Na_2SiO_3 + H_2O + 2HCl \longrightarrow Si(OH)_4 + 2NaCl \quad (1)$$

In the 1960s, Teichner and his co-workers simplified and accelerated the method of synthesis of silica aerogels. They substituted sodium silicate by an organosilane compound, known as tetramethoxysilane (TMOS), to eliminate the salt washing and solvent exchange steps. Teichner and his group dissolved TMOS in methanol and added a defined stoichiometric amount of water to prepare a silica alcogel (Reaction 2), which was subjected directly to supercritical drying [12].

$$Si(OCH_3)_4 + 2H_2O \longrightarrow SiO_2 + 4CH_3OH \quad (2)$$

Since then, several studies have been dedicated to the development of silica aerogel synthesis techniques to expand and vary the applications of these materials [10, 14-18].

Several methods based on different criteria classify aerogels. These methods can be divided into film, powder and monolith taking into account their appearance and shape; or because of the preparation and treatment methods, aerogel can be produced as different types including aerogel, xerogel, cryogel, as well as other aerogel-related materials. In contrast, given different pore structures, aerogels can be categorised as microporous (<2 nm), mesoporous (2-50 nm) and mixed-pore aerogels. The vital point for consideration while classifying the aerogels is to differentiate them by their composition.

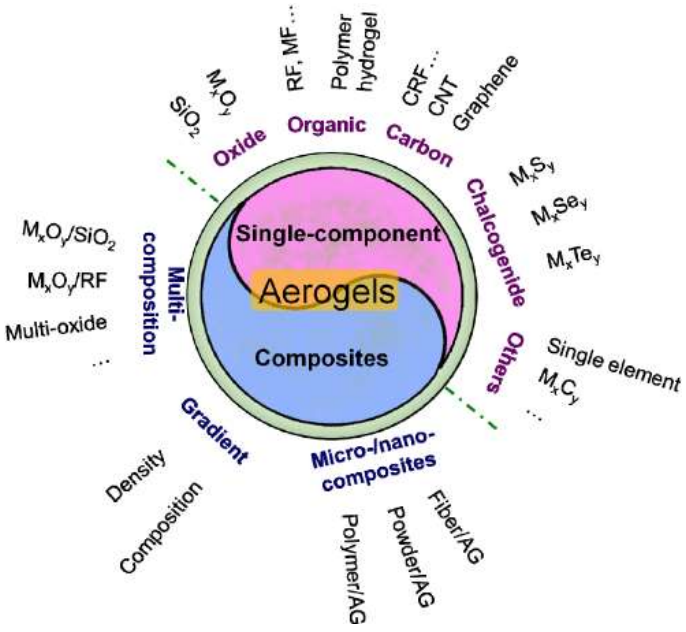

Figure 2: Classification of aerogels by composition [19].

Figure 2 shows that aerogels can be allocated into two groups: single-component and composite aerogels. Single-component aerogels comprise oxide aerogels (silicon alkoxides and metal oxides), organic aerogels (phenolic-based and cellulose-based), carbon aerogels and other types of aerogels, while composite aerogels include nano-composite, gradient and multi-composition aerogels [19, 20].

1.2.1 Silica aerogels

Amongst the class of aerogels, silica forms are perhaps the most studied and investigated aerogels [21-24]. The essential activities have been focused on the synthetic routes for silica aerogels, in order to prepare transparent, amorphous or monolithic aerogels from silica alkoxides or water glass solutions [25, 26]. The sol-gel process is a commonly used method to produce nanoporous silica gels, where the silicate monomer solution undergoes polymerisation [22, 27], as illustrated in Figure 3.

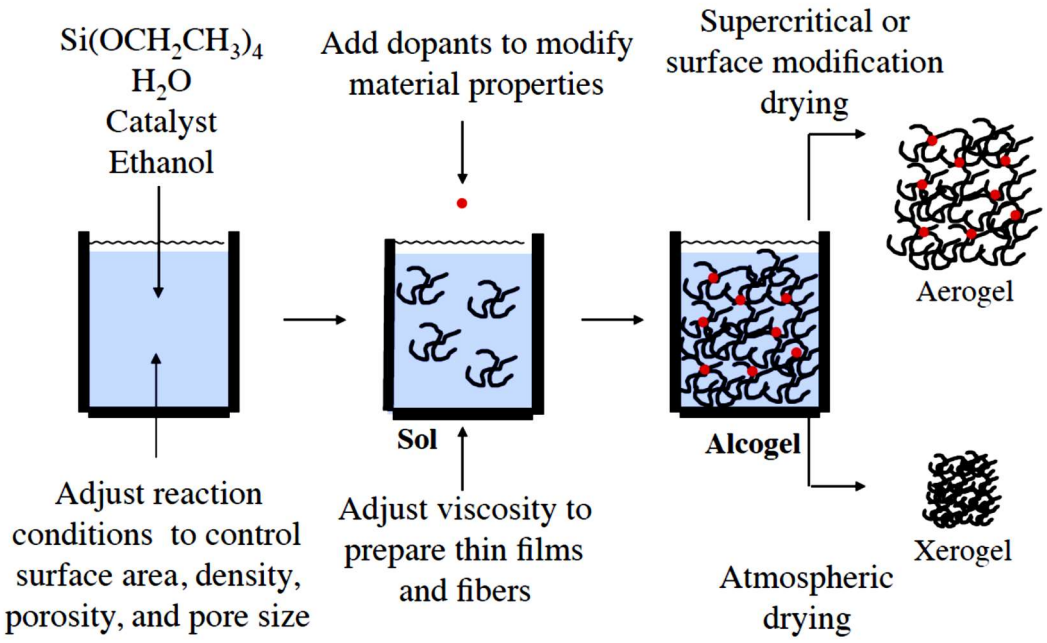

Figure 3: Explanation of the standard sol-gel process for silica gel synthesis [27].

Synthesis conditions play a significant role in controlling the growth of the gels, to optimise the properties of silica aerogels [25, 28, 29]. The resulting materials have extraordinary physical properties, including ultralow density (0.003-0.8 g cm^{-3}), low thermal conductivity (~ 0.001 $Wm^{-1}K^{-1}$), low refractive index (~ 1.05), high specific surface area (1000 $m^2 g^{-1}$), high porosity (~ 99%), low sound velocity (100 ms^{-1}) and low dielectric constant ranging between 1.0 and 2.0 [30-32]. The combination of these exceptional properties in one material is the unique feature of aerogels. The essential characteristics for various applications are therefore combined, such as thermal insulation (Figure 4), catalysis, energy storage, optics, sensors, adsorption and environmental remediation [13, 33].

Scientists at Lawrence Livermore National Laboratory (LLNL), U.S.A, developed the lowest density silica aerogel in the 1990s. This ultra-lightweight material has been produced using a distillation process to substitute the alcohol with an aprotic solvent; since then NASA used on the tiles of silica aerogels (Figure 4) on the space shuttle to capture dust particles [2, 22].

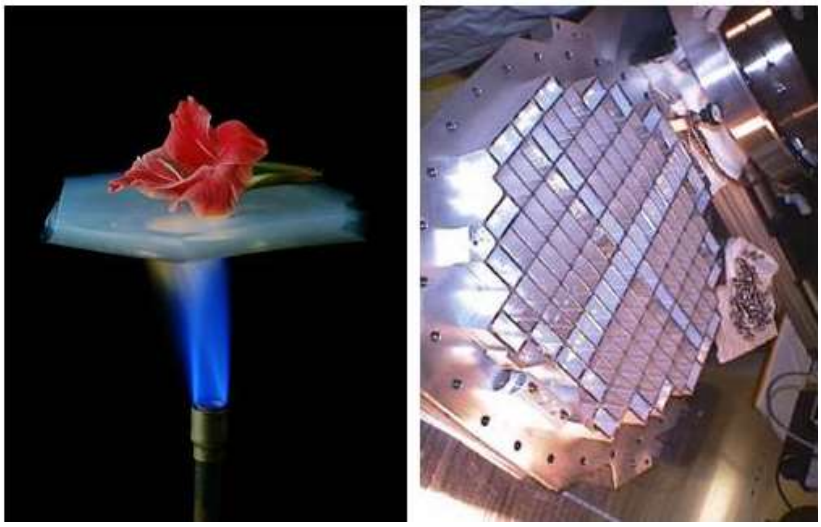

Figure 4 : (Left) Excellent insulating properties of silica aerogel, (Right) STARDUST Dust Collector with aerogel [34].

1.2.2 Resorcinol-Formaldehyde (RF) aerogels

In the late 1980s, the first organic aerogel was reported by Pekala and co-workers (from LLNL) via an aqueous polycondensation reaction of resorcinol (R) with formaldehyde (F), in the presence of sodium carbonate (Na_2CO_3) as a catalyst [35, 36]. Interestingly, the mechanism of this reaction is analogous to the inorganic sol-gel system [37, 38]. The resultant hydrogel was washed with acetone and then dried by a supercritical method using carbon dioxide (CO_2) liquid at an elevated pressure [35, 39].

This pioneering work remarkably inspires the field of organic aerogels, as several studies have been conducted to describe different techniques of synthesis and processing conditions. Much of the research has investigated the mechanism of synthesis and has focused on elucidating how the synthetic route and processing conditions affect the final structural properties of the RF gel [40-47].

1.3 Chemistry of RF sol-gels

The nano-morphology of aerogel constituents influences the large-scale features of the resulting material. The understanding and knowledge of the chemistry and nature of raw materials (precursors) and the chemical behaviour of the solid are vital for the considered tailoring and optimisation of the properties of these materials [13].

Resorcinol-formaldehyde gels are classified as phenolic-based polymers. Since the phenol-formaldehyde condensates (Bakelite) were launched commercially in the earlier part of the twentieth century, phenolic polymer chemistry has contributed much to this field through a substantial amount of research information. These processes can be applied to the full understanding of the synthesis of RF sol-gels [44, 48].

1.3.1 Reactants (raw gradients/precursors)

1.3.1.1 Resorcinol

Resorcinol is a white crystalline dihydric benzene compound, also known as resorcin, 1, 3-dihydroxybenzene, 1, 3-benzenediol, 3-dihydroxy phenol, and meta-dihydroxybenzene. The condensates of resorcinol-formaldehyde are mainly used in the rubber industry and wood processing (wood adhesives). Compared to other phenols, the resorcinol exhibits a significantly higher reaction rate towards formaldehyde [49-51]. The chemical structure of resorcinol is shown in Figure 5.

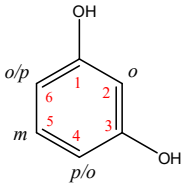

Figure 5: Resorcinol molecular structure [51].

Electrophilic substitution is the most common reaction, which occurs on an aromatic ring. The electrophile reacts with an aromatic ring and replaces one of the hydrogens. This reaction is typical of all aromatic compounds, not only benzene and benzene derivatives. Different substituents are already bonded to the aromatic rings through the substitution reactions. The benzene ring can be substituted by various electrophile groups such alkyls (-R), nitro (-NO_2), halogens (-Cl, -Br, I), hydroxyls (-OH), sulfonic

acid (-SO_3H), or acyls (-COR). The presence of these substituents has two effects [52-55]:

a. Reactivity of the aromatic ring

Some substituents enhance the activity of the ring, making it more reactive than the benzene, and others deactivate the ring, causing less reactivity than benzene. In the nitration of aromatic compounds, for example, an –OH substituent increases the ring reactivity to 1000 times more than benzene, while –NO_2 group makes the ring less reactive (Figure 6).

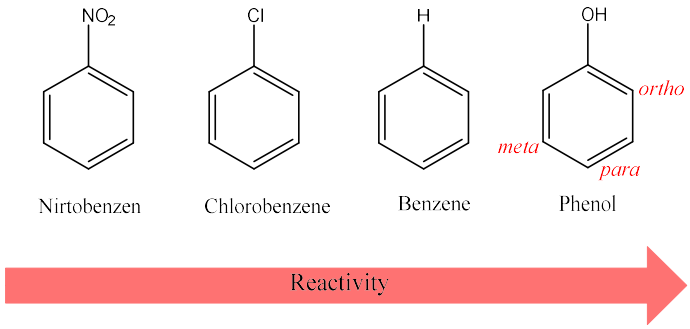

Figure 6: Effect of substituents on the aromatic nitration.

The general mechanism form of electrophilic substitution reaction can be stated in two stages: electrophilic attack to give an intermediate cation and restoration of the aromaticity by deprotonation of the cation (Figure 7).

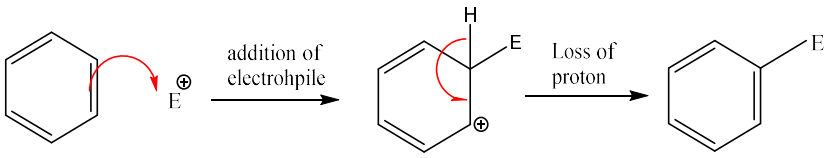

Figure 7: Proposed mechanism of electrophilic aromatic substitution [54].

b. Orientation of the reaction

The pre-existing substituent controls both the rate and distribution of products formed in the second electrophilic substitution reactions. The incoming substituent attacks the aromatic ring at three possible positions of ortho (*O*-), meta (*m*-), and para (*p*-) in respect to the already present substituent. It is crucial to control factors that are likely to stabilise or destabilise the different possible intermediates formed during the reactions as these intermediates affect the properties and feature of the final products. The ability of the already present substituent either donate or withdraw electron density

from the aromatic ring determines the orientation/structure of products. Figure 7 shows the effect of a considered group Y, on the electron density of the benzene ring.

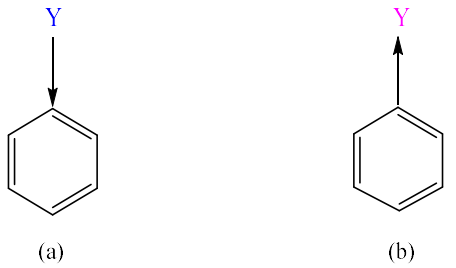

Figure 8: Effect of a substituent on the electron density of the aromatic ring [53].

If Y is an electron-donating group, the ring gains electron density and becomes more reactive toward attacking by an electrophile (Figure 8a). The aromatic ring loses electron density if the Y is an electron-withdrawing group (Figure 8b). Low electron density of the aromatic ring makes it less reactive toward an electrophilic attack. Substituents can be categorised into three groups: ortho-para directing activators (-OH, $-NH_2$, -R, -OR, -SR), ortho-para directing deactivators (Halogens), and meta directing deactivators ($-NO_2$, $-CF_3$, $-CO_2R$, $-NR_3$).

For the ortho-para directing substituents, a ring substituent (Y), which possesses an electron pair on the atom adjacent to the ring contributes to ortho-para substitution in favour of meta substitution (Figure 9). Therefore, the intermediate can be stabilised by the electron-donating resonance effect from the substituent that activates the ortho and para positions only.

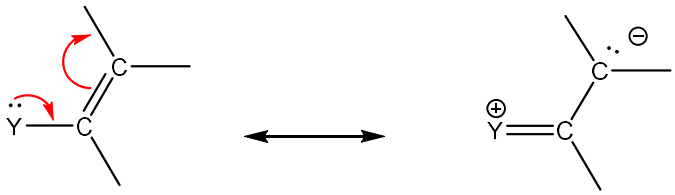

Figure 9: Electron-donating resonance effect [55].

This consequence can be undoubtedly noticed in the structure of ortho and para intermediates from phenol, which is stabilised by the oxygen atom, as illustrated in Figure 10. In contrast, there is no such effect for the electrophilic attack on the meta position. The ^1H NMR (proton NMR) also indicated that the high electron density

surrounding the nucleus results in the smaller shift. Hence, the chemical shifts for the ring proton in the benzene are larger than those for phenol.

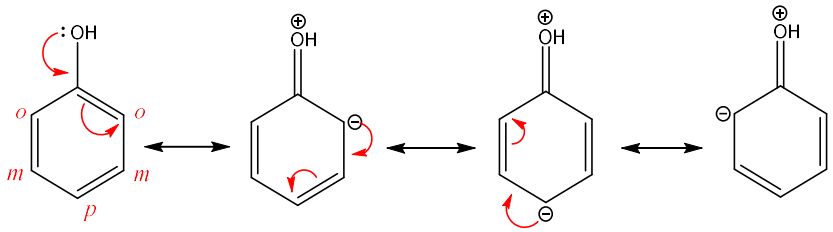

Figure 10: Resonance structure of phenol [56].

The resorcinol is a trifunctional monomer (Figure 5) with two hydroxyl groups, located at the 1- and 3- positions in the benzene ring. This unique structure allows adding of up to three equivalents of formaldehyde 2,4 and 6 positions [57], which makes the resorcinol highly reactive precursor compared to the phenol. The hydrogen atoms next to the hydroxyl groups are reactive positions, specifically those bonded to the carbon atoms at 2, 4 and 6 positions, while hydrogen atom at position 5 is an unlikely reactive position.

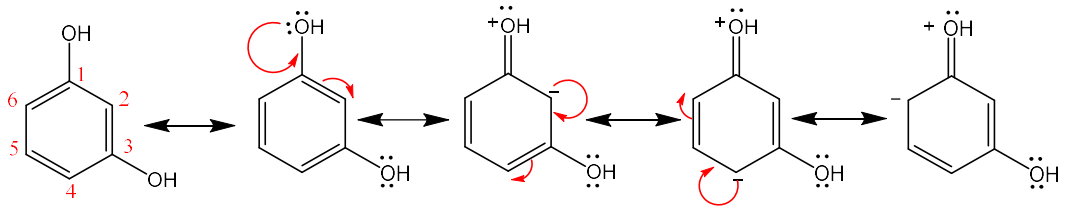

Figure 11: General resonance forms of resorcinol anion [48, 58].

In order to understand the ionisation processes, which are responsible for the substitution reactions, it is essential to consider the probable resonance structure of resorcinol (R). These forms are represented in Figure 11 and show the activation nature of carbons 2, 4 and 6, while carbon 5 remains unreactive under standard reaction conditions. Lack of stability on meta-position can hinder the electrophile attack at this carbon atom, as shown in Figure 12 [49, 51, 58-60]. Also, extensive studies have indicated that there is no evidence of electrophilic substitution reactions at carbon 5 (meta) position [50, 61-66].

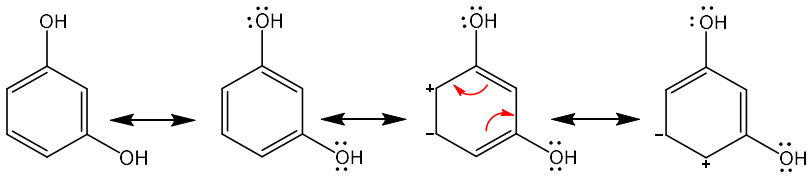

Figure 12: Resonance of resorcinol anion at the meta position [53].

1.3.1.2 Formaldehyde

Formaldehyde (F), or methanal, is the simplest aldehyde compound containing a carbonyl group (C=O). The carbonyl is the most critical reactive functional group among the organic compounds used here [52, 54]. Figure 13 shows this highly polar electrophilic carbon centre, which can react with the active positions in the resorcinol ring.

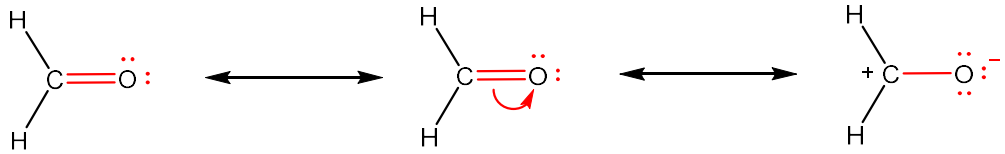

Figure 13: Resonance forms of formaldehyde molecule [54].

In the resonance form of F (Figure 13), The carbonyl carbon atom has a positive charge, and carbonyl oxygen has a negative charge. As a result of this dipolar resonance structure, the carbon atom attracts the negatively charged nucleophiles (like an activated carbon in resorcinol anion). Conversely, the oxygen atom reacts with electrophiles [52, 56].

The most common reaction of aldehydes is the nucleophilic addition reactions, in which a nucleophile (Nu^-) attacks the electrophilic carbonyl carbon atoms. The nucleophile adds an electron pair to the carbon atom moving an electron pair from the carbonyl double bond toward the oxygen atom to give an alkoxides anion (tetrahedral) intermediate. The nucleophilic addition is followed by protonation of the alkoxide ion [52, 67] as shown in Figure 14.

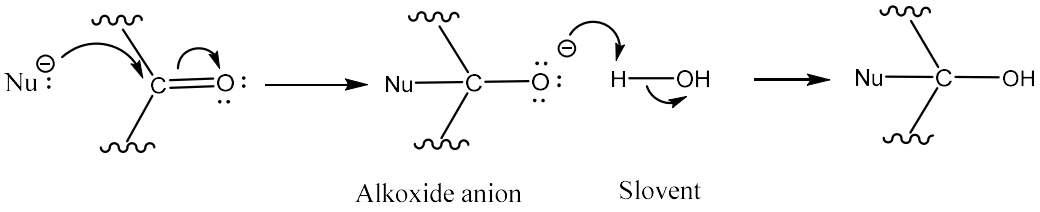

Figure 14: Nucleophilic addition reaction of aldehydes under basic condition [52, 54].

Figure 14 represents the nucleophilic addition reaction under basic condition. However, under acidic condition, a proton reacts with the carbonyl oxygen atom to produce a conjugated acid (oxonium ion). The conjugate acid is an alternate resonance form with a positive charge, which makes the structure more reactive than the uncharged carbonyl group [54], as illustrated in Figure 15. Therefore, the nucleophilic addition reaction can occur with less reactive electrophiles under this condition.

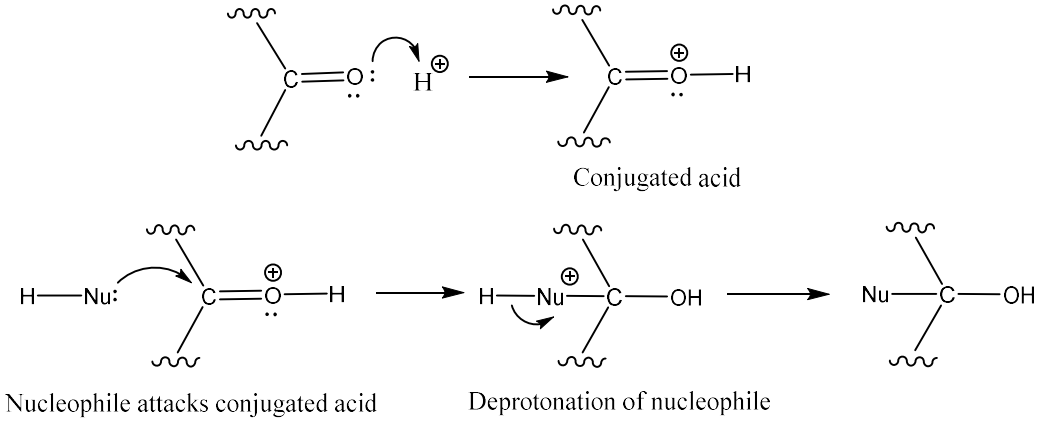

Figure 15: Nucleophilic addition reaction of aldehydes under acidic condition [54].

In the case of using a hydroxylic solvent as a reaction medium (Figure 16) such as ethanol, C_2H_5-O-H protonates the alkoxide ion. The conjugate base of solvent regenerates the uncharged nucleophile by removing a proton from H-Nu [67].

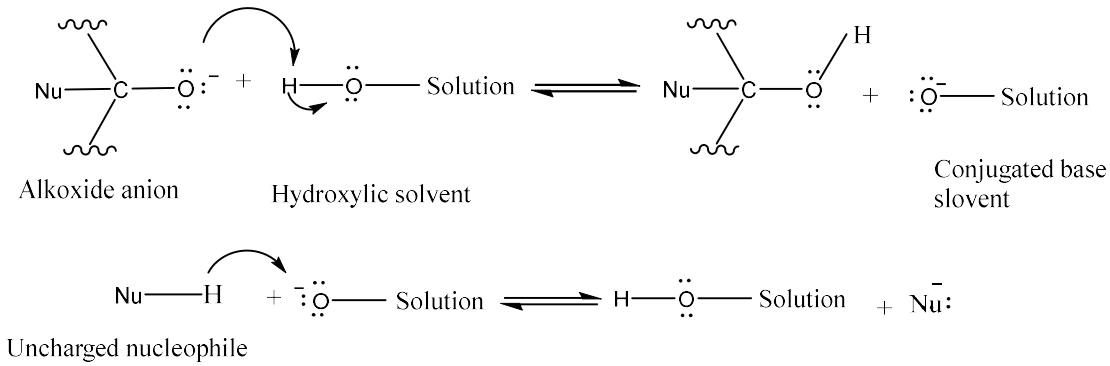

Figure 16: Effect of hydroxylic solvents on the uncharged nucleophiles.

At ambient pressure and temperature, formaldehyde is a colourless gas with strong and pervasive odour. As a result of high reactivity and instability of a gaseous state of formaldehyde, it is usually handled as aqueous solutions. These solutions contain variable concentrations of methanol and formaldehyde [59, 68]. In such aqueous solutions, formaldehyde is chemically dissolved in solvents, where it is hydrated and methoxylated (Scheme 1) to form monoglycol (MG, HO-CH_2-OH), methoxy monoglycol (MMG, CH_3O-CH2-OH), poly (oxymethylene) glycols ($HO(CH_2O)_n$ H; n>1), and hemiformals of methylene glycols with methanol. [59, 69-71].

$$CH_2O + H_2O \rightleftharpoons HOCH_2OH \qquad \text{Hydration}$$

$$CH_2(OH)_2 + HO(CH_2O)_{n-1}H \rightleftharpoons HO(CH_2O)_nH + H_2O \qquad \text{Polymerisation}$$

Scheme 1: Hydration and polymerisation of Formaldehyde in aqueous solution.

As shown in Scheme 1, MG polymerises to produce a series of polyoxymethylene glycols (oligomers) such as dimethylene (DG, $HO(CH_2O)_2H$) or trimethylene glycol (TG, $HO(CH_2O)_3H$). Since these polymerisation products cause solid precipitation in, methanol is added to form hemiformal (hemiacetal), i.e. methoxylated methylene glycol (MMG, $HOCH_2OCH_3$), which condenses to give poly(oxymethylene) hemiformals $HO(CH_2O)_n$ CH_3 [70, 72] (Scheme 2).

$$HOCH_2OH + CH_3OH \rightleftharpoons HO(CH_2O)CH_3 + H_2O$$

$$HO(CH_2O)_{n-1}\,CH_3 + HO(CH_2O)CH_3 \rightleftharpoons HO(CH_2O)_nCH_3 + H_2O$$

Scheme 2: Methoxylation of MG and polymerisation of its oligomer.

Gaca et al. [65, 72, 73] have recently investigated species present in formaldehyde aqueous solution and early stage of RF polymerisation. Infra-Red, Raman spectra and nuclear magnetic resonance (NMR) were exploited to detect these intermediates in the formaldehyde-water-methanol system. For formaldehyde aqueous solutions, the obtained results indicated that these solutions contain formaldehyde species, including MG and MMG at the excessively water and methanol diluted system, respectively. While at the highest formaldehyde levels, a complex mixture of oligomers was present. On the other hand, during the initial reactions of RF solution, it was also confirmed the presence of species of MG, DG and MMG within the mixture. These observations were in agreement with the previous findings reported by Lewicki et al.[74], Kristin [63] and Werstler [57].

The diversity of formaldehyde aqueous solutions reflects the addition of a methylene group, diglycol or both to resorcinol ring [62, 65]. However, the presence of these formaldehyde-derived species could lead to the formation of other complex structures during the RF polymerisation reactions [74].

1.3.2 Alternative raw ingredients

1.3.2.1 Alternative phenols

Phenols are aromatic compounds with at least one hydroxyl group attached to one or more carbon atoms in the benzene ring. Phenol (carbolic acid) is the most common precursor in the synthesis of organic aerogels. All other members of the phenolic family can be considered as derivatives of phenol, and different species have been used to prepare various phenolic-based materials. These phenol derivatives include alkylphenols (cresols and xylenols), di-hydroxybenzene (catechol and hydroquinone), bisphenols (bisphenol-A), and tri-hydroxybenzene (pyrogallol, hydroxyhydroquinone, and phloroglucinol) [75-81]. Figure 17 shows the chemical structures of some of these substances.

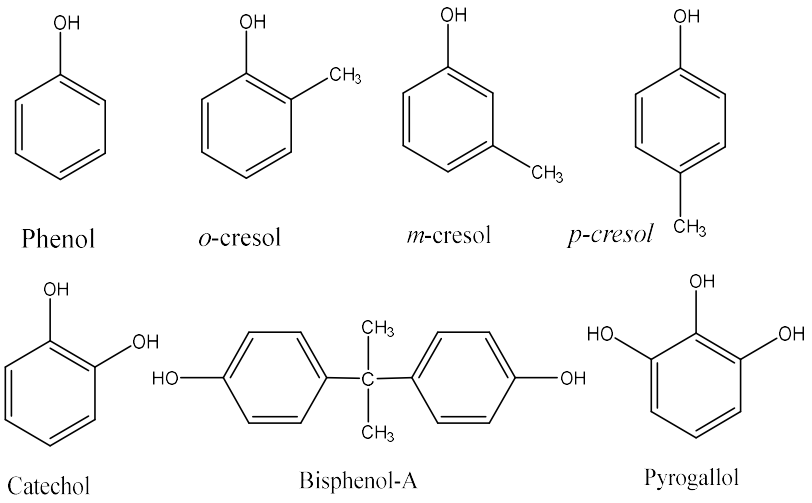

Figure 17: Alternative phenols to resorcinol for the synthesis of phenolic gels [81].

Phenol has been extensively used in the preparation of the phenolic resins [78, 82-85], because of its low production cost and availability [59, 86]. In contrast, the multi hydroxyl phenols (e.g. pyrogallol) have shown remarkable structural textures. The pyrogallol and formaldehyde can rapidly react to provide higher density cross-linked network compared with resorcinol-formaldehyde reactions. This highly branched structure results in low shrinkage gels during the drying step. It is essential to produce Low shrinkage organic gels, to synthesis carbon aerogels for particular applications such as the electrical conductors [87, 88].

However, these compounds have lower reactivity than the resorcinol. They also possess health and safety issues such as the high toxicity (e.g. phenol, pyrologl), which requires controlled and restricted exposure limits [51, 59]. The alkylphenols (cresols and xylenols) exhibit lower active carbon atom positions due to the presence of alkyl groups [52]. Low solubility in water considered as another drawback of these compounds [81].

1.3.2.2 Alternative aldehydes

Formaldehyde is principally the only aldehyde compound used in the synthesis of common phenolic-based materials. The other aldehydes, such as acetaldehyde, propionaldehyde, glyoxal or furfural (Figure 18) can be utilised in the preparation of particular materials. These alternatives have not attained much commercial significance [59].

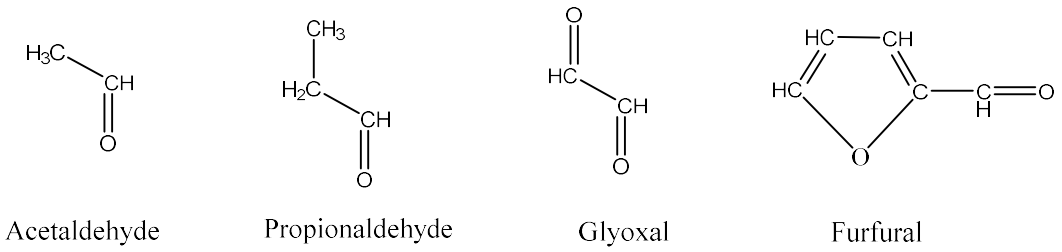

Figure 18: Alternatives to formaldehyde as a reagent in the synthesis of phenolic gels [59].

Phenolic resins obtained using the aliphatic aldehydes exhibit specific characteristics, which may not be provided by the RF resins [51]. The cyclic aldehydes such as furfural can react with the resorcinol and produce organic gels; with large mesoporous volume and high surface area [89]. Recently, the furfural has been derived from renewable resources (biomass), resulting in low environmental impact. It possesses low toxicity compared with the formaldehyde [90].

In the other hand, the alternative aliphatic aldehydes have shown low solubility in water. They are also highly flammable and explosive materials [59]. The low production capacity of furfural using the promising synthesis methods can limit its applications [90].

1.3.3 RF reaction

The mechanism of resorcinol-formaldehyde (RF) reactions has been considered by many researchers [37, 63, 65, 66, 74, 91-94]. The RF polymerisation process involves two primary reaction steps: (1) an addition reaction between resorcinol and formaldehyde to produce hydroxymethyl derivatives of resorcinol; and, (2) the condensation of these hydroxymethyl groups to form clusters, which then crosslink to create the three-dimensional network structure of the gel.

Since these polymerisation steps take place simultaneously, the ratio between addition and condensation has a significant effect on the determination of the final texture of the wet gel. In fact, at faster addition reaction rate, several hydroxymethyl derivatives are formed before the gelation occurs, leading to the formation of small primary clusters; which give small solid structures and small pore sizes. On the other hand, when the condensation reaction is faster, large primary clusters are formed as a result

of the quick reaction between the hydroxymethyl derivatives with each other; which leads to sizeable polymeric structure and large pore sizes [38, 95, 96].

The addition reaction depends mainly on either the deprotonation of resorcinol or the protonation of formaldehyde (see Section 1.3.1) [96]. This reaction begins with the formation of the resorcinol anion (alkaline condition) or activation of the carbonyl carbon on formaldehyde molecule (acidic conditions), such ionised products are more reactive and sensitive than the original molecules of resorcinol and formaldehyde. These ionised molecules can prompt the addition of formaldehyde to the benzene to produce hydroxymethyl derivative intermediates [37, 51, 97]. The formation degree of these reactive intermediates determines the rate of subsequent condensation reaction [66]. The condensation reactions are more complicated than the addition reactions. These reactions are catalysed by proton H^+ (in the form of H_3O^+ anion at an acidic condition). During this stage, the hydroxymethyl groups condense with each other to form methylene linkages [95, 96, 98, 99]. The average number of formed methylene bridges depends on the rate of both addition and condensation reactions. Those simultaneous polymerisation reactions result in the cross-linked network of the wet RF gels [64].

The kinetics of RF reaction were studied using various techniques. However, there are a few contributions to that part of reaction kinetics concerning the rate and heat of reactions [35, 61, 74, 93]. In 1981, Šebenik et al. were the first who used the differential scanning calorimetry (DSC) combined with high-performance liquid chromatography (HPLC) to investigate the reaction between R and F [61]. Based on the analysis of Borchardt and Daniel [100] and validation of Reed et al. [101], they applied the activation energy and reaction order calculations to determine the kinetic parameters for these reactions. The obtained result showed that the activation energies for addition and condensation reactions were 95.0 and 120.0 kJ $mol^{-1,}$ respectively. For the first RF polymerisation step, order two kinetics, and for the second step, order one of the reaction was achieved [61]. These observations are consistent with the proposed reaction of other two phenols (phenol or o-cresol and formaldehyde) [102, 103], and in agreement with the recent findings concluded by Kinnertova et al. [93] and Lewicki et al. [74] on the reaction order for the addition and condensation respectively.

The RF polymerisation reaction scheme depends on the synthesis conditions, such as temperature, initial pH, and concentration of reactants (dilution rate). These factors could influence the nanometre-sized cluster formation. At room temperature, the rate of these reactions is prolonged, and the solution of precursors is generally heated to initiate the gelation reaction. The polymerisation reactions occur under basic or acidic conditions. Therefore, different catalysts can be used to promote gelation; sodium carbonate (Na_2CO_3) is the most widely used catalyst in the preparation of RF sol-gels [19, 51, 104-106].

1.3.3.1 Base-catalysed reactions

Under alkaline conditions, resorcinol anion is formed as a result of deprotonation of the resorcinol ring. This proton abstraction activates the benzene ring, and the electron density increases at positions *ortho* and *para* [48, 106], as shown in Figure 19. The resorcinate ion increases the reactivity of the aromatic ring, which favours the formaldehyde attack, and subsequent formation of hydroxymethyl derivatives known as methylol groups ($-CH_2OH$).

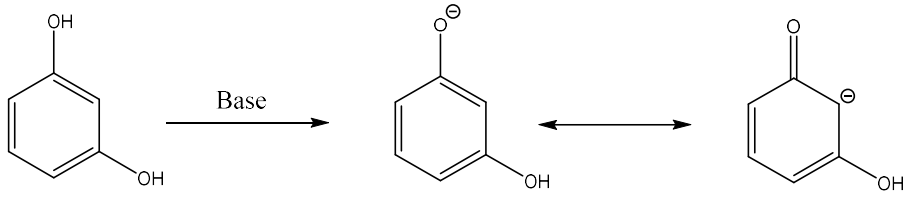

Figure 19: Deprotonation of resorcinol to form a resorcinate ion.

These intermediates can activate the other ring positions and react with excess formaldehyde to form hydroxymethyl (dimethylol) groups. Hydroxymethyl derivatives undergo further substitution reaction with resorcinol and formaldehyde, before condensing to form a methylene ($-CH_2-$) and methylene ether ($-CH_2OCH_2-$) bridges, which crosslink to form oligomer chains. The final gel is formed as a result of aggregation and curing of these oligomer chains [48, 51, 107, 108]. The general mechanism (proposed) of the RF base catalysed reactions can be seen in Scheme 3.

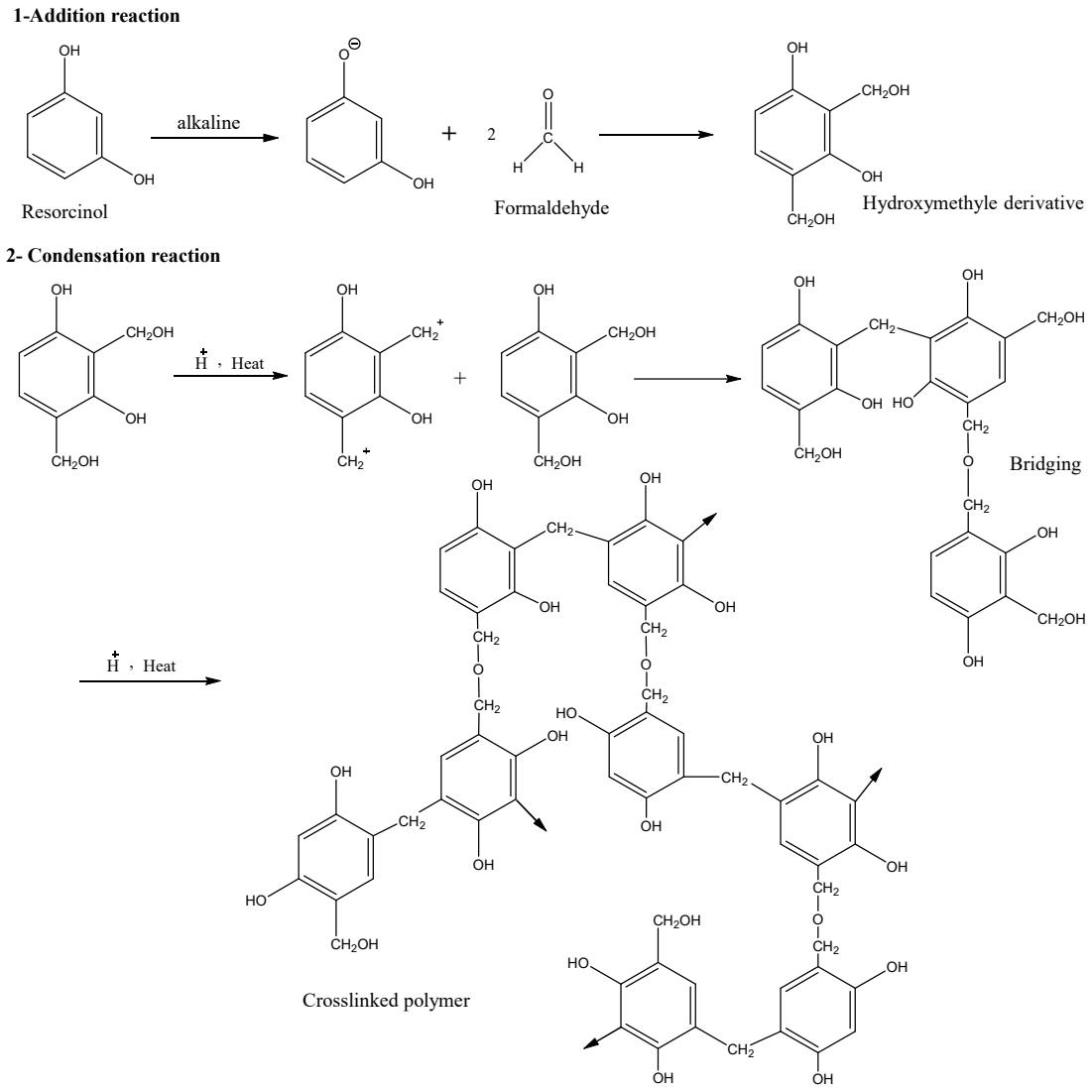

Scheme 3: General proposed base-catalysed RF reactions [48, 98, 109].

Also, Scheme 3 depicts that most of the methylene groups (-CH_2OH) are absent in all RF condensates due to the high reactivity of resorcinol under alkaline conditions. Under the basic condition, the methylene groups are unstable, and could rapidly convert to hydroxybenzyl carbonium ions or quinone methides in the presence of the resorcinate anion. Formation of quinone methides can enhance the reactivity of resorcinol. These quinone methides undergo further reactions with another resorcinol molecule to form stable methylene bridges [48, 50, 51, 66]. Scheme 4 shows the formation of quinone methides and its reaction to produce the methylene linkages.

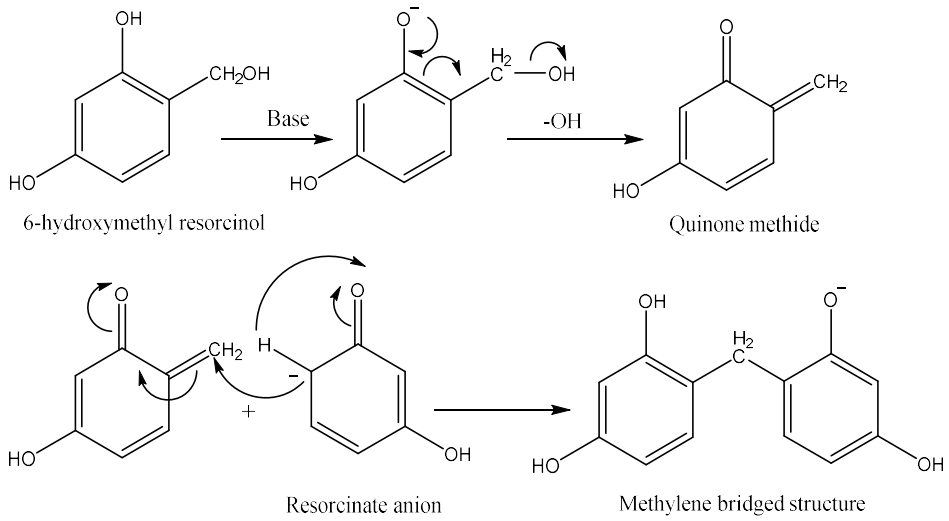

Scheme 4: Proposed mechanism for formation of resorcinol- quinone methides and subsequent methylene bridged intermediates under basic conditions [48, 51].

1.3.3.2 Acid-catalysed reactions

By contrast, the acid-promoted reaction between resorcinol and formaldehyde is based on enhancing the reaction by activating of formaldehyde. Under acidic conditions, formaldehyde is activated through the protonation reaction illustrated in Scheme 5.

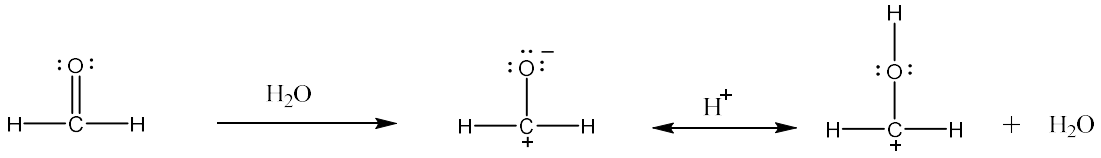

Scheme 5: Protonation reaction of formaldehyde [58].

Scheme 6 depicts that the protonated formaldehyde species can be attacked by the high electron density positions of resorcinol molecule to form hydroxymethyl derivatives. Subsequently, these intermediates react with resorcinol, formaldehyde and other hydroxymethyl derivatives via condensation reactions, which involve the production of water, leading to methylene bridged oligomers formation. During this type of polymerisation, the intermediates such as quinone methides can be formed as a result of inter-molecular water elimination. Quinone methides can lead to further condensation. The produced oligomers grow to form clusters, which then crosslink, forming the polymeric gel network [51, 110].

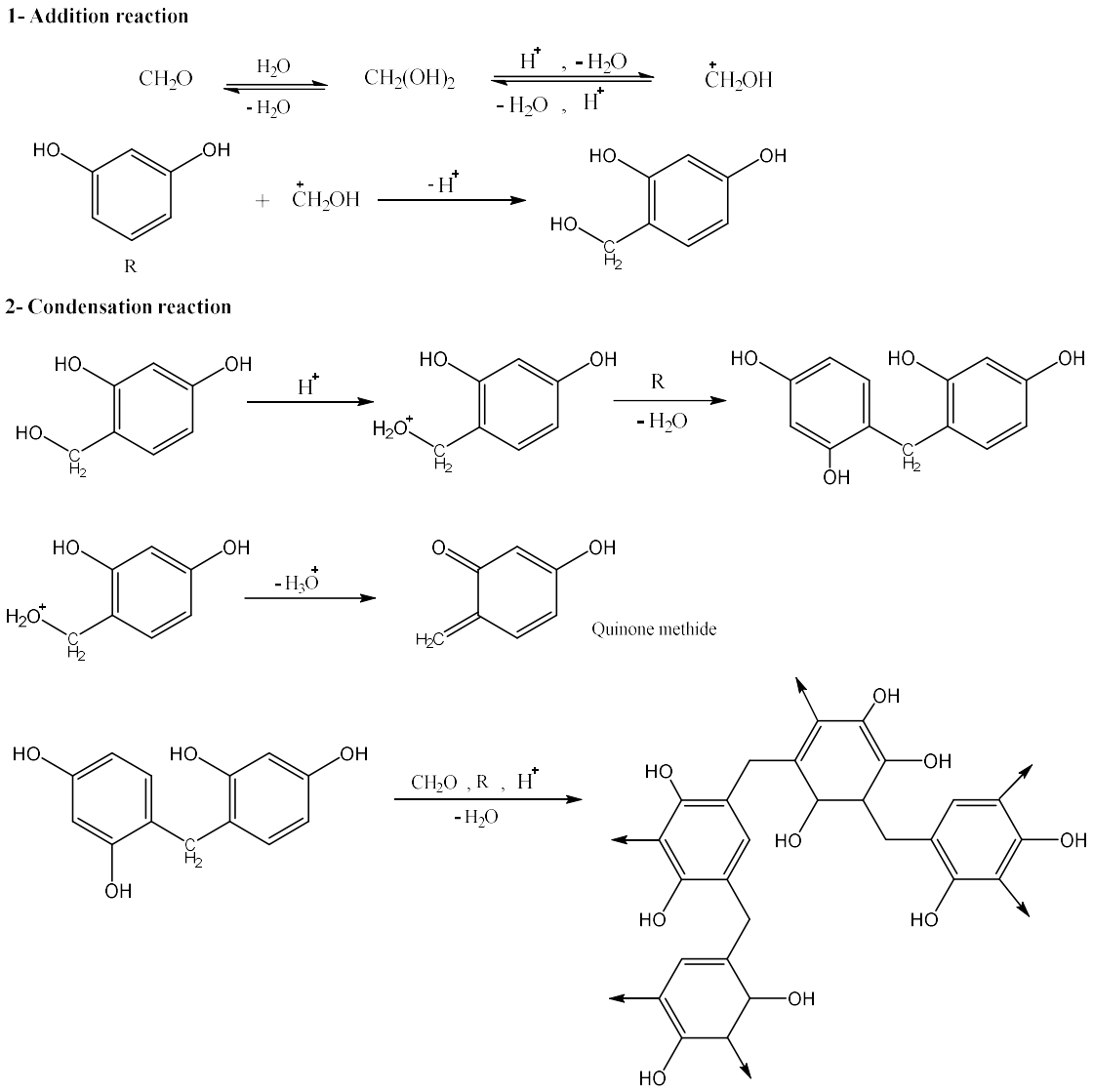

Scheme 6: Proposed acid-catalysed RF Reactions.

1.3.3.3 Uncatalysed reactions

Due to the high reactivity of R compared to other phenols (Section 3.2.1), resorcinol can react with formaldehyde at ambient condition without any catalyst [51]. Raff and Silverman [111] investigated the kinetics of the uncatalysed resorcinol-formaldehyde reaction. This study reported that the reaction was the first order for different molar ratios of resorcinol to formaldehyde (R/F) at various temperatures. It also compared the rate constant for this reaction at, 90 ºC, to the rate constant of a catalysed phenol (P) and F reaction, at 98 ºC, and concluded that the rate constant for uncatalysed RF reaction was 2.54 times that of the PF reaction. This comparison reveals the considerable reactivity of R toward F without the presence of the catalyst. Another

study focused on a non-catalysed equimolar RF (1:1) reaction conducted at room temperature [57]. A quantitative ^{13}C NMR spectrometry was used to monitor the reaction. The assignments of NMR peaks indicated that methylene bridges appeared as intermediates during the early stages of this polymerisation reaction.

1.4 RF gel synthesis

As previously mentioned (Section 1.2.2), resorcinol-formaldehyde gels can be processed via a sol-gel route. Multi-step sol-gel processing is the most commonly utilised method in the preparation of these materials. This synthetic technique involves a sequence of steps starting with initial precursors to achieve the desired final product. However, these steps required to be conducted individually, and it can be noticed that this method is not a complicated process. A typical flowchart for multi-step sol-gel synthesis [8] to produce RF gels according, to Pekala's approach [36], is shown in Figure 20.

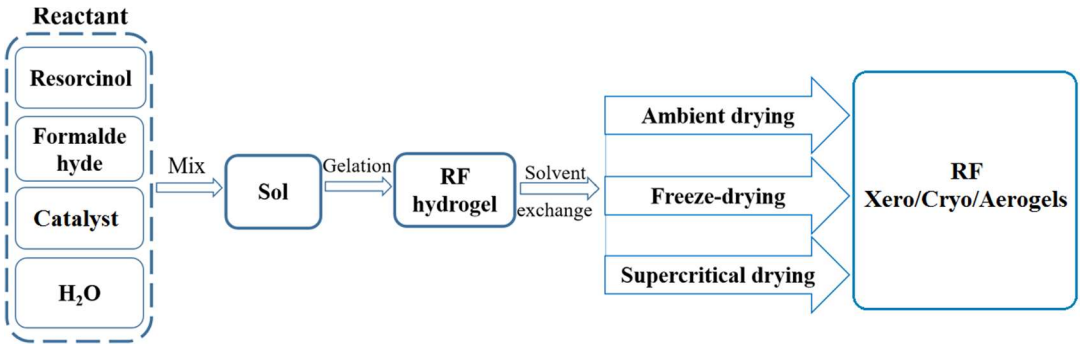

Figure 20: Multi-step RF gels/carbons synthesis [112].

1.4.1 Sol-gel transition

As discussed above (Section 1.3.3), the mechanism of RF polycondensation is associated with two essential reactions: (a) formation of hydroxymethyl derivatives of resorcinol via an addition reaction, and (b) condensation of these derivatives to form methylene and methylene ether bridged intermediates, leading to highly cross-linked clusters. Primary particles are then formed, and start to aggregate; as a result, the initial precursor solution loses fluidity (a sol no longer pours at an angle of 45°), producing a three-dimensional solid network, referred to as a gel. The period that it takes to transition from sol to gel is called gelation time, while the precise moment at which the gel is acquired is named as the gelation point. This multi-stage process is known as the sol-gel transition. The porous structure of the formed wet gel is controlled by

this sol-gel transition process [9, 43, 48, 106, 113-115]. General sol-gel conversion merely is illustrated in Figure 21.

As mentioned earlier (Section 1.3.3), the activated resorcinol and formaldehyde molecules can increase the reactivity of RF mixture via electrophilic and nucleophilic attacks, respectively. The number of formed hydroxymethyl derivatives (substituted resorcinol molecules) during the addition reaction plays a crucial role in the extent of condensation reactions, hence the degree of branched structure of this material [62]. The phenolic sol-gel transition is considered as a step-growth polymerisation process. It is a dynamic process in which the continuing cross-linking clusters result in the solidification of the gel network.

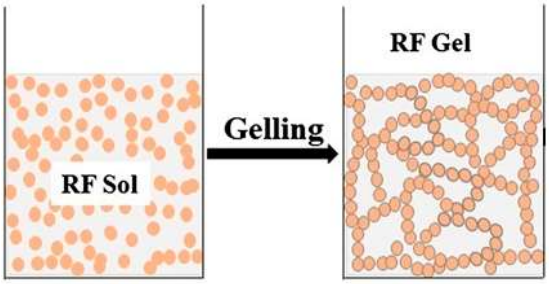

Figure 21: Schematic diagram of a simple sol-gel transition [116].

It should be noted that the sol-gel mechanism has been disputed in previously published works, with two opposing theories suggested; (1) colloidal aggregation or (2) microphase separation [117].

1.4.1.1 Colloidal aggregation

The International Union of Pure and Applied Chemistry (IUPAC) defined the colloidal suspensions (a state of subdivision) as systems in which particles of colloid size (ranging from 1-1000 nm in diameter) of any state of matter (gas, liquid or solid) are dispersed in a continuous phase of a different composition or state [118]. Yamamoto *et al.* traced the RF sol-gel transition by light-scattering techniques. The obtained results revealed that colloidal particles proliferate during the early stages of the sol-gel transition process. The growth of these colloidal particles could be related to the aggregation process [119]. Firstly, each particle grows at the active positions, before aggregation with each other to form a consistent structure, and finally the formation of the cross-linked network (formation of RF hydrogel) [120] as shown in Figure 22.

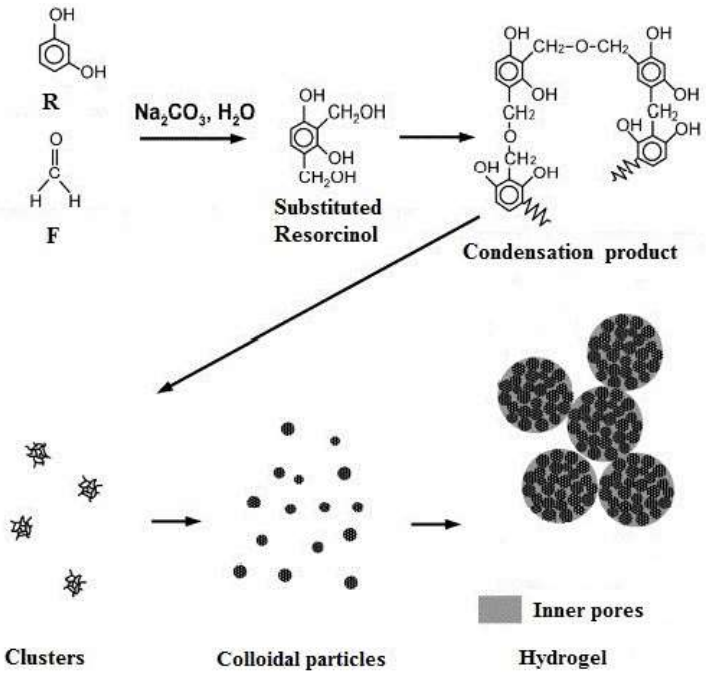

Figure 22: Aggregation of colloidal particles in sol-gel polymerisation of resorcinol and formaldehyde [114].

Other studies agree with this hypothesis; Tamon and Ishizaka [121] investigated the formation of RF hydrogel using a small-angle X-ray scattering (SAXS) technique. The proposed model is based on the formation of small clusters of ~ 2 nm during the initial stage of the processing of RF hydrogel. These clusters comprise branched arrays with a mass fractal characteristic. Then the clusters aggregate to form particles of ~ 3 – 6 nm, which exhibit surface fractal features. The final hydrogels consist of the particles of ~ 4 – 7 nm.

1.4.1.2 Microphase separation

According to this model, the monomer molecules polymerise and form branched structure, in which the cross-linked polymer network and the solvent (reaction medium) are mixed at the molecular level. As the molecular weight of the branched polymer increases, the solubility of the polymer in the solvent decreases, which initiates a demixing process. During the demixing, the significant particles phase separation causes polymer network to fold up, creating a dense structure (i.e. gel) filled with solvent [117]. The microphase separation can occur in two different mechanisms: nucleation-growth and spinodal decomposition (Figure 23). Within this theory, the transition from nucleation-growth to spinodal decomposition as the polymerisation

proceeds, leading to the string-pearl structure of the formed material [40]. The period between phase separation and sol-gel transition, along with the stability of the different phases determine the texture of the obtained porous structures [122].

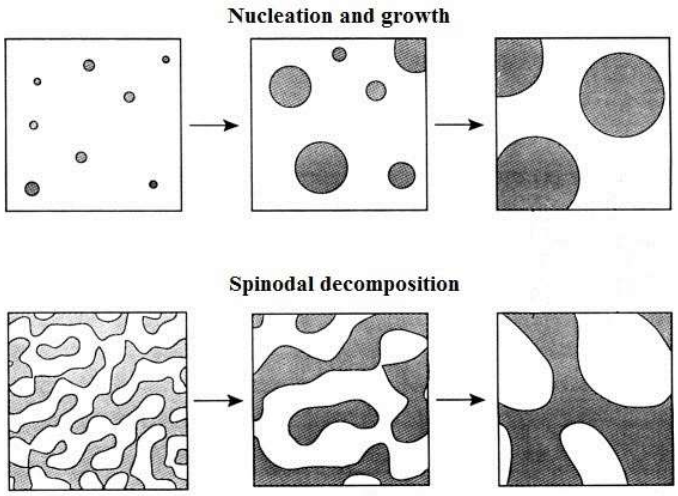

Figure 23: Schematic of time evolution of structure in phase separation phenomena [123].

The theory of microphase separation has been emphasised for RF gels and other organic sol-gels. Pekala et al. [40, 124, 125] reported no evidence of fractal clusters within the final gel structure within the studied organic aerogels. For all synthesis conditions, the findings demonstrate that microphase separation is the dominant process controlling the morphology of these materials with restriction to a specific nanometre scale. In their study, Schwan and Ratke [45] were mostly in agreement with these findings. It was noticed that the phase separation could occur as a result of changing the concentration of the precursors within the solvent.

The two theories discussed above represent two opposing processes of RF sol-gel transition; however, both result in similar morphologies with '*string of pearl'* form. Berthon et al. [115] proposed that both mechanisms (microphase separation and colloidal aggregation) occur, but not at the same time as the RF polymerisation proceed.

With a further study by Gommes and Roberts [117], observed the formation of RF gels using SAXS analysis. They assumed two different mechanisms; (i) biphasic RF gel contains polymer and solvent, with retaining the total volume of the polymer during the sol-gel transition (ii) the RF gel morphology exhibits two different length scale.

These specific structure models involve (Figure 24): model A, in which the gel skeleton consists of a dense polymer with a small-scale structure that filled with colloidal suspension, while in model B, a liquid phase filling the largest pores. The model B also comprises micropores within the gel backbone.

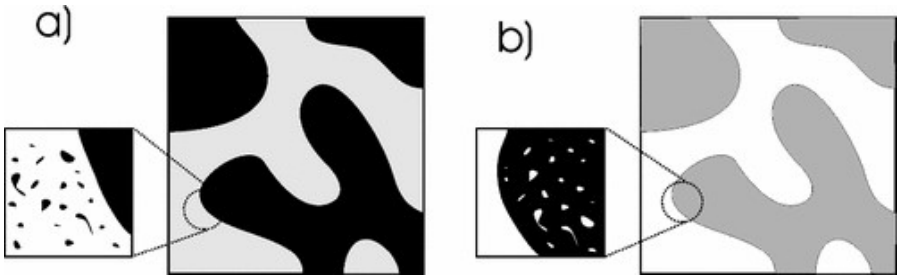

Figure 24: Schematic of the proposed two-scale models: model A (a) and model B (b) [117].

The interpretation of SAXS data corresponds to the two discussed theories. In the model A (colloidal aggregation), as the RF reactions proceed the polymer network reacts with the surrounding liquid suspension (condensation), leading to an increase in the volume of RF backbone and decrease in the polymeric suspension, however, some of this suspension within the pores aggregates increasing the colloidal suspension inside the pores. In model B (phase separation), it is hypothesised that the polymer backbone consisting of a high volume of polymeric particles with several pores. As the polymerisation proceeds and the polymer network becomes incompatible with the solvent liquid, the solvent extraction from the pores is propagated, resulting in a decrease in the total volume of the polymer backbone. This model also indicated a decrease in the volume fraction of the pores within the polymer structure. However, an increase in the overall volume of micropore has been reported. It was stated that the SAXS data do not enable differentiation between the two mechanisms of sol-gel transition. The findings also reveal that aggregation and microphase separation can generate identical morphologies at the particular length scales investigated by the SAXS technique [117].

More recent work by Gaca and Sefcik [92] suggests that the polymerisation, phase separation, coalescent and colloidal aggregation phenomena, could eventually collaborate in the gel formation process, depending on the concentrations of reactants and catalyst. Furthermore, their finding stated that the size of primary clusters is

thermodynamically controlled, in agreement with the succeeding study conducted by Taylor et al. [126].

1.4.2 Curing

After the gelation point, the previously formed polymeric clusters continue to grow for an extended period under high-temperature conditions. This step is named as curing, in which the material reinforced as a result of further condensation reactions and limited evaporation of the solvent. Curing time is crucial to allow satisfactory completion of cluster crosslinking, which prevents swelling of the structure during the subsequent stages described below [35, 43, 106]. The structure of expected clusters growth during the gel formation is illustrated in Figure 25, showing the curing step.

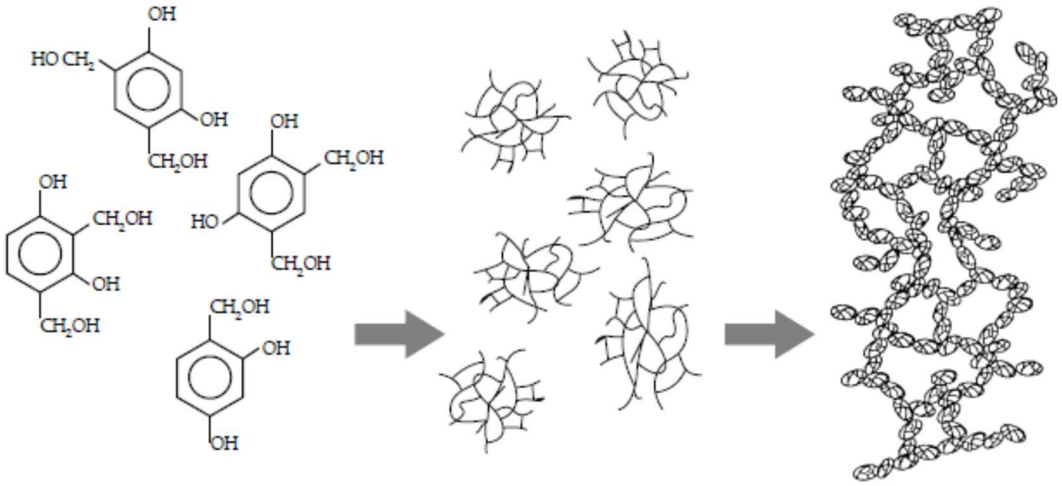

Figure 25: Schematic diagram of the structure of expected cross-linked polymer network of RF gel. Left: substituted resorcinol (initial reaction), middle: cross-linked clusters (during the gelation), and right: Inter-connected cluster (curing) [127].

1.4.3 Solvent exchange

Once the gelation and curing steps are complete, it is essential to replace the remaining aqueous solution (reaction medium) with a fresh organic solvent, such as acetone. The solvent exchange process reduces deviations of surface tension within the evaporation stage, which plays a significant role in minimising any cracking and shrinkage during the drying of the gel. Multiple exchanges can be performed to enhance the removal of the residual solvent. Different liquid solvents have been used in exchange processes, including methanol, ethanol, isopropanol, and cyclohexane. Solvent selection is based on the solubility of water, and the drying approach implemented [9, 35, 37, 106, 128].

Solvent selection criteria and their influences on the prepared RF gels are discussed in Section 1.5.10.

1.4.4 Drying

The final stage involved in the RF gel synthesis is the drying process. The drying of nanoporous materials is a complicated process compared with that used for conventional materials; as the solvent trapped in the network structure, need to be carefully removed to avoid damaging the skeletal microstructure of the gels. During the drying step, it is vital to consider the collapse of porous structured gels, agglomeration of clusters (primary particles), the persistence of chemical reaction, and evaporation of solvents [129-132].

Solvent evaporation occurs during the three stages of the drying process: constant rate period (CRP), first fall rate period (FRP1) and second fall rate period (FRP2). In the CRP, the rate of drying is independent of time and thickness of the gel. Furthermore, the decrease in gel volume is equal to the solvent evaporation rate. Hence, the pores of the gels are always filled with solvent during this stage, as illustrated in Figure 26 (b). As the shrinkage of gels initiated, the backbone of the gel is downy and capillary tension taking place on the gel is negligible. When the gel backbone shrinks and tends to become harder, its resistance against shrinkage is reinforced, while the capillary force increased simultaneously. In the CRP, liquid (solvent and residual reactants) flow rate from the interior pores to the surface is equal to the liquid lost by evaporation. Liquid transport occurs by flow; whereas the diffusion represents a small fraction of the total liquid flux. At the end of this stage, the shrinkage rate of the gel is no longer equal to the solvent evaporation rate, resulting in the exposure of the solid surface to the first falling rate drying period. The transition stage from CRP to FRP1 refers to the critical drying point, at which the radius of curved liquid is close to the size of gel pores, the capillary force attains the highest rate, and shrinkage of the gel backbone is most likely to stop. After the critical point, the liquid/vapour meniscus draws back into the gel pores [3, 129].

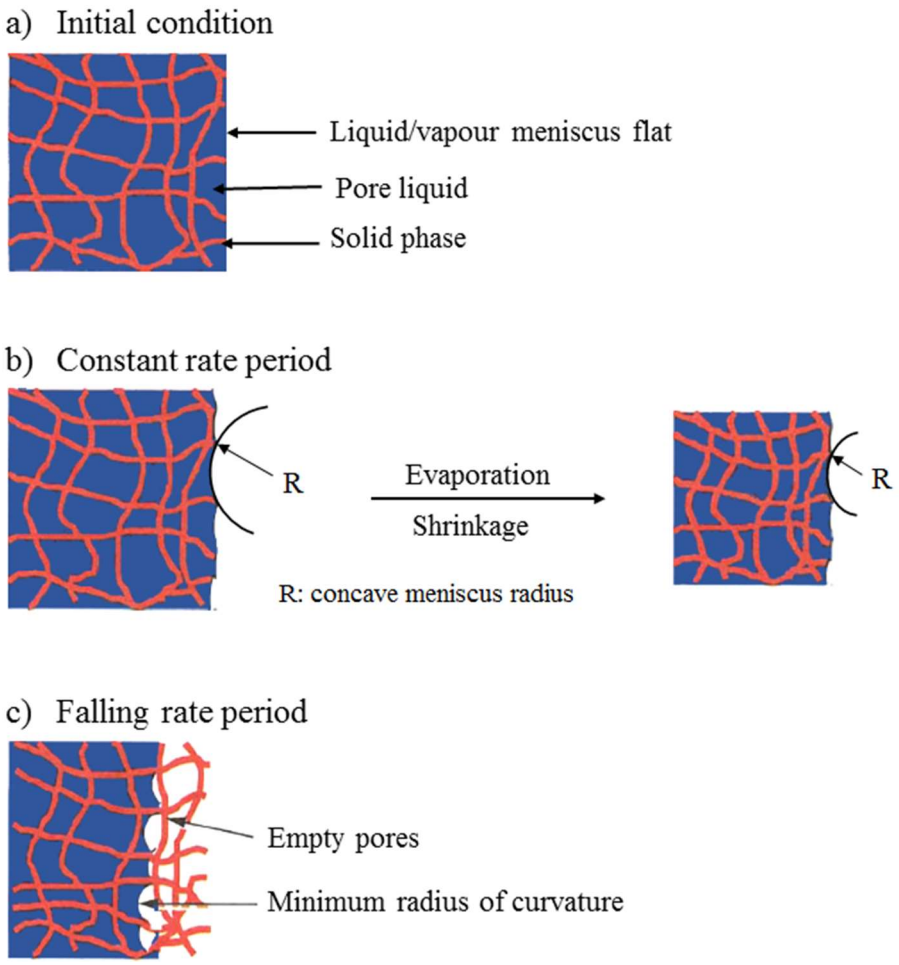

Figure 26: Schematic diagram of drying process during solvent evaporation [133].

In the FRP1, the unsaturated area of the pores is covered by a thin liquid layer, providing a continuous liquid flux from the pores to the exterior surface. Therefore, the surface structure of the gel would not be affected promptly as long as this liquid flux is proportional to the evaporation rate. At this stage, some liquid within the unsaturated pores evaporates concurrently with vapour transfer by diffusion. However, as the evaporation proceeds, the pathway from the solid exterior surface to the front drying increases, the capillary pressure gradient decreases, and so does the flux. Because of isolation of the liquid near the outer surface within pockets, the liquid distribution on the exterior surface stops and drying undergoes into the second falling period. In this period, the evaporation occurs inside the gel body. The solvent evaporation rate is less sensitive towards the conditions outside the gel surface (temperature, humidity), while the liquid transfers mainly from the partially empty pores to outside via molecular diffusion. The total stress applied to the gel is

considerably reduced during the FRP2. Hence, the gel body may expand slightly. As the saturated gel side (non-drying) is being compressed more than near the drying side, cracks and collapse are often originated near the non-dying side of gel backbone [129, 133]. The effects of falling rate periods on the final gel structure at the ambient condition are illustrated in Figure 26 (c).

There are several techniques used to dry gels; each of which results in materials with altered characteristics. Thus, drying plays a significant role in determining the final properties of the nanostructured materials, and the type of dried gel depends on the technique used in the drying stage (Figure 27). The most commonly used methods include subcritical, supercritical, freezing and microwave drying [9, 37, 120, 134-136].

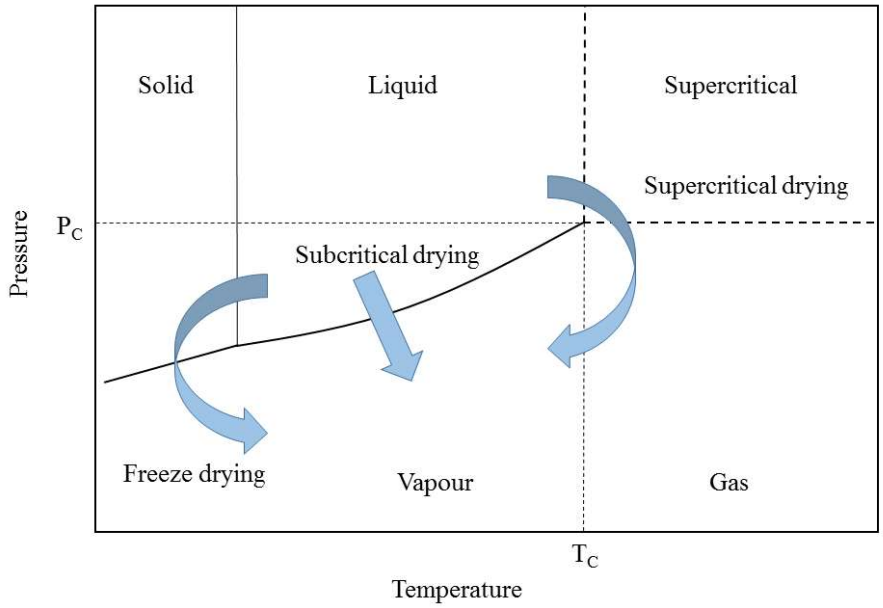

Figure 27: Phase diagram showing effect of drying method on produced porous materials [137, 138].

1.4.4.1 Ambient drying (Subcritical drying)

Drying of the wet gel under subcritical conditions is based on the heating of samples at ambient pressure or decreased pressure (vacuum) [9]. As a result, the liquid-vapour interface generated leads to high surface tension, causing capillary forces and partial collapse of the pore structure. For low mechanical strength gel materials, the network structure could be destroyed [106]. Figure 28 shows the occurrence of capillary forces within the pore, where the liquid evaporates from the pore, and the molecules of liquid flow from the interior to replace the evaporated molecules at the surface. The

remaining liquid transfer covers the recently exposed solid-vapour interface, but this cannot be achieved without creating a concave meniscus [3].

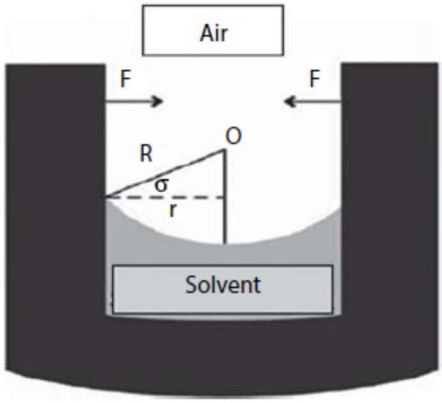

Figure 28: Schematic of capillary forces involved in the drying of porous materials [108].

The relationship between the capillary radius (r), concave meniscus radius (R), and the contact angle (σ) can be defined as:

$$r = R \cos \sigma \qquad \text{Equation 1}$$

There is a force (F) towards the centre of meniscus due to the curvature of the surface; this force represents the capillary force, which is given by the Young-Laplace equation, where γ_{LV} is the liquid-vapour surface tension. Laplace' law demonstrates that the change in pressure (ΔP) depends on the contact wetting angle between the solid and liquid, the specific energy of the surface and pore size [3, 106, 108].

$$\Delta P = \left(\frac{2}{R}\right) \gamma_{LV} \cos \sigma \qquad \text{Equation 2}$$

Therefore, in the case of using water as the reaction medium, before performing the evaporation process; it is essential that another solvent replaces the liquid water (see Section 1.4.3) with a lower tension force. A possible exchange process is to use acetone or another volatile organic solvent (surface tension of water at 20 °C is 75.25 $\times 10^3$ Nm^{-1}, while for acetone it is 23.7 $\times 10^3$ Nm^{-1}); however, partial shrinkage of the structure can be observed after this process. The produced gel via this method is known as a xerogel [9].

1.4.4.2 Supercritical drying

In contrast to ambient drying, supercritical drying (SCD) was developed to avoid the collapse of the structure by preventing the capillary pressure between the liquid-vapour interface and the solid phase of the material. The resulting gel is called an aerogel. As mentioned previously (Section 1.2.2), supercritical drying is performed using carbon dioxide (CO_2) under extreme conditions of temperature and pressure (above the critical points). It is also necessary to exchange the solvent (water) with an organic solvent. The entrapped organic solvent is replaced with the liquid CO_2, and then the CO_2 can be removed under controlled supercritical conditions. The structure of the obtained aerogel is preserved as the original pore structure with minimal shrinkage. However, this method involves both a high level of time and cost of production [9, 35, 37, 108].

Practically, the supercritical drying process can be achieved via two routes: hot drying and cold drying. In the hot drying process, the drying process is performed by the supercritical transition of the original pore fluid (solvent). This process does not apply to water as a solvent because of its extreme critical parameters. In case organic solvents such as methanol, ethanol, acetone, or acetonitrile, high critical temperature and pressure are required. These hot drying parameters could lead to different reactions and modification of the gel material. Also, the high flammable liquids at high pressure may associate with significant risk. The gel obtained after the hot drying exhibit partly modified surface functional OH groups. Hydroxyl groups on the surface of the gel can be replaced with the functional groups (e.g., CH_3) of the organic solvent used as a supercritical fluid, resulting in a hydrophobic material. While in the cold drying process, the supercritical transition of CO_2 or other low critical parameters solvents are employed (Table 1).

Table 1: Critical parameters for different solvents [130].

Fluid	T_C (°C)	P_C (MPa)
Acetone	235.0	4.7
Ethanol	243.0	6.3
Methanol	240.0	7.9
Water	374.0	22.1
Carbon dioxide	31.0	7.3

During the drying process, the pore solvent is exchanged with a liquid having a low critical temperature (e.g. CO_2). Critical parameters for various solvents are presented in Table 1. For hydrogels, because of the limited solubility of carbon dioxide in water, water needs to be exchanged with an organic solvent (e.g. acetone) before replacing the pore liquid by the supercritical solvents [25, 129, 139, 140].

In the cold supercritical process, the pore liquid (organic solvent) is replaced with CO_2 in a high-pressure vessel (autoclave) with liquid carbon dioxide at relatively low temperature (10 ºC) and increasing the pressure up to all pore liquid exchanged. The wet gel is placed into the high-pressure vessel and then heated to a temperature that is marginally above the critical temperature of the CO_2. The supercritical CO_2 liquid is passed continuously over the wet gel, replacing the solvent entrapped within the pores. At the exit of the autoclave, the mixture of CO_2-solvent is subjected to a low pressure resulting in two phases: vapour phase rich in the CO_2 and liquid phase with high solvent content. The rich-phase of solvent is collected, and the CO_2 vapour is recycled to the vessel through a provided compression facility. The solvent extraction process is continued until the solvent is completely removed from the gel pores. Subsequently, the system is depressurised slowly to avoid the formation of the vapour-liquid interface. Finally, the produced aerogel can be taken out of the autoclave after the pressure is reduced to the normal atmospheric conditions [138, 141, 142]. Figure 29 shows a typical continuous supercritical drying process.

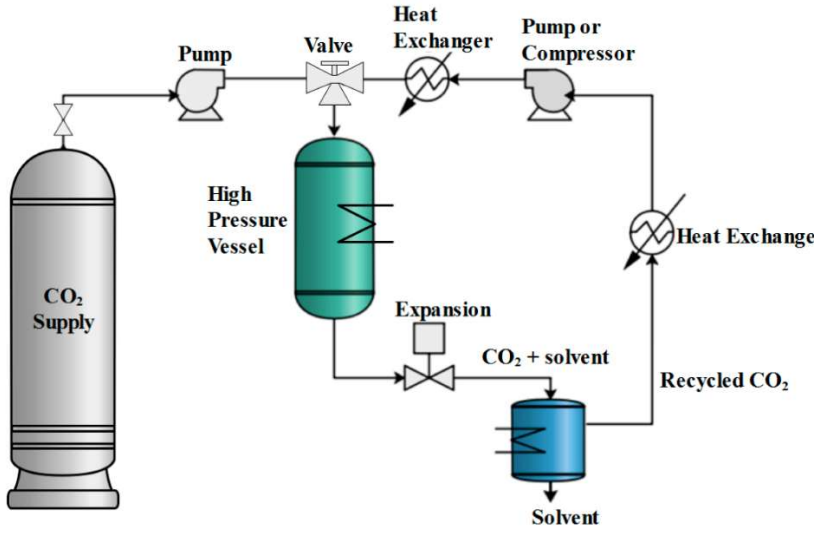

Figure 29: Schematic flowsheet of CO_2 supercritical drying [138].

The supercritical drying with CO_2 produces transparent aerogels, depending on the amount of pore liquid removed during the process. For solvent-water replacement inside the gel pores, it is essential to select the solvent regarding its availability, vapour pressure, health and safety consideration. Solvents which are generally used for the process are acetone, ethanol, and methanol.

1.4.4.3 Freeze drying

Cryogels are obtained via drying, based on the freezing of the wet gel and subsequent solvent elimination by sublimation. This process is another technique to prevent the collapse of the gel structure by avoiding the liquid-vapour interface, and the direct change from the solid phase to gas reduces the surface tension forces experienced by the material. It is essential to select an appropriate solvent to achieve this task [9, 129].

1.4.4.4 Microwave drying

Microwave (MW) drying is an alternative method to synthesise RF gels with short drying time. In this technique, the drying rate of the wet gel increases rapidly as a result of a significant increase in the dipole reaction of dielectric molecules under electromagnetic fields [143]. Yamamoto *et al*. investigated the effect of drying method on the structure of the RF gel; the findings indicate that the dried RF gels prepared during the microwave process showed lower shrinkage rate than during ambient drying. RF MW gels demonstrated desirable mesoporous structures if the synthesis conditions were adequately selected [144].

1.4.5 Further processing techniques

Dried RF organic gels can be transformed, or chemically modified, using different approaches [13]. Post-treatment methods depend on the final applications of these materials. Carbon gels can be prepared by the carbonisation (pyrolysis) of RF gels. In this process, the organic gel is heated in a tube furnace at temperatures above 600 °C and ambient pressure with a constant flow of inert gas [33, 145]. The produced pure carbon gels are thermally stable materials, with a promoted contiguous microporous network. Like other synthesis steps, the variations in carbonisation conditions also have a significant impact on the final properties of the materials. This type of products is viable for various applications, such as energy storage, catalysis, environmental remediation, etc. [9, 43].

The activation processes can be introduced, either after or during pyrolysis. They are generally based on two methods: (1) chemical activation, with acids (e.g. nitric acid and phosphoric acid) or bases (e.g. potassium hydroxide) and (2) physical activation, with water vapour or carbon dioxide at temperatures in the range 700-1000 °C. Activation processes can notably increase pore volume, size and surface area [9, 106].

1.5 RF sol-gel synthesis process variables

The processing of RF gels involves three main stages, as shown in Figure11. Typically, the preparative procedures can be summarised as follows. First, the required amount of resorcinol is dissolved in deionised water with sodium carbonate or another similar basic (or in particular cases, acidic) catalyst; formaldehyde is added to the desired molar ratio. The mixture (sol) is heated in a closed container to a determined temperature (80-90 °C range) for an adequate period to form a stable gel [48]. The wet gel is washed many times with a fresh organic solvent to remove the aqueous solvent. Subsequently, as described in Section 1.4.4, the wet gel is subcritically dried by simple evaporation of the organic solvent or supercritically with CO_2 liquid at elevated pressure, or by freeze-drying [9].

Several factors are involved in the synthesis conditions. The variation of these factors has a significant impact on the final physical properties of the obtained nanoporous materials. These variables include the concentrations of primary precursors (resorcinol and formaldehyde), catalyst (C) type and level, initial solution pH, gelation and curing conditions, heating methods, and drying technique [37, 106]. Furthermore, carbon gels that are derived from RF gels are influenced by pyrolysis temperatures and activation procedures [43].

1.5.1 R/F molar ratio

The most published works on the synthesis of carbon gels from resorcinol-formaldehyde mixtures use a stoichiometric R: F molar ratio of 1:2 [35, 43, 95, 146, 147], corresponding to the stoichiometric fraction of R/F 0.5. Although some researchers have sought to use a lower R/F ratio (excess of F), this has been reported to result in enhancing the formation of clusters and the cross-linked density of the gel [51]. Also, the low R/F ratio can lead to a dilution effect, which increases the particle size near the gelation limit [43].

Rey-Raap *et al*. extensively studied the effect of resorcinol-formaldehyde molar ratio upon the final porous characteristics of the base-catalysed RF gels. It was found that decreasing the R/F ratio increases both the micropore and mesopore volumes [148]. In contrast, Mulik *et al.* [110] indicated that there are no significant effects of this value on the structural properties of the gel prepared under acid-catalysed conditions.

1.5.2 Initial pH of RF solution

Previous studies reported that the initial solution pH (at ambient temperature) plays a crucial role in RF gel synthesis [43, 48, 95, 98, 149, 150]. It was found that changing the pH has a significant effect on aerogels compared to xerogels [98]. The pH can be adjusted either by altering the resorcinol to catalyst molar ratio (R/C) during the regular synthesis or by adding an acidic compound to based-catalysed solutions [151, 152].

In the base-catalysed synthetic route, the typical pH values of the precursor solution range between 5.5-7.5 to produce RF gels with extraordinary properties. At low pH ($<$ 5.5), the obtained material tends to contain macroporous (with pore size $>$ 50 nm) structure and loses the mechanical strength. When very low pH ($<$ 0.8) is chosen, the precipitation of reactants occurs. On the other hand, if the pH value exceeds the upper limit, non-porous materials are produced. Further increases in this value ($>$ 9) could lead to the limitation of RF polymerisation reactions [37, 95].

The pH effect needs to be elucidated regarding the initial reaction between R and F and consideration of promotion by both basic and acidic catalyst. In basic catalyst solutions, the reaction begins when a proton abstracted from a resorcinol molecule; in turn, resorcinol anions are formed. The concentration of R anions can be increased as the pH value increases. Subsequently, the addition reactions proceed more quickly, resulting in the growth of a large number of clusters. Therefore, gelation time is shorter in such conditions, and the produced RF gel shows a narrowing porous structure.

Conversely, low pH creates a small number of R anions. The reaction solution continues for a longer gelation time as a result of the formation of a few clusters. These structures lead to RF gels with larger pore sizes.

Likewise, the variation in the initial pH value of the sol used in the preparation of the RF gels via an acid-promoted route has a considerable impact on R and F reactions. As described in Section 1.3.3, the acid-catalysed process is based on promoting these reactions by protonation of formaldehyde molecules. The protonation reactions are followed by an attack on resorcinol anions to form hydroxymethyl derivatives. These intermediates condense with each other to produce methylene and methylene bridges.

From this point of view, the chemical composition of RF gels is identical whether produced by acid or alkaline catalysed the reaction. However, some studies observed that the porous structure is not similar. For example, under acidic conditions, structures with larger pore size are attained [48, 106].

As the initial sol pH influences the R and F polymerisation reactions, the formation of clusters and degree of gel network crosslinking is altered simultaneously. Job et al. [95] indicated that as the initial pH decreases, the obtained clusters are less branched system and phase separation of spinodal decomposition is hindered. As a result, the number of formed particles in the gel decreases, but the size of these particles increases. In contrast, at high pH, the crosslinking between particles is enhanced, resulting in a substantial variation in pore size. The findings indicated that at high pH, the produced small particles have more robust interconnection than large particles obtained at low pH. The study also reported that the dried RF gel shows two types of pores: voids between the polymer particles denoting meso- and macropores, and voids inside the particles denoting micropores.

1.5.3 Catalyst species

As described previously (Section 1.3.3), adding catalysts can inversely influence the morphology of the produced gel at set reactant and catalyst concentrations. Catalysts can be basic compounds, such as alkaline carbonates, hydroxides or acetates, or acidic, which includes hydrochloric acid, nitric acid, acetic acid or phosphoric acid [105, 106].

1.5.3.1 Alkaline catalysis

Alkali catalysts are employed to promote resorcinol-formaldehyde reactions. Sodium carbonate is the most generally used catalyst in the synthesis of RF gels [51]. It was initially used by Pekala to prepare and develop RF organic gels [35].

Morales-Torres *et al*. performed a comparison between Group I carbonates based on the size of the ion (cation) radii of these alkali species. The results showed that the gelation time increases as cation size increases. Subsequently, the slow gelation time leads to extreme concurring of primary particles formation, and cluster aggregation; causing significant displacement of pore size distribution towards larger pores, and enhancing the mechanical properties the gel network [153]. In contrast, Job *et al*. examined the effects of different alkaline hydroxyls. It was reported that the pore structure of the organic gel is entirely independent of cation size, but is influenced by the charge and concentration of the cation [154].

Similarly, Horikawa and co-workers investigated two factors of cation and anion species, utilising carbonates, and hydrogen carbonates of both sodium and potassium. At a molar ratio of resorcinol to the catalyst (R/C) of 50, the average pore volume in hydrogen carbonates of each of sodium and potassium was a larger size than in carbonates of the same cation [155]. Also, Calvo *et al.* indicated that the anion in a basic catalyst is the most critical factor to demonstrate the final porosity of the RF gels [156].

1.5.3.2 Acid catalysts

Mulik *et al.* prepared hydrochloric acid-catalysed RF gels, reporting that the gelation time could be substantially shortened to only 10 minutes at 80 °C, while the gels obtained were chemically similar to base-catalysed gels synthesised over a longer time (week) period [110]. Merzbacher *et al*. used nitric acid as an alternative catalyst; optical properties of the compared RF gels showed that the usual base-catalysed RF gels exhibit lower reflectance compared with the acid-catalysed materials. It was observed that the porosity of base catalysed gels is higher than products from acidic promoted processes [157].

Brandt *et al*. reported results from a study of RF gels synthesised using acetic acid as the catalyst [158, 159]. They found that altering both the acid and reactant concentrations is a robust method to produce RF gels with different morphologies.

1.5.4 Catalyst concentration

The catalyst used level in the sol-gel process is referred to by the term of resorcinol: catalyst molar ratio (R/C) [110, 160]. It is a dominant variable controlling the final porous structure of the RF gels [161, 162]. In general, the high alkali catalyst concentration (low R/C ratios) leads to the formation of small particles with reduced pore sizes, larger surface areas, and hence denser gels compared to the low concentrations. On the contrary, high R/C ratios result in larger particle sizes and pore sizes, with smaller surface areas; hence, low-density materials are formed. These two different gel structures are known as polymeric and colloidal RF gels, respectively [43].

Gaca and Sefcik have observed the early stage of RF sol-gel transition at different basic catalyst concentrations [92]. The obtained results indicated that at higher catalyst concentration (lower R/C ratio), a large number of primary clusters is formed, which is due to the higher substitution rate and subsequent faster condensation reactions. These observations are consistent with the previous experimental results [119]. In more recent work, Taylor et al. also reported that the R/C ratio is the main factor that controls the cluster formation and growth process in RF gel synthesis [126]. It was observed that low catalyst concentrations (e.g. high R/C) result in the formation of large clusters and low cluster number concentration. In contrast, high catalyst concentrations result in the formation of higher cluster number concentration and small clusters.

The size and number of RF clusters formed during the sol-gel transition, determine the porosity of the final produced gels. The presence of the small particles leads to a microporous structure, whereas the formation of large particles results in a mesoporous structure [44].

Acidic and alkaline catalysts influence the morphology of the synthesised gel differently at the same solid content and R/C ratio. It has been observed that the primary particles of base catalysed RF gels array in clusters of several microns in size. In contrast, acid catalysed gels are sphere-shaped particles arranged in a branched pattern [37]. Effects of R/C ratios in acid and alkaline catalysed processes can be seen in Figure 30.

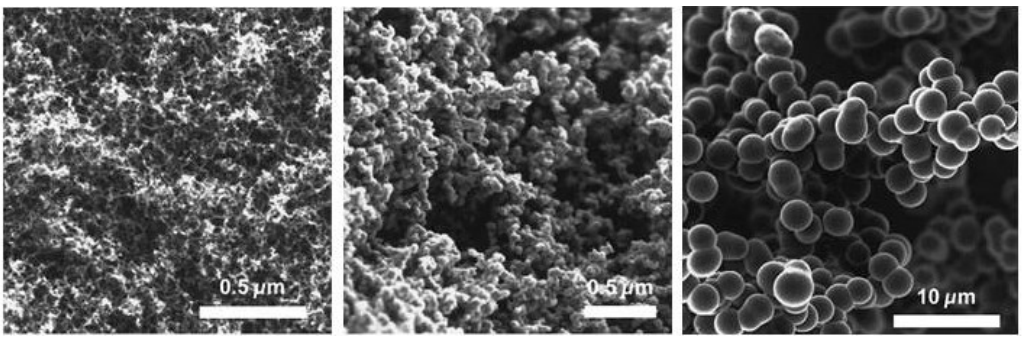

Figure 30: SEM images of RF gels produced with: (left) low and (middle) high resorcinol to alkaline catalyst ratios, and (right) low resorcinol to acid catalyst ratio [157].

1.5.5 Solids content (Dilution)

Total solids content (wt.%) is expressed merely in term of percentage of the mass of the monomers (Resorcinol and Formaldehyde) and catalyst to the total volume of solvent liquid [37]. Increasing the solids content increases the concentration of the reactants radically, which in turn results in a higher amount of small clusters, smaller particles, smaller pore sizes and then higher densities [163]. In contrast, Gels prepared with higher dilution levels possess weaker structures caused by a lack of cross-linking. The surface area appears to be independent of solids content [164]. Figure 31 shows the effects of the combination of these factors on the early stage of particle formation.

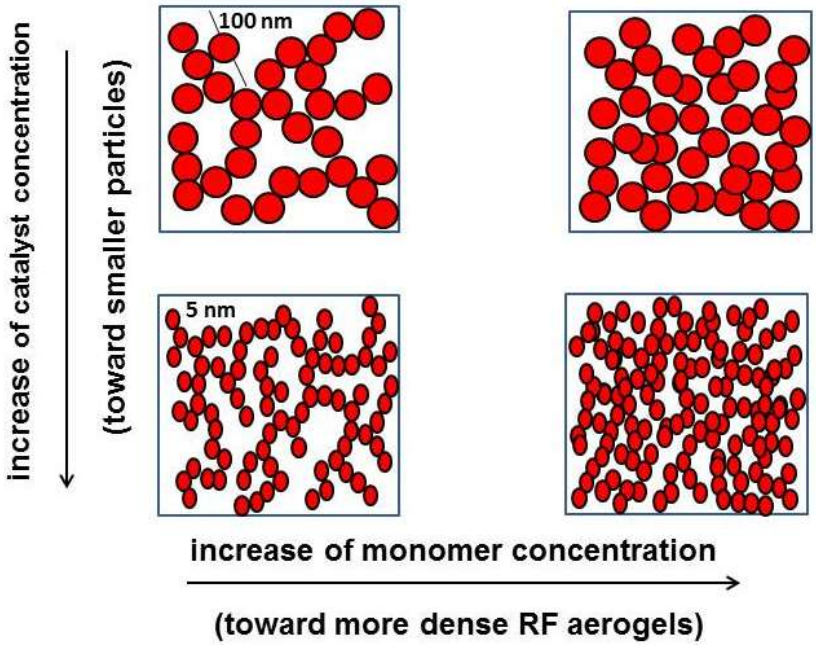

Figure 31: Variation in the structure of RF gels with catalyst and monomer concentrations [145].

Rey-Raap *et al*. observed that a decrease in the solids content of the initial solution causes an increase in micropore (< 2 nm) volume at high pH and vice versa [109]. Whereas Zanto *et al.* reported that surface areas of the RF xerogel increases when the concentration of reactants is decreased at relatively high pH [165]. Solids content and R/C molar ratios could be combined to control the main structural properties of these materials [163].

1.5.6 Reaction medium

It is common, in RF sol-gel synthesis, for deionised water to be used as a solvent. The presence of water in RF gel structures introduces the need for a stage of solvent exchange within the processing procedures. As this step requires time and a fresh organic solvent, some studies focus on the use of organic solvents, such as alcohols, acetone or cyclohexane in place of water [43, 106, 115, 166]. The water-organic solvent mixtures cause an increase in the shrinkage rate during the drying process, density, and change the gelation time of RF gels. The adjustment in gelation time leads to variation in the primary cluster interconnection of the obtained gels [166, 167].

It has been found that using acetone as a solvent precursor can affect the properties of RF aerogels produced at modified R/C molar ratio, solids content or acidity/alkalinity of initial solution [115, 160]. This route eliminates the need for a solvent exchange step before the drying stage. It is also quite successful in producing RF xerogels with little shrinkage during the drying process [168, 169]. However, the most carbonate and hydrogen carbonate catalysts used in the preparation of RF gels are unable to activate the R-F sol-gel polymerisation, because of their low solubilities in acetone solvent [170]. Therefore, acid catalysts have been assigned to induce the polymerisation of R and F [160, 168]. Using acetone as reaction medium under acidic condition, resulting in rapid condensation reactions after mixing the precursors [104]. It was observed that the aggregate structure differs from the base-catalysed conventional methods (water as a solvent). The produced gels consist of fractal aggregates, with a fractal size of about 2.5 nm. Also, they have larger pores and broad pore size distribution (PSD) [160]. Acetone solvent has a low flashpoint temperature of 253 K (- 20 °C), and flammability limits of 2.5-12.8 by volume in the air as the synthesis temperature above this flashpoint, vapour-air mixtures represent an explosive atmosphere within the

flammability limits stated above [171]. Hence, special precautions are necessary to handle and use acetone solvent during the synthesis of RF xerogels using this method.

The difference in surface tension of these compounds influences the behaviour during their curing and drying steps, which results in the different pore structures of the final gels [106]. As mentioned in Section 1.4.4, the solvent exchange of a high surface tension solvent, such as water, is a critical stage before the drying process. However, water is much less expensive than other solvents, and its amount (dilution of initial sol) shows a significant effect on the porosity of all organic gels [106].

1.5.7 Stirring time and speed

Lee et *al.* reported that increasing the stirring rate of sol mixtures produces smaller RF particles [172]. Conversely, longer agitation time leads to increases in particle size of the obtained gels [151]. Stirring time can also affect the gelation process, as a sufficient stirring of the precursors is essential to produce a homogenous RF sol, resulting in complete gelation [173].

1.5.8 Gelation temperature

During the synthesis of organic and carbon gels, to perform the gelation and curing stages, the monomer solution is heated to temperatures ranging between 50 and 90 °C for 3-7 days [35, 37, 44, 47, 164]. It is even possible to perform the aqueous polymerisation reaction at temperatures as low as 25 °C [65, 174]. However, longer gelation times are required compared to using higher temperatures, such as 80 °C. Nevertheless, the heating conditions depend on the nature of the reaction medium, for instance, if acetone is used as a solvent, the temperature needs to be lowered to ~ 40 °C to avoid the evaporation of solvent during the polymerisation.

The gelation stage (up to the gelation point) involves the formation of hydroxymethyl derivatives followed by initial cluster formation. This process occurs within an hour but can take up to a next day, depending on the synthesis conditions used [43].

Pekala *et al.* indicated that solutions with low solids contents (< 10 %) can gel when heated at 95 °C for seven days, while solutions with higher solids contents can gel within a day at a temperature of 50 °C and curing for three days at 95 °C [161]. Also, Tamon and Ishizaka used gradual heating, starting with low temperature (25 °C) to

reach the gelation point, before the gels were cured at 90 °C [174]. In another study, the author reported that the gelation temperature has no considerable impact on the porous structure of RF gels [175].

1.5.9 Curing conditions

Curing results from the increasing of the cross-linking process of the clusters; hence hardening the gel. It takes a longer time than the gelation process. Acid treatment could be used to accelerate the degree of curing after the gelation point. This additional step increases the crosslinking density by enhancing the evolution of condensation reaction rates. The acid-treated gels exhibit a strong structure. However, such a treatment method is a time-consuming process, and the obtained gels showed a slightly lower surface area [43, 128, 176]. In most research studies, the temperature is held at 85 ± 3 °C for 3-7 days in order to enhance the mechanical strength of the samples for handling in further processing steps [43].

1.5.10 Drying process

After the curing step, the synthesised the RF hydrogels are solvent-exchanged with an organic solvent (e.g., acetone) to reduce shrinkage within the pores. Subsequently, the RF gels can be dried by one of three different methods: subcritical, supercritical or by freezing [151]. According to some studies [9, 132, 177], the comparison between these drying approaches shows that RF aerogels and cryogels possess larger pore sizes and surface areas, because that they can preserve their pore structures. In contrast, RF xerogels are vulnerable to high shrinkage of their nanoporous structure, and, as a result, they exhibit smaller pore sizes than the aero and cryogels.

Over the years, efforts have been made to avoid the supercritical drying method, as this process requires complicated operating procedures, and there is a high cost of equipment utilised [145]. Kraiwattanawong *et al.* investigated different alternative drying methods, including ambient drying, vacuum drying (subcritical), and freeze-drying. In order to reduce the capillary forces associated with these drying techniques, low surface tension solvents were examined. It was found that pore shrinkage during the synthesis of RF gels during the subcritical drying, can be significantly reduced by proper selection of solvent. In consideration of the critical physical properties (Table 2), such as low surface tension force, low vapour pressure and low polar index [128].

Table 2: Physical properties of some solvents used in solvent exchange processing of RF gels [128].

Solvent	Surface tension (at 25°C) mN/m	Boiling point °C	Polarity index P	Vapour pressure kPa	
				25°C	50 °C
Water	71.99	100.0	9.0	3.16	12.31
Ethanol	21.79	78.5	5.2	7.83	29.45
Acetone	23.46	56.5	5.1	30.66	81.69
Toluene	27.93	110.6	2.4	3.15	12.33
t-Butanol	19.96	82.4	4.1	5.64	23.89

Recently, Prostredný et al. introduced a regular replacement of solvent exchange fluid in order to prepare the wet gel for drying process [47]. The dried gels obtained by this post-synthesis method show a remarkable effect on the total pore volume, resulting in larger average pores diameters, which is due to a reduction in shrinkage during the drying stage.

Even though the drying techniques used for RF gels influence the structure and properties of the resulting material, the alteration in synthesis parameters, such R/C molar ratio, the initial sol pH, solids content, gelation and curing conditions are considered as the most critical variables.

1.6 Characteristics and applications of RF gels

Organic gels are broadly used, particularly in separation technologies, energy storage, thermal insulation and catalysis. The wide variety of RF organic gel applications are due to their unique properties, including the high porosity (>80 %), large surface area (400-1200 $m^2 g^{-1}$), low thermal conductivity, excellent electrical conductivity (5 to 40 $\Omega^{-1} cm^{-1}$), controllable pore size distributions (1 to 50 nm) and mechanical properties [43, 48, 98, 152]. The use of these materials in different areas also depends on the flexibility of changing the final form of the obtained material.

1.6.1 Mechanical properties

The mechanical properties of the different aerogels and related materials have been extensively investigated [24, 41, 178-183]. Organic aerogels, such as the phenolic materials, exhibit impact strength values of about 12 J/m [184]. The variations in microstructure are reflected in the compressive characteristics of the material [178].

The mechanical properties of the ambient dried RF xerogels were investigated by Léonard et al. [180]. They reported that the mechanical behaviour of gels shows a significant dependence on the R/C and water content (or solid contents) of the initial RF solutions.

Schwan et al. were the first to investigate a synthesis route for rubber-like or flexible RF aerogels. They observed that a minor change in the process variables (water and catalyst amount, and pH of the initial solution), has a curtail impact on the flexibility and density of RF aerogels [45, 173, 185]. This development is consistent with the effect of these parameters on the cluster formation and growth during the sol-gel transition process.

1.6.2 Electrochemical applications

Carbon gels are porous materials derived from RF gels via pyrolysis in order to enhance some of the essential properties. Carbon gels are remarkably attractive materials for use as supercapacitors and lithium-ion (Li-ion) batteries, because of their monolithic structure, large surface area and high pore volume. These RF-based products are also stable thermally and chemically, with low production cost [147, 186, 187].

1.6.2.1 Double-layer capacitors

Electrochemical double-layer capacitors (EDLCs) or supercapacitors are moderate energy storage devices with high energy density. Carbon gels are mainly used as electrodes in the EDLCs [145]. The principal of stored electrical energy is based on the separation of the charges across the electric double layer in the electrode/electrolyte interface [186]. A schematic diagram of the proposed mechanism is shown in Figure 32. During the charging phase, the positively charged cations are attracted by the negative plate, while the oppositely charged anions are accumulated at the surface of the positive electrode [187].

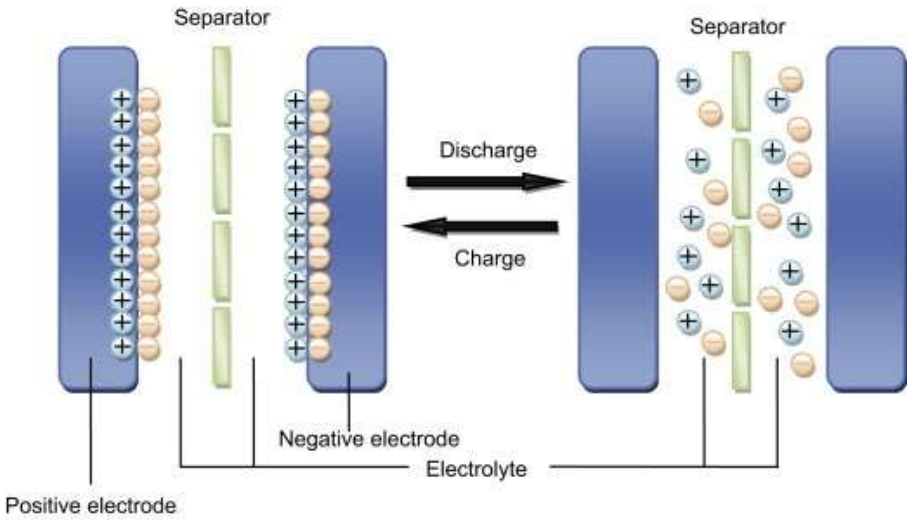

Figure 32: Schematic diagram of EDLC [188].

Carbon-based supercapacitors are distinguished by their long life, as the charges are accumulated in the electrode/electrolyte interface without precipitation of electrode materials [186, 188]. The field of application of this technology includes electric vehicles, pulsed laser systems, digital communication components and computers [147].

1.6.2.2 Li-ion batteries

The porous structure of carbon gels is utilised as a gas transport medium in lithium-ion batteries. It is essential to control the pore size distribution of RF carbon gels, to increase the storage capacity and enhance the power capability and kinetics of these systems [106]. In Li-ion batteries, carbon represents a catalytic surface for the lithium-oxygen reaction [189]. Generally, carbon gels are preferred as a negatively-charged electrode due to their higher negative reduction-oxidation potentials compared to other materials [145].

1.6.3 Catalyst applications

The unique structural properties of RF carbon gels make them excellent candidates as catalysts and for use in catalyst support systems [13]. Catalytic processes play a crucial role in various reactions and applications, such as fuel cells, liquid streams treatment by oxidation of volatile organic compounds (VOC), removal of nitro and sulphur oxides from polluted air, and fine chemistry processes [190-192]. It is an essential feature of these applications to dope the carbon gel with metal, and metal-doped carbon

gels are prepared by adding soluble metal salts to the initial sol. During the gelation step, the metal salt is incorporated within the gel structure, and then metal ions can be attached to the functional sites of the polymer substrate. Large internal surface area and pore volumes are essential properties in this process. Catalytic activity and stability of catalyst can be enhanced by the modification of the surface chemistry of these materials. Other methods can be employed to prepare metal-doped carbon gels such as impregnation or adsorption [106, 145].

1.6.4 Thermal insulations

Similarly, RF gels are considered one of the most promising candidates as thermal insulating materials [193]. Their nanoporous structure means that RF gels show a high thermal resistance (low thermal conductivity). Thermal transport in the porous materials is entirely different than in conventional insulators. In general, heat transport through a porous solid occurs via three mechanisms: gaseous conduction, solid conduction, and infrared radiative transmission. The combination of these three heat transfer phenomena gives the total thermal conductivity of the material [145, 194]. This important characteristic of these materials leads to several applications, including insulation for building purposes, piping, cooling and heating systems, industrial process equipment [195], etc. Figure 33 shows the simple mechanisms of thermal transport through gel nanostructure.

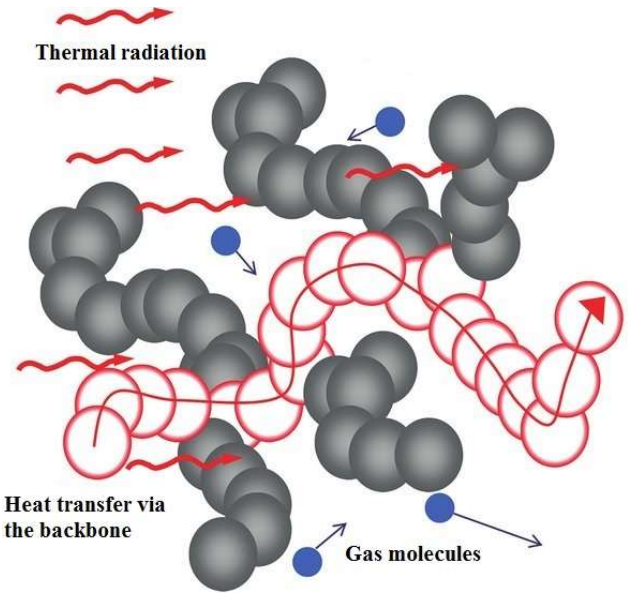

Figure 33: Heat transfer through nanoporous materials [196].

Generally, aerogels have been extensively studied in the literature as superinsulators [14, 179, 197-199]. These materials, with very low thermal conductivity (~ 20 mW/m.K), exhibit remarkable features compared to the traditional thermal insulating materials. Aerogels can be used in windows for insulating purposes due to their high visible transparency. In the case of cryogenic applications, high vacuum at 27 °C could optimise thermal conductivity of the material (~ 10 mW/m.K). However, the limitation of these superinsulating materials is mainly related to their high production costs, weak mechanical structures, health and environmental issues [194]. RF gels, among of these different rages of aerogels, offer lower radiative transmittance and are stiffer and more durable than silica-based gels. Furthermore, they retain very high thermal resistance and have six times greater resistance than fibreglass materials [48, 51].

1.6.5 Gas storage and separation techniques

As mentioned above, resorcinol-formaldehyde carbon gels have nanoporous structures with the high surface area, high porosity (pore size < 100nm) and low density. These properties allow them to be used in the fields of gas storage and separations.

1.6.5.1 Hydrogen storage

It has been reported that doping carbon gels with metals such as nickel, cobalt, titanium, or manganese improves hydrogen (H_2) storage [106, 200, 201]. Most studies determine that there is a linear dependence of H_2 uptake capacity with surface area and micropore volume. Also, the micropore size distribution is considered a critical factor in controlling the final H_2 storage capacity [202-204]. As this process is based on the physical adsorption of hydrogen on the surface of the H_2 storage material, it is essential to prepare metal-doped carbon gels, which in turn show high surface areas with narrow micropore distributions to achieve an efficient H_2 sorption process [9].

1.6.5.2 Separation applications

RF carbon-based membranes have been developed to provides efficient separation of gases or liquids [48]. Recently, carbon gel monoliths have been examined as adsorbents in the separation of flue gas components (CO_2, N_2, O_2, and H_2O). Results revealed that the activation severity of carbon gels represents a key role in selectivity during the adsorption. For moderate activation, maximum CO_2 adsorption capacity and selectivity can be achieved [205]. Zheivot *et al.* used phenol-formaldehyde carbon

xerogels in gas chromatography. They indicated that the adsorption and gas chromatographic properties of these materials could be efficiently tailored via their preparation methods [206].

In water treatment, silver (Ag) loaded carbon gels have been examined as adsorbents to remove bromide and iodine ions from drinking water. The study showed that Ag-doped carbon gels are more efficient than commercial activated carbons [207]. Also, RF gel-based products can be utilised in the elimination of heavy metals from industrial wastewater effluents [208].

1.6.6 Other applications

As described above (Section 1.5), the structural and chemical properties of RF gels can be tuned through the variation in synthesis conditions. The acoustic resistance of carbon gels can be changed to meet different applications; for example, carbon gels are used as pad materials in the crash helmet to absorb the impact energy. This property is mainly dependent on the density of the materials. Carbon gels have also been introduced into cigarette manufacture, as filler materials. As they are consistent with living organisms, carbon gels are employed in artificial organs, drug delivery systems (carrier) and biological tissue engineering, as well as, in the synthesising of the cosmetic products, and nontoxic and effective pesticides [106, 145].

1.7 Thermal insulating materials- pipe insulation

Currently, energy-saving and the reduction of carbon dioxide (CO_2) emissions are the main issues gaining the attention of modern society. Developing countries, such as China and India, encounter fast population growth, leading to substantially increasing energy demands [209]. As energy consumption increases, energy conservation strategies and associated research continue to gain momentum. While the expansion is limited by crucial energy sources, i.e. the fossil fuels, the effect of rising of CO_2 levels in the Earth's atmosphere, and associated impacts, including those on the global climate, have become increasingly apparent [210].

The proposed actions for immediate CO_2 reduction and a quickly growing demand for renewable energy sources has led to an overestimation of the prospects of such technologies. The expansion of alternative energy systems has experienced difficulties

in development, and it is likely that full development, to replace current technology completely, will take a significantly long time. Besides, fossil fuels dependency (expected to account for 77% of energy demand by 2040 [211]) is higher than the efforts to admit those assumptions. In other words, technological complexities and economic barriers are the main adversaries to the immediate implementation of the suggested actions. This understanding leads to a small number of practical strategies and policies for the global mitigation of CO_2 and other pollutant gas emissions. In order to bridge the gap while emerging long-term renewable energy schemes are developed and implemented, the typical sequence of steps requires a combination of short-, medium-, and long-term strategies [210].

Remarkably, buildings are considered to contribute the highest share of total energy consumption (around 40%) [212]; the heating, ventilation, and air conditioning (HVAC) accounts most of this energy demand. Heat losses from domestic and industrial establishments also represent a critical feature among this value; therefore, for energy savings and CO_2 reduction, thermal insulation of buildings must be considered as a short-term scenario [210], as shown in Figure 34.

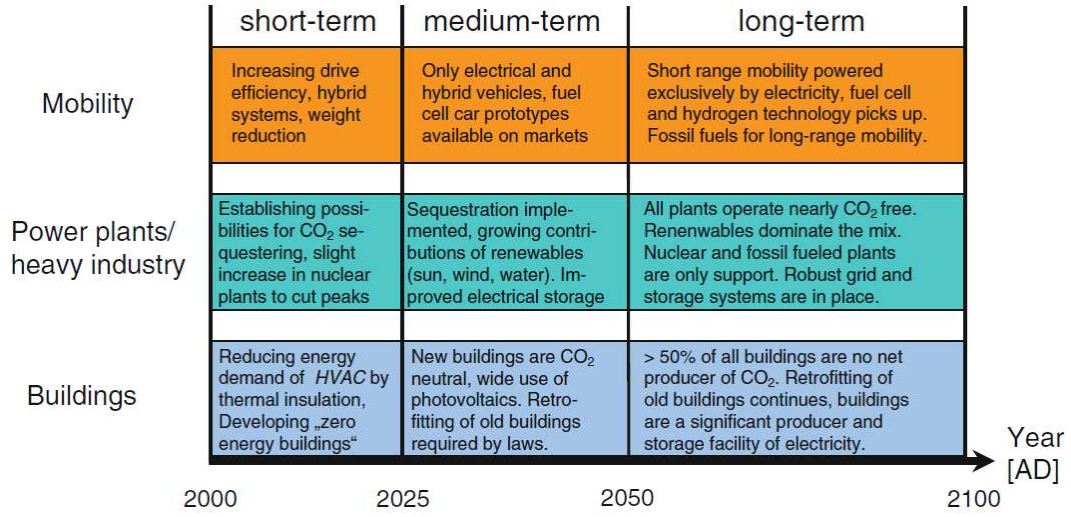

Figure 34: Different scenarios and plans to address global climate change [210].

Some critical insulation applications, other than those used in the building sector, such as thermal insulation for aerospace, petrochemical processing, oil and gas industry, and extremely low-temperature processes are discussed later (Section 1.7.3) [210]. In 1991, a study from Drexel University showed that thermal insulation saves U.S.

industry ~ $60 billion a year in energy costs, and this can be further increased by utilising better insulation materials and technology [213].

Oil and gas processing plants comprise complicated and costly piping and equipment structures (Figure 35). These piping systems are also employed in other processes, such as water supply, fire protection systems, and cooling-heating applications. In the crude oil production industry, the hot oil-gas composition flows through pipelines and key instruments before the drilling riser bringing the oil to the surface. Thermal insulation is necessary to reduce associated heat losses or gain, and to avoid the formation of hydrate plugs and paraffin wax build-up [209].

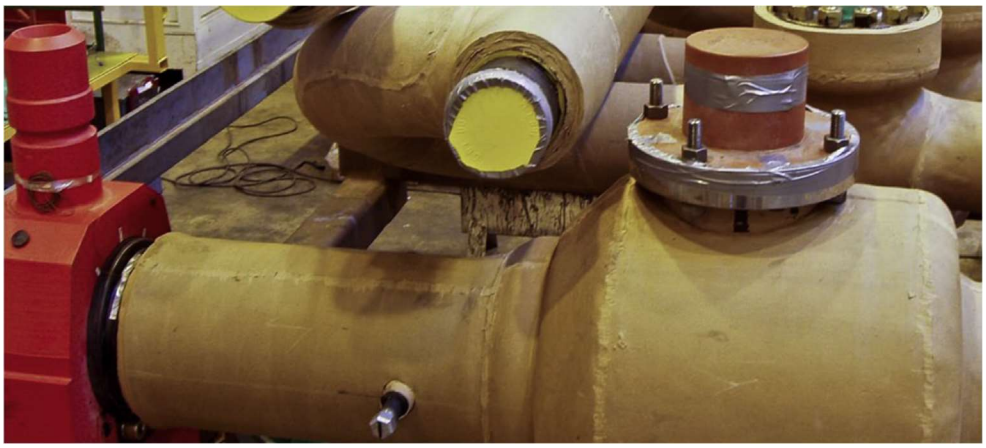

Figure 35: Example of thermal insulation applications [209].

1.7.1 Purpose of thermal insulation

Insulation is a material or combination of different materials, which are applied to one or more of the following purposes [209, 213]:

- Saving energy by reducing the rate of heat transport
- Providing an accurate temperature control for a process
- Prevention vaporisation, condensation, or freezing
- Controlling surface temperature for personnel protection from injury
- Preventing phase changing and water condensation on cold surfaces of equipment
- Reducing damage to equipment from exposure to outside fire or corrosive materials
- Improving the efficiency of HVAC, steam, process, and power systems
- Conserving refrigeration
- Preserving the process temperature and dampening the vibration and noise.

1.7.2 Pipe insulation

The piping system is a crucial element in a closed-loop network, which is employed to transport energy in municipal heating-cooling systems, and industrial applications. However, pipes are also characterised by the issue of heat losses, i.e. for uninsulated steam and condensate distribution system, heat loss from pipe 1" diameter and 1m length, through natural convection and 25 °C temperature difference, is estimated to be ~ 50 $\times 10^6$ kJ/yr. Heat transfer processes and temperature changes in pipelines are significantly affected by the insulation material used, the surrounding environment (air or soil), and pipe configurations [214, 215]. For cylindrical pipe geometry, as shown in Figure 36, the total thermal resistance to heat transfer of an uninsulated pipe is given as [214]:

Equation 3

$$R_{P,un\text{-}ins} = \frac{1}{h_i A_i} + \frac{\ln\left(\frac{r_1}{r_o}\right)}{2\pi l k_P} + \frac{1}{h_o A_o}$$

where A_i and A_o are the internal and external surface areas of the pipe, respectively, k_P is the thermal conductivity (TC) of the pipe material, l is pipe length, and h_i and h_o are the convection heat transfer coefficients for internal and external surfaces, respectively.

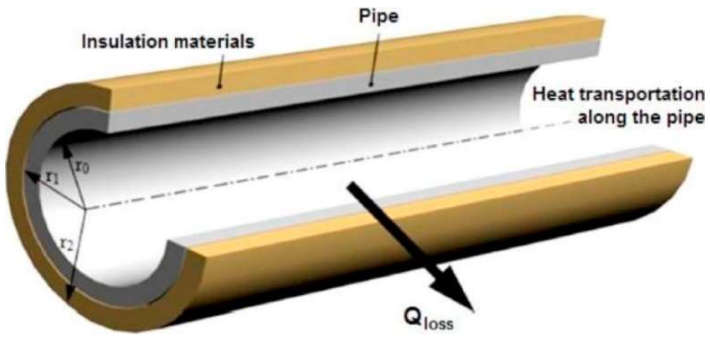

Figure 36: Principle of insulated pipe system [214].

While the total resistance of the insulated pipe can be expressed as:

Equation 4

$$R_{P,ins} = \frac{1}{h_i A_i} + \frac{\ln\left(\frac{r_1}{r_o}\right)}{2\pi l k_P} + \frac{\ln\left(\frac{r_2}{r_1}\right)}{2\pi l k_{ins}} + \frac{1}{h_o A_o'}$$

where A_o' is the external surface area of the last layer (insulation) of the piping system, and k_{ins} is the thermal conductivity of the insulation material.

The rate of heat transfer (Q) through the pipe can be calculated [213] as:

$$Q = \frac{T_i - T_o}{R_{total}} \qquad \text{Equation 5}$$

where T_i and T_o are the bulk fluid and ambient surrounding environment temperatures, respectively.

1.7.3 Insulating materials

There is a wide range of thermally insulating materials that exist for various applications. They are mainly made of inorganic fibrous materials (e.g. glass wool, mineral wool), and foamy organic materials (e.g. expanded polystyrene and polyurethane). Conventional insulating materials are categorised by their chemical compositions and physical structures [216], as illustrated in Figure 37.

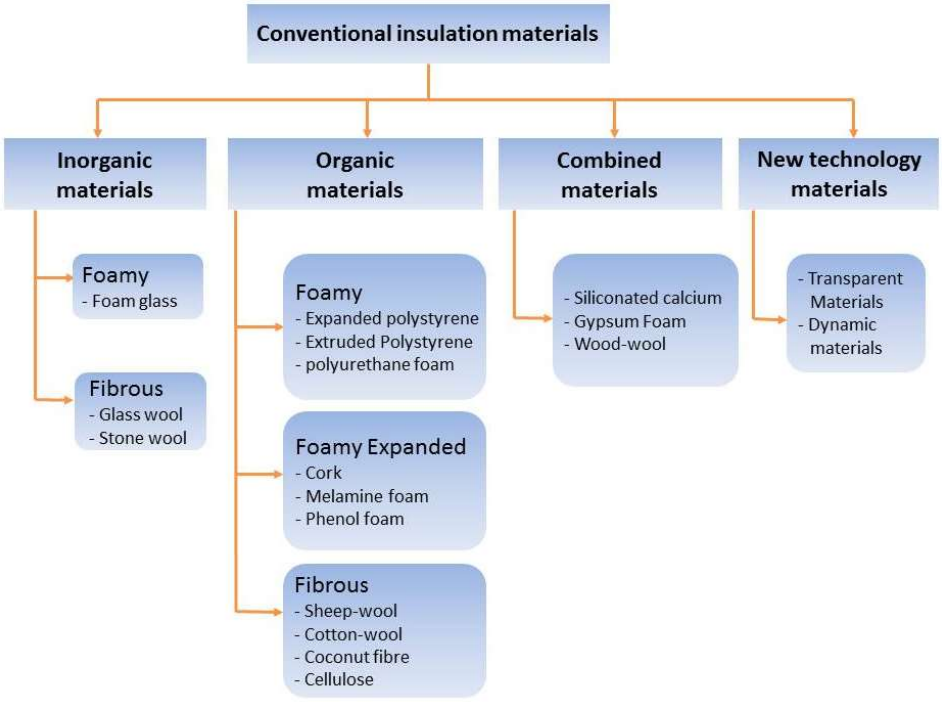

Figure 37: Proposed classification of conventional insulating materials [216].

Different forms of glass wool (fibreglass) are broadly used in process industries and HVAC applications due to their low cost, lightweight, flexibility, and adaptability; however, they are not useful for other applications as a result of their weak resistance to moisture (hydrophilic) and fire, as well as, their limited maximum service temperature. Stone wool (mineral wool) is fibrous, lightweight, flexible, and thermally active; it exhibits high fire resistance up to 1100 °C and reduces sound transmission.

Calcium silicate is a solid material that is usually used to insulate high-temperature pipes and equipment. However, it is an expensive material and also requires a longer time for installation [213].

1.7.4 High-performance thermal insulation

High-performance insulation or superinsulation is a term that refers to materials with thermal conductivity values below 0.020 W/m.K, at ambient conditions. Thermal conductivity (k) is an inherent physical property of a material and is defined as the ability to conduct heat [210, 217, 218]. Metals are identified as outstanding thermal conductors, with k values ranging from tens to hundreds of W/m.K. Glass, sand, and minerals typically possess typical single numeral thermal conductivities. In contrast, conventional thermal insulators, and associated products, have k values of < 1 W/m.K [210, 217]. It can be noted that the thermal conductivity of stationary air at ambient (standard) conditions is 26 mW/m K, which is lower than the TCs of most conventional (traditional) insulating materials [213]. Table 3 provides an overview of insulating materials based on their thermal conductivity range.

Table 3: thermal insulation materials sorted by ambient condition thermal conductivity [212].

Insulation product	Chemical composition	k [W/m.K]
Mineral wool	Inorganic oxides	0.034-0.045
Glass wool	Silicon dioxide	0.031-0.043
Foam glass	Silicon dioxide	0.038-0.050
Expanded polystyrene (EPS)	Polymer foam	0.029-0.050
Extruded polystyrene (XPS)	Polymer foam	0.029-0.048
Phenolic resin foam	Polymer foam	0.021-0.025
Polyurethane foam	Polymer foam	0.020-0.029
Silica aerogels	SiO_2 based aerogel	0.012-0.020
Organic aerogels	Aerogels derived from organic compounds	
Vacuum insulation panels (VIP)	Silica coresealed and evacuated in laminate foil	0.003-0.011
Vacuum glazing (VG)	Double glazing unit contains evacuated space and pillars as supports	0.003-0.008

It can be seen that aerogels, vacuum insulation panels (VIP), and vacuum glazing (VG) exhibit ultralow thermal conductivities, which sees them described as super-insulating materials [217]. Among nanostructured materials, aerogels are considered as one of the most promising high-performance thermal insulating materials, with their extraordinary features and vast emerging share market [194].

1.7.4.1 Silica aerogels

One of the critical properties of SiO_2-based aerogels is their low thermal conductivity, typically in the range of 13-20 mW/m K [194, 219, 220]. In 1934, Kistler and Caldwell recognised the potential of silica aerogels as insulating materials [221], and White subsequently investigated the influence of synthesis variables on the thermal conductance of these materials [222]. More recently, several studies have reported thermal conductivities for different forms of silica aerogels using various synthetic routes [197, 223-225]. Silica aerogels were introduced commercially, in 1993 by Aspen Systems, Inc. and NASA as the first aerogel blanket was developed [226]. Aspen's technology is based on the integration of silica aerogel into a carrier to create flexible and durable aerogel blankets (Figure 38) as superinsulators [209].

Figure 38: Aspen aerogel (grey spaceloft).

1.7.4.2 Organic aerogels

In parallel to improvements in silica aerogel superinsulation, some organic aerogels have been studied to explore their thermal properties. As mentioned in Section (1.6.4), organic aerogels are characterised by their very low thermal conductivities combined

with desirable mechanical behaviour. Early, interesting works investigated organic aerogels with a focus on polyisocyanurate aerogels. The findings led to thermal conductivities higher than 20 W/m K, as a result of porous structure issues. These materials have since been extensively investigated for insulating systems, by studying, for instance, polyamines, polyurethane aerogels (14 mW/m K), and other organic aerogels [210, 227].

Among the organic aerogels, RF systems present the lowest TC values [228]; however, large-scale of this material, as thermal insulation, has not been adopted due to the brittleness of these materials and the fact that the synthetic process comprises relatively expensive techniques (supercritical drying) [210]. However, the fragility can be tackled by adding a reinforcement material, such as fibreglass or polyester, to the sol-gel. At the same time, costly methods can be efficiently replaced with similar processing steps at ambient conditions, resulting in thermal conductivity values slightly higher than that of air [229, 230].

1.7.4.3 Hybrid and composite materials

An overview of thermo-mechanical properties, shows inorganic-organic aerogel hybrids or composites produce astonishing materials as superinsulation, especially for applications in space and defence industries. Silica aerogel possesses excellent thermal performance, but it is also dusty and weak material. By contrast, organic-based aerogels are mechanically more robust, although they are produced using flammable materials [210].

Figure 39: RF-silica aerogel blanket [20].

Lately, Berthon-Fabry et al. have prepared superinsulation blankets for space applications, through the development of a novel material (Figure 39). It has been based on the synthesis of silica and RF aerogels solution within the same vessel, subsequently, impregnated into a nonwoven fibrous substrate (PET, polyethylene terephthalate) [20, 231].

2 Aims and objectives

RF xerogels have found use in a range of applications, covering a wide range of sectors, and these are deliberated in more detail in Section 1.6. Among these diverse applications, the thermal insulation filed undoubtedly one of the significant potentials, as the thermal properties of RF gels make them useful as insulators. As discussed earlier (Section 1.6.3), heat transfer processes involve conduction, convection and radiation, contributing to the overall thermal conductivity of the material; due to their highly porous texture, optimally structured RF xerogels can minimise the heat transport via all above mechanisms owing to their highly porous texture. Consequently, it is crucial to be able to carefully optimise the textural and physical properties of these materials in order to improve their performance in particular applications. These properties can be controlled by tuning the synthesis parameters, and processing conditions use to manufacture RF gels, and their composites, thereby allowing the final porous properties; hence the thermal conductivity of the final material, to be tailored to the chosen application. Despite recent advances in the controlled synthesis of RF gels, additional research is still required to fully understand the link between synthesis and process changes and the resulting impact in various final properties of the gels.

In order to report the issues highlighted above, this work aims to develop xerogel materials exhibiting potentially useful thermal insulating capability concerning their thermal conductivities; this will build on the previously published literature [42, 162, 228, 229, 232-236], who reported RF organic gels with extremely low thermal conductivities, and thermal analysis will be used to estimate the thermal conductivity of the xerogels studied here. While the synthesis of RF gels involves the formation of cross-linkages, it should be noted that many of these materials, particularly those with pores in the mesoporous range are weak mechanically; however, the strength of the RF xerogels can be drastically enhanced by combining them with reinforcing fibres [20, 230, 231, 236]. When creating these composite materials, it is essential to select a suitable reinforcement that does not adversely affect the thermal conductivity of the gel material.

In order to enhance the thermal insulating properties of the polyester blanket, Razzaghi et al. [230] investigated the effect of impregnation of this fibrous material into a pre-prepared phenol-formaldehyde (PF) solution at different compositions. The experimental findings show a substantial reduction in the thermal conductivity of the polyester mat as the concentration of the PF solution increased. These findings confirmed the notable insulator properties of these phenolic resins.

Recently, Berthon-Fabry eta al. [20, 231] have developed a light, natural to handle, flexible superinsulating material. The novel hybrid organic-inorganic aerogel blankets were produced using a synthesis approach with a PET fibrous network as reinforcement, RF sol, and a silica precursor (MTES or MTMS). The final product exhibits a desirable characteristic due to the materials utilised to synthesise it. However, the production of these hybrid materials involves the handling of different harmful and expensive materials, high cost, and time-consuming processes.

In the current work, the effort is focused on RF xerogel blanket synthesis with RF sol and the PET fibre as core materials, and using subcritical drying to remove the solvent entrapped within the gel structure. The advantages involve using highly reactive precursor (resorcinol), elimination of expensive and hazardous materials (silica raw materials) and processes (supercritical drying). However, the obtained products have relatively higher thermal conductivities, which can be tackled by further investigation.

The products presented in this study included parent RF xerogels, and composite materials, known as RF blankets. The overall aim of producing a thermally insulating material is underpinned by the controlled manufacture and characterisation of RF-based materials, with particular reference to their suitability as insulating materials. This package of work is realised by focussing on the following objectives:

1) Synthesis of a wide range of RF xerogel products to provide data to understand how synthetic parameters and process variables alter textural properties, and their blankets, as determined in (2).

   In order to obtain a varied range of products, different compositions of the initial RF solution were studied. Sodium carbonate was initially used as the catalyst in these systems, with a wide range of R/C ratios and solids contents.

Alternative basic catalysts were also employed, in place of sodium carbonate, thereby allowing examination of their impact on the gel texture and thermal properties. These catalysts included potassium carbonate and sodium and potassium hydrogen-carbonate.

2) Conduct low-temperature nitrogen sorption measurements to determine the structural properties of RF xerogel materials synthesised in this study. The results obtained allow correlation of observed changes in conductivity with changes in synthetic variables.
3) Monitoring the thermal stability of the final materials via thermogravimetric analysis (TGA); this allows the determination of reasonable working temperature intervals and may indicate the need for additional drying process or post heat treatment.
4) Perform heat flow meter (HFM) measurements to determine the thermal conductivity of the blankets produced in this study. The variations in conductivity can be subsequently compared across the series of samples, as various synthesis parameters are altered, indicating the influence that these changes have on the thermal conductivity of the final product.
5) Economic evaluation of RF blankets, based on underpinning sol-gel process, allows gaining valuable data to be obtained, in order to assess the possibility of introducing such blankets to the insulation market.

Overall, the findings of this investigation will provide information on the optimisation of process parameters in gel RF xerogel, and associated blanket, production. Additionally, the evaluation of these materials through synthesis to economic potential will inform the future potential prospective marketability of these materials for thermal insulation applications.

3 Theoretical framework

In this chapter, various techniques and theories, used to study the morphology and characteristics of RF gels, are presented. In general, the characterisation of porous solid materials comprises two main routes: structural analysis and property measurements. The structural properties can be investigated using a variety of gas adsorption, microscopic and spectroscopic techniques. In contrast, the characterisation of bulk properties requires consideration of the desired application of these materials.

3.1 Introduction to the porous texture of solid materials

Materials with porosity in the nanoscale are essential from the perspective of their application in the field of emerging technologies [40, 164]. The term 'porous solid' is qualitatively described by IUPAC as '*any solid material which contains cavities, channels or interstices, which are deeper than they are wide*' [237]. Porosity is among the essential properties of RF gels. Understanding the relationship between the pore structure and synthesis process is crucial to attaining tailored porosity [40]. As mentioned previously, the initial reaction parameters and the successive processing steps control the final pore structure, and the aggregation of small clusters and subsequent cross-linking to form pores [238].

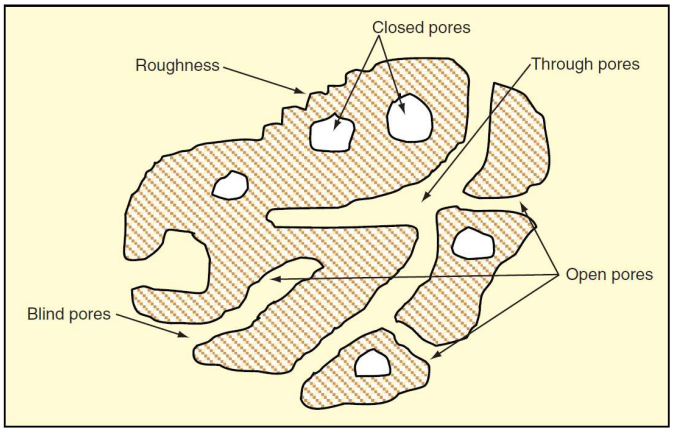

Figure 40: Schematic showing different types of porosity [237].

Based on their availability to an external fluid, pores can be categorised, as shown in Figure 40. Open pores are bridged to the external surface of the material body, whereas closed pores are voids and, thus, are not accessible [238]. Therefore, closed pores do not contribute to the external surface area; however, they do influence the porous

material properties such as bulk density, mechanical strength and thermal conductivity (TC) [237]. Transport pores connect internal areas to the external surface and are also known as through pores; some blind pores are connected to transport pores but not to the external surface [238].

IUPAC classified pores using a broader logic with relation to their diameter [152], the standardised distinctions are shown in Table 4. Nowadays, the term 'nanopore' is used to describe both micropores and mesopores [239]. Gas adsorption is employed to determine the internal pore size, so the pores must be accessible by the gas molecules used for analysis [238].

Table 4: IUPAC classification of pores.

Pore Classification	Pore Width Range (nm)
Micropores	< 2
Mesopores	2-50
Macropores	> 50

The external surface area takes into account the surface area of the outer shell of the material including its roughness, as well as cavities that cannot be defined as pores as they are wider than deep, while the internal surface comprises the pore wall area [237]. RF aerogels with a surface area of 400-900 $m^2 g^{-1}$ have been reported by Pekala [75], further process developments have since been established, and this figure has been extended to surface areas as high as 1200 $m^2 g^{-1}$ [43].

3.2 Gas adsorption in porous solids

In these systems, adsorption occurs when solute molecules diffuse from the bulk of a fluid (gas or liquid) to the surface of a solid material (adsorbent) generating a different adsorbed phase [240]. Recent industrial expansion in adsorption processes has been concerned mainly with gas-solid and liquid-solid interfaces, where the adsorption system is defined as '*an equilibrium one including the adsorbent being in contact with the bulk phase and the so-called interfacial layer'* [239]. The converse process of adsorption is denoted as desorption [240].

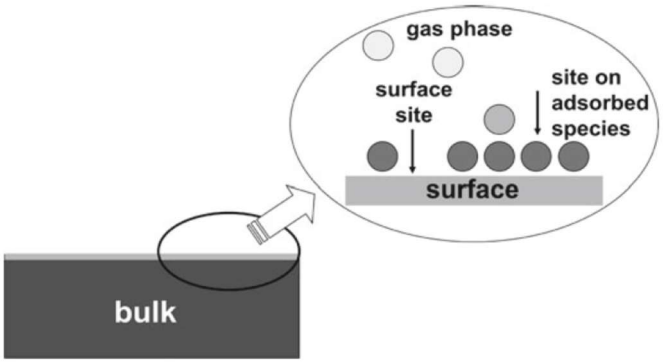

Figure 41: Schematic of adsorption process at the surface of a solid material [241].

Based on the nature of the interactions between the adsorbed state (adsorbate) and solid surface (adsorbent), adsorption can be classified into two categories: physical adsorption (physisorption) or chemical adsorption (chemisorption) [239]. Figure 41 illustrates a simple schematic of an adsorption process.

3.2.1 Physisorption of gases by porous solids

Molecules and atoms of a gas or vapour attach to the adjacent surfaces of a bulk porous material, due to the existence of attraction forces, i.e. van der Wall's forces, which originates from molecular dispersion forces or a dipolar interaction between the adsorbate and the adsorbent surface [242]. The inherent weakness of van der Waals attractive forces allows a physisorbed molecule to retain its character, and on desorption, it recovers its original form in the liquid phase [243].

Figure 42 indicates the stages encountered during physisorption. Initially, at low pressure, adsorbate molecules are adsorbed on the isolated sites at the adsorbent surface. Secondly, as the pressure increases, excess adsorbate molecules adsorb to form a thick molecular layer (monolayer); followed by the formation of the multilayers can be initiated by further increasing the pressure; finally, multilayer coverage is complete, and all pores are filled as the pressure increases to the saturation level [244].

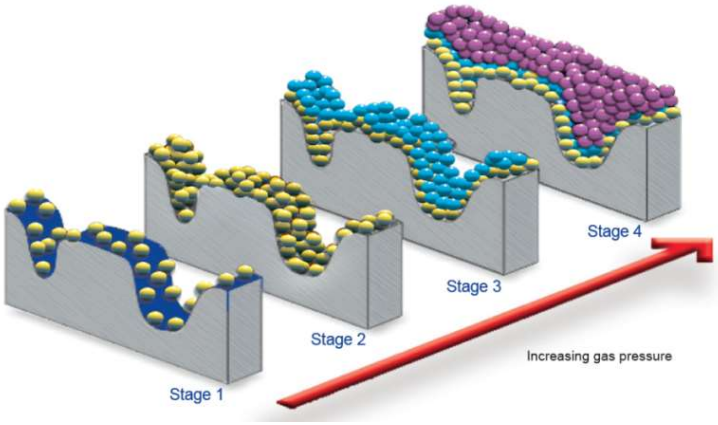

Figure 42: Stages of gas physisorption process, depicting mono and multi-layer formation [244].

The extent of adsorption on a surface [242] is expressed in terms of the fractional surface coverage, θ:

$$\theta = \frac{\text{Adsorbent surface occupied by adsorbate}}{\text{Adsorbent surface available}} \qquad \textbf{Equation 6}$$

It is common to denote the fraction of the surface covered by adsorbate as the volume of adsorbate adsorbed:

$$\theta = \frac{V}{V_M} \qquad \textbf{Equation 7}$$

Where V_M is the volume of adsorbate required to complete monolayer coverage, i.e. once the monolayer is complete and θ =1.

Pore size plays a significant role, particularly in physisorption processes; because the pore size of micropores is small, adsorbate molecules can be attracted to the surface of the adsorbent. However, in the case of mesopores, the walls are created from a large number of adsorbent molecules, and the surface area is higher than in micropores. Since the adsorption forces are more active at a distance near to the adsorbent walls, the surface area of mesopores attracts the adsorbed gas molecules less strongly, but can form both mono- and multi-layers [9]. As the adsorbed layers reach a critical thickness, the intermolecular forces increase, resulting in surface tension. The outer layer will condense below its saturation vapour pressure; this known as capillary condensation; this phenomenon occurs mostly with mesoporous materials, and leads to differences in the adsorption and desorption isotherms, consequently forming hysteresis loops in the isotherms obtained [239].

3.2.2 Adsorption isotherms

For physisorption onto porous solids, the amount of gas adsorbed on the surface depends on equilibrium pressure p, temperature T, and the physical properties of the gas and the solid [243]:

$$\theta = f(p,T,gas,solid) \quad \text{Equation 8}$$

Adsorption equilibrium is achieved when the rate at which gas molecules are adsorbed on the surface is equivalent to the rate at which they are desorbed. The fractional coverage of the surface depends on the pressure of the covering gas. Variation of this value (θ) with pressure, at a fixed temperature for a known solid, is known as an adsorption isotherm [242, 243], so the above equation can be simplified to:

$$\theta = f(p)_{T,gas,solid} \quad \text{Equation 9}$$

When the gas temperature is below its critical condition, the vapour pressure can be introduced [243] as:

$$\theta = f\left(p/p_o\right)_{T,\ gas,\ solid} \quad \text{Equation 10}$$

where p/p_o is the relative pressure.

Adsorption isotherms of gas-solid systems reveal various shapes depending on the type of gas used for analysis, the porous structure of the solid, and the nature of interactions incurred. According to IUPAC recommendations, most of the physisorption isotherms can be divided into eight categories, as shown in Figure 43.

Reversible Type I isotherms are characteristic of an adsorbent with microporous texture and small external surface area. In Type I isotherms, micropore filling occurs at extremely low relative pressures $\left(p/p_o\right)$. Because of the interactions between the adsorbate and the narrow pore walls, the uptake process is influenced by accessible microporosity. For nitrogen adsorption at – 196 °C (77K), Type 1(a) isotherms are found in microporous materials having predominantly narrow micropores; Type 1(b) isotherms are obtained for materials, having broadly ranged pore size distribution; that comprise broader of micropores and possible some narrow mesopores. Typical absorbents that exhibit Type I isotherms are activated carbon, zeolites and some porous oxides [245].

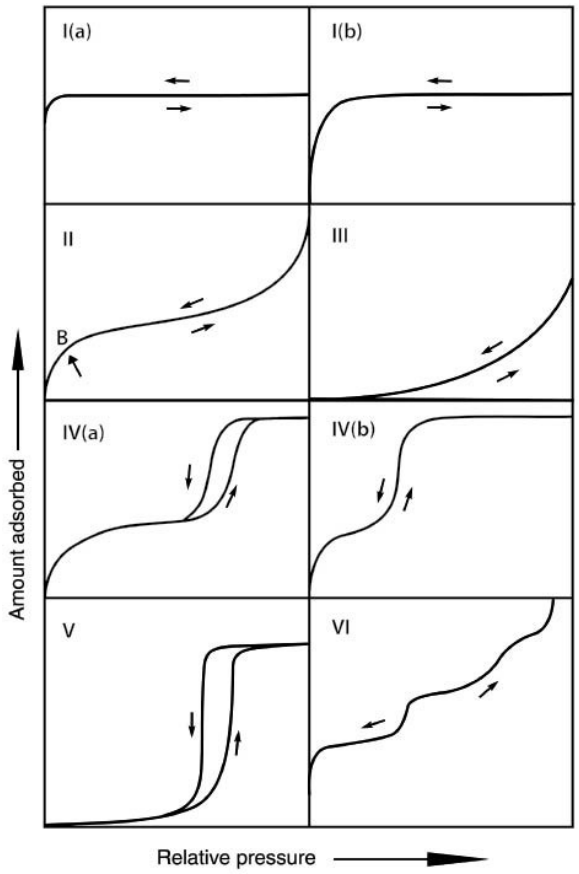

Figure 43: IUPAC adsorption isotherm classification [245].

Type II isotherms are obtained for non-porous or solids with pore diameters larger than macropore. At low relative pressure, monolayer coverage processes prevail, while multilayer adsorption occurs at high relative pressure. In general, the mono- and multilayer adsorption are overlapping processes, as shown in Figure 43 (part B of Type II). Materials with both micro- and mesopores demonstrate Type II isotherms [245-247]. Type III isotherms are uncommon; they exhibit weak interactions between the adsorbate and the adsorbent surface. The interaction within Type III isotherms is weak compared with those between the adsorbate and adsorbed layer.

Type IV shows a hysteresis loop, caused by capillary condensation within a mesoporous material. The early part of the isotherm represents monolayer-multilayer adsorption; the uptakes are limited as the pressure increases to high (p/p_o). The variation in a final saturation plateau is the main feature of Type IV isotherms. A Type IV (a) isotherm shows that capillary condensation is accompanied by hysteresis; which occurs when the pore diameter exceeds a specific critical width. When the adsorbents

possess a small mesopore width, reversible Type IV (b) isotherms are perceived [245]. Type V is a different isotherm, that is related to Type III; as a result of the weakness of the adsorbate-adsorbent interactions in porous solids. The Type VI isotherm shows the sharpness in steps obtained, which correspond to stepwise multilayer formation on a non-porous solid [248].

3.2.3 Adsorption isotherm hysteresis

Adsorption hysteresis occurs when the desorption isotherm follows a different path to that for adsorption [249]. Hysteresis appears in the multilayer region of physisorption isotherms and is related to the phenomenon of capillary condensation, which happens in mesoporous structures. The shapes of adsorption hysteresis loops have been classified by IUPAC, as shown in Figure 44.

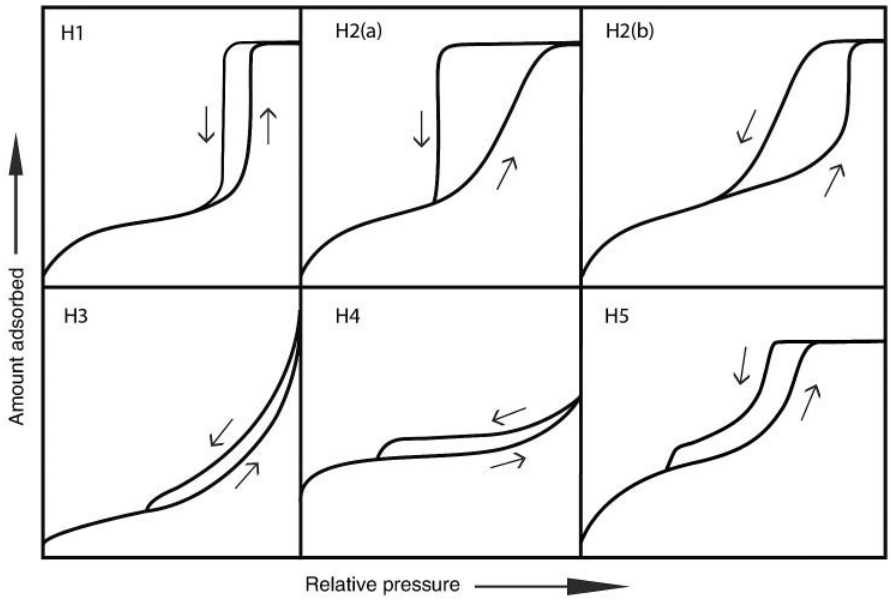

Figure 44: Classification of hysteresis shapes [245].

Pore shapes present within the materials studied (Figure 45) can be interpreted from the type of hysteresis loop observed for the adsorption-desorption isotherm. Hysteresis loop H1 occurs when the porous material consists of agglomerates of uniform spheres in a regular array, and, thus, has a narrow pore size distribution. In contrast, Type H2 loops are observed for more complex pore shapes. They are attributed to condensation and evaporation in materials with broad pore size distributions. H2 (a) loops exhibit very steep desorption isotherms, which can be caused by either pore blocking in the pore neck for narrow ranges or a high evaporation rate. These loops have been found

in isotherms obtained for many silica gels. Type H2 (b) is also related to pore blocking, but the pore size distribution is much broader. At high relative pressure, Type H3 loops do not exhibit any limiting adsorption and are related to slit-like pore aggregation. Similarly, Type H4 loops are obtained for narrow slit-shaped pores; however, the adsorption trend of H4 loops is a combination of Type I and II isotherms. Type H5 loops are uncommon with contributions from both open and partially blocked mesopores [245, 246, 250].

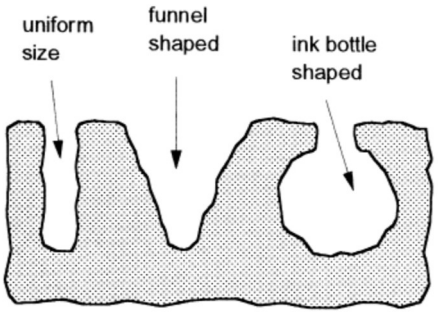

Figure 45: Some typical pore shapes [246].

3.3 Determination of surface area

Adsorption methods are frequently used to characterise a range of porous solids. Of particular significance is the utilisation of physisorption isotherms for the determination of specific areas and pore size distributions of adsorbents, catalysts, dyes, and other materials [251]. The publication of Langmuir's model for monolayer adsorption, in 1918, encouraged researchers to examine the probability of employing gas adsorption for surface area determination. Williams and Benton conducted early works, but these yielded indecisive results [239, 252]. The first major advanced studies were achieved by Brunauer, Emmett, and Teller in 1938 [252]. Their developments in adsorption methods paved the way to multilayer isotherm theory, the so-called Brunauer, Emmett, and Teller (BET) theory [239].

3.3.1 The Langmuir isotherm

It is a simple method of surface area assessment used to derive an equation for isothermal adsorption, and is based on three assumptions [242]:

- The solid sorbent has a uniform surface on a microscopic scale;
- Only a monolayer of adsorbed molecules is formed;

- There is a lack of interactions between adsorbed molecules.

For an adsorption-desorption process, where molecule A is adsorbed molecularly from the bulk gas at a surface site (M), the equilibrium can be described as [242]:

$$A_{(g)} + M_{(surface)} \rightleftharpoons AM_{(surface)}$$

$$\text{Rate of adsorption} = k_a[A][M] \quad \text{Equation 11}$$

$$\text{Rate of desorption} = k_d[AM] \quad \text{Equation 12}$$

Rate constants k_a and k_d are applied to adsorption and desorption, respectively. The equation can be modified in terms of pressure p of the adsorptive and number of empty sites $N(1-\theta)$ on the surface of the adsorbent, where N is the total number of sites on the surface:

$$\text{Rate of adsorption to the vacant sites} = k_a pN(1-\theta) \quad \text{Equation 13}$$

The rate of desorption is proportional to the number of adsorbed molecules $N\theta$:

$$\text{Rate of desorption from a monolayer} = k_d N\theta \quad \text{Equation 14}$$

At equilibrium:

$$\text{Rate of adsorption} = \text{rate of desorption}$$

$$k_a p(1-\theta) = k_d\theta \quad \text{Equation 15}$$

$$K = \frac{k_a}{k_d} \quad \text{Equation 16}$$

solving for θ, the Langmuir isotherm can be expressed as:

$$\theta = \frac{Kp}{1+Kp} \quad \text{Equation 17}$$

Using $\theta = V/V_M$, the above expression can be rearranged as:

$$\frac{p}{V} = \frac{1}{KV_M} + \frac{p}{V_M} \quad \text{Equation 18}$$

From Equation 17, a plot of p/V against p will yield a straight line with a gradient of reciprocal monolayer volume $(1/V_M)$ moreover, from which the monolayer volume (V_M)can be estimated.

The specific surface area can then be calculated from [253] :

$$S = \frac{V_M A_m L}{V_{STP} m} \qquad \text{Equation 19}$$

Where S= specific surface area ($m^2\ g^{-1}$)

A_m= average area covered by one molecule during monolayer coverage

L = Avogadro's number [6.02×10^{23} molecules $mole^{-1}$]

m = mass of adsorbent sample (g)

V_{STP} = molar volume of the gas at STP ($22.414 \times 10^{-3}\ m^3\ mole^{-1}$)

3.3.2 Brunauer-Emmett-Teller (BET) Model

BET theory is a generalisation of the Langmuir isothermal model to include multilayer formation, assuming that multilayer formation is infinite and that Langmuir theory can be applied to each layer in turn [254]. Also, the BET model was developed by assuming [246] that:

- The first monolayer has a constant heat of adsorption, while the heat of adsorption of all other layers is equivalent to the heat of condensation;
- Adsorbed molecules are considered to provide new sites for adsorption of subsequent layers;
- The molecules of the second and upper layers are in equilibrium with the adsorbate molecules (free gas molecules) rather than the adsorbent surface;
- There are no lateral attractions between the adsorbed molecules.

According to these assumptions, at any pressure below the saturation vapour pressure, the fractions of the surface available for multilayer adsorption ($\theta_o,\theta_1,\theta_2,\ldots\ldots,\theta_i$) are covered by the adsorbed layers (0,1,2,……..,i), where θ_o represents the fraction of uncovered surface. It follows that the adsorbed layer is predicted not to possess a uniform thickness, but alternatively is formed from random stacks of molecules, as shown in Figure 46.

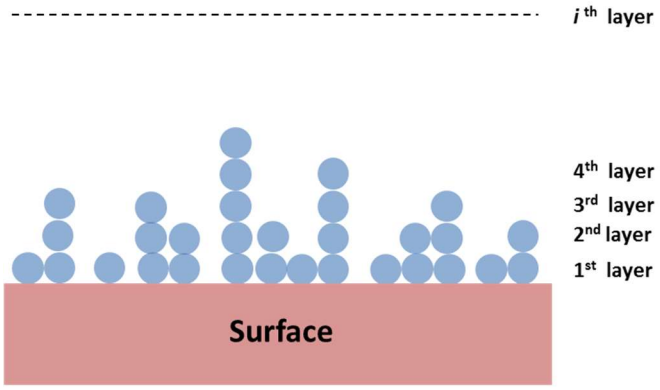

Figure 46: BET theory for adsorption [243].

From the kinetic theory of gases, desorption is dependent on the activation energy E, because each molecule requires sufficient energy to overcome surface forces. Hence, at the pressure p, the fractions of uncovered and covered surface sites θ_o, θ_1, constants k_a and k_d, dynamic equilibrium can be related as:

$$k_{a1} p\theta_o = k_{d1}\theta_1 \exp\left(-\frac{E_1}{RT}\right) \quad \text{Equation 20}$$

Likewise, at equilibrium pressure, the fractional coverage of the surfaces $\theta_2, \theta_3, .., \theta_i$ must also be kept in constant and their equilibrium can be written as:

$$k_{a2} p\theta_1 = k_{d2}\theta_2 \exp\left(-\frac{E_2}{RT}\right) \quad \text{Equation 21}$$

$$k_{a3} p\theta_2 = k_{d3}\theta_3 \exp\left(-\frac{E_3}{RT}\right) \quad \text{Equation 22}$$

Continuing for all surfaces, up to layer i:

$$k_{ai} p\theta_{i-1} = k_{di}\theta_i \exp\left(-\frac{E_i}{RT}\right) \quad \text{Equation 23}$$

where the terms θ_{i-1} ,θ_i denote the fraction covered by layers i-1 and i, respectively, the constants of adsorption and desorption are k_{ai} and k_{di}, and the adsorption energy E_i applies for layer i.

The total fractional coverage over n layers is:

$$1 = \theta_o + \sum_{i=1}^{\infty} \theta_i \quad \text{Equation 24}$$

Also, the total amount of adsorbed can be given as:

$$V=V_M(1\theta_1+2\theta_2+\ldots+i\theta_i+\ldots)$$ **Equation 25**

The BET model depends on the fact that the activation energies after the first layer, taken as the latent heat of condensation E_L of the adsorptive, so that :

$$E_2= E_3= E_i= E_L$$ **Equation 26**

The multilayer thickness is infinite at $p/p_o=1$, and:

$$\frac{k_{d2}}{k_{a2}}=\frac{k_{d3}}{k_{a3}}=\ldots\frac{k_{di}}{k_{ai}}=g$$ **Equation 27**

where g is considered as constant since all layers (except the first layer) exhibit the same characteristics.

The fractions θ_1, θ_2, θ_3,.., θ_i can be expressed regarding θ_o:

$\theta_1= y\theta_o$, where $y = \frac{k_{a1}}{k_{d1}} p \exp\left(\frac{E_1}{RT}\right)$ **Equation 28**

$\theta_2= x\theta_1$, where $x = \frac{p}{g}\exp\left(\frac{E_L}{RT}\right)$ **Equation 29**

$$\theta_3= x\theta_2= x^2\theta_1= yx^2\theta_o$$ **Equation 30**

and, similarly:

$$\theta_i= x^{i-1}\theta_1= yx^{i-1}\theta_o$$ **Equation 31**

If a constant C is used to rearrange rewrite Equation 26, this gives:

$$C=\frac{y}{x}=\frac{k_{a1}}{k_{d1}} g \exp\left(\frac{E_1-E_L}{RT}\right)$$ **Equation 32**

then:

$$\theta_i = Cx^i\theta_o$$ **Equation 33**

the total adsorption can be stated as:

$$\frac{V}{V_M}=\sum_{i=1}^{\infty} i\,\theta_i = C\sum_{i=1}^{\infty} i\,x^i.\theta_o$$ **Equation 34**

considering the value of the sum of an infinite geometric series:

$$\sum_{i=1}^{\infty} x^i = \frac{x}{1-x}$$ **Equation 35**

hence:

$$\sum_{i=1}^{\infty} i\, x^i = \frac{x}{(1-x)^2}$$ Equation 36

as derived in Equation 24:

$$\theta_o = 1 - \sum_{i=1}^{\infty} \theta_i$$ Equation 37

From Equation 33, the above relationship can be written as:

$$\theta_o = 1 - C\theta_o \sum_{i=1}^{\infty} x^i$$ Equation 38

$$\theta_o = 1 - C\theta_o \left(\frac{x}{1-x}\right)$$ Equation 39

This equation can be rearranged as:

$$\theta_o = \frac{1}{1 + C\,x/(1-x)}$$ Equation 40

The value of θ_o and the sum of the geometric series can be substituted in Equation 34 as:

$$\frac{V}{V_M} = \frac{C\,x}{(1-x)^2[1+C\,x/(1-x)]}$$ Equation 41

$$\frac{V}{V_M} = \frac{C\,x}{(1-x)(1-x+Cx)}$$ Equation 42

When the saturated vapour pressure is reached, $p=p_o$ and $V/V_M \rightarrow \infty$, so Equation 20 can be expressed as:

$$x = \frac{\theta_2}{\theta_1} = \frac{k_{a2}}{k_{d2}}\, p_o \exp\left(\frac{E_L}{RT}\right) = 1$$ Equation 43

$$\frac{k_{d2}}{k_{a2}} \exp\left(-\frac{E_L}{RT}\right) = p_o$$ Equation 44

Comparing Equations 44 and 29 gives:

$$x = \frac{p}{p_o}$$ Equation 45

Equation 42 can then be expressed as:

$$\frac{V}{V_M}=\frac{C(p/p_o)}{(1-p/p_o)(1-p/p_o+C(p/p_o))}$$ Equation 46

This equation represents the standard BET model if it is plotted in the form of V/V_M against p/p_o at a constant value of C >2, it gives a curve that is indicative of the shape of a Type II isotherm. When the value of C is positive but less than two, a curve of the shape of a Type III isotherm is obtained [255].

From Figure 47, it can be observed that the shape of the curve depends significantly on the value of constant C.

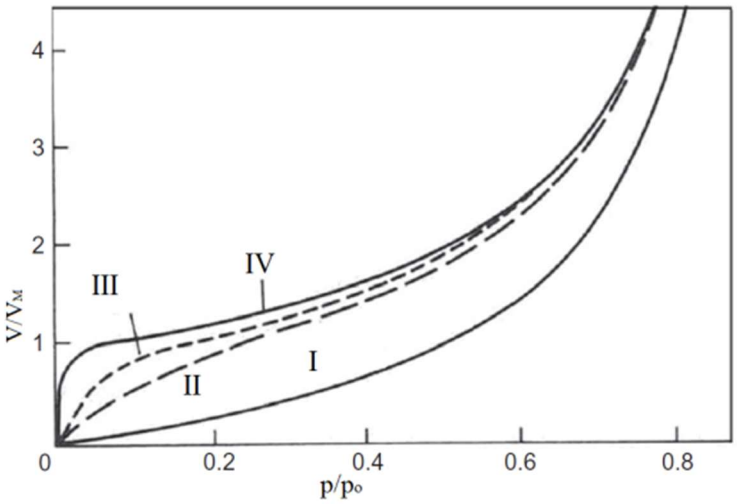

Figure 47: Curves of V/V_M against p/p_o calculated from the BET equation (40) for different value of C. I: C =1, II: C=11, III: C=100 and IV: C = 1000 [243].

Equation 46 can be transformed into a linear BET equation as:

$$\frac{p}{V(p_o-p)}=\frac{1}{V_M C}+\frac{C-1}{V_M C}\frac{p}{p_o}$$ Equation 47

where C is the BET Constant and p_o is the saturation pressure. According to this equation, a linear relationship is obtained if $p/V(p_o-p)$ is plotted against p/p_o. In this case, the slope $(C-1/V_M C)$ and the intercept $(1/V_M C)$ can be used to determine V_M, but the linearity of this relationship is restricted to a limited part of the isotherm that does not exceed 0.3 of the relative pressure (p/p_o) range [251]. Based on this knowledge, Equation 13 can be used to calculate the BET specific surface area.

3.4 Analysis of the porosity of porous materials

Nitrogen adsorption-desorption represents the most common method to characterise the porous texture of nanostructured materials. The texture of these materials is concerned with the geometry of the pores and available pore sizes. Porosity (ε) is expressed as the ratio of the total volume of open pores (V_P) to the apparent volume of the adsorbent [249], this ratio can be given as:

$$\varepsilon = \frac{V_P}{V_P + V^S} \qquad \text{Equation 48}$$

where V^S is the total closed pore volume, and the total pore volume can be obtained from the amount of vapour adsorbed at a relative pressure p/p_o ~1 [256].

This characterisation model for porous solids depends on the geometry and dimension of the pores to be investigated.

3.4.1 Barrett-Joyner-Halenda (BJH) Model

BJH theory is a computational method used to determine mesopore size and distribution. This technique was published in 1951 and is based on the application of the Kelvin equation for pore size estimation [257]. The BJH theory depends on the assumptions that [258]:

- All pores are cylindrical;
- The adsorbent maintains the equilibrium between the adsorbate and the gas phase through two sorption mechanisms: physisorption on the pore walls and capillary condensation into the pores.

The BJH model centres on the Kelvin equation, which addresses the pressure at which capillary condensation arises during nitrogen (N_2) gas adsorption [257], expressed in terms of the surface tension (γ) of the bulk fluid and the molar volume of the liquid adsorbate V_L. For cylindrically shaped pore, the Kelvin equation is generalised as [245]:

$$\ln\frac{p}{p_o} = -\frac{2\gamma V_L}{r_K RT} \qquad \text{Equation 49}$$

where r_K is the Kelvin radius (or capillary) radius, p_o is the saturation vapour pressure; hence, T is absolute temperature, and R is the gas constant. The value of the Kelvin radius depends on the contact angle ∅ between the adsorbed film (liquid) and the capillary condensate on the walls, as shown in Figure 4.

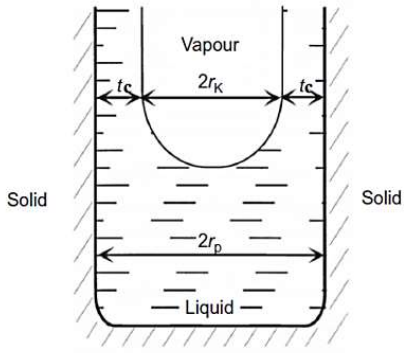

Figure 48: Cylindrical mesopore showing the relation between Kelvin radius and pore radius [259].

If the contact angle is assumed to be zero, the Kelvin radius can be expressed in the main equation as:

$$r_K = (r_P - t_c) \quad \text{Equation 50}$$

where r_p is the pore radius, and t_c is the thickness of adsorbed multilayer.

However, when there is a finite contact angle (β) between the adsorbed film and the capillary condensate, the relation between r_P and r_K can be given [260] as:

$$r_K = \frac{r_P}{\cos \emptyset} \quad \text{Equation 51}$$

The thickness of the desorbed film (nm) as a function of nitrogen pressure at, 77 K, can be estimated by using the Halsey equation [246]:

$$t_c = 0.354 \left[\frac{5}{\ln(p_o/p)}\right]^{1/3} \quad \text{Equation 52}$$

Barrett, Joyner, and Halenda proposed a simple method to characterise the pore size. From nitrogen adsorption-desorption data, the distribution curve can be presented as the volume of adsorbed gas ($dV_P/d\ d_P$) alternatively, specific surface area ($dS/d\ d_P$) as a function of pore size (diameter), d_P . The cumulative BJH surface area is estimated from this correlation [261] as:

$$S_{BJH} = 2\frac{\sum V_{Pi}}{\sum r_{Pi}} \quad \text{Equation 53}$$

Where S_{BJH} is BJH cumulative surface area (m^2), V_{Pi} is the pore volume (m^3) at the pressure of stage i , and r_{Pi} is the pore radius (m) at the pressure of stage i.

Again, considering a cylindrical form of pores, the average pore diameter can be calculated from:

$$d_P av = 4\,V_P / S_{BJH}$$ Equation 54

where V_P is the total pore volume (m^3)

The working BJH equation for pore volume distribution can be illustrated as:

$$V_{Pn} = \frac{r_{Pn}^2}{(r_{Kn}-\Delta t_c)^2}.\Delta V_n - \frac{r_{Pn}^2}{(r_{Kn}-\Delta t_c)^2}.\Delta t.\sum_{j=1}^{n-1}\frac{r_{Pj}-t_{cj}}{r_{Pj}}.A_{Pj}$$ Equation 55

where V_{Pn}= pore volume (m^3)

V_n = observed volume of desorbed gas at n^{th} desorption step, m^3

r_{Pn}= empty pore radius of a desorbed layer during n^{th} desorption step, m

r_{Kn}= capillary radius, m

A_{Pj}= area from which the adsorbed gas is desorbed; $A_{Pj} = 2V_P/r_P$

Δt_c= change in thickness of an adsorbed layer during n^{th} desorption step, m

Thommes *et al.* reported that the BJH method could not be used to achieve a reliable pore size analysis of narrow mesopores; however, this technique is still utilised for some industrial operating purposes [245].

3.4.2 t-plot method

The t-plot method was proposed by Lippens and co-workers in 1964 and is based on plots of adsorbed volumes (V_{ads}) of nitrogen at various relative pressure values as a function of the thickness of the adsorbed multilayer (t). In the t-plot model, a simple procedure is used to compare the shape of the given isotherm curve with that of the standard non-porous solids (Figure 49). The slope of the t-plot (V_{ads}/t) represents the external surface area (slope of the dashed red straight line). The obtained external surface area involves the areas of the mesopores, macropores and the outer surfaces of the particles [246, 261, 262].

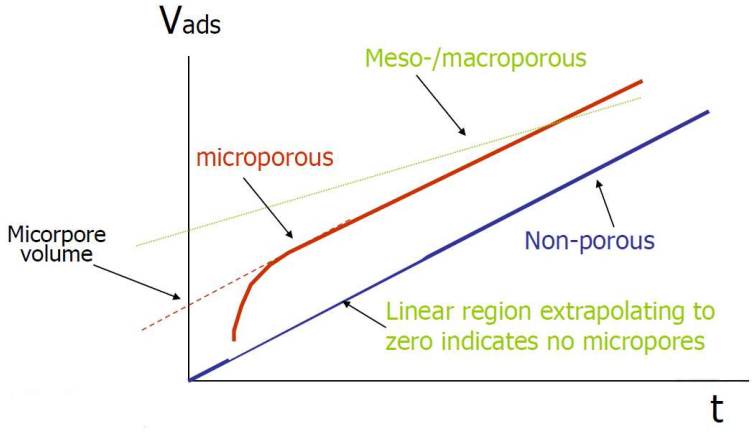

Figure 49: The t-plot shapes of nitrogen adsorption isotherms [263].

In the figure above, the intercept of the dashed red straight line with the volume axis gives the micropore volume, while the meso-/macropore volumes can be observed from the intercept of the green line with the y-axis. Meso- and macropores can form multilayers, while the micropores are first filled by adsorption fluid. The number of layers of nitrogen adsorbed on the surface can be estimated merely via:

$$n = \frac{V}{V_M} \qquad \textbf{Equation 56}$$

where n = the number of layers

V = the amount of nitrogen adsorbed at a given pressure (m^3)

V_M = the amount of nitrogen adsorbed in a monolayer (m^3)

The micropore volume can be separated from the larger pores by [261]:

$$V\left(\frac{p}{p_o}\right) = V_{(micro)} + k\, S_{Ex}\, t\left(\frac{p}{p_o}\right) \qquad \textbf{Equation 57}$$

Lippens *et al.* defined the external surface area S_{Ex} for nitrogen [262] as:

$$S_{Ex} = 1.547\frac{V}{t} \qquad \textbf{Equation 58}$$

Also, they assumed that if there are no micropores within the structure, then the external surface area would be equal to the total surface area, or BET specific surface area. For nitrogen, a value of 16.27×10^{-20} m^2 can be taken as the surface area occupied by one molecule. If the volume of the monolayer (V_M) is given in cm^3; the BET surface area can be calculated from:

$$S_{BET} = 4.37\ V_M \qquad (m^2\ g^{-1})$$ Equation 59

by substituting this value into Equation 58, the thickness of the layer can be expressed as:

$$t = 0.354 \frac{V}{V_M} \qquad (nm)$$ Equation 60

Comparing the above equation with Equation 51, gives:

$$t = 0.354\ n$$ Equation 61

Due to the nature of the interpretation, it is possible to have different correlations of the value of t, such as that proposed by Harkins and Jura [261]:

$$t = \left[13.99/\left(0.34 - \log p/p_o\right)\right]^{1/2}$$ Equation 62

The t-plot model can also be used to calculate the total pore volume (V_p) as:

$$V_p = (V_f/22414)\ M/\rho_L$$ Equation 63

where V_f = the amount of gaseous nitrogen required to fill the pores (cm^3)

M= Molecular weight of nitrogen (28.014 g $mole^{-1}$)

ρ_L= Density of liquid nitrogen at given adsorbate temperature (g cm^{-3})

The surface area contributed by micropore can also be calculated, based on the BET surface area and the external surface area obtained from the t-plot method:

$$S_{Micro} = S_{BET} - S_{Ex}$$ Equation 64

3.4.3 Gas pycnometry and density analysis of porous solids

Gas pycnometry is an effective method used to measure the apparent volume of solid particles. This technique is based on the main Boyle-Mariotte volume and pressure relationship of a gas at a constant temperature. The literature reports three types of gas pycnometer, including 'constant – volume', 'variable volume' and 'comparative' [264-266]. Gas pycnometry theory depends on several essential hypotheses:

- the gas used as a displacement medium behaves ideally (i.e. gas compressibility is negligible, and it does not adsorb on solids at temperatures, generally used for analysis);
- the sample and the pycnometer constituents are rigid;

- the apparatus is gas-tight, and the expanding gas rapidly reaches a stable equilibrium;
- the gas temperature is constant and uniform throughout the apparatus.

Although various inert gases could be used, helium (He) is preferred as a displacement medium, because of its unique characteristics such as its small atomic size. The typical constant – volume helium pycnometer is provided by sample chamber and reference tank with premeasured volumes, a pressure observing device, and a controlled high-pressure source of gas [265, 266] as shown in Figure 50.

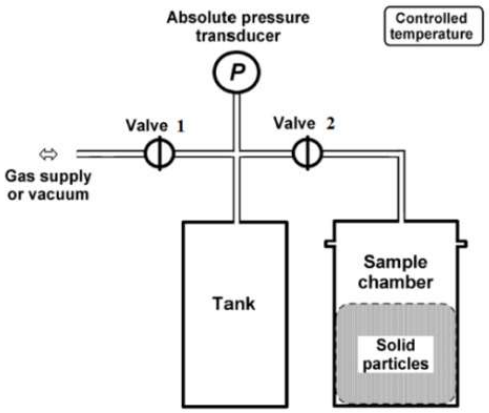

Figure 50: Constant-volume gas pycnometer [265].

Before commencing measurement, it is essential to purge the pycnometer with helium to remove any traces of entrained air. In order to determine the volume of a sample, three steps [265, 266] are considered:

i. the chamber and reference tank is pressurised to the same moderately low pressure; this pressure is denoted as the initial pressure (p_i);
ii. the sample chamber is isolated, and the tank is pressurised to a higher pressure value (p_j);
iii. the sample chamber and reference tank are reconnected so the helium can expand to the sample chamber and the pressure is equalised between them; the final pressure is then measured (p_f).

The sample volume (V_s) can be estimated using the following equations:

$$V_s = V_c^o + V_t^o \tau \qquad \text{Equation 65}$$

$$\tau = \frac{p_f - p_j}{p_f - p_i}$$ Equation 66

where V_c^o and V_t^o are the sample chamber and reference tank volume coefficients, respectively, determined using a calibration procedure.

Gas pycnometry methods have been commonly utilised to determine the volume, and, hence the density of the powders, porous rock pieces, salts, aerogels, plastic films, and coals, etc. [265].

3.5 Infrared (IR) spectroscopy

Electromagnetic radiation (light) can be considered as an oscillation of electric energy and magnetic field, travelling at the speed of light through space. There is a broad range of the electromagnetic spectra including; visible light, ultraviolet, infrared radiation, X-rays, microwaves, radio waves, cosmic rays etc.[267-270].These spectra differ from each other in the wavelength and frequency, as shown in Figure 51. The infrared (IR) is that part of the electromagnetic spectrum lies between the visible light and microwaves. Virtually any organic or inorganic compound having a covalent bond absorbs various frequencies of radiation in the infrared region [271]. Absorption or emission of IR radiation can cause variations in the vibrational energy level within the examined molecule. IR Spectroscopy focuses on the study of the interaction between the infrared radiation and the vibrations of the chemical bonds of materials [242, 272, 273].

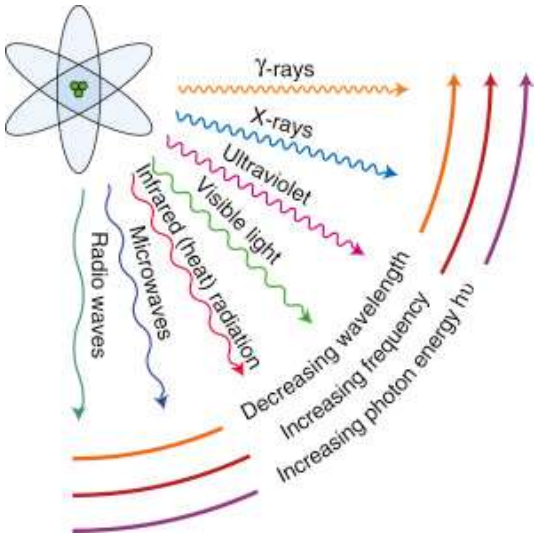

Figure 51: Illustration of the electromagnetic spectrum [274].

Some porous solid surfaces are covered by different functional groups, which influence the final properties of these materials [264]. Attenuated total reflectance (ATR) method can reveal the presence of any of those groups. ART has been discussed in the subsequent sections. It is based on the analysis of the vibrational behaviour of the molecules or atoms, which exposed to infrared radiation [275].

3.5.1 Properties of Infrared spectrum

The typical IR spectrum is described as a relation between the infrared light intensity and property of light (frequency, wavelength or wavenumber) [268, 272]. Either absorption or transmission can measure the light intensity (Figure 52).

Absorbance spectrum (A) can be calculated [272] as:

$$A = \log\left(\frac{I_o}{I}\right) \qquad \text{Equation 67}$$

Where I_o = Intensity in the background spectrum (incident light)

I = Intensity in the sample spectrum (transmitted light)

Absorbance can also be influenced by the concentration of the molecules within the sample, and can be determined using Beer-Lambert's laws:

$$A = \varepsilon\, l\, C \qquad \text{Equation 68}$$

where ε = molar absorptivity, L mol cm^{-1}

C = concentration of molecules, mol L^{-1}

l = path length of the sample, cm; Similarly, the infrared spectrum can be plotted as transmittance (T), either as percentage or unity versus wavenumber. The transmittance can be calculated [272] from:

$$T = \frac{I}{I_o} \quad \text{or} \quad \%\, T = 100\left(\frac{I}{I_o}\right) \qquad \text{Equation 69}$$

From Equations 67 and 69, it can be noted that the absorbance and transmittance are related to each other through:

$$A = \log\left(\frac{1}{T}\right) \qquad \text{Equation 70}$$

As mentioned above, the property of light can be expressed as wavelength (λ) alternatively, wavenumber (W). As the unit of wavelength is distance per cycle, and wavenumber is a cycle per distance, the relation between these two quantities is:

$$W = \frac{1}{\lambda}$$ Equation 71

The wavenumber is related to the energy of the light wave (E, in J) through:

$$E = hcW$$ Equation 72

where c = velocity of light ($\sim 3 \times 10^{10}$ cm s^{-1})

h = Planck's constant (6.63×10^{-34} J.s^{-1})

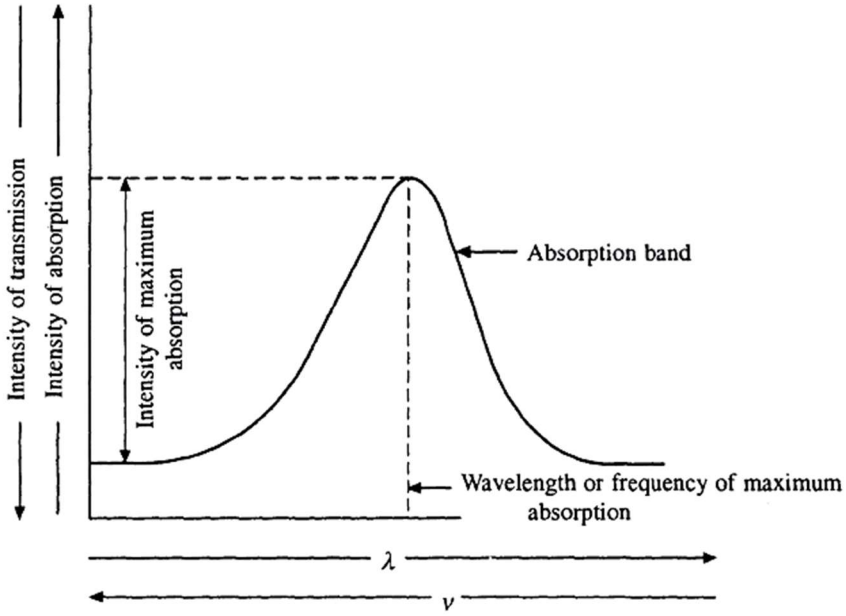

Figure 52: Schematic showing absorption spectrum [268].

The wavenumber is proportional to the energy of light; at a high wavenumber, light exhibits more energy than for low wavenumber light. Another essential property of the light wave is its frequency (ν). It is measured in cycles per unit time (s) or Hz. The relationship between radiation frequency and wavelength is given as [269, 272]:

$$\nu = \frac{c}{\lambda}$$ Equation 73

From Equations (72 and 73), the higher the frequency of radiation, the greater is its energy.

3.5.2 Absorption and emission IR spectra

As the molecule absorbs electromagnetic radiations, they undergo energetic transitions as a result of the energy transfer. The electromagnetic radiations in ultraviolet-visible (UV/Vis) region are sufficiently active to excite bonding electrons into upper energy orbitals. In contrast, the absorption of IR radiations can cause an increase in vibrational

and rotational energy levels within the molecules [267, 268]. Therefore, promoting an electron from a ground state to an excited state requires more energy than promoting the vibrational state of a molecule which in turn needs more energy than promoting energy for the rotational state. For a given electronic energy (E_{el}) level, there are several probable vibrational energy (E_{vib}) levels; similarly, with the vibrational energy level; many probable rotational energy (E_{rot}) levels exist [276], as presented in Figure 53.

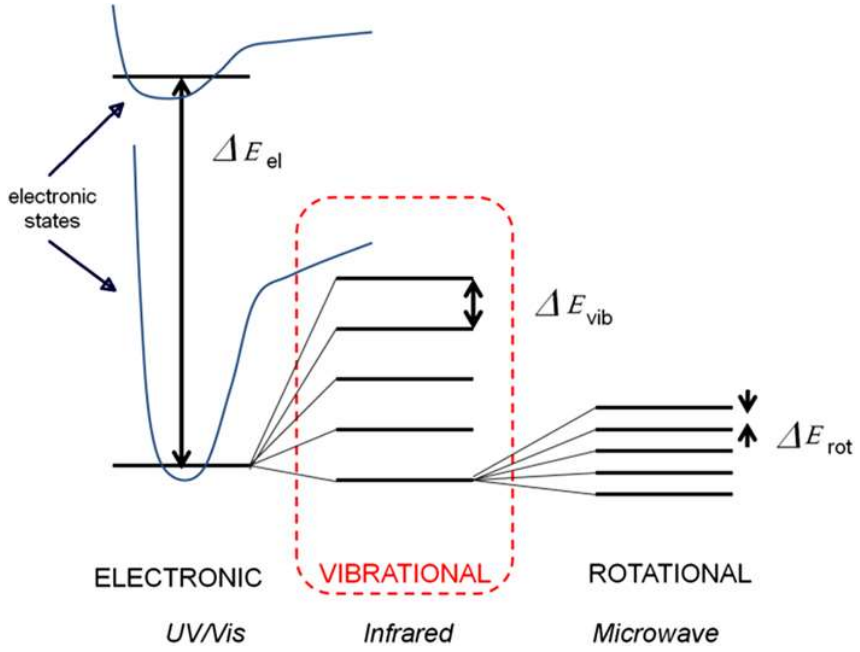

Figure 53: Energy level differences associated with molecular spectra [276].

When the molecules are irradiated with IR light, they absorb energies that correlate with an energy difference between a particular energy level of vibration and another energy level of vibration (excitement); while the unabsorbed light is transmitted [277]. In the absorption spectrum, any peak appears correlating to a specific frequency of a molecular vibration [267, 278]. There are two modes of the vibrational motion in a molecule that infrared excited, stretching and bending vibrations. These vibrational motions occur because of the relative movement of the atoms in molecules to each other, resulting in variation of the bond lengths (stretching) and atom displacements (bending). In general, stretching vibrations occur at higher frequencies (higher energy) than bending vibration (lower energy) [267, 271, 278, 279]. Several atoms can be

regarded as balls with different masses and the covalent bonds between them as tiny springs; with stretching and bending motions, as depicted in Figure 54.

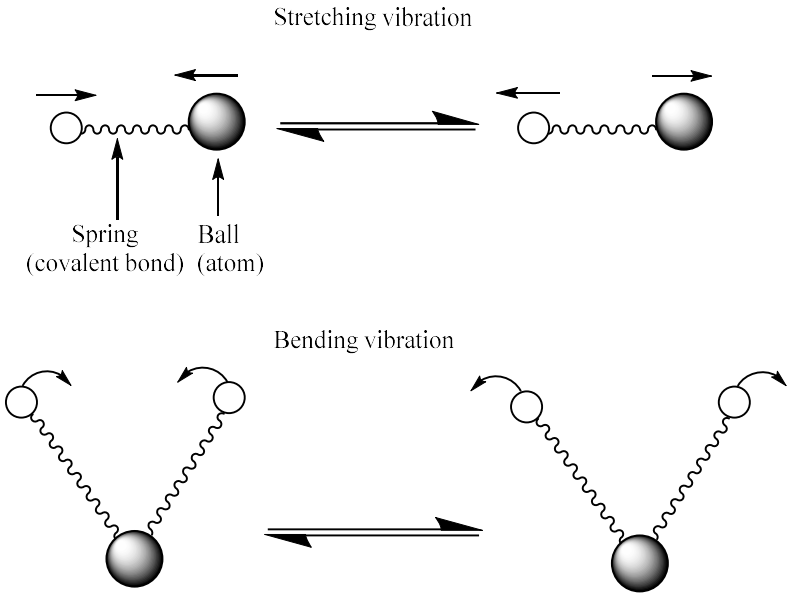

Figure 54: Schematic showing stretching and bending vibrational modes [267].

The stretching mode can be either symmetric or asymmetric, and the bending mode is denoted to as scissoring, rocking, twisting and wagging. A molecule consisting of n atoms possess the net number of fundamental vibration modes of $3n - 6$ for the non-linear system, while the linear molecule has $3n - 5$ vibrational modes [267, 278-280].

At temperatures above absolute zero, the atomic weight and the nature of the chemical bonding have significant effects on the vibration frequency of the atoms, and to the region of the IR spectrum [275]. For practical purposes, the IR spectrum is often classified into three regions [269, 279]:

- Near-infrared (NIR): 12500-4000 cm^{-1}
- Mid-infrared (MIR): 4000-400 cm^{-1}
- Far infrared (FIR): 400-10 cm^{-1}

3.5.3 Mid-infrared (MIR) spectroscopy

The most valuable spectral region is the mid-infrared (MIR), as the majority of organic compounds absorb the IR radiation within this region [269]. The MIR can be sub-divided into three regions [281]: (i) from 4000 to 1400 cm^{-1}, (ii) from 1400 to 900 cm^{-}

[1], and (iii) from 900 to 400 cm^{-1}. A shortlist of frequencies of some typical chemical groups is given in Table 5.

Table 5: Typical vibrational wavenumber for selected chemical groups [242, 281].

Chemical group	Spectral range (cm^{-1})
O – H stretch	3700 – 3200
N – H stretch	3500 – 3200
H – bonds	3750 – 3200
C – H (aromatic) stretch	3065 – 3050
- CH_3 stretch	3020 – 2860
- CH_2 stretch	2960 – 2840
C ≡ C stretch	2260 – 2100
C = C stretch	1680 – 1620
C – H bend	1465 – 1340
C – C stretch, bend	1250 – 700
CO_3^{-2}	1450 – 1410
NO_2^-	1250 – 1230
Silicates	1100 - 900

There are two types of mid-infrared devices: dispersive and Fourier Transform Infrared (FTIR) spectroscopies, but the most extensively used ones are the FTIR techniques [282].

3.5.3.1 Dispersive infrared spectrometers

Dispersive spectrometers are simple MIR instruments, used to obtain the spectral information directly (Figure 55). The IR beam is divided into double parallel beams of identical intensity radiation. The beams are then directed to a sample and a reference inside the sample chamber. After passing the chamber, both beams are combined by movable chopper mirror for the dispersion process in the monochromator (containing grating). For the complete range of the MIR spectra, more than one grating is required. Finally, the dispersed spectrum reaches the detector. All spectral elements are directed to the detector by turning the grating. The obtained spectrum is recorded as the ratio between the intensities of the sample (I) and reference (I_o) beams. This ratio is used to

estimate the absorbance or transmittance (Section 3.5.1). In this method, the detector determines frequencies, which have been absorbed by the sample [271, 282, 283].

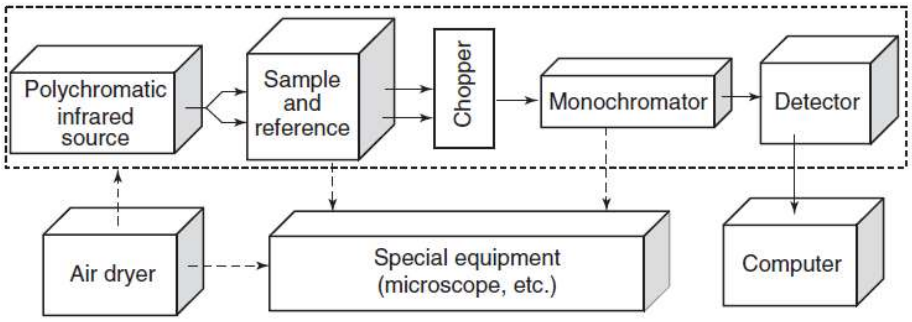

Figure 55: Schematic diagram of dispersive spectrometer [282].

However, the main issue of using the dispersive spectrometers to characterise the materials is the limitation of the wavenumber ranges of the radiation. Also, the low sensitivity of the detector (thermocouple or thermopile), prevents rapid measurements by this type of MIR instruments. These constraints can be overcome through the use of FTIR spectrometers [282, 283].

3.5.3.2 FTIR spectrometers

FTIR is non-destructive spectroscopy, and relatively superficial to alter the infrared spectrum from absorbance to transmittance. It is a vital tool in the characterisation of a varied range of materials [272]. Unlike the dispersion techniques, FTIR spectroscopy involves an entirely different principle, which is based on the interference of radiation between two beams to obtain single-channel spectra for sample and reference. The main parts of an FTIR spectrometer are shown in Figure 56. The IR radiation emerging from the source first passed through an interferometer to the sample before reaching a detector. Signal to exit from the detector amplified (eliminating the high-frequency contribution) and passed via data converter before transferring to a computer for Fourier transformation [271, 282, 283].

Figure 56: Basic parts of FTIR spectrometer [283].

FTIR spectrometers centre on the interferometer which modulates the wavelengths of the IR radiation. The interferometer also allows a broad wavelength range of radiation to pass through the sample with minimal absorption. This optical device comprises a beam splitter, stationary and moving mirrors. The beam splitters are mainly made of potassium bromide (KBr) optical crystal with a multilayer coating. They should have no absorption within the MIR range of use. The interferometer divides the single IR beam into two equal intensity IR beams. The two IR beams travel different paths; after that, they are reflected by the stationary and movable mirrors back to the beam splitter. As the beams return to the splitter, they recombine and interfere. The produced beam emerging the interferometer passes the sample and reaches the detector. A Michelson interferometer is the most common interferometer used for the measurement of infrared spectra [272, 282, 283]. The basic principle of the Michelson interferometer is shown in Figure 57.

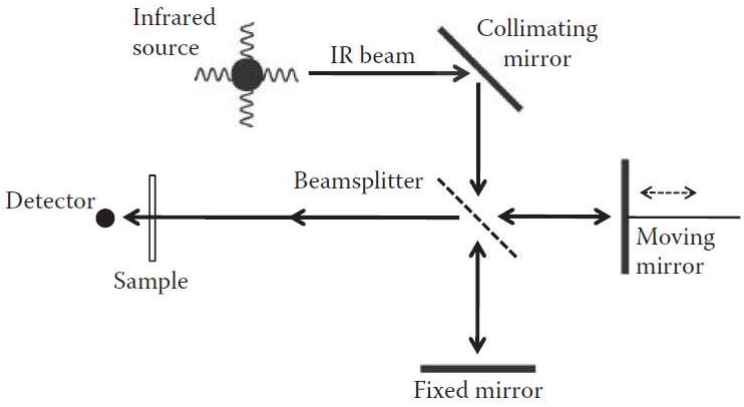

Figure 57: Schematic diagram of Michelson interferometer [272].

During excitation of the different vibrational energy levels of molecules, the resulting transitions can be observed using a variety of measuring techniques. As IR beam interacting with a sample, the incident beam of intensity (I_0) can partly undergo a reflection at interfaces (I_R), scattering (I_S) and absorption in the sample (I_A), the remaining part will be transmitted (I_T) (Figure 58). Based on the law of energy conservation, the energy balance of the incident beam can be given as,

$$I_0 = I_R + I_S + I_A + I_T \qquad \text{Equation 74}$$

The radiation intensities I_0, I_R, I_T, and I_S can easily be measured by insertion the detector at the appropriate position. Absorbance intensity (I_A) provides the essential

chemical data about the studied sample. This intensity value cannot directly be measured, but it can be derived from Equation 74. In the majority of spectrometers, only a single detector used to measure specific two intensity values involving incident beam either reflected, transmitted or scattered, as illustrated in Table 6. Sample techniques are utilised to neglect the remaining intensities; however, disregarding these fundamental values will result in measurement errors [284].

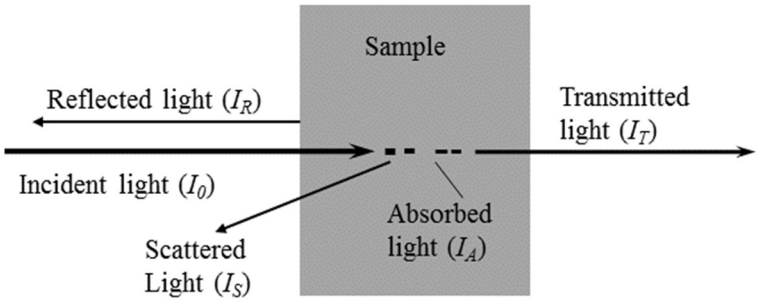

Figure 58: Energy balance of incident beam as interacting with a sample [284].

Table 6: Measured intensities of light [284].

Measured intensity	Aim of sample preparation	Evaluation	Measuring Technique
I_0, I_T	$I_R = I_S = 0$	$I_A = I_0 - I_T$	Transmission
I_0, I_R	$I_T = I_S = 0$	$I_A = I_0 - I_R$	Reflection
I_0, I_S	$I_T = I_R = 0$	$I_A = I_0 - I_S$	Diffuse reflection

For transmission measurement, solid samples can be prepared in the form of thin-film or powder. The thin films are mainly made by polymer solution casting process. The mechanical pressing under high temperature is also used to prepare some polymeric films. For analytical purposes, the powder samples are made by grinding solid to powder, and then diluted with IR-inert materials. The powder sampling process is based on one of the two methods: pelletising or making mulls processes. Pellets are mainly used for solid samples which are difficult to dissolve or melt in solvents. The sample is ground into a fine powder and mixed with a dry alkali halide powder. The mixture is then subjected to compression pressure of ~ 0.6 GPa in an evacuated die to

produce a transparent pellet. The most commonly used alkali halide is potassium bromide (KBr), because of its high transparency in the mid-infrared region.

On the other hand, the mull method for solid samples involves suspending the solid powder into a mulling agent such as Nujol (paraffin oil). This suspension is then spread between two windows (IR transmitting materials) and pressed to form a thin film. Liquid and gas samples do not require complicated preparation methods, but it is essential to used special cells to contain these samples [272, 281, 283, 285].

However, the spectral range covered by these techniques is limited by different factors. In KBr pellets, it is challenging to produce homogenous pellets, and the transparency of the alkali halide (KBr) could be cut off at 500 cm^{-1}. The KBr pellets technique is not recommended for water-sensitive sample and samples that interact with the KBr. While in the mull method, the spectra exhibit a strong absorption around 3000-1400 cm^{-1} in case of using Nujol as mulling agent [281, 286, 287].

Reflectance techniques are used for obtaining the IR spectra by reflecting IR radiations from the surface of solid and liquid samples. These techniques are especially preferred for solid samples that are difficult to examine by the conventional transmittance methods, and for fast sample measurement. Various types of reflection can occur depending on the nature of the reflecting surface (Figure 59).

As an IR beam strikes a rough surface, diffuse reflectance takes place, resulting in many reflectance angles. The diffuse reflectance can be used to investigate a sample with an extremely low mass. It is also utilised to measure the spectra of intractable objects. The specular reflection occurs when the incident beam encounters a smooth surface of the sample (e.g. mirrors and shiny metals). It can also be called external reflection, in which the beam propagates within the rare optical medium. The observations show that the angle of reflectance is the same as the angle of the incident beam. The reflection-absorption is applied to examine thin films adsorbed on IR opaque substrates [272, 283-285].

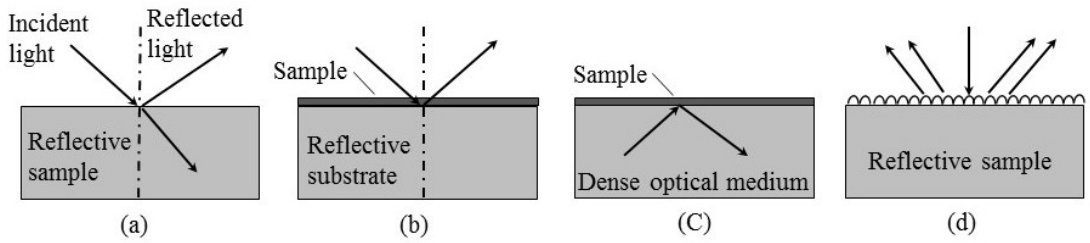

Figure 59: Reflectance types (a) Specular reflection, (b) Reflection absorption, (c) Attenuated total reflectance (internal reflection) and (d) Diffuse reflection [284, 285].

Internal reflection is another type of reflectance, which is illustrated in Figure 59C. The internal reflectance examinations can be performed by using an attenuated total reflectance (ATR) method, which employs the phenomenon of total internal reflection.

3.5.3.3 Attenuated total reflectance (ATR)

ATR is a versatile, non-destructive method for obtaining IR spectra of the surface of a sample. Unlike several other sampling methods utilised in IR spectroscopy, radiation is not transmitted through the sample; thus, there are no further sample preparations as mentioned above in section 3.5.3.2. In the ATR, the infrared beam transfers within a dense optical medium (crystal), and is reflected from its internal surface when the incident angle (θ) on the interface between the sample and the crystal exceeds the critical angle (θ_c). The critical angle is a function of the refractive indices of the two media; crystal (n_1) and sample (n_2) , and is given as [272, 283, 284, 288],

$$\theta_c = \sin^{-1}\frac{n_2}{n_1} \qquad \text{Equation 75}$$

During the total reflection, the IR beam wave propagates through the optical interface creating an evanescent wave, which penetrates the rare crystal surface (Figure 60a). As the sample absorbs a small fraction of energy and the evanescent wave becomes attenuated. The decay rate of this evanescent field depends on the wavelength of the IR beam. The evanescent wave intensity decreases exponentially with the distance above the surface of the internal reflection element (ATR crystal). The depth of penetration (D_p) is a distance at which the strength of the evanescent field is decayed to *1/e* (where *e* is the base of natural logarithms) of its initial intensity at the interface. The depth of penetration can be calculated by the following equation [272, 276, 277, 281, 283, 287, 288]:

$$D_p = \frac{\lambda}{2\pi(n_1^2 \mathrm{Sin}^2\theta - n_2^2)^{1/2}}$$ Equation 76

Where λ is the wavelength of IR radiation within the ATR crystal, and it can be expressed in the form of wavenumber for absorption spectrum ($W = 1/\lambda$).

It can be observed that the depth of penetration is directly related to the wavelength of the incident radiation. At longer wavelength (low wavenumber) radiation, the evanescent penetrates further into the sample (D_p increases); as a result, in the ATR spectra at lower wavenumbers are more intense (high peaks) than those in at higher ones. The depth of penetration is also dependant on the angle of the incident; therefore, the angle of 45º, which allows deeper penetration, is commonly used for bulk samples of the organic substances, rather than the larger angles (e.g. 60º), which result in weaker spectra due to the shorter depth of penetration. The refractive index of the ATR crystal is another critical factor controlling the depth D_p, so it is crucial to select the correct ATR crystal for a specific application. The crystals used in the ATR-FTIR devices are made from different materials such as zinc selenide (ZnSe), germanium (Ge), thallium–iodide (KRS-5), and diamond [272, 276, 283, 287]. Hardness tests on materials could be advised before ATR measurement to avoid scratching the crystal surface. For example, ZnSe is prone to scratches at hardness knoop more than 130 kg-f.m^2 [289]. Properties of some common materials used for the fabrication of ATR crystals are shown in Table 7.

Table 7: Common materials used as ATR crystals [272, 288, 289].

Material	Refractive index	Wavenumber ranges (cm^{-1})	Critical angle* (θ_cº)	Hardness Knoop (kg-f. m^{-2})
Si	3.41	8900 – 600	26	11150
KSR-5	2.37	20,000 – 250	40	-
ZnSe	2.40	15,000 – 600	40	130
Ge	4.00	5500 – 600	22	550
Diamond	2.41	30,000 – 2200 2000 – 400	40	9000

* Critical angel when Refractive index of the sample (n_2=1.5)

Since the sample absorbs some IR radiations, the intensity of the evanescent wave is changed, and the beam loses energy. The resultant attenuated IR beam is internally reflected and then directed to the detector, as illustrated in Figure 60b. The detector measures the changes in the intensity of the evanescent wave to produce the IR spectrum [272, 276, 290].

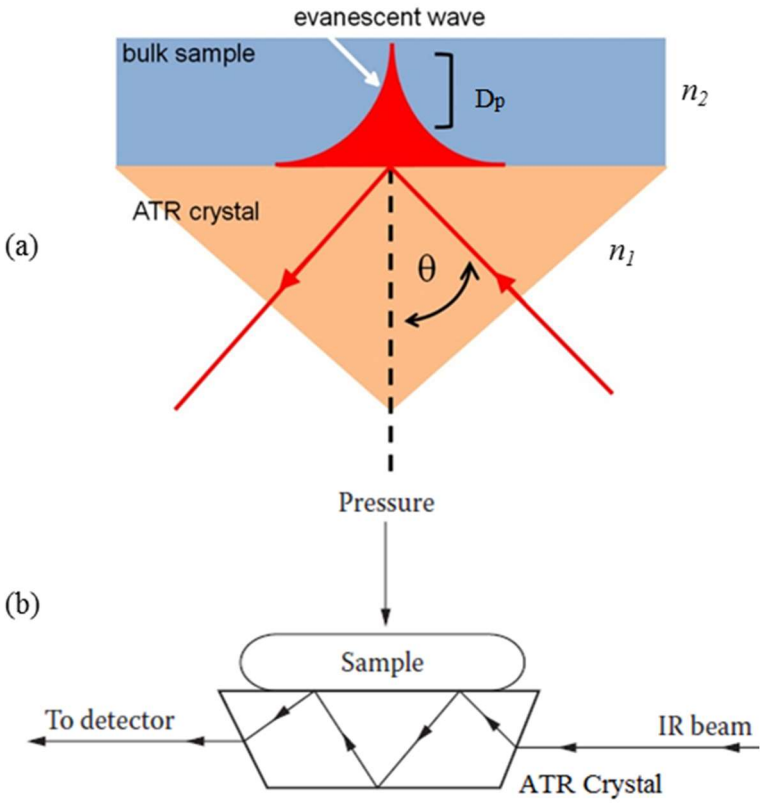

Figure 60: Schematic of typical ATR technique showing (a) evanescent wave, and (b) multiple reflection ATR [272, 276].

Implications for how the ATR spectra can be used and interpreted are due to the dependency of the ATR intensities on the wavelength (wavenumber) of IR radiation. In this context, it is rigorous to compare the ATR spectra to spectra obtained using other sampling methods, because the spectra of the same sample will look different. The ATR technique has several issues that mainly related to ATR crystal. The crystal must be clean and high surface polish. Scratches could interfere with sample/ evanescent wave contact. Weak spectra are obtained as a result of improper contact between the sample and the crystal. As the evanescent wave propagates above the crystal, any dirt or residues on the surface of the crystal could contaminate the resultant

spectrum. Another drawback is the wavenumber ranges of the crystal materials. Several ATR crystals absorb in the mid-IR, for example, diamond absorbs in the wavenumber range of 2200-2000 $cm^{-1,}$ and ZnSe absorbs below 600 cm^{-1} (Table 8). However, the lack of sensitivity is the most significant issue of the ATR technique, which caused by the limitation of the depth of penetration [272, 290].

3.6 Scanning electron microscopy

Scanning electron microscopy (SEM) is mainly used for analysis and characterisation of the microstructural and characteristics of bulk materials. The SEM depends on the release of the electron beam to produce a magnified image of the object. The electrons interact with atoms on the material, generating a various form of signals (Figure 61) that are spotted by a detector, and the varying intensity of the signal is imitated on a screen [275, 291, 292].

When the incident electron beam hit a sample, some electrons lose most of their initial energy and are scattered from the surface with low energy due to the absorption. These electrons are known as secondary electrons (SE), which can escape only from the low depth of the sample providing topographic information. With no loss of energy, the friction of incident electrons undergoes a large deflection as a result of a positive charge of the nucleus. These electrons are reflected backwards as Backscattered electrons (BSE), which are employed to perform a quantitative image analysis of the material morphology. Some absorbed electrons into the sample lose energy resulting in x-ray fluorescence or Auger electron emission, which can be used for element analysis [293, 294].

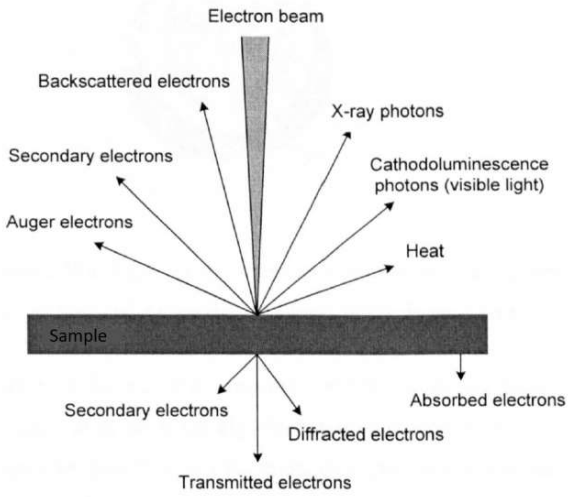

Figure 61: Form of electron beam-sample interactions [295].

The SEM instrument comprises different components; electron gun, condenser lenses which are utilised to de-magnify the electron beam, objective lenses that focus the probe onto the sample surface, a control system for the beam movement, sample stage, electron detector, signal amplifier and a display unit. The schematic of the design principle of the SEM instrument is shown in Figure 62. The electron gun generates a broad beam of electrons, with accelerating energy via an electrical potential (anode) to a range of 1-40 keV, down the evacuated column, allowing the path of the electrons to travel without obstructs. A condenser lens focuses this resulting electron beam to a fine electron probe. It is then directed onto a specific cross-section of the sample by an objective lens and bitmap-scanned over the sample by the scanning coils [292, 296, 297].

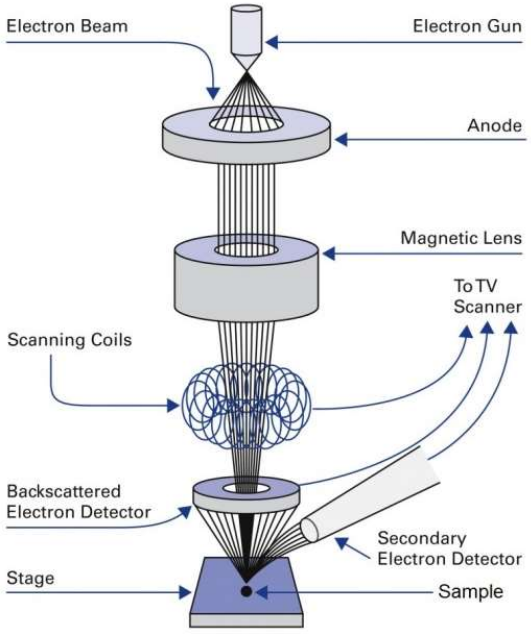

Figure 62: Schematic diagram of the SEM instrument [298].

When the primary electron probe strikes the sample, many types of signal are produced as described above. The SEs with lower energies are collected by Everhart -Thornley detector, which converts these signals to a voltage, and then amplifies to create the images. The obtained images are displayed on a Cathode Ray Tube (CRT) screen. The intensity of the collected SE signal is displayed versus the position of the primary beam on the sample (synchronising). The samples for SEM observation must be either conducting or coated with a thin metal layer to avoid charging effects. Also, the scanning occurs at low pressure, so that the gas molecules do not scatter the electrons as they travel inside the instrument chamber [291-293].

3.7 Heat transfer in porous solids

Heat transfer in porous media is more complicated than in conventional solids, because it occurs not only through the solid but also in a gas phase. Figure 63 depicts the involved heat transport modes schematically. Resistance to thermal conduction of these materials (i.e. aerogels, composites, etc.) depends on their structural properties, such as pore size, pore morphology, and porosity, along with properties, including the TCs of the solid backbone and fluid (gas) in the pores, as well as emissivity and transmissivity of the solids [299].

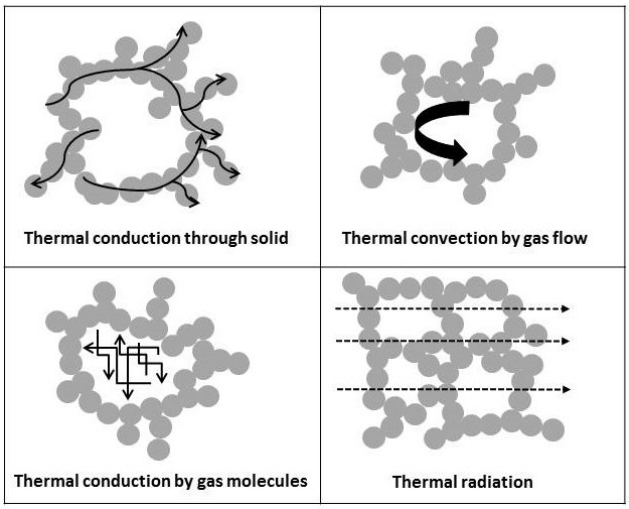

Figure 63: Heat transfer mechanisms in porous solids [300].

The heat transfer equation focuses on the physical properties of a porous material and its TC. The equations for heat transfer can be presented as:

$$\nabla\vec{q} + \Phi = \rho.c.\frac{\partial T}{\partial t} \qquad \textbf{Equation 77}$$

$$\vec{q} = -k\,\nabla T \qquad \textbf{Equation 78}$$

with q = heat flux (W m^{-2}), k = thermal conductivity ($Wm^{-1}.K^{-1}$), ρ = density (kg m^{-3}) , c = specific heat (J $kg^{-1}.K^{-1}$), Φ = heat generated (W) and T = local temperature (K). Equation 77 considers the first law of thermodynamics (energy conservation) and equilibrates the heat flux across the boundaries of a finite volume. Equation 78 represents Fourier's law, which reveals that the heat transfer rate is proportional to the temperature gradient. The heat source Φ involves processes that occur within the porous solids such as the release or absorption of reaction enthalpies, and the gain or loss of thermal radiation, which is crucial when studying the thermal radiation in infrared optically transparent materials, for example, silica aerogels [220]. The generated heat term Φ, which relates thermal radiation, is illustrated by:

$$\Phi = \nabla\,\overrightarrow{q_r} \qquad \textbf{Equation 79}$$

where q_r is radiative heat flux, it denotes transportation of thermal energy through an electromagnetic field, and appears in the forms of reflection, absorption, and scattering, all of these are vital factors in the heat transfer phenomena observed in superinsulation [301]. For a homogenous porous material, and if the heat transfer is

based only on the temperature gradient [220], in the absence of the internal heat generation [299], Equation 77 can be simplified as:

$$\Delta T = \frac{1}{a} . \frac{\partial T}{\partial t} \quad \text{Equation 80}$$

where the thermal diffusivity is:

$$a = \frac{k}{(\rho . c)} \quad \text{Equation 81}$$

From this definition, it can be noted that TC is a property of the material. The term ρ.c is designated as the volumetric specific heat and is related to non-stationary heat transfer where the temperatures and heat fluxes vary with time. For porous media, conduction via the solid backbone structure and gaseous phase, convection by the gas flow, and radiation, all contribute to the heat transfer process. However, for the material of this study, the average size of the pore is sufficiently small to mean that the influence of natural convection is negligible [220, 299].

3.7.1 Solid conduction

Conduction of heat through the solid backbone (i.e., the primary chains of material molecules) of a porous material depends on its mainstay structure, particle connectivity, and chemical composition. Studies have indicated that heat conductance via the solid phase, which is termed as solid TC, has a considerable impact on the thermal insulation capability of material [232, 233]. Fricke *et al*. derived an expression for the solid TC (k_s) of silica aerogels by measuring their sound velocities [28]:

$$k_{sc} = k_{so} \frac{\rho}{\rho_o} \frac{v}{v_o} \quad \text{Equation 82}$$

where ρ and ρ_o are the corresponding densities of the aerogel and the full solid from when synthesised (backbone material), v and v_o are their average sound velocities respectively, and k_{so} is the backbone TC.

From the phonon diffusion model, developed by Debye, the TC of the backbone material, at a given temperature, is described as [220]:

$$k_{so} = \frac{1}{3} \rho_o C_V l_{ph} v_o \quad \text{Equation 83}$$

where c_v is the specific heat at constant volume, and l_{ph} is the phonon mean free path in the backbone material.

According to Gross *et al*., the sound velocity of porous materials (aerogels) can be given by [302]:

$$v(p_{gas}) = \left[\frac{(c_{11} + x\, p_{gas}\, \Pi)}{(\rho + \Pi \rho_{gas})}\right]^{1/2} \quad \text{Equation 84}$$

Here, c_{11} is the elastic modulus, Π is the porosity of the aerogel, p_{gas} and ρ_{gas} are the pressure and density of the gas occupying the pore, respectively, and x is related to the specific heat of the aerogel. Gross and co-workers measured the sound velocities for the aerogels at different densities. Their results indicate that the sound velocity decrease linearly with decreasing density, but it is influenced by the pore gas for aerogels with densities less than 100 kg m^{-3}. This relation can be illustrated by the scaling law [302]:

$$v \propto \rho^{\alpha} \quad \text{Equation 85}$$

with α =1.3 at density higher than 100 kg m^{-3} (non-evacuated aerogel).

It can be noticed (Equations 78 and 80) that the density of the porous material is the most crucial factor for the solid TC. For aerogels [198]:

$$k_{sc} \propto \rho^{\alpha} \quad \text{Equation 86}$$

Here, α =1.5, at densities ranging from 70 to 300 kg m^{-3}

A key objective in the design of thermal insulation is to reduce the contribution of solid conduction. This process cannot be easily achieved without affecting other heat transfer modes, specifically radiative heat transfer, as well as many other mechanical properties [301].

3.7.2 Gaseous heat conduction

In nano-porous solids, the characteristic pores exhibit dimensions of 1-100 nm, which results in the fact that gas heat conduction through the network structure is reduced compared with the free gas. Thus, at ambient pressure and temperature, the gas trapped within the low-density nano-porous solid has a significant influence on the total TC [198, 220, 233]. Some porous materials, such as silica aerogels show total TC values

far lower than the TC of the free air (0.026 $Wm^{-1}K^{-1}$) at ambient conditions. In addition to the sharply reduced solid TC, these are the main reasons for the selection of aerogels as typical thermal insulation materials [220]. The TC of a pore gas (k_{gc}) in aerogels is given by [232]:

$$k_{gc} = \frac{k_{go}\,\Pi}{1 + 2\beta\,K_n} \qquad \text{Equation 87}$$

where k_{go} is the TC of non-convective free gas in the pores, Π is the porosity of the material, β is a constant depending on the gas (~2 for air), and K_n is the Knudsen number, which is the ratio of the mean free path of the gas atoms or molecules (l_g) and the average pore diameter or size (d_p):

$$K_n = \frac{l_g}{d_p} \qquad \text{Equation 88}$$

Heat within the gas phase is transferred via interaction of the gas molecules with each other and with the adjacent solid backbone via molecular collisions. As a result, the gaseous heat conduction depends on the Knudsen number. For $K_n \gg 1$, the average pore diameter is considerably smaller than the mean free path of the gas molecules. In this case, collisions mainly occur between the gas molecules and surrounding solid pore walls of the porous material, which results in a TC effect proportional to the number of gas molecules (i.e. gas pressure). Contrarily, when the mean free path of the gas molecules is much smaller than the average pore size ($K_n \ll 1$), the gas molecules collide with themselves, causing the thermal conductivity of the gas phase system to equal the TC of the free gas. This regime is independent of gas pressure and is classified as diffusive heat transfer. For $K_n \sim 1$, the gas molecules strike both the pore walls and each other [303].

Equations (87) and (88) show that pore size is a predominant factor in reducing the gaseous heat transport contribution to conductivity. Pore size reduction could lead to the lowering of the gaseous conductivity and, as a result, reduce the total TC of the material. Another critical factor in controlling gaseous heat conduction is the gas pressure within the pore; the effect of this factor can be illustrated [233] as:

$$k_{gc} = \frac{k_{go}\,\Pi}{1 + \frac{p_{1/2}}{p_g}}$$ Equation 89

here, $p_{1/2}$ is the gas pressure at which the value of the gaseous TC is one-half of the value of the free gas (k_{go}). The influence of gas pressure on the total TC of the aerogels has been extensively studied [28, 301, 304-306]; the obtained results demonstrate that the gas pressure could affect both solid and gaseous TCs. Solid conduction can be lowered by reducing of the gas pressure, which plays a significant role in reducing the contact area of the chain particles (small contact area will increase the resistance to heat transfer within the material) as shown in Figure 64 [220].

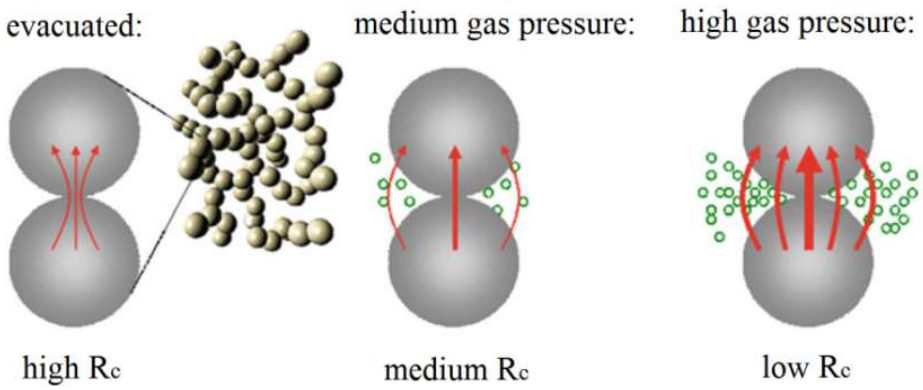

Figure 64: Coupling effect between the heat transfer in the gas and solid phases of an aerogel [220].

3.7.3 Radiation

Radiative heat transfer denotes the transport of energy by electromagnetic waves, and attenuation of radiation occurs in the form of scattering and absorption processes. Radiative transfer within porous materials such as aerogels, is noticeable in the significant difference between diffusive and non-diffusive radiation, depending on the optical thickness of the material(τ). This property can be expressed concerning the geometrical thickness (d) [220, 301], as:

$$\tau(\Lambda) = \frac{d}{l_{pht}} = E^{*}(\Lambda)\, d = e^{*}(\Lambda)\, \rho\, d$$ Equation 90

where $E^{*}(\Lambda)$ is the average extinction coefficient and l_{pht} is the mean free path of the photons of the wavelength (Λ).This relation shows the degree of the interaction between the photon and the mean free path (l_{pht}) and the material thickness (d). The

wavelength-based specific extinction $e^*(\Lambda)$ is a material characteristic, and depends on the chemical nature and structure of the medium [220]. Figure 65 shows the specific extinction of non-opacified and opacified aerogels as a function of the wavelength.

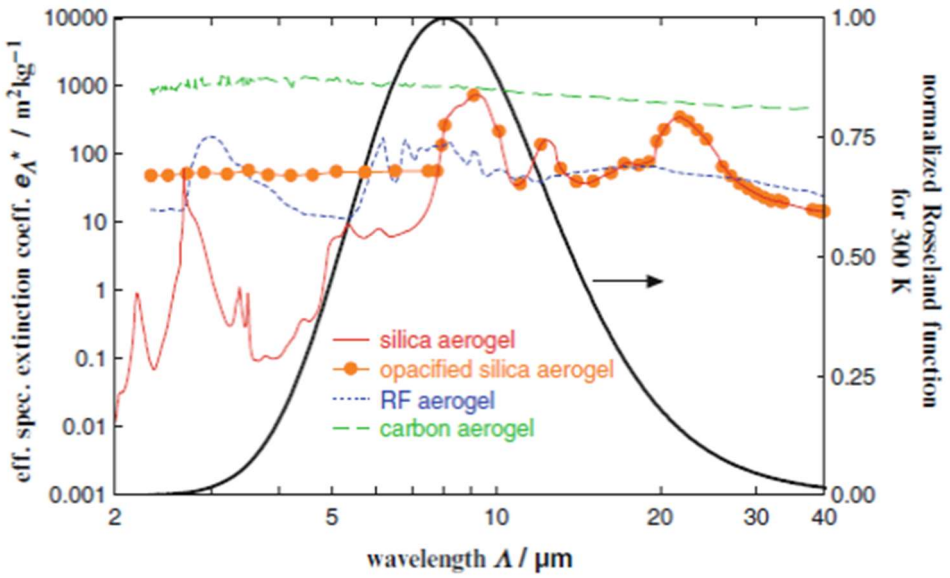

Figure 65: Specific extinction of different aerogels with the normalized Rosseland weighting function, showing the maximum thermal radiation for 300 K at a wavelength of 8 µm [220].

For optically thick media, e.g. organic, opacified or carbon aerogels, radiative transport is described by the concept of diffusion of photons. As long as the mean free path (l_{pht}) of a photon is very short compared with the geometric distance (d), the thermal radiative transfer can be derived analogously to solid conduction, as [307]:

$$q_r = -k_r(T)\,\nabla T \qquad \text{Equation 91}$$

where k_r is the radiative conductivity [220]:

$$k_r = \frac{16\,n^2\,\sigma\,T_r^3}{3\,\rho\,e^*(T)} \qquad \text{Equation 92}$$

Here, n is the average index of the refraction of the porous material (for low-density aerogels ~ 1), σ is the Stefan-Boltzmann constant (5.670367×10^{-8} kg s^{-3} K^{-4}), T_r is the mean radiative temperature, ρ is the density of the material, and $e^*(T)$ is temperature-dependent specific extinction. The term $e^*(T)$ can be calculated using the Rosseland weighting function $f_R(z)$[220]:

$$\frac{1}{e^*(T)} = \int_0^\infty \frac{1}{e^*(\Lambda)} f_R(z)\, dz$$ Equation 93

with

$$f_R(z) = \frac{15}{4\pi^4 z^6} \cdot \frac{e^{1/z}}{(e^{1/z}-1)^2}$$ Equation 94

$$z = \frac{\Lambda . T . B}{h . c}$$ Equation 95

Where h: Planck constant, c: velocity of light and B: Boltzmann constant.

The radiative temperature T_r can be calculated from the boundary temperatures T_1 and T_2 (K)[198]:

$$T_r^3 = \frac{1}{4}(T_1^2 + T_2^2)\,(T_1 + T_2)$$ Equation 96

3.7.4 Determination of thermal conductivity in porous solids

Thermal conductivity (k) is defined as the capability of a material to transport heat. In general, Fourier's law for heat transfer can be used to determine the TC of the material as [308]:

$$k = \frac{q}{A} \cdot \frac{x}{\Delta T}$$ Equation 97

where q is the rate of heat transfer, A is the cross-sectional surface area of the conducting material, ΔT is the temperature difference, and x is the thickness of the conducting material separating the two temperatures. In other words, TC can be defined as the rate at which the heat is transported by conduction through a unit cross-sectional area of the material when the temperature gradient vertically spans the area. The SI units of TC are $Wm^{-1}K^{-1}$. There are several techniques for measuring the TC of porous materials. Each technique has been designated for a particular range of TC values (Figure 66).TC measurement techniques can be classified into two groups: steady-state methods and transient methods [309].

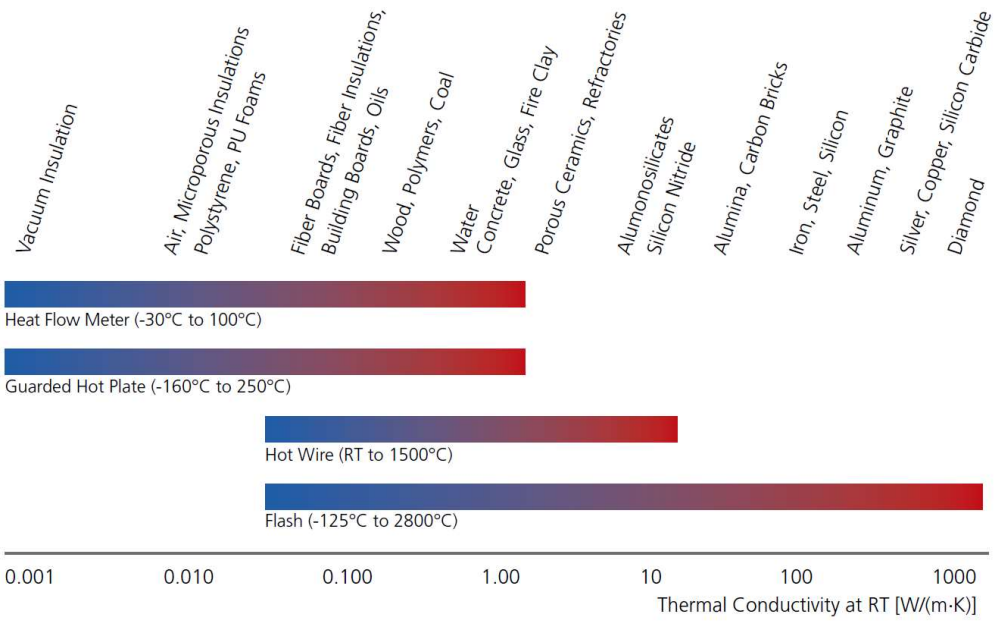

Figure 66: Measurement techniques for thermal conductivities [310].

3.7.4.1 Steady-state methods

The steady-state techniques are applied when the thermal condition of material reaches equilibrium; this condition can be achieved as the temperature at each point of the sample is constant and time-independent. The main drawback is that it is a time-consuming method to reach equilibrium, and requires a significant specimen size. The determination of TC is generally based on the measurement of heat flux and a temperature difference according to Fourier's law (Equation 97). The primary steady-state methods consist of either guarded hot plate (GHP), heat flow meter (FHM), axial flow, or pipe method [309, 311, 312].

Guarded hot plate

The guarded hot plate method is commonly used for testing materials with low TC. It can be utilised efficiently to determine the TC of various nanomaterials such as polymers, porous ceramics, glasses, and thermal insulations (Figure 66). The GHP instrument comprises one or two cold plates, a hot plate, a system of guard heaters and thermal insulation. In this technique, the thermal gradient across the sample is formed by exerting a heat flux on one side of the slab-like sample and allowing heat transport through the tested sample to a cold plate on the other side of the sample. The temperature difference (ΔT) between the two plates is measured when the system reaches a steady-state. The TC can be then calculated, based on the applied heat flux

and temperature difference, as well as the thickness and surface area of the sample. There are two types of GHP: two-specimen and single-specimen device [291, 309, 311, 312], as shown in Figure 67.

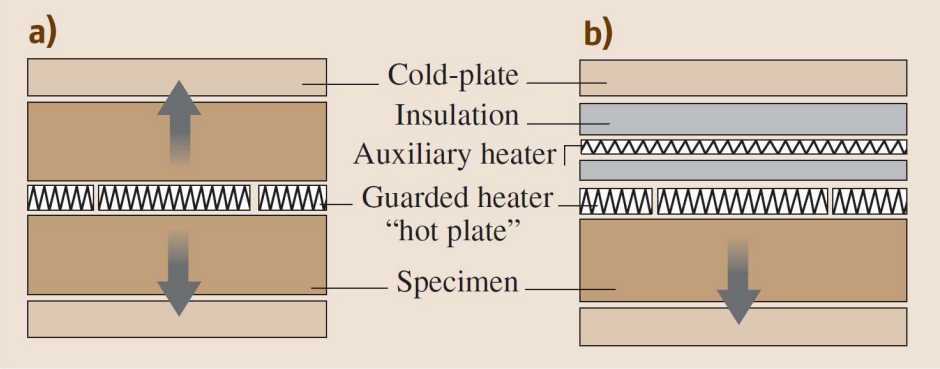

Figure 67: Schematic of the guarded hot plate method: (a) two-specimen device, (b) single-specimen device [291].

In the two-specimen system, heat losses can be controlled more efficiently as a result of the symmetrical arrangement of the specimen. Unlike the single-specimen apparatus, only the solid material can be measured because of the effect of convection on the TC measurement [291, 312]. The GHP method can be used in conjunction with international standards, including ASTM C177, ISO 8302 and EN 12667 [309].

Heat flow meter method

The concept behind the heat flow meter is based on the same principles as the guarded hot plate method, with a difference in that the main heater is replaced by a heat flux sensor (transducer). The temperature gradient is measured across a thermal resistor, which is equipped with a series of thermocouples. The advantage of the heat flow meters is that they are more accurate and faster than the GHPs. The typical maximum temperature limits are approximately 473 K for the heat flow meter technique and roughly 373 K for practical applications. The HFM method is compliant with different standards such as ASTM C518, ISO 8301, DIN EN 12664, DIN EN 12667, and DIN EN 13163 [309, 312].

The design of the HFM resembles the single-specimen GHP apparatus. The method determines the heat flux passing through the test sample by measuring a temperature drop across a thermal resistor, which is in correlation with the determination of a current by the measurement of the voltage drop through an electrical resistor. As

illustrated in Figure 68, the sample is placed between two plates held at different temperatures; with the upper plate being heated and the lower one being cooled.

Heat flux transducers (sensors) provide an electrical output signal. The measured signal is a thermovoltage related to temperature drop occurring across the plate. In order to reduce measurement duration and determine radial heat losses, another heat flux is applied at the cold plate. The temperature of the plates is determined and regulated to the desired set-point when reaching a constant value. Steady-state conditions occur when the heat flux at each point of the layered system is the same. The TC can be calculated as in the gauged hot plate method. The heat flux sensor is calibrated with a reference standard of a known TC [291, 312].

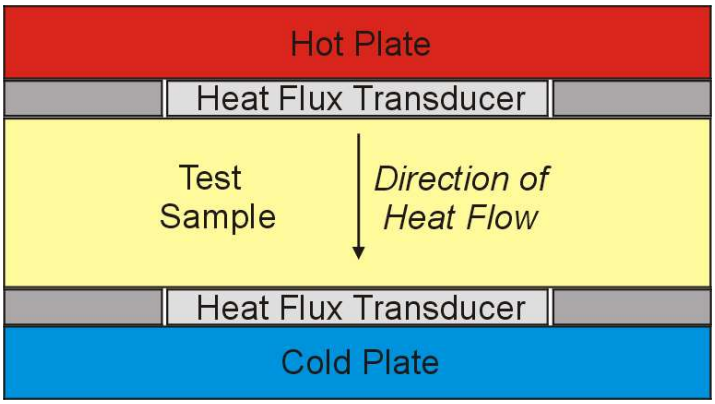

Figure 68: Principle design of heat flow meter [312].

Heat flow (q) passes through the sample and is measured by the (calibrated) heat flux sensors; the calibration factor is characteristic of the device. In the case of one calibration standard, this factor can be determined according to ASTM C518 as:

$$S_{cal} = \frac{c(T_h - T_c)}{(E_1 + E_2)} \quad \text{Equation 98}$$

where S_{cal} is the calibration factor ($Wm^{-2}\,\mu V^{-1}$), E_1, E_2 are heat flux transducer signal outputs (μV), T_h and T_c are the temperature of the upper and lower plates, respectively, and c is the thermal conductance of the reference material ($Wm^{-2}K^{-1}$), given as:

$$c = \frac{k_{Ref}}{x_{Ref}} \quad \text{Equation 99}$$

Here, k_{Ref} and x_{Ref} are the TC and thickness of the standard material, respectively.

It is crucial to maintaining the mean temperature and the plate temperature equal to those used in the calibration process [313]. The calibration factor is used to calculate the TC of the test sample (k_{test}) as:

$$k_{test} = S_{cal}\, E\, \frac{x_{test}}{(\Delta T_{test})} \qquad \text{Equation 100}$$

where E is the total signal output of the heat flux transducers, x_{test} is the thickness of the specimen, and ΔT_{test} is the temperature difference across the specimen.

3.7.4.2 Transient methods

Non-steady state or transient methods are applied to determine thermophysical properties using transient sensors. In transient heat conduction, the temperature field T(x, t), is in a one-dimensional geometry, and dependent on the location (x) and time (t) as [291]:

$$\frac{\partial T}{\partial t} = a\, \frac{\partial^2 T}{\partial x^2} \qquad \text{Equation 101}$$

Here, a is the thermal diffusivity (m^2s^{-1}), which can be estimated from the specimen thickness and the time required for the temperature rise to reach a percentage of its maximum value. The TC (k) is given as a product of the density (ρ) and the thermophysical properties (a C_p) as:

$$k = a\, C_p\, \rho \qquad \text{Equation 102}$$

Where C_p is specific heat ($J\, kg^{-1}K^{-1}$), these measurements can be made more quickly than for steady-state techniques. However, transient methods usually give lower accuracy and require more complicated data processing. The main transient techniques include laser flash and hot-wire methods [309].

Laser flash method

The most commonly used method for measuring solid thermal transport properties is the laser flash method. The method can be used for a wide range of temperature and TC. The concept of the laser flash method is based on heating a small disk specimen, which is placed in a vacuum furnace, by a low laser beam on the front side of the sample, and on measuring the temperature change at its rear side [291, 309, 314]. Figure 69 shows the schematic and theory of this method.

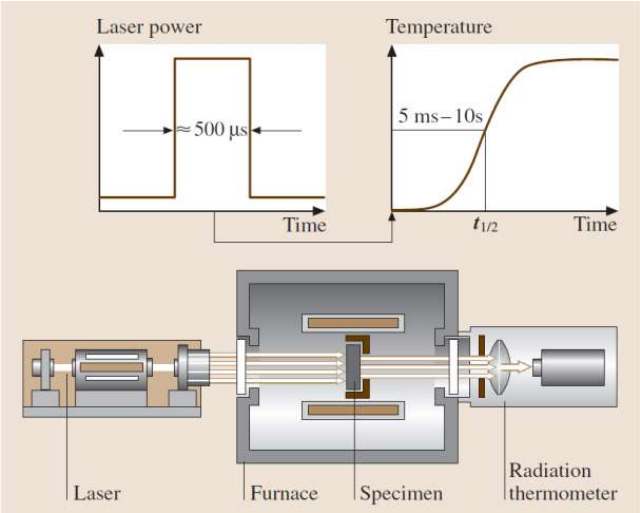

Figure 69: Schematic design and principle of laser flash method [291].

Under the adiabatic condition, the thermal diffusivity is calculated from [314]:

$$a = 0.1388\frac{d^2}{t_{1/2}}$$ **Equation 103**

where d is the thickness of the specimen (~2mm), and $t_{1/2}$ is the time needed for the rear specimen surface to reach half of the maximum temperature after pulse heating, as shown in Figure 69. In order to obtain the TC, the specific heat (C_p) of the test sample can be measured using a differential scanning calorimeter.

3.8 Thermal analysis

In materials science, the term thermal analysis is concerned with any method involving characterisation of material as the temperature is changed or maintained under controlled conditions [315]. Several techniques of thermal analysis are used to analyse and study solids (e.g. porous solids), and these are differentiated from each other by the property that is measured [275]. For the characterisation of sol-gel based materials, the most frequently used methods are thermogravimetric analysis (TGA) and differential scanning calorimetry (DSC). These techniques can be employed in the field of aerogels to determine their degradation, glass transition temperature (T_g), specific heat, and other properties [316]. The coinciding applications of TGA and DSC, or any other technique to the same specimen in a single apparatus, can be referred to as a simultaneous thermal analysis (STA).In STA, the test conditions are ideally uniform for DSC and TGA (or another technique) signals [275].

3.8.1 Differential scanning calorimetry

With DSC, the difference in the amount of heat required to increase the temperature of a specimen being analysed and reference material is measured as a function of temperature. In this technique, the physical changes within the sample are monitored and recorded over time. A test sample undergoes physical transformation such as phase transition, which can be observed as an additional or reduced heat amount to flow to the sample than the reference in order to retain both at the same temperature (Figure 70). The output DSC systems output represents the amount of this additional heat [275, 291].

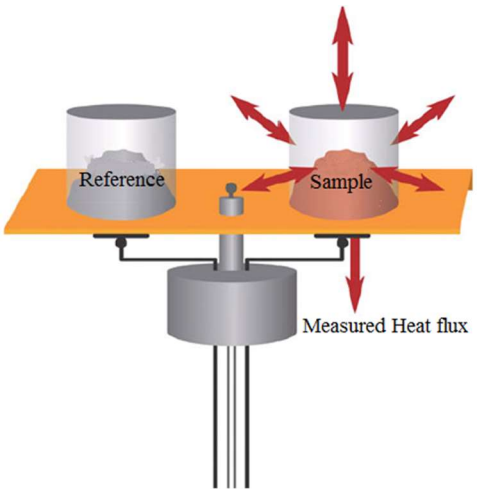

Figure 70: Heat flow DSC principle [291, 317].

The DSC measures the difference between heat flow into a sample, and the heat flows into a reference inert sample. The net heat flow rate (Q') is given as [291, 318]:

$$Q' = \frac{dQ}{dT}$$ **Equation 104**

This proportional difference in the heat flow rate (Q') is caused by the difference in temperature (ΔT) between the sample and the reference. The extent of the heat flow rate can be expressed as a function of thermal resistance (R) using Fourier's law for heat conduction [318, 319]:

$$Q' = \Delta T/R$$ **Equation 105**

When a solid specimen melts to a liquid, it will require more heat to raise its temperature to the same extent as the reference, which due to the endothermic phase transition from solid to a liquid, where heat is absorbed. Similarly, less heat is required to increase the sample temperature as it undergoes exothermic processes (e.g., crystallisation). By monitoring the difference in heat flow between the sample and reference, DSCs are capable of measuring the amount of heat absorbed (endothermic transition) or omitted (exothermic transition) during these phase transitions. DSC may also be applied to observe other physical changes such as glass transition temperature, the heat of fusion, and kinetics of reactions. As the temperature of a molten polymer is decreased, it reaches its glass transition temperature (T_g) at some point. At the T_g, the mechanical properties of the polymer change from those of an elastic material (rubber) to those of a glassy [102, 275, 320, 321].

Figure 71 shows the most frequently transitions obtained from the DSC measurement. A plot of heat flow either exothermic (Exo) or endothermic (Endo) as a function of the sample temperature. For example, in thermoplastics (e.g. polyethylene), the most of these transition temperature could be detected, while in the thermosets (e.g. RF gels) the glass transition, curing, and decomposition temperatures could be observed [319].

In DSC measurement, both a transition temperature and a heat of transition can be determined. The transition temperature can be derived from the extrapolated onset temperature, while the enthalpy of transition is determined from the peak area of the heat flow curve. There are two modes of DSC instruments: Heat flux DSC and power-compensated DSC. The heat flux DSC is based on the measurement of the difference in heat flow rate to, as mentioned above. There are two different design principles of the heat flux DSC type, these being disk-type and cylinder-type DSC systems. In the power compensation DSC, the sample and the reference are heated separately in two micro-furnaces according to a given temperature programme. The difference in temperature between these micro-furnaces is measured and controlled to acquire the same profile of temperature versus time. This instrument type is also based on measuring the heat flow rate difference [291, 321].

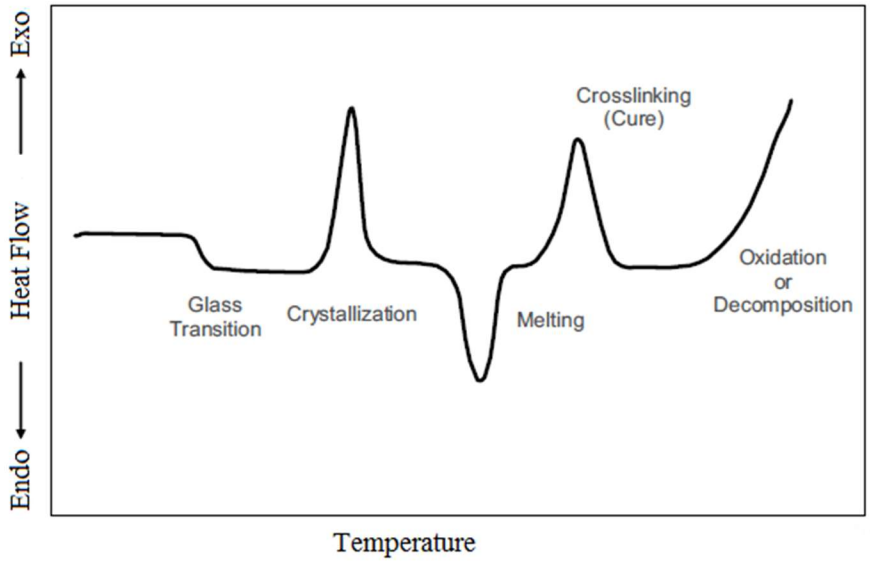

Figure 71: Schematic of typical transitions in DSC curve [275, 319].

DSC method is also widely used to determine the specific heat or heat capacity (C_p) of materials. The specific heat is the total heat required to raise the temperature of a unit of mass of a material by 1 K. It is a property of the material that indicates its ability to store heat at constant pressure. Specific heat can be derived from the heat flow and heating rate [320]:

$$\text{Heat flow} = \frac{\text{heat}}{\text{time}} = \frac{q}{t} \qquad \textbf{Equation 106}$$

and:

$$\text{Heating rate} = \frac{\Delta T}{t} \qquad \textbf{Equation 107}$$

where ΔT is the change in temperature. The specific heat can be obtained as:

$$C_p = (q/t)/(\Delta T/t) = \frac{q}{\Delta T} \qquad \textbf{Equation 108}$$

At constant C_p for a material, over a range of temperature, the plot of heat flow versus temperature will be a straight line with a slope of zero, as shown in Figure 72. While, at a constant heating rate, the distance between the line and the x-axis would be proportional to the heat capacity. If the heat is plotted against temperature, then the heat capacity is obtained from the slope [320]. The specific heat measurement is usually conducted at adiabatic conditions [291].

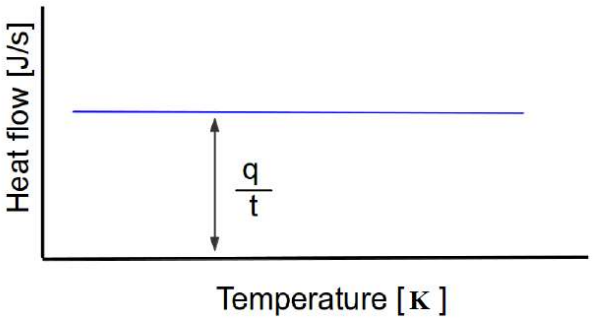

Figure 72: Plot of heat flow against the temperature for a system with no change [322].

As the sample properties, the temperature, heating rate, sample holder and pans are critical parameters for reliable DSC measurements, and it is essential to calibrate the instrument at conditions identical to those for actual measurement [318, 319, 321].

3.8.2 Thermogravimetric analysis

TGA is one of the most common tools for thermal analysis. It is applied to measure the amount and rate of change in mass of a sample as a function of temperature or time, under a regulated temperature programme, in a controlled environment (e.g. air, nitrogen, or argon). TGA is used to evaluate and characterise the materials that reveal mass loss or gain as a result of their decomposition, oxidation or impurity content [275, 291, 323]. Mass losses can be classified as volatile components that typically evaporate at a temperature range of 298-573 K, such as absorbed moisture, remaining solvents, low-molecular-weight additives or oligomers, residual reactants, reaction intermediates and by-products; for example, phenolic resins have been characterised by mass loss and volume change during thermal decomposition; the small mass loss (1-2%) at 573 K, which has been ascribed to the release of water and unreacted compounds (phenols and formaldehyde) trapped within the material structure. Mass losses also involve the generation of volatile degradation products resulting from the chain scission that generally require temperatures between 473 K and 1073 K.

Typical applications of this method involve analysis of thermal stability, oxidative stability, extent cure, moisture and volatile content of materials such as polymers [275, 316, 324]. The combination of the TGA and DSC allows acquiring the simultaneous TGA-DSC measurements for the sample. In the TGA-DSC, the heat changes can be correlated with the mass variations [317].

4 Methodology

This chapter describes the various experimental techniques and methods used to manufacture RF impregnated blankets. Beginning with the preparation of an RF sol, on through the subsequent procedure to create an RF xerogel or RF blanket products. Furthermore, the different characterisation and measurement techniques required to study the core material properties are also detailed.

4.1 Sol-gel synthesis of RF xerogel

Altering the critical processing parameters has significant effects on the final textural characteristics of the RF xerogels, so it was essential to making various samples (specimens) at different compositions. These formulations can be categorised by the type of an individual variable to construct several comparison criteria. All synthesis processes used in this study were based on the same basic sol-gel route with slight variations, as required, allowing investigation of the effects of changing specific parameters.

4.1.1 RF hydrogel formation

Standard RF hydrogels were synthesised via polycondensation of resorcinol (R) with formaldehyde (F) according to the method proposed by Pekala (Chapter 1). A series of samples were prepared with slight modifications as adopted in previously established works [112, 325]. It is essential to verify consistency between the samples made during this study, to allow a proper comparison with those prepared by other gel makers either working within the broad research group or the published works in the open literature.

4.1.1.1 Nomenclature for hydrogel samples

Preparation of several gel formulations requires the standardisation of a sample identification (sample ID) system. The sample ID could potentially contribute to the reliability and uncertainties of the obtained results by reducing the errors associated with sample measurements. Thus, before performing these experiments, a defined naming practice was implemented; which took the form of X_R/C_R/F_Y_Z, where X is the metal carbonate species used as catalyst, R/C is the resorcinol to catalyst ratio, R/F is the resorcinol to formaldehyde ratio, Y is the solids content percentage (weight/volume %) of reagents (R+F+C), and Z is the date of preparation of the RF

hydrogel. For example, Na_2CO_3_300_0.5_20%_14/10/16 would indicate an RF hydrogel produced on 14th October 2016 using sodium carbonate as a catalyst, at an R/C of 300, 0.5 is the molar ratio of resorcinol to formaldehyde, while the solids content is 20 w/v %.

4.1.1.2 Parameters and composition

As previously mentioned in Section 4.1, different series were allocated for processing the RF hydrogels. Each series was based on changing a critical variable, while all other parameters remained constant. For instance, to investigate the effects of catalyst concentration on the final gel properties, the R/C molar ratio was altered, while R/F molar ratio and solids content were kept constant at a chosen metal carbonate, 0.5, and 20 wt.%, respectively. When synthesising the RF xerogel, a fixed volume of 60 ml solvent per sample was used to prepare all hydrogels. This amount allows the total solids mass and individual masses of each solid required to be calculated, using the information on the molar ratios of the reactants and the solids content percentage. Table 8 depicts the method employed to estimate the composition of each formula for the hydrogel synthesis, using Na_2CO_3 at R/C of 200 as an example; (solids content of 20 wt%, and R/F of 0.5). Other series compositions used are shown in Appendix A.

Table 8: Hydrogel parameters for Na_2CO_3_200_0.5_20%.

	Equivalent Moles	Equivalent Mass (g)	Percentage solids %	Required Mass (g)
Resorcinol	1	110.11	64.5079	7.7409
Formaldehyde	2	60.0524	35.1817	4.2218
Catalyst	0.005	0.5299	0.3104	0.0373
Totals		170.6923	100.0000	12.0000

According to the previous works [112, 325-327], in this table, the actual mass of resorcinol (R) is used as a basis from which to calculate the exact masses of formaldehyde (F) and the selected catalyst (C) as:

$$\text{Mass of F(g)} = \frac{(\text{mass \% of F} \times \text{actula mass of R})}{\text{mass \% of R}} \qquad \text{Equation 109}$$

$$\text{Mass of C(g)} = \frac{(\text{Mass \% of C} \times \text{actual mass of R})}{\text{mass \% of R}} \qquad \text{Equation 110}$$

Formaldehyde was used as received from the supplier, as an aqueous solution (formalin) containing 37 wt% formaldehyde and 10-15 methanol as a stabiliser. As the density of formalin is 1.09 g/l, the corresponding volume of formalin was calculated using:

$$1 \text{ ml Formalin} = 1.09 \text{ g Formalin} = 37\ \% \times 1.09 = 0.4033 \text{ g Formaldehyde}$$

$$\text{Volume of Formalin required (ml)} = \text{mass of F(g)} / 0.4033$$

The density of formaldehyde is 0.815 g/ml, therefore:

$$\text{Volume of F in Formalin (ml)} = \text{mass of F} / 0.815$$

Water and methanol (H_2O/MeOH) constitute the remaining volume of formalin solution, therefore:

$$\text{Volume of } H_2O/\text{MeOH(ml)} = \text{Volume of Formalin required-Volume of F in Formalin}$$

The volume of water and methanol in the formalin contributes to the total volume of solvent required for gel preparation, so the required amount of deionised water to give the desired total volume of solution is, therefore given by:

$$\text{Volume deionised water (ml)} = \text{total volume of solvent -Volume of } H_2O/\text{MeOH}$$

Table 9 illustrates the values calculated for the reactants required to produce a Na_2CO_3_200 gel, as previously outlined in Table 8.

Table 9: Reactants and solvents quantities required for Na2CO3_200_0.5_20% hydrogel formation.

Reactants and solvents	**Volume* (ml)**
Formalin	10.47
Due to Formaldehyde	5.18
Due to water/methanol	5.29
Additional deionised water	4.71

*Calculations are based on Table 8 (Formaldehyde quantity)

These calculations were repeated for all hydrogels prepared in this study, with details presented in Appendix B.

4.1.1.3 Hydrogel preparation

Based on the selected parameters for the specific gel to be synthesised, the appropriate mass of resorcinol [white chips] was first added to 50ml of deionised water into a clean 500ml sealed-glass jar. A magnetic stirrer bar was placed into each jar, and by using a magnetic stirrer plate, the solution was stirred to dissolve the resorcinol. The required mass of a catalyst was accurately weighed into an antistatic weighing boat. After the resorcinol was dissolved, the catalyst then added to the mixture in the jar with continued stirring. Once the complete dissolution of the solids was achieved, the additional deionised water and the required volume of formalin were added to the jar, which was firmly sealed and the reaction mixture allowed to stir for 30 min to ensure proper mixing. All reagents are outlined in Table 10 and were used as received.

Table 10: Reactants **and** metal carbonates (catalysts) used for hydrogel preparation in this study

Catalyst	Formula	Description
Resorcinol	$C_6H_6O_2$	Merck, ReagentPlus 99 %
Formaldehyde	CH_2O	Merck, Formaldehyde solution 37% (stabilized with about 10% methanol)
Sodium carbonate	Na_2CO_3	Merck, ACS anhydrous, 99.5 %
Potassium carbonate	K_2CO_3	Merck, ACS anhydrous granular, 99.99 %
Sodium hydrogen carbonate	$NaHCO_3$	VWR, granular
Potassium hydrogen carbonate	$KHCO_3$	Merck, ACS reagent granular, 99.7 %

During this period (30 min), a Hanna Instruments pH20 benchtop pH meter equipped with a HI 1110-B pH electrode probe (Figure 73) was calibrated using buffer solutions (Fluka Analytical) of pH 4 and pH 7. After 30 min mixing, the stirrer bar was removed from each jar, and the initial sol pH was measured and recorded. The jar was resealed, and subsequently placed in an electric oven (Memmert ULE-500), preheated to 85 ± 5 °C, for three days.

Figure 73: Hanna instruments pH Benchtop Meter [328].

4.1.1.4 Gelation and curing

As the RF reaction solution was heated up to 85 ± 5 °C, it could potentially lose its fluidity during the reaction phase. In this stage, the gelation point was determined for the sol-gel based on its composition. Gelation time for each sample was determined visually by tiling the jars to a 45° angle at preselected time intervals with continued heating in the oven [38, 92, 113]. This tilting was conducted at first intervals dependent on the solids content and R/C. For example, low R/C ratios require shorter gelation times, hence, shorter intervals. However, as the sample approached the gelation point, and its viscosity started to increase, these time intervals were decreased to ~ 30 s for all conditions [325]. Gelation was determined to have occurred when the viscous fluid transformed into an elastic solid.

4.1.2 Solvent exchange for synthesised hydrogel

As previously described (Section 1.4.3), extraction of the water trapped within the cured gel structure, and its replacement with another solvent of lower surface tension, will reduce shrinkage and collapse during drying. The solvent used for this process in this study was acetone, because of the combination of low surface tension and relatively low cost, as well as its pervasive use within the open scientific literature. Using this solvent allowed a greater comparison to RF gels prepared in other studies.

After three days, the cured hydrogels were removed from the oven and allowed to cool. Once cooled, any extra water was drained from the bulk material, and the monolithic hydrogel was cut into several chunks. A100ml of acetone (VWR Chemicals, ACS Reagent, ≥ 99.8 %) was discharged into the jar to initiate the exchange process. The

gel was shaken briskly for a few minutes. Subsequently, the waste acetone was drained off and replaced by a further 120ml of fresh acetone and the jar resealed. The solvent exchange process was performed via daily replacement of any extracted water with pure acetone for at least three days. The contaminated acetone was managed as a waste material according to local safety regulations.

4.1.3 Drying of wet RF gel (RF xerogel synthesis)

Subcritical drying was implemented to produce RF xerogels, due to the simplicity, cheapness, and reduce time requirements of this process.

Once the solvent exchange process was complete, the gel system was removed from the shaker, the jar was unsealed, and the acetone drained off. A piece of aluminium foil was to cover the open jar, and several holes pierced in the foil. The jar was then placed in the chamber of a vacuum oven (Towson and Mercer Vacuum Oven 1425-2), with connected Vacuubrand MZ 2C NT vacuum pump. The samples were heated under vacuum to 85 °C, while two solvent traps containing ice-water were used to condense the acetone vapour released from the chamber. The solvent traps were checked at regular intervals and emptied as required. For safety purposes, the oven was cooled down and held at full vacuum overnight, whereafter the gels were heated to 130 °C for the second day to ensure more significant removal of acetone from the porous network.

Once the drying cycle was complete, the samples were taken out from the vacuum oven and transferred to labelled vials for further analysis and characterisation. To donate that the sample had been dried, _D was added to the sample ID.

4.2 Fabrication of RF xerogel blanket

In thermal insulating applications where excellent mechanical properties are required alongside the intrinsic properties of the material, RF xerogels can be combined with reinforcements to enhance these features. Processing of RF xerogel blankets is analogous to the concept of fibre-reinforced polymer (FRP) composites, which are composed of fibres (e.g., glass fibre, wool, polyester) embedded in matrix materials (e.g., silica aerogel, phenolic resins, epoxy) to ensure that the composite material exhibits a consistent performance. There are several methods for manufacturing FRP

composites, including hand lay-up, filament winding, moulding, and pultrusion [316, 329, 330].

Coronado *et al*. invented a practical method to produce a flexible aerogel blanket [331]. This patented technology, as shown in Figure 74, relates to the fabrication of aerogel type insulation where the aerogel reaction solution (inorganic, organic, or hybrid) is moulded with fibres and allowed to gel. Subsequently, the wet gel-fibre structure is processed by supercritical drying or conventional air drying. Similarly, an RF xerogel blanket combines RF gel with reinforcing fibres to produce a high performance, simple to handle insulating material.

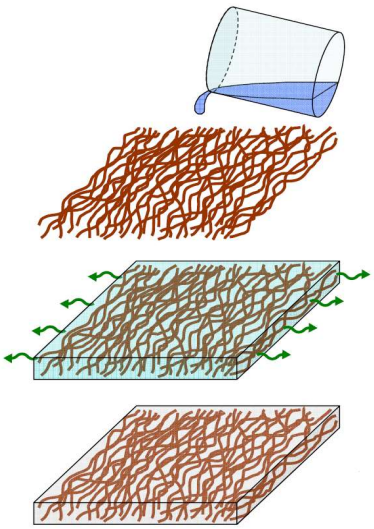

Figure 74: Fabrication steps of a flexible aerogel composite [331].

4.2.1 Reinforcements for RF-based blanket

Once a composite (RF blanket) undergoes a special force, the matrix (RF xerogel) transfers the load to the reinforcing material via the interface. The critical function of the reinforcement is to convey the load along its dimensions. The criteria applied to select the type, amount, thickness and other properties of the enforcing agent depend on the matrix characteristics, and the desired application [316].

Nonwoven fabrics are well-known as reinforcements, due to their light-weight, high porosity, low-price, chemical resistance, and mechanical properties [332]. The most commonly utilised nonwovens used as reinforcing agents include glass fibres, carbon fibres, polyethene terephthalate (PET), etc.

4.2.2 Hydrogel-fibre composite preparation

The reaction solution of resorcinol-formaldehyde was prepared as previously described in Section 4.1.1.3 (hydrogel preparation) but for a larger total reaction volume of 180 ml. A non-woven fibrous PET mat (Figure 75) received from Cytec Process Materials Keighley (Breather fabric type AB10) was used in manufacturing the blankets.

Figure 75: PET mat (AB10) from Cytec.

The desired size of the PET mat (180 mm × 180 mm × 6 mm) was prepared for RF blanket fabrication. After 30 min mixing was achieved for the RF solution (see Section 4.1.1.3), the volume of 180 ml of RF solution was made from three separate jars. The PET mat was transferred into a square silicone mould and then placed in the polypropylene (PP) container. The obtained RF mixture was poured into the mould, impregnating and covering the PET fibre, then the PP container was tightly closed and placed in the oven to gel and cure at 85 °C for three days. Figure 76 illustrates the main steps of hydrogel-fibre composite preparation.

Figure 76: Hydrogel-fibre composite preparation steps.

4.2.3 Hydrogel blanket nomenclature

According to the composition of the RF sol, the resulting hydrogel blankets were categorised into different series. The first group was based on an altered R/C ratio with constant solids content and the R/F ratio of the RF gel. The second set correlates the RF sol prepared at different solids content at constant R/C and R/F ratios, while the third series involved RFgels synthesised at different R/F ratios with constant solids content and R/C ratio. The nomenclature of hydrogel blankets is similar to that established for the RF hydrogels, but the abbreviation of the fibre (i.e. PET) was added to the label.

4.2.4 Solvent exchange for hydrogel-fibre blanket

After the three-day incubation (gelation and curing) period, the samples were removed from the oven and allowed to cool to ambient temperature. Then, the obtained hydrogel blanket was transferred from the mould to a second PP container. The workpiece was soaked in 4 times the gel volume of acetone (Figure 77), after which, the container was sealed completely. The indicated volume of acetone was replaced every day with a fresh solvent for three days. It is essential to remove the lower surface of the workpiece during the solvent exchange process to attain a smooth surface of the final product.

Figure 77: Photograph of an RF hydrogel blanket undergoing solvent exchange.

4.2.5 Subcritical drying for the wet blanket

Following the solvent replacement step, the wet workpiece was placed on the stainless steel plate to avoid the adherence of the gel material to the plate material and maintaining regularities on the surfaces. After that, it covered by punched aluminium foil to reduce the rapid removal of solvent from the hydrogel blanket. Subcritical drying was carried out in an oven chamber under vacuum at 85 °C for the first day. The process was paused overnight, as mentioned above. In the second day, the temperature was increased to 130 °C, again under vacuum. Finally, the dried RF blanket was removed from the oven chamber, and packaged in a labelled plastic bag and D added to the naming code.

4.3 Structural properties analysis

Structural analysis of solid materials is commonly performed using a variety of gas adsorption, spectroscopic and microscopic techniques [275], as outlined below.

4.3.1 Surface area and porosity measurements

Textural properties of the synthesised materials (RF gel and blanket) were determined by the analysis of nitrogen adsorption/desorption isotherms. In this study, nitrogen sorption isotherms were measured at – 196 °C (77 K) using a Micromeritics ASAP 2420 Surface Area and Porosity Analyser (Figure 78). The analysis theories described previously (Sections 3.3.2 and 3.4.1) were applied to characterise these materials.

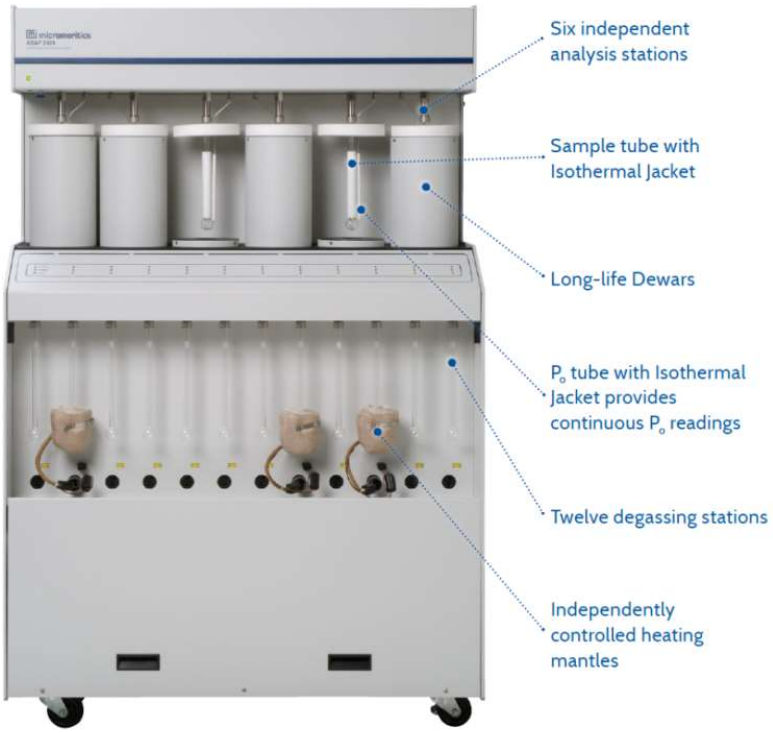

Figure 78: Micromeritics ASAP 2420 surface area and porosity analyser [333].

BET specific surface area was estimated from nitrogen-adsorption isotherms. The total pore volume was determined from the volume of N_2 adsorbed at the highest relative pressure (~ 1.0). In contrast, the pore size distribution was obtained by applying the BJH model to the desorption branch of the isotherm. The t-plot method and the Harkins-Jura model were used to analyse the microporosity of each sample.

Prior to analysis, all samples were pre-treated to remove any adsorbed impurities, which would affect the accuracy of measurements.

4.3.1.1 Samples degassing process

As the surface of the analysed material could be contaminated with residual acetone or moisture, it was essential to subject the samples to additional heating under vacuum.

Approximately 0.5 g of the gel sample was accurately weighed into a sample tube. The tube was then fitted and secured to a degassing port on the ASAP analyser. A heating mantle was wrapped around the bulb of the sample tube, ensuring that the internal thermocouple was in contact with the glass tube. Moreover, to prevent the heating mantle from moving during this process, it was held in place with a clip. The degassing

process involved initial heating of the samples to 50 °C while reducing the pressure first from atmospheric to 5 mmHg, followed by a further decrease to 10 µmHg. Once this pressure was achieved and maintained, the samples were held at 50 °C for 30 min before heating to 110 ºC and holding for 120 min.

Upon completion of the degassing cycle, the treated samples were cooled to ambient temperature and backfilled with the analysis gas (N_2). However, inadequate degassing could lead to insufficient removal of impurities from the surface of the material, resulting in an apparent reduction in the surface area, and potential filling or blocking of pores within the gel structure.

4.3.1.2 Nitrogen physisorption analysis

Upon termination of the backfilling, the sample tube was removed from the de-gas port and reweighed, with the value recorded. The liquid nitrogen level in the cooling dewar was checked to ensure that it met the required criteria for analysis. A volume displacement glass rod was inserted into the analysis tube (see Figure 79), and an isothermal jacket was attached over the sample tube neck before the whole assembly was and secured on an analyser port.

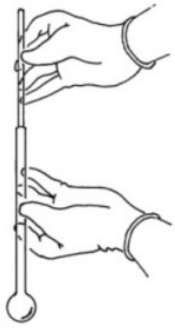

Figure 79: Glass sampling tube with a volume displacement glass rod [334].

The analysis was conducted at -196 ºC (77 K), using a dewar filled with liquid N_2 to surround the sample tube and maintain the analysis temperature. Adsorption of nitrogen gas from the mixture of He/N_2 was considered for 40 steps between the relative pressures of 0.01 – 1.0, followed by 30 steps of desorption, performed in the relative pressure range of 1.0 – 0.1. The measurements were repeated three times for each sample with the disposal of a tested material after each analysis trial.

4.3.2 ATR-FTIR analysis

As seen in the theory section (Section 3.5), the infrared (IR) spectroscopy is a dominant tool to characterise the surface of the materials (functional group identifying). The challenge with this technique is the spectral interpretation, although, is that with various of known functional groups that absorb IR radiations at the mid-infrared region and the resultant broad ranges of peaks, it becomes difficult to understand what peaks correspond to what functional groups. Subsequently, the right process is followed; the IR spectra can be interpreted successfully.

The spectral interpretation depends on the quality of the spectrum obtained during the experimental work. There are some features of a remarkable IR spectrum (Figure 80) involving low noise, inconsequential or no baseline offset, a plane baseline, lack of spectral artefacts, and peaks on the scale [335].

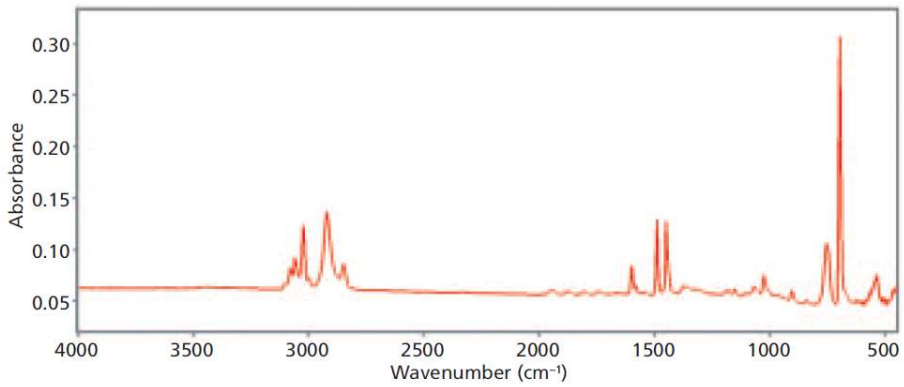

Figure 80: An example of good IR spectrum [335].

The too-large noise level in the spectra reveals that more scans need to be carried out or repeating the sample preparation process. The distance from the spectral baseline to the zero of the intensity scale is referred to as baseline offset. The spectrum baseline should be as near to zero as possible; however, running a plain background spectrum could overcome this issue. The IR spectrum peaks should be in a range of 0 to 2 absorbance unit or, 10% to 90% transmittance. Off the scale, peaks require a reduction in the depth of penetration (a high-refractive-index material for the ATR crystal and a high incident beam angle are used) or sample concentration. The spectral artefacts are peaks not originated by the sample. Water vapour and CO_2 peaks are the most common types of artefacts prevailing in the IR spectra. These peaks can also be minimised by running plain background scan (no sample in the path). The system memory then stores

the background spectrum. After that, the system subtracts the background spectrum from the sample determined spectra, to remove these artefacts peaks. Cleaning the surface of the ATR element and purging by nitrogen can also be used to reduce the effects of artefacts [271, 272, 285, 287, 335].

ATR-FTIR measurement can be conducted under severe conditions (high pressure, temperature, or corrosive environment). Most of the internal reflection elements (ATR crystals) cannot tolerate these conditions, for example, the zinc selenide (ZnSe) crystals exhibit a low absorbance at wavenumber less than 1000 cm^{-1} (wavelengths >10 μm), but they are not resistant to scratches. Therefore, the design of the ART crystals has been modified to overcome these disadvantages (e.g. coating the ZnSe with a thin film of a diamond)[284, 288].

4.3.2.1 IR Sample preparation

Dried xerogels and unreacted solid samples were ground into fine powders before performing the FTIR measurement. The solid sample was placed into a mortar which was carefully ground by a pestle (Figure 81), to uniform particles approximately. While the liquid sample was transferred directly into the measurement cell.

Figure 81: Agate mortar and pestle used in solid samples preparation [336].

4.3.2.2 Methodology

Prior to commencing measuring IR spectra of the samples, it was essential to collect the background spectrum with no sample (clean ART crystal, sample holder, cell etc.) in the beam path. This background spectrum could be a convenient indication of the cleanliness of the ATR crystal; absorbance line close to zero (transmittance line of 100%) should be acquired with no spectral attributes.

Determination the nature of the functional groups (chemical bonds) present on the surface of the analysed materials, the IR spectra were recorded over the range 4000 – 600 cm^{-1}, using FTIR ABB MB3000 spectrometer (see Figure 82). A small spatula was utilised to transfer the powder onto a single reflection diamond crystal on the spectrometer, in which the IR spectra were collected. It was crucial to maintain good contact between the sample and the crystal surface in order to ensure the occurrence of total internal reflectance. For the practical purpose, the ATR accessories include a clamp to apply pressure on the sample. The IR analysis was performed on a small amount of each selected dried gel.

Figure 82: FTIR ABB MB3000 Lab spectrometer (used in the study)

The sample was scanned 32 times with a detector resolution of 4 cm^{-1}. The signal strength value should be set to below 85%, which can be optimised by adjusting the detector gain value. For solid samples, the air set as background, while de-ionised water used for liquids. All measurements were performed at room temperature. The sample was irradiated, and the reflected beam was then transformed into an absorbance or transmittance, which was presented as a function of the wavenumber. The data collected and processed using the Horizon MB FTIR software, in which the baseline correction can be applied for multiple points.

Baseline correction is mainly used to encounter the baseline problems such as offset from zero, sloped spectrum, and curvature [272].

4.3.3 SEM imaging

Selected RF gel and RF blanket samples were examined via SEM to investigate the surface morphology, structural properties, and the interaction between the RF gel and the fibre (PET). A Keysight 8500B Field-Emission Scanning Electron Microspore was utilised (Figure 83), run at 1000 V at different magnifications of 450, 900 and 1300.

Figure 83: Keysight 8500B field-emission scanning electron microscope.

The cross-section of the sample was attached to the aluminium stubs with carbon tape and coated with 20 nm gold layer using a Leica EM ACE200 sputter coater (Figure 84) before analysis. Such a coating can enhance the conductivity of the sample because imaging can be affected by surface charge.

Figure 84: Leica EM ACE200 sputter coater.

Upon the completion of the coating, the vacuum was switched on, and an incident electron beam hit the sample allowing surface morphology to be investigated. SEM images were recorded in secondary mode.

4.4 Thermal conductivity measurements

There is no particular measurement method to determine all thermal conductivity (TC) of porous materials. The physical properties, and other factors, mainly restrict the accuracy of any method used. The selected TC measurement technique has to be chosen based on sample sizing and shaping, applicable temperature range, and appropriate TC range as shown above (Section 3.4.6), because a material with low thermal conductivity such as silica aerogel or RF gel requires different techniques than for the high conductivity materials. The methods must be approved and defined in order to analyse the thermal behaviour of the materials. During this study, different techniques were used to determine the thermal conductivity of both RF gels and RF blankets, which are based on the criteria mentioned above.

The crucial factors in selecting the appropriate TC measurement method were the sampling requirement and the minimum TC value that could be measured.

4.4.1 Determination of RF xerogel thermal conductivity

For TC measurements, it is difficult to obtain RF xerogels of sizes compatible with specific measurement techniques, due to the brittleness, cracks, and shrinkage of these materials. Therefore, steady-state methods would not be applied in this case. Thus, the thermal conductivity, k, for the RF gel was calculated using the thermophysical properties, thermal diffusivity (α), specific heat capacity (C_p), and bulk density via Equation 102:

$$k = \alpha C_p \rho$$

Thermal diffusivities were derived using laser flash analysis (LFA) under argon, using a Netzsch LFA 427 (Figure 86). According to ASTM 1461 [337], the required sample is a thin circular disc with a front faced area less than that of the laser beam. Typical sampling sizes are of 10 to 13 mm in diameter, and the thickness can range are between 1-6 mm (as an opacified material, a thickness of less than 2 mm was used during this study).

As previously described (Section 4.1.1.3) after mixing all raw materials on the magnetic stirrer plate for 30 min, RF sol samples were transferred into different size glass culture tubes and placed in the oven to gel and cure at 85 ± 5 °C for 72 h. The

moulded hydrogel was cut manually by scalpel into discs, with a thickness between 3-8 mm, and then immersed in fresh acetone for three days, changing the spent acetone with fresh solvent daily. The gel discs were placed in the vacuum oven and dried using the same procedure illustrated above (Section 4.1.3). Figure 85 shows the preparation steps of disc-shaped RF gel samples.

Figure 85: Preparation of disc-shaped RF gel samples for LFA.

With relatively low R/C ratios of 400, the dry disc-shaped RF xerogels with 12.7-13 mm diameter were carefully polished into smooth surface discs with thickness 1.5-2 mm; the sample was then sandwiched between two aluminium square plates and coated with a thin layer of POCO Graphite spray on both sides. A thin coat of graphite is applied on the sample surface, in order to enhance the absorbance of the flash energy used in this technique [338].

At the high R/C ratios, samples were ground into powders, because of that, the gel structure is weak, so it is difficult to form into a disc-shaped sample. The gels at high R/C ratios could absorb the glue material used for attaching the sample to the aluminium plate. Before commencing the analysis of any material, it is crucial to calibrate the device by testing one or more materials of known thermal diffusivity. The importance of this calibration is to verify the performance of this apparatus. However, calibration is affected by issues such as non-uniformity of the sample thickness during surface polishing, which disturbs the heating process through the tested material. Also, the presence of trace solvent within the gel structure contributes to uncertainties in the obtained diffusivity of the RF gel; hence, the final thermal conductivity.

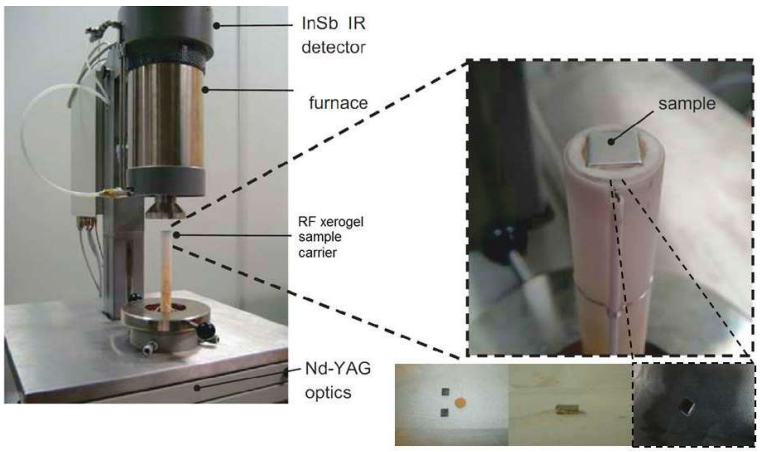

Figure 86: Schematic of RF gel sample loading to Netzsch LFA 427

Heat capacities were measured using Differential Scanning Calorimetry (DSC) under nitrogen using a Netzsch STA 449F3 thermal analyser (Figure 87). As the specific heat capacity is a quantitive measurement of energy as a function of temperature, it was essential to perform a calibration of the device before sampling. The most common methodology applied for acquiring the specific heat capacity by DSC measurement is a *continuous heat flow method* [318, 339]. It is essential to ensure that the weight, temperature and enthalpy have been calibrated before commencing the DSC measurements.

The heat flow rate of the zero baselines (Φ_0) was firstly determined by conducting measurement, using two empty and pre-weighed alumina (Al_2O_3) crucibles in the sample (front) and reference sides, as shown in Figure 87. These crucibles should be equal in weight and covered with lids, and the chamber was then closed to begin the measurement. As the isothermal heat flow at the initial temperature (T_{int}) had been constant for at least one minute, the temperature programme could be performed from 25 to 200 °C (289 to 573 K) at the heating rate (β) of 10 °C min-1 under a dry nitrogen gas flow (10 to 50 ± 5 mL per min). The scanning was carried out from the initial temperature to the final temperature (T_{final}). The T_{final} was also subjected to isothermal heat flow rate before ending the temperature programme. The zero baseline reveals the probable irregularity in the DSC. Calibration of a reference substance (Cal) of known specific heat capacity (C_{cal}) was placed into the sample crucible. In contrast, the crucible in reference side remained empty as in the zero baselines. The Heat flow calibration (Φ_{cal}) was performed using synthetic sapphire (α-aluminium oxide;

alumina) with a mass of m_{cal} as a standard material. The probes were heated the same as in the experimental procedure for the zero baselines; the following equation can be used to describe the process [340]:

$$C_{cal}\, m_{cal}\, \beta = K_{\Phi}(T)\, (\Phi_{cal} - \Phi_0) \qquad \text{Equation 111}$$

where $K_{\Phi}(T)$ is a temperature-dependent calibration factor, and m_{cal} is the mass of Sapphire (mg).

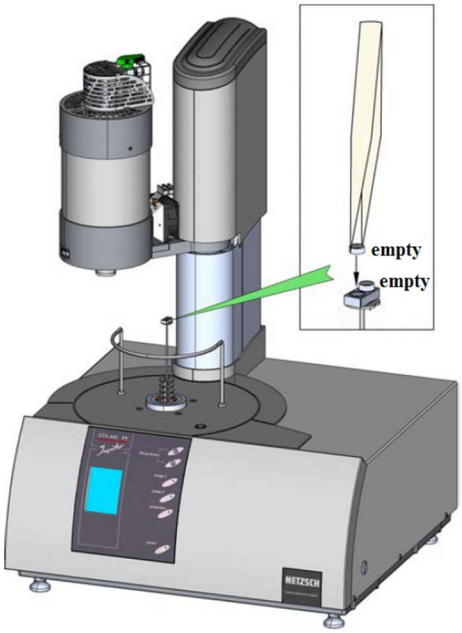

Figure 87: Schematic diagram showing sample (front) and reference sides in the STA analyser [341].

For RF gel samples, a weighed sample (m_s) was placed on the sample crucible (s), the heat flow rate can be expressed as [340],

$$C_s\, m_s\, \beta = K_{\Phi}(T)\, (\Phi_s - \Phi_0) \qquad \text{Equation 112}$$

By comparison of two identical heating rate performed for the sample and reference material (Sapphire), the specific heat capacity of the sample (C_s) is given by:

$$C_s = C_{cal}\, \frac{m_{cal}}{m_s}\, \frac{\Phi_s - \Phi_0}{\Phi_{cal} - \Phi_0} \qquad \text{Equation 113}$$

All three measurements were carried out under identical conditions, and masses of approximately to 10 ± 0.5 mg were used. For optimum results, it is necessary to ensure good thermal contact between the sample crucible and heat-flux sensor. Issues such as

sensor contamination, uncleaned pans, and improper position of the sample in the crucible have a significant impact on the accuracy of the DSC measurements.

4.4.2 TC measurements for RF xerogel blanket

For RF blankets, the thermal conductivity measurements were directly performed in air at atmospheric pressure using an HFM 436 Lambda heat flow meter (Figure 87) from Netzesch, housed within the Advanced Materials Research Laboratory (AMRL) at the University of Strathclyde. The validity and performance of this apparatus had been confirmed by testing reference materials of well-known thermal conductivities using the same conditions applied to the RF blankets. The accuracy of this apparatus is in the range of 1 – 3%.

The tested blanket (180 × 180 × 6 mm) was inserted between the two plates of the apparatus, the temperatures of the upper and the lower plate were held at 30 °C and 10 °C, respectively. The heat flux transducer measured the heat flow created by this temperature difference. Prior to the measurement, the pre-defined parameters such as applied compression and heat flux sensor calibrating conditions were imported into the system. The TC measurement was repeated until the status result of the HFM displayed Fine. At this point, the measurement was terminated, and the thermal conductivity was recorded.

Figure 88: Heat flow meter HFM 436 Lambda AMRL at the University of Strathclyde

It is essential to test the RF blanket under the same conditions applied to those of super-insulating materials to attain a proper comparison.

4.5 Density measurements

For the RF gels, gas displacement pycnometry was used to determine the skeleton density as described above (Section 3.4.3). Densities of selected samples were measured using a Quantachrome MicroUltrapyc1200e pycnometer (Figure 86). The RF gel was subjected to a degassing process before performing the density measurements in order to remove any residual moisture from the gel structure. The empty sample cell (1.8 cm^3) was weighed, filled with small sample pieces (ideally at least ¾ of the cell volume), and re-weighed to calculate the actual sample weight. The sample cell was then placed in the sample chamber and sealed with a cover. The calibrated amount of helium was inserted, and the resulting pressure was recorded. The pressure difference between the reference chamber (tank) and the sample chamber was equivalently related to the volume occupied by the solid backbone of the sample present as of the gas will diffuse into the open pores. The solid backbone volume was calculated from Equation 65, as illustrated in Section 3.4.3.

Figure 89: Quantachrome MicroUltrapyc1200e pycnometer used in this study

4.6 Thermal analysis (TGA/DSC)

Thermal behaviour and decomposition (degradation) profiles of selected samples of both RF gels and blankets were acquired using TGA/DSC analysis, as described previously (Section 3.7). TGA/DSC measurements were conducted using a simultaneous thermal analyser NETZSCH STA 449 F3 Jupiter (Figure 87) to characterise these materials.

The validity of achieved measurement is the most significant aspect of the TGA/DSC operation. Regular calibrations for both mass and temperature scales are prerequisite for the confidence data collected via this analysis technique. These calibrations must be conducted according to the standard test methods of the ASTM. However, there are some crucial experimental factors can influence the TGA results. Interferences in the measurement of mass arise from three main sources: atmosphere effects, secondary reactions, and electrical issues [323, 324, 342, 343]. TGA experimental conditions such as temperature variations, flowing gases, and evolving gases can also affect the accuracy of the sample mass through the bouncy effects. In the TGA, the bouncy is an upward force on the sample caused by different factors (surrounding atmosphere conditions) [324, 344]. Bouncy correction can be performed by running the TGA test with empty crucibles in both sides (sample and reference) under the same experimental conditions. Furthermore, bouncy effects can be compensated by adjusting the inert gas flow rate on both sides identically [317, 324]. Major sources of error in The TGA are summarised in Table 11.

Table 11: Potential artefacts affecting TGA results [324, 344].

Mass	Temperature
Bouncy effects and thermal expansion (in balance)	Heating rate
Condensation and secondary reactions	Thermal conductivities of purge gases
Atmosphere changes	Enthalpy changes
Effects of electrostatic and magnetic fields	Chamber components configuration
Sudden loss of sample mass	Electronic implication
Electronic implication	

As mentioned above, before starting the TGA measurements, it was essential to carry out TGA test on the empty alumina crucibles in both sides with the experimental condition as stated below. This step is essential to encounter bouncy and baseline issues [324].

Approximately 10 ±3 mg of sample was weighed into an 85 µL alumina crucible (pan) and placed onto a thermobalance, within the TGA. It was essential to ensure that the

sample pieces were settled at the surface of the crucible, to minimise buoyancy during the gas purge process. The measurements were performed under a nitrogen atmosphere, at a constant gas flow rate of 50 mL/min on the sample, and a flow of 20 mL/min was set to protect the balance. The purge step was included to avoid oxidative processes. The sample was heated from 25 to 600 °C (289 to 873 K) at a rate of 10 °C min^{-1}, and the mass loss behaviour was monitored at four isothermal temperatures: 100, 200, 300, and 600 °C (each temperature was held for 15 min). When the sample undergoes a thermal decomposition involving a mass alteration, that change could be observed by departure from the initially originated baseline of the mass record. The isothermal temperature steps used here follow those applied by Frollini *et al*. to study the decomposition of phenolic thermosets [316]. The authors investigated the residual curing stage between 100 and 200 °C. They indicated that the decomposition of material began from 300 °C. While, above 600 °C, a release of the remaining components and gases was observed.

Once the isothermal stage at 600 °C was complete, the gas atmosphere was switched from N_2 to air for a further isothermal step, resulting in the strongly exothermic decomposition of all sample contents.

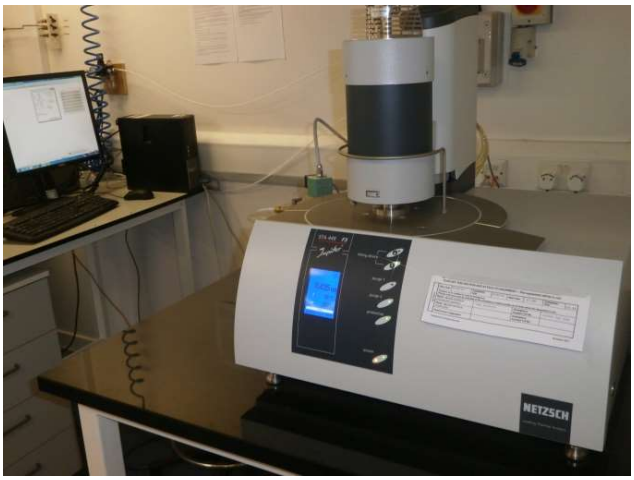

Figure 90: Netzsch STA 449 Jupiter F3 combined TGA-DSC instrument used in this study.

Once the analysis was complete, the system was allowed to cool down to the room temperature before commencing a subsequent measurement. Each sample was analysed three times, and the average values were recorded.

Most TGA curves show the mass losses, which are typically caused by the chemical reactions (e.g. curing, decomposition, combustion, pyrolysis), and physical transition (e.g. evaporation, drying, sublimation). While the mass gain can be observed as a result of the chemical reactions (e.g. reaction with purge gas components such as O_2 and CO_2 to form non-volatile compounds), and physical changes (e.g. hydration, adsorption of gaseous constituents on the surface of the sample such as active charcoal) [317]. In case of uncertain TGA effects, the DSC data can be used to gain additional information [345].

For the quantitative evaluation of TGA data (Figure 91), it is essential to divide the TGA curve into step heights, in which several changes occur one after another and sometimes partially overlap. The change in mass before and after the effect determines the step heights (Figure 91a). The total of all steps and residue (using the air to burn out the remaining content) at the end of the last step is equal to the original mass of the sample (no oxidation). The limitation of the step evaluation depends on the sample material investigated under specific conditions [345].

Mass changes produce steps in the TGA curve or peaks in the derivative of the TG (DTG) curve. The DTG curve shows the rate at which the mass changes concerning the temperature or time. It is a useful tool to differentiate overlapping mass loss steps, determine the shape and maximum of mass-loss processes, and to detect the minor loss steps. The overlapped transitions, which are observed as a tenuous slope, changes in the TGA curve, appear more obviously (Figure 91b) shown as DTG peaks. In contrast with the TGA curve, the DTG curve indicates more than one process, physical phenomenon, and chemical reaction occur as the mass changes observed. It is a sensitive measurement and provides the information on relative vaporisation rates of the volatile components and polymer decomposition. The noise produced by this curve is more than that in the DSC curve. Therefore, the DTG curve should not be used in the kinetic measurement [323, 324, 345, 346].

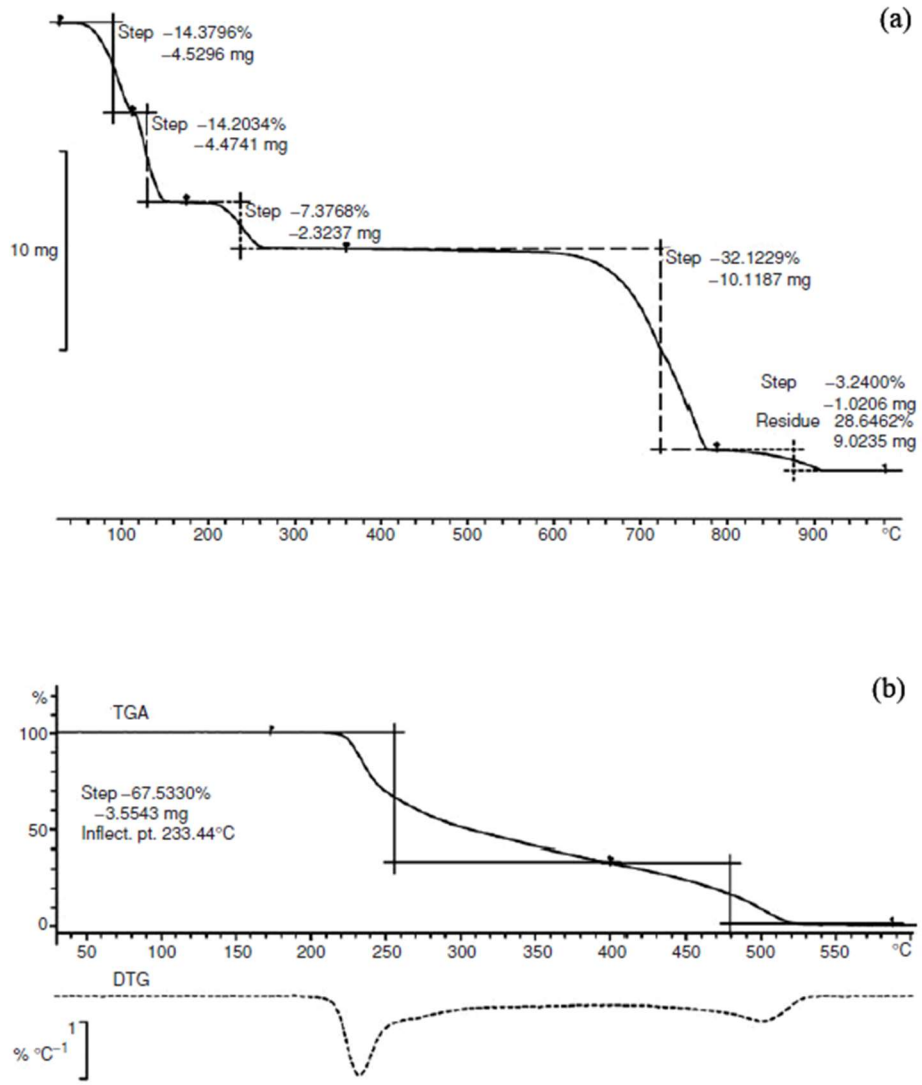

Figure 91: Quantitative evaluation of TGA data showing individual steps of TGA curve. Additional DTG curve (b) showing the temperature with maximum mass loss [345].

5 Results Part 1 – RF gel synthesised at varied parameters

Because of its foreseen contribution to various applications, it is essential to elucidate the effects of the synthesis variables on the RF xerogel properties. Several RF xerogels of varying solids contents, at different R/C molar ratios, were investigated. The gelation times of standard solutions were monitored to evaluate the influence of this parameter on the structure of the gel. The dried gels were analysed using nitrogen (N_2) sorption at – 196 °C (77 K), in order to determine the structural characteristics, including the specific surface area, average pore diameter, total pore volume, and pore size distribution. These results have been presented so that trends can be evaluated and compared to those observed in the literature. IR spectroscopic analysis was performed on the dried gel to understand the impact of synthesis conditions on the nature of the chemical bonds present in the obtained gels.

5.1 Gelation time observation

The gelation time monitoring process was conducted for gels synthesised using sodium carbonate catalyst at different concentrations. At a constant solids content of 20% and gelation temperature of 85 °C, a total of 6 samples of chosen R/C ratio (100, 200, 300, 400, 500 and 600) were visually monitored to determine their gelation times. All gelation times were measured as described in Section 4.1.1 and given in Table 12.

Table 12: Gelation times for sodium carbonate catalysed RF gels (20% solids content) with a different R/C ratio.

R/C	Gelation time (t_g) (s)
100	2280
200	2820
300	3180
400	3840
500	4740
600	7500

In general, the gelation time (t_g) determined by visual observation is based on the gelation rate. The synthesis conditions have significant impacts on the gelation rate,

hence, influencing the experimental error in the visual determination of the gelation time. For quick gelation processes (< 5000 s), the sol-gel transition is rapid and easy to detect visually. While, for the longer gelation time (> 5000 s), the transition occurs gradually and is sometimes difficult to determine accurately. On the other hand, the accuracy of the rheological measurements relates to the consistency of experiments. It has been stated that there is a logical difference in gelation time between both methods for similar RF synthesis systems. The observations indicated that the gelling times obtained via the visual method were 5-45% longer than those measured rheologically. The time intervals for the visual observation increases with increasing the gelation time, therefore, the gelation times can be determined within ± 60 s if the t_g< 5000 and ± 120 s if the t_g > 5000 [38].

Gelation time is essential to perform further investigations on the RF reaction mixture, such as the mechanisms of gelation and polymerisation [68, 325].

Table 12 shows that decreasing the R/C ratio leads to a noticeable reduction in the gelation time. These results agree with those of Job et al. [38], who also found that the effect of R/C ratio on gelation time, at a constant temperature, was an increased time for increased catalyst concentration. Moreover, the gelation time has a significant impact on the formation of a crosslinked gel network; at prolonged gelation time, the condensation reaction is dominant resulting in larger particles, while at shorter gelation times, a large number of branched clusters leads to the formation of small interconnected gel particles.

Gaca and Sefcik [92] also reported an increase in the gelation time with decreasing the concentration of sodium carbonate at constant temperature and solid contents. They have also investigated the effect of R/W molar ratio (solid contents), the observations show that the gelation time decreases as R/W increases. The dependency of the gelation time on R/C is also in agreement with an earlier study conducted by Hwang and Hyun [347].

5.2 Xerogel characterisation

One of the most crucial aspects of RF gels is the change of structural features with various synthesis conditions. In order to illustrate the effects of these parameters, a

range of xerogel structural characteristics and other experimental outputs were investigated.

5.2.1 Structural properties

N_2 adsorption-desorption analyses were performed on all the synthesised RF gels synthesised in this study to determine their textural properties. These porous structure measurements allow the evaluation of the specific surface area (S_{BET}), total pore volume ($V_{Tot.pore}$), micropore volume (V_{Mic}) and average pore diameter (d_p) from BJH analysis. Table 13 shows a summary of the structural properties obtained for different RF xerogels. These results indicate that the porous structures of the RF xerogel differ from those of the RF xerogel-based blanket. This deviation complements the technique proposed by Al-Muhtaseb and Ritter [43], in which the RF gels could be reinforced with organic fibres to reduce the shrinkage and fragility of the final product. Various formulations of RF xerogel are presented in Table 13. It can be seen that the composition of the initial sol governs the final structure of the products, hence their thermal performance as RF xerogel blankets.

N_2 sorption is not capable of detecting pore diameters larger than 200 nm, so the total pore volume appears smaller in the blanket. Observing the variation in pH of the initial RF solution, this quantity appears to be influenced by both the catalyst concentration and the total mass of solids. As mentioned above (Section 1.5.4), the pH of the initial RF solution can be adjusted by altering the R/C ratio. At the constant R/C ratio, increasing the solids content leads to a decrease in the pH value. As the percentage solids content is proportional to the quantity of formaldehyde, the pH of the initial sol would be lowered in the presence of excess formaldehyde (acidic nature) quantity [348].

Table 13: Porous characteristics of RF xerogels synthesised using various R/C ratios and percentage solids contents.

R/C	pH[1]	S_{BET}[2] (m^2g^{-1})	V_{Tot} (cm^3g^{-1})	V_{Mic} (cm^3g^{-1})	d_p (nm)
		Solids 10%			
100	7.34	494.7 ± 1.2	0.32	0.04	3
300	7.06	366.4 ± 2.3	0.85	0.02	9
400	6.84	272.6 ± 1.3	0.84	0.02	12
500	6.61	167.8 ± 2.4	0.64	0.01	16
		Solids 20%			
100	7.25	490.8 ± 3.8	0.36	0.05	3
300	6.86	477.1 ± 2.5	0.92	0.04	8
400	6.67	406.6 ± 4.9	0.98	0.04	11
500	6.56	345.3 ± 2.0	1.09	0.04	14
600	6.50	274.8 ± 2.2	1.00	0.03	18
		Solids 25%			
100	7.06	537.2 ± 4.6	0.42	0.04	3
300	6.81	404.7± 4.2	1.00	0.03	10
400	6.65	344.8 ± 2.5	1.17	0.03	15
500	6.51	264.1 ± 2.3	1.44	0.03	24
600	6.47	179.0 ± 1.1	1.07	0.02	32
700	6.38	85.8 ± 4.9	0.22	0.01	16
		Solids 30%			
100	6.95	565.8 ± 3.6	0.46	0.04	3
300	6.79	479.0 ± 2.4	1.08	0.04	9
400	6.64	395.3 ± 0.5	1.31	0.04	15
500	6.49	329.7 ± 1.2	1.54	0.04	24
600	6.41	248.4 ± 1.5	1.17	0.03	28
700	6.25	164.9 ± 1.2	0.34	0.02	14
800	6.17	100.5 ± 0.3	0.17	0.01	13
		Solids 35%			
100	6.95	557.5 ± 6.7	0.45	0.03	3
300	6.64	438.1 ± 4.5	0.98	0.03	9
400	6.44	375.0 ± 4.3	1.28	0.03	14
500	6.36	315.0 ± 2.8	1.65	0.03	23
600	6.24	247.5 ± 2.4	1.23	0.02	27
700	6.15	190.5 ± 0.3	0.47	0.02	16
800	6.01	128.6 ± 1.7	0.26	0.01	14
900	5.93	79.3 ± 0.8	0.16	0.01	15

[1] pH error is ± 0.02 from the instrument. [2] Error estimation was based on 3 repeats of measurement. Error was obtained using the standard deviations. Error bars are included in Appendix C.

For the dried RF xerogels, the results reveal that the total pore volume and average pore diameter increase with decreasing Na_2CO_3 concentration (higher R/C ratios) till near the gelation limit value. On the other hand, the decreasing in the amount of catalyst results in a decrease in the specific surface area and micropore volume. This marked tendency agrees on the gel properties reported by Pekala [35]. As the micropore volume represents a small fraction of the total pore volume, the meso-macroporosity is dominant within the gel structure. At the lowest catalyst level that near the gelation limit, a reduction in total pore volume and pore size is observed, which is due to shrinkage and collapse of the gel structure during the drying stage.

Analysis error was performed for the results of three trails of physisorption analyses. The errors associated with the BET surface area showed high figures at low R/C ratios, which could be due to the microporosity of these formulations of RF xerogels. It was observed that the time taken to analysis these compositions is much longer than at those with high R/C ratios. This could lead to an increase in the error values. The error values of RF formulated with high R/C ration are much lesser than that of the device errors. The repetition of these measurements could improve the confidence and quality of the obtained results

5.2.1.1 Effect of R/C ratio

R/C ratios between 100 and 800 were used to investigate the influence of catalyst concentration on the textural characteristics of the final gel. The adsorption-desorption isotherms obtained for all dried RF xerogel samples exhibited Type IV character. This trend is similar to the findings reported by Horikawa *et al*. [155] and Oyedoh *et al*. [208]. The Type IV isotherm is an indication of the presence of porous structures, which are mainly mesoporous, and it can be seen that the hysteresis progresses from Type H2 to Type H1 as R/C ratio increases (Figures 92a and 92b). Also, the isotherms show that, at low pressure, the adsorption capacity is low before rising with increasing relative pressure. The change in hysteresis type occurs at higher R/C ratios and leads to the improved thermal performance of the material. Therefore, the RF blanket prepared with R/C 500 provides the lowest thermal conductivity of the 25% solids content xerogel series.

From Figures 92a and 92b, it can be seen that the increase in R/C ratio corresponds with the higher N_2 uptake of the gels. It can be seen that the R/C 100 xerogel shows a significantly decreased N_2 uptake, resulting from its low pore volume, and shrinkage of the material. As a result of undesirable properties of the R/C 100 xerogel, it was excluded from the subsequent RF blanket fabrication phase. While, xerogels obtained under the synthesis condition of the R/C ratio, which could proceed to gel, the isotherm can be classified of Type I. It is different from the other ratios as the adsorption occurs at low pressure as a result of micropore filling. This threshold R/C value can be increased by increasing the total mass content of the initial RF sol (Figure 92b).

As shown in Table 14, the BET surface areas obtained from these sorption isotherms decrease as the micropore volumes decreases, which results from an increase in particle size formed during the sol-gel transition process. However, the N_2 adsorption method used in this study is not capable of detecting larger pore sizes that may be present in the more macroporous structures. Hence, it appears that the total pore volume at R/C 600 decreases as the average pore diameter increases, after which both characteristics decline with increasing the R/C ratio.

Pore size distributions (PSDs) of selected RF xerogels are depicted in Figure 93. It can be observed that the pore width (diameter) peak shifts to a larger range of sizes, and the PSD becomes broader as the R/C ratio increases. The samples with R/C of 100 have the narrowest PSDs and an approximate pore size peak of 3 nm. For samples synthesised with R/C ratios of 500, at a solids mass of 25% or 30%, the PSD curves are broader and exhibit pore size peaks that are shifted to the right (wider pores), sitting at 24 nm. This trend shows the effect of the R/C ratio on the mesoporous structure of the gel. In the RF xerogels, PSDs are narrower compared with those of the RF blankets. Also, the pore diameter peaks observed, at various R/C ratios, are smaller in the gel than in the blanket. It should be noted that the PET fibre has a considerable impact on the gelation process of the RF solution and therefore, the final texture of the RF blanket.

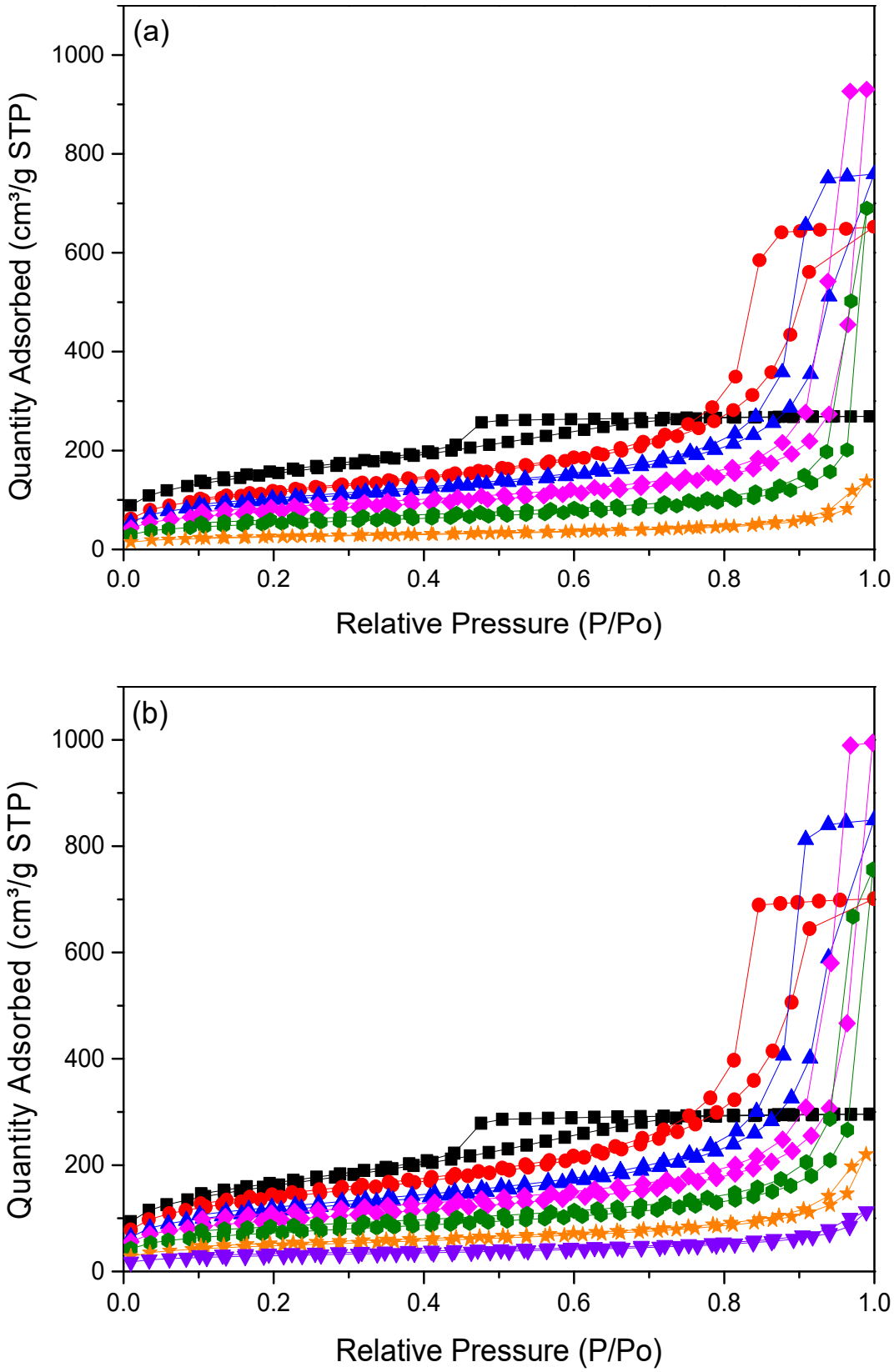

Figure 92: Nitrogen adsorption/desorption isotherms for (a) 25% and (b) 30% solids content RF xerogels, at R/C ratio of: 100 (■), 300 (●), 400 (▲), 500 (◆), 600 (⬢), 700 (★) and 800 (▼).

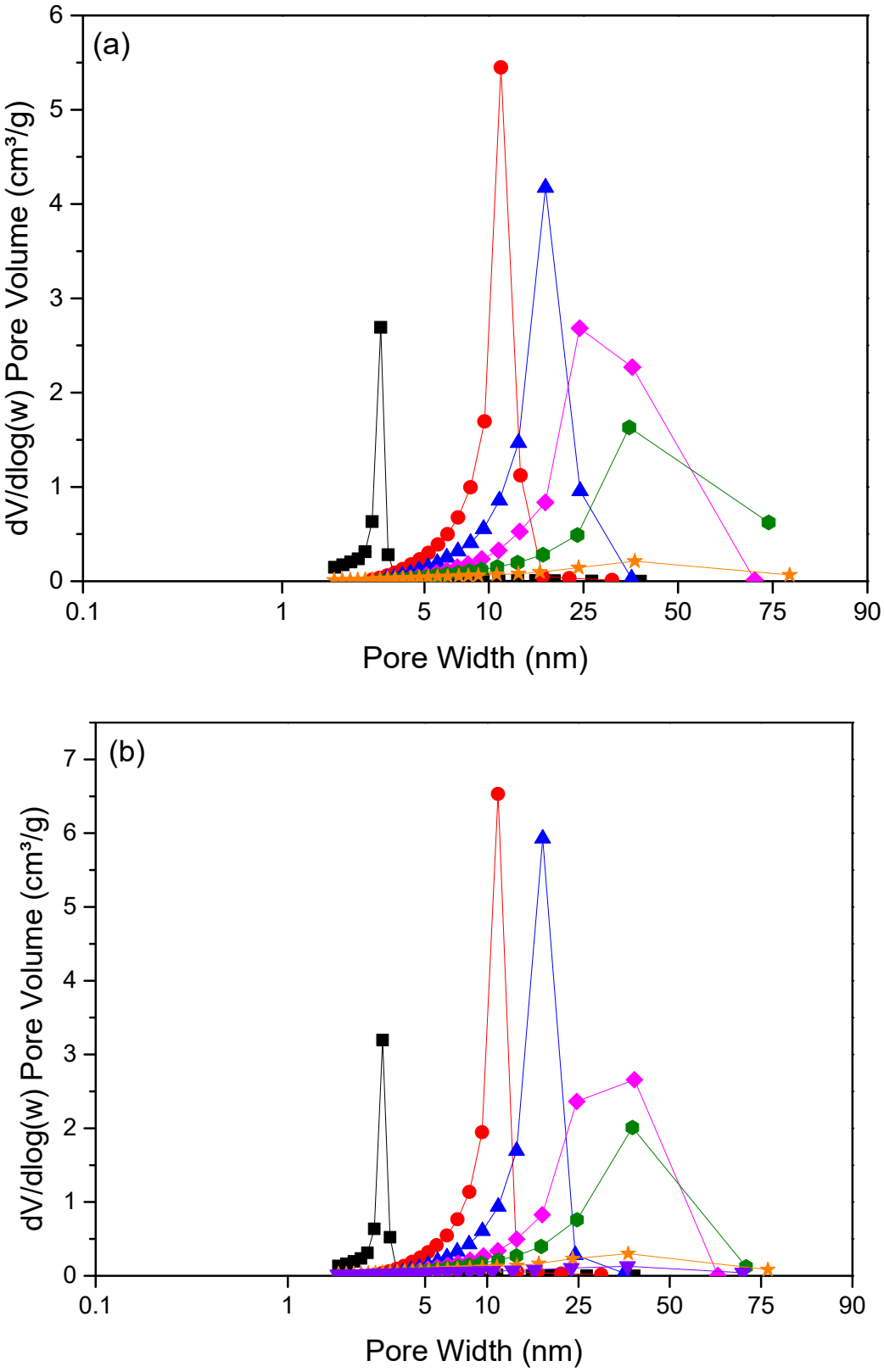

Figure 93: Pore size distributions for (a) 25 % and (b) 30% solids content RF xerogels, at R/C ratio of: 100 (■), 300 (●), 400 (▲), 500 (◆), 600 (⬢), 700 (★) and 800 (▼).

The morphological analysis of xerogel samples prepared with R/C ratios 100 and 600 are shown in Figure 94, which exhibits apparent differences in the textural structure. It can be seen that the sample synthesised with R/C ratio 100 (Figure 94a,b) shows a compact textural feature at this scanning level, which is expected according to the results obtained from nitrogen sorption measurement. The pore width for this sample is small, not observable at the given magnifications, and it was not possible to attain higher magnification without increasing the thickness of the gold coating, which would shroud any narrow textural feature. In contrast, reduction of the catalyst concentration (R/C 600) resulted in a typical porous structure, composed 3D network of the cross-linked clusters (Figure 94c and 94d). This higher R/C ratio leads to xerogels revealed some of the macropores visible. The observation is in agreement with the textural data from nitrogen sorption analysis.

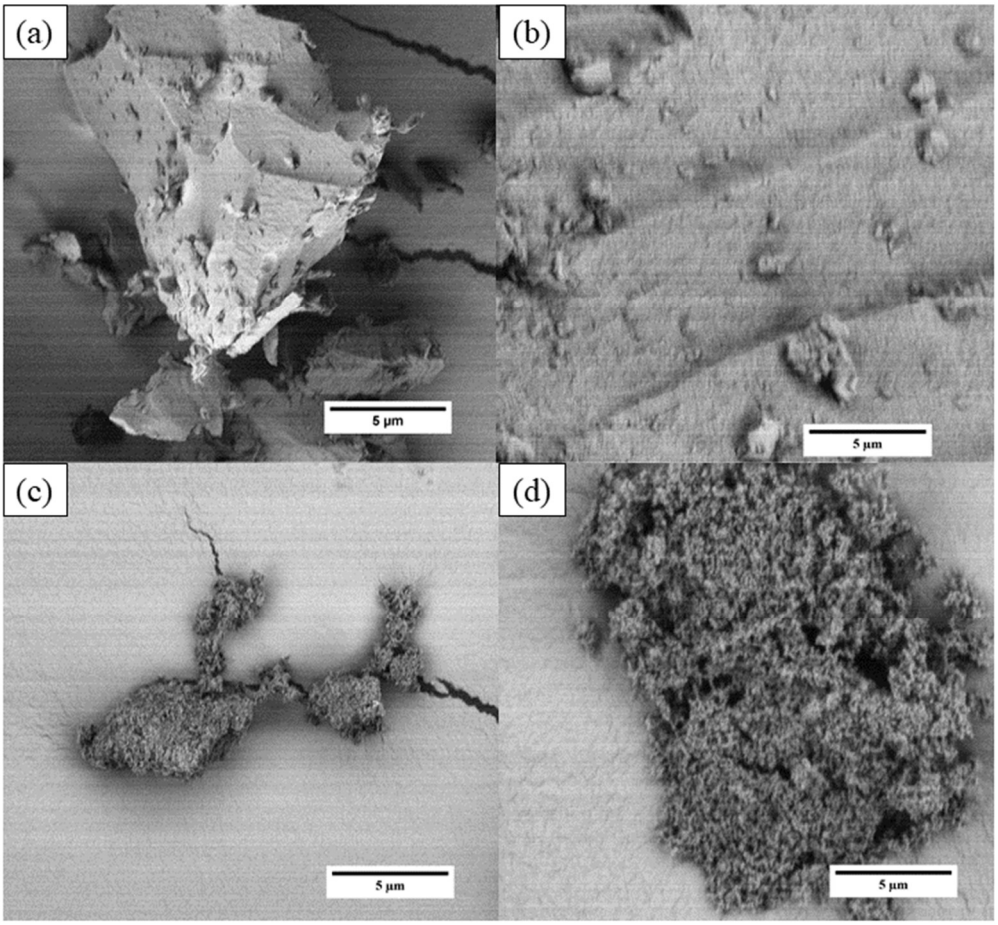

Figure 94: SEM images of RF xerogels at different R/C ratios : (a,b)100, (c,d) 600 , at 6000 and 20000 x magnifications respectively.

5.2.1.2 Effect of the solids content

N_2 adsorption-desorption isotherms and PSDs of some of the samples prepared with different solids contents at R/C ratios of 300 and 500 are shown in Figures 95 and 96.

One can see that the RF xerogels exhibit Type IV isotherms. For the same R/C (300), the amount of N_2 adsorbed is large at high relative pressure except for the 10% solids content sample (Figure 95a). While at a higher R/C of 500, the N_2 uptake is substantial at high relative pressure and increases with an increased solids content (Figure 95b). Table 14 also shows that V_{Tot} exhibits very little change with solids content at the low R/C ratio compared to the higher R/Cs. It can thus be observed that the gelation time influences the textural properties of Na_2CO_3-catalysed RF xerogels. Increasing the solids content at a high R/C ratio (long gelation time) could affect the number and size of cluster particles formed, thus the pore volume and pore size of the produced gel.

As seen in Figure 96, pore size distributions (PSDs) obtained for selected xerogels synthesised in this part of the study. The xerogels made using R/C 300, at different solids contents, have well-defined PSDs, and the diameter peak of PSD remains relatively constant (~ 4 nm) for most of the solids content series (Figure 96a). Notably, it can be observed that at R/C 300, there is no significant change in the average pore diameter as the solids content rise from 10 to 35 % (Table 14). Conversely, for xerogels prepared using R/C 500, at different solids contents (Figure 96b), the PSDs are wider and shift to larger pore diameters with increasing solids content. 10% solids content is an exception in this case, which is potentially due to the collapse of the gel structure during the drying process as a result of low reactant concentration (a small number of particles). The diameter peak values of xerogels range from 4 to 40 nm as a result of changing the solids content at the same R/C value (500).

RF xerogels exhibit different PSD trends than for the RF blankets. At low R/C (300), the xerogels exhibit sharp PSDs with constant diameter peaks. Broader PSDs and different diameter peaks are observed at an R/C of 500. In contrast, the blankets show marked changes, narrow PDSs and different diameter peak values at R/C 300.

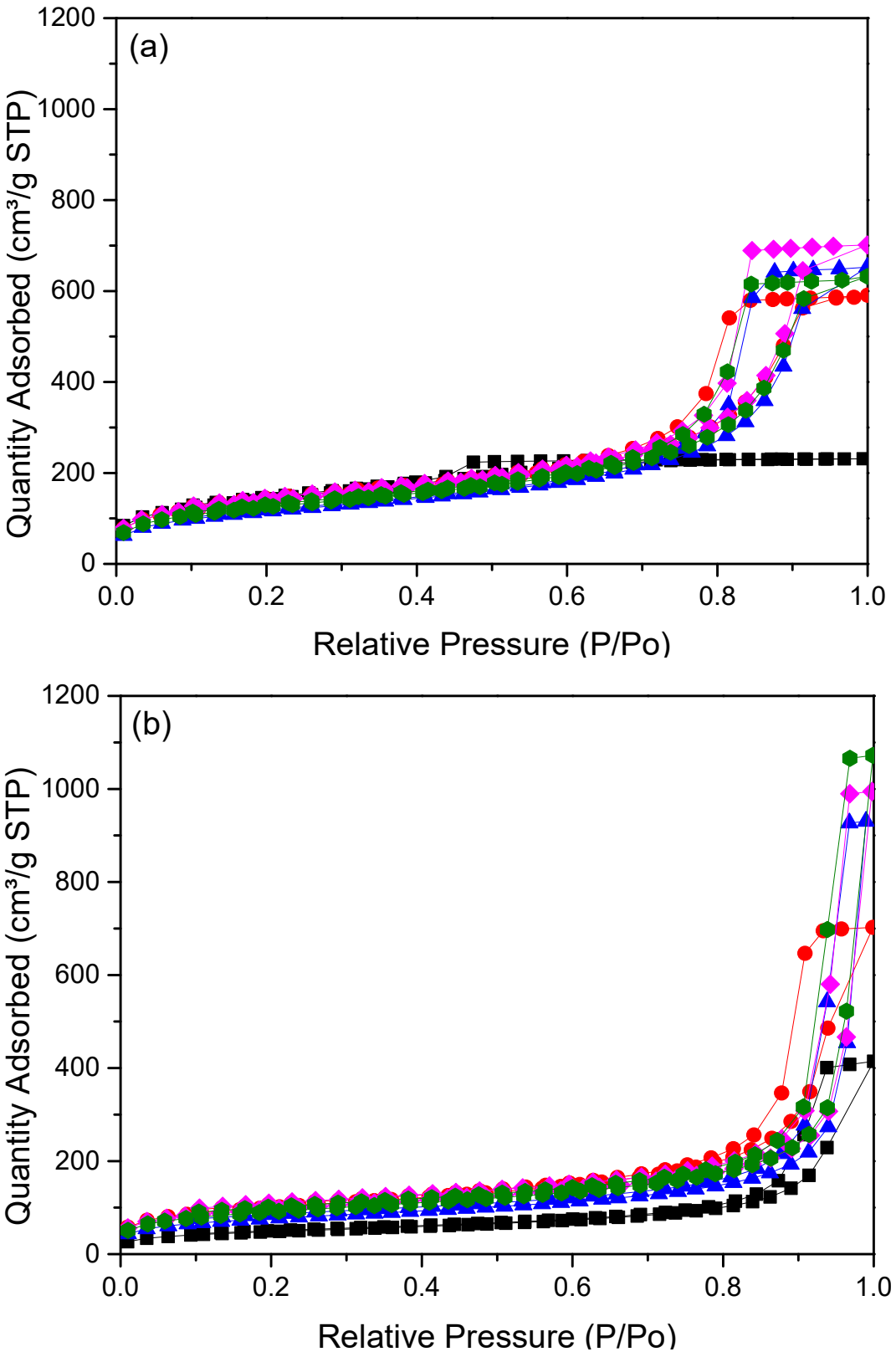

Figure 95: Nitrogen adsorption/desorption isotherms for (a) R/C 300 and (b) 500 RF xerogels, at percentage solids contents of: 10% (■), 20% (●), 25% (▲),30% (◆) and 35% (⬢).

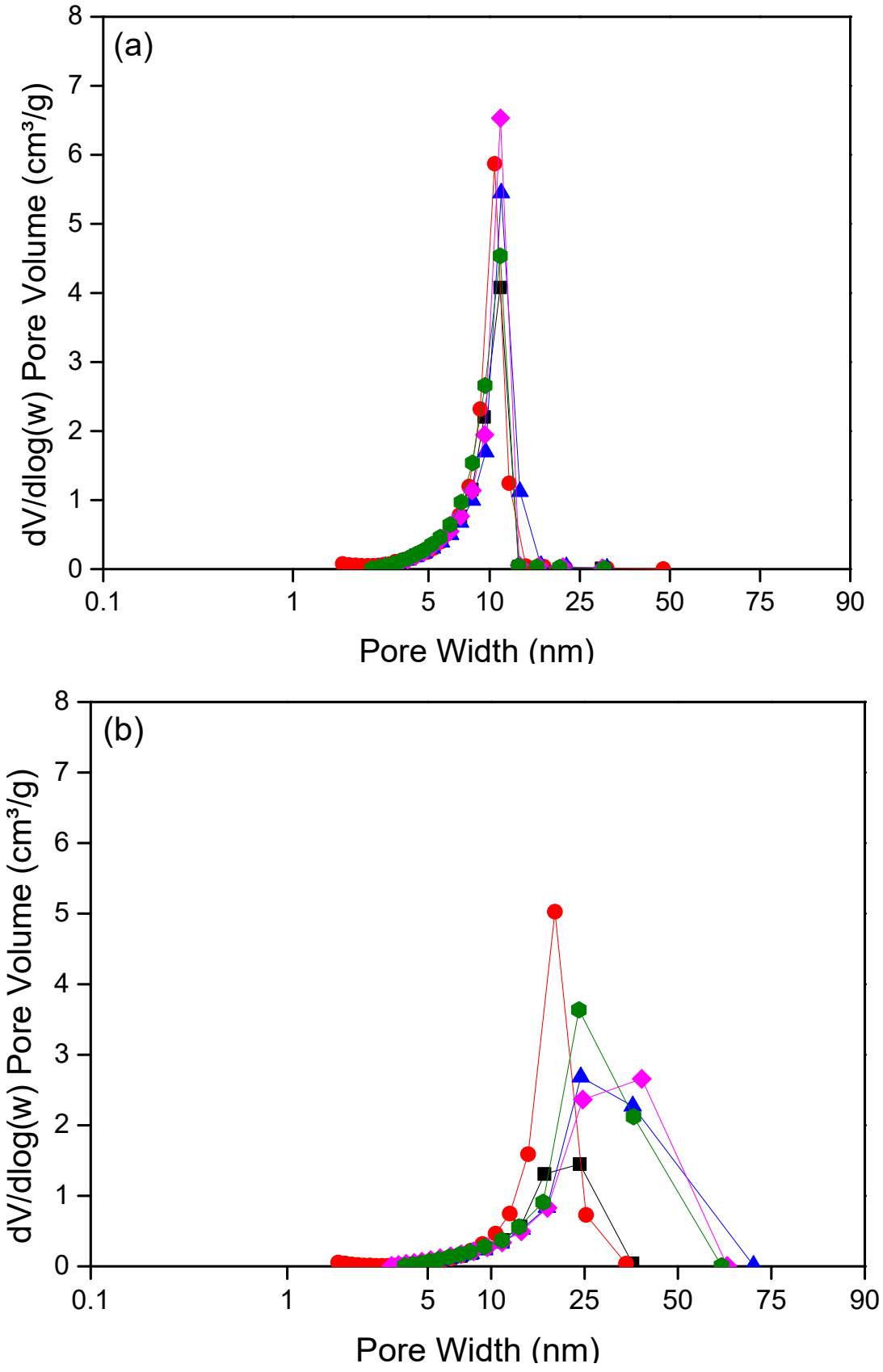

Figure 96: Pore size distributions for (a) R/C 300 and (b) 500 RF xerogels, at percentage solids content of 10% (■), 20% (●), 25% (▲),30% (◆) and 35% (●).

5.2.1.3 Effect of the catalyst type

For the investigation, the effect of the type of catalyst on the textural characteristics of the gels, the commonly used Na_2CO_3 catalyst was replaced with alternative catalysts from Group 1 metal carbonates, such as $NaHCO_3$, K_2CO_3 and $KHCO_3$. The xerogels were synthesised using a standard gel solids content of 20%. Table 14 displays information obtained for the porous structure of the gels using various catalysts, based on different R/C ratios.

Table 14: Porous Characteristics of RF xerogels with alkaline catalysts at varied levels.

Actual R/C	Equivalent (carbonate) R/C	S_{BET} * (m^2g^{-1})	V_{Tot} (cm^3g^{-1})	V_{Mic} (cm^3g^{-1})	d_p (nm)
		$NaHCO_3$			
50	100	511.33	0.34	0.05	3
150	300	501.94	0.82	0.04	7
200	400	450.69	0.94	0.04	10
250	500	383.15	1.03	0.03	13
300	600	332.42	0.91	0.03	14
		K_2CO_3			
100	100	529.30	0.39	0.04	3
300	300	466.77	0.91	0.04	9
400	400	340.24	1.03	0.03	15
500	500	330.76	1.05	0.03	17
600	600	253.46	0.72	0.03	16
		$KHCO_3$			
50	100	495.76	0.32	0.05	3
150	300	494.90	0.81	0.04	7
200	400	465.15	0.94	0.04	9
250	500	403.18	1.01	0.04	12
300	600	344.90	0.89	0.03	14
		Na_2CO_3			
100	100	490.80	0.36	0.05	3
300	300	477.10	0.92	0.04	8
400	400	406.60	0.98	0.04	11
500	500	345.30	1.09	0.04	14
600	600	274.80	1.00	0.03	18

* For the catalysts, The error has not been estimated as the measurement conducted one time.

From the viewpoint of the deprotonating ability of the catalysts used in RF sol-gel process, the carbonate bases possess the ability to deprotonate R twice (hydrogen

abstraction). In contrast, the bicarbonate bases can deprotonate R once, at the same catalyst concentrations [112]. Therefore, the bicarbonate base concentration assumed to be double of the concentration of carbonate base, to attain similar protonating ability. As depicted in Table 14, the actual R/C ratios of the bicarbonate base corresponded to the equivalent R/C ratios of the carbonate base.

Again, a general trend is observed for an increase in R/C ratio, an increase in average pore size and total pore volume, as well as a decrease in the specific surface area. Also, Table 14 shows that the average pore size increases almost linearly as the R/C ratio is increased for all catalysts used in the synthesis process. However, at the highest R/C ratio used (600), it was observed that, for K_2CO_3, the average pore size decreased. This effect may occur as a result of the shrinkage of these gel pore structures. Figure 97 shows that the isotherms belong to the Type IV category with hysteresis loops of Type H1 and H2. One can see that the amount of N_2 adsorbed on the K_2CO_3-based gels is slightly higher than on the Na or K hydrogen-carbonates analogues at a high relative pressure (Figure 97a). However, at R/C 500; all gels tend to have similar N_2 uptakes.

PSDs of these different catalysed gels are presented in Figures 98a and 98b. The PSD diameter peak values of the xerogels are sharp for the hydrogen-carbonates and broader and shifted to the right for the potassium-carbonates at an R/C ratio of 300.

As mentioned above, PSDs shift to larger pore diameters with an increasing R/C ratio. At an R/C ratio of 500, the PSD becomes more complex as the $KHCO_3$-based gel exhibits a narrow distribution, while for the other catalysts the distributions tend to cover a broad range of pore diameters.

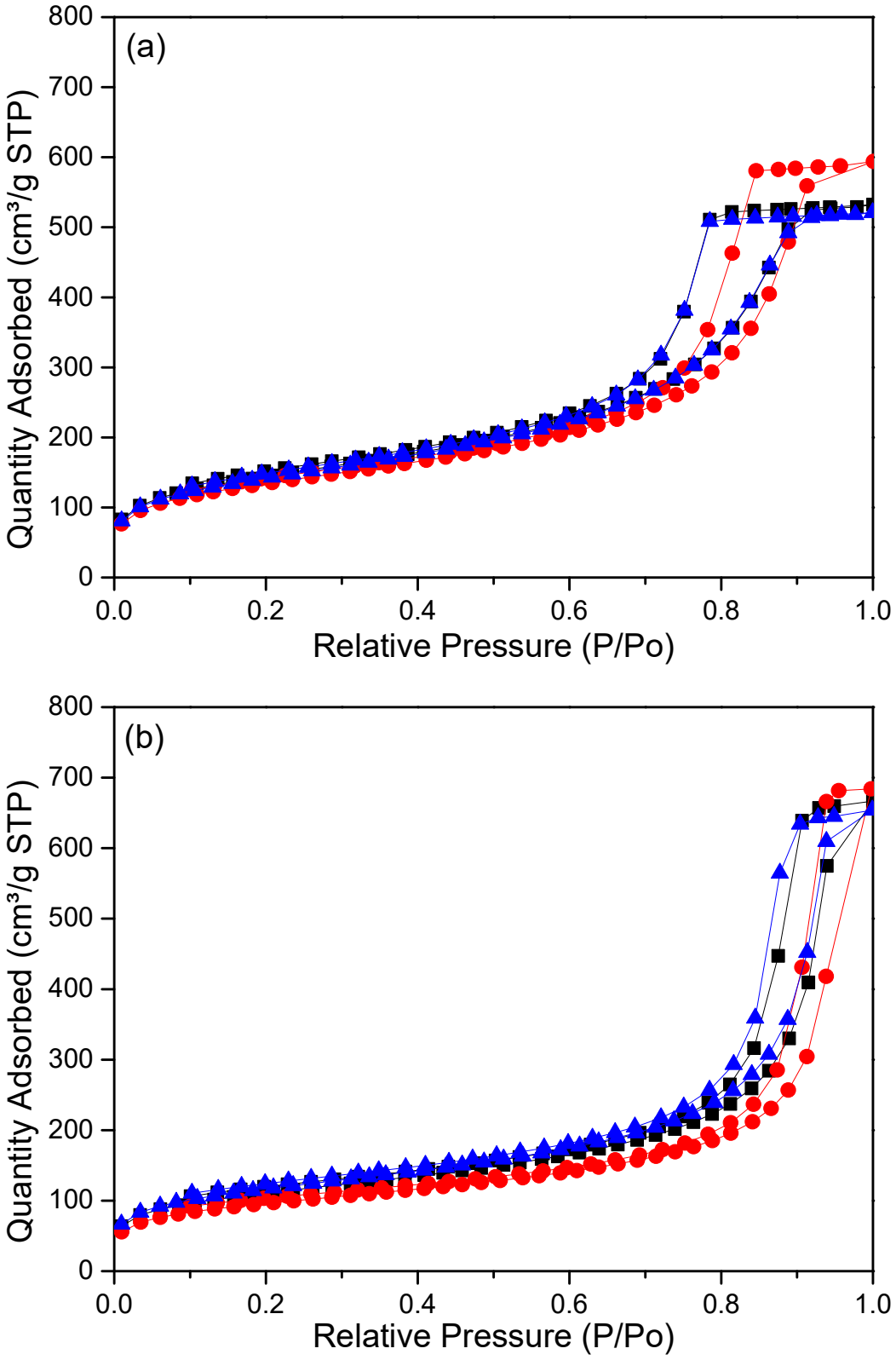

Figure 97: Nitrogen adsorption/desorption isotherms for (a) R/C 300 and (b) 500 RF xerogels, at different catalysts: $NaHCO_3$ (■), K_2CO_3 (●) and $KHCO_3$ (▲).

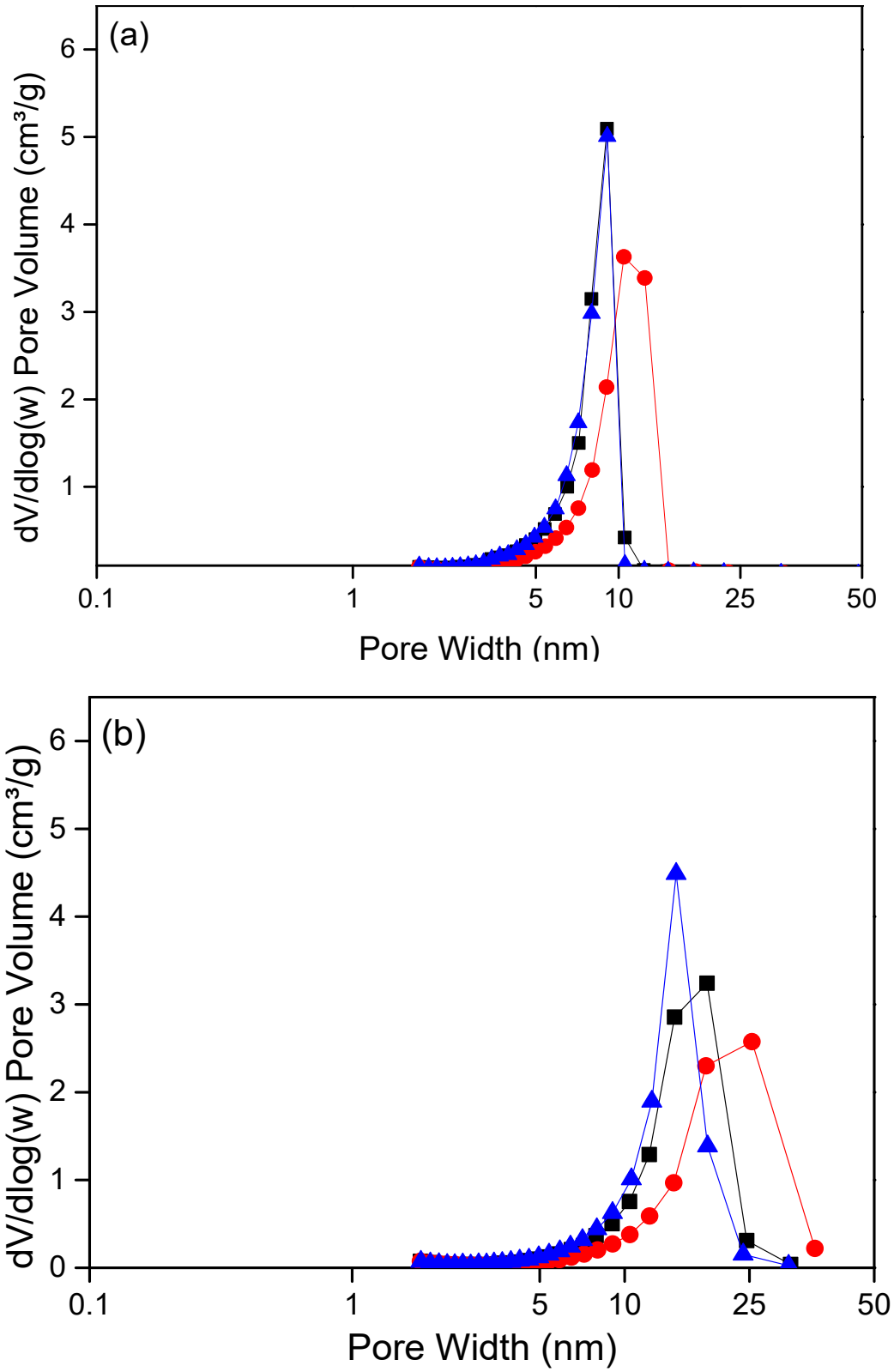

Figure 98: Pore size distributions for (a) R/C 300 and (b) 500 RF xerogels, at different catalysts: $NaHCO_3$ (■), K_2CO_3 (●) and $KHCO_3$ (▲).

5.2.2 Study of the structure of RF xerogels using ATR-FTIR

FTIR analyses were conducted to identify the various functional groups of the RF xerogel synthesised in this part of the study. Prior to measuring the IR spectra of the gel samples, it was vital to probe the reactants used in the preparation of the gel materials. The spectra of these reactants could be used to determine the traces of the unreacted resorcinol, formaldehyde and sodium carbonate within the RF xerogels.

Figure 99 shows the ATR-FTIR spectrum of these unreacted substances, including resorcinol (solid-state), formaldehyde (37% formaldehyde aqueous solution), and sodium carbonate (solid-state). For pure resorcinol, the spectra reveal different absorption bands. The broad absorption band at 3200 cm^{-1} observed in the spectrum indicates the O – H stretching vibration. The peaks at 1604 and 1481 cm^{-1} are associated with the aromatic C=C stretching vibrations. The energetic band due to C – O stretching vibration of the phenolic compounds was assigned at 1140 cm^{-1}. The O – H bending was detected at bands of 1373 and 1296 cm^{-1}. The band at 957 cm^{-1} is attributed to the C – C stretching, while the aromatic C – H out-of-plane bending can be observed at 771 and 732 cm^{-1}.

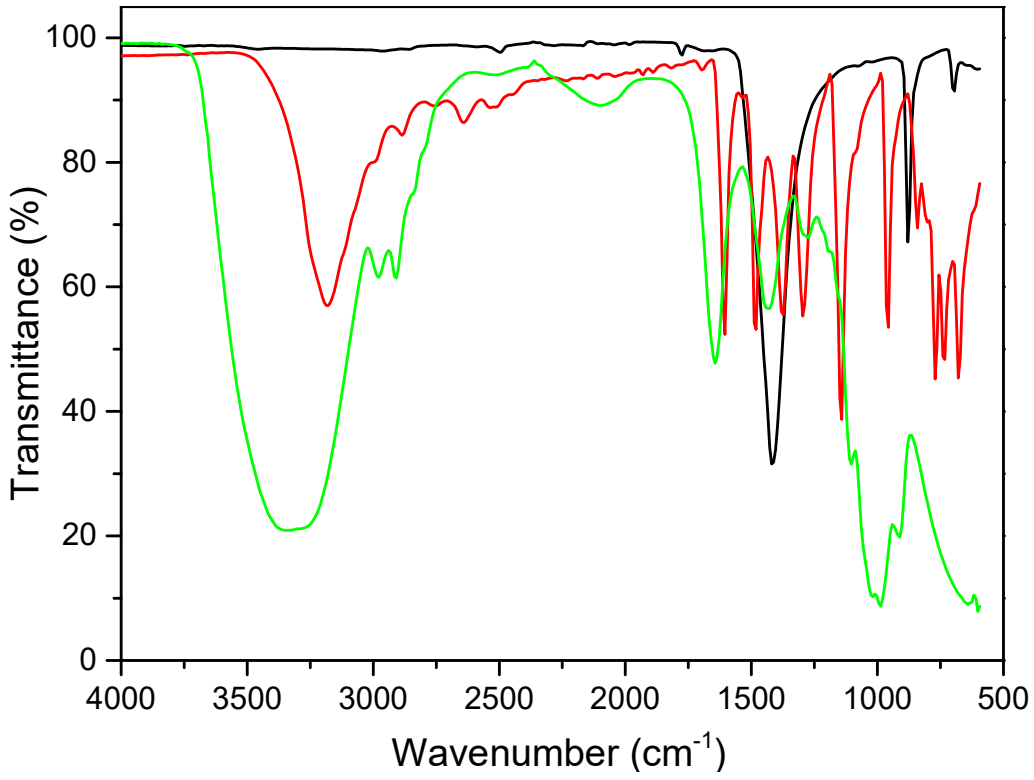

Figure 99: ATR-FTIR spectra of reactants used in RF xerogels production: resorcinol (—), formaldehyde (—), and sodium carbonate (—).

The spectrum of the stock formaldehyde solution exhibits characteristics absorption peaks due to the presence of the methylene glycol, methanol, and water. The ATR-FTIR analysis indicated broad bands at 3340 cm^{-1} representing – OH group. The weak band observed at 2977 cm^{-1} could reflect the C – H stretch of methyl or methylene group while the band at 2908 cm^{-1} corresponded to C – H bend overtone. The bands at 1434 and 1273 cm^{-1} were assigned to C – H bend and C – O stretch frequencies, respectively. The strong peak observed at 1643 cm^{-1} could result from a prominent C=O stretch of aldehydes. The methylene glycol peaks of C – O, O–H, and C –H bends could be observed at 1103, 987, and 910 cm^{-1}, respectively. A weak band at 1018 cm^{-1} was assigned to methanol. Similar IR spectra for formaldehyde and other aldehydic compounds were reported previously in the literature [68, 279, 349, 350]. The sodium carbonate spectrum revealed two sharp peaks at 1420 cm^{-1}, and 880 cm^{-1} corresponded C – O stretch and O – C – O bending of carbonate ions (CO_3^{-1}), respectively.

Selected xerogel samples were examined to determine the functional surface groups present (Figure 100). The IR spectra of the representative xerogels (25 and 30% solids contents) indicate that both formulations incorporate similar chemical character. Significantly, the spectra of these materials exhibit characteristics bands due to the aromatic C=C stretches (1600-1620 cm^{-1}), C=C stretches (benzene ring) obscured by $–CH_2–$ methylene bridge (1450-1465 cm^{-1}), and broad stretching O-H band (3270-3350 cm^{-1}). Two bands, observed around 1090 and 1220 cm^{-1}, corresponding to the C-O-C stretching vibrations caused by the methylene bridges between resorcinol rings [35, 82, 351, 352]. The C=O stretches were observed at a range of 1720-1740 cm^{-1}, which corresponded to the saturated ketones (acetone) or formaldehyde. The carbonyl group indicated to the presence of traces of unreacted formaldehyde (H(C=O) H) or the acetone trapped within the pores during the gelation or solvent exchange process, respectively.

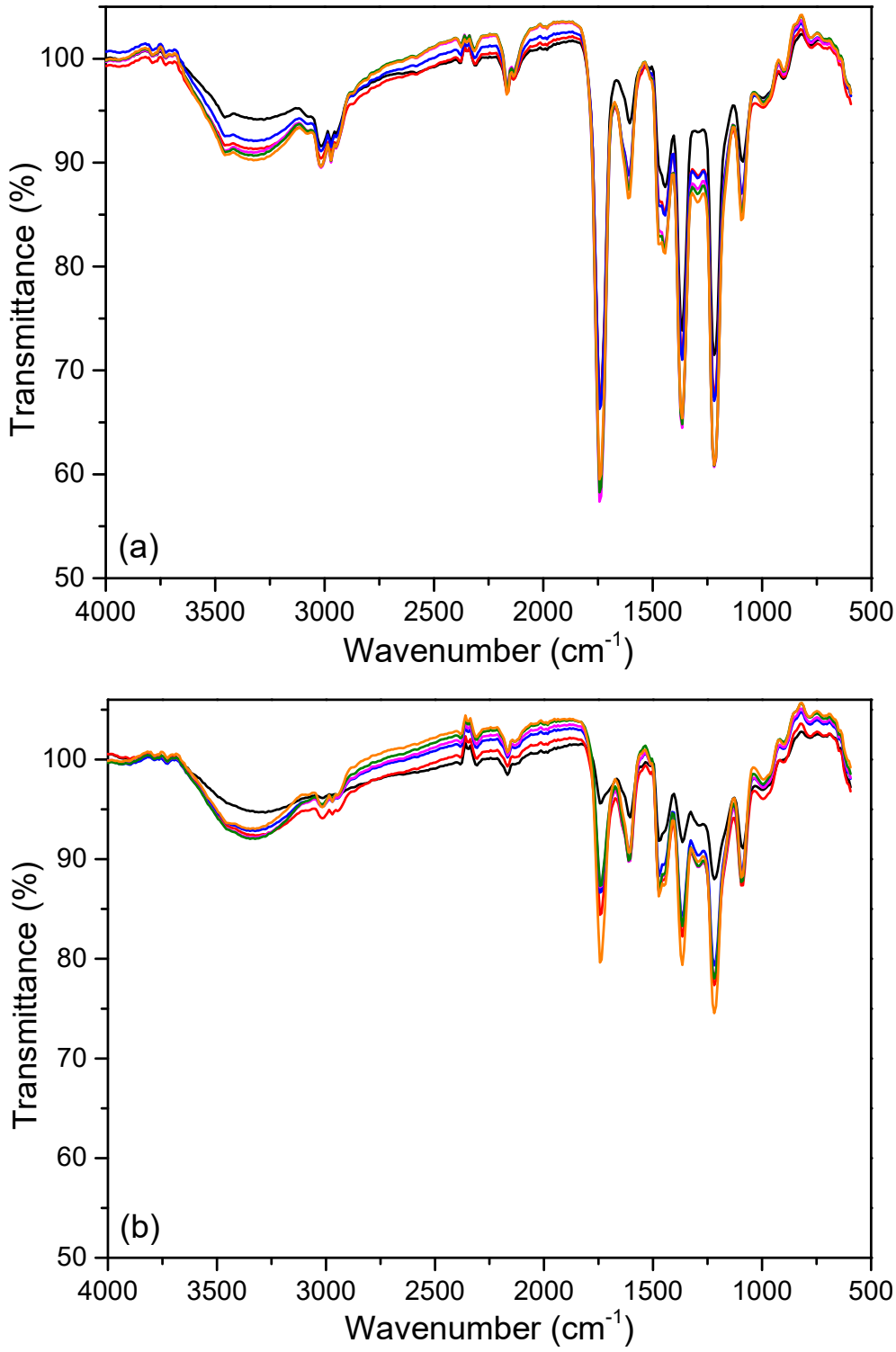

Figure 100: ATR-FTIR spectra for (a) 25 % and (b) 30% solids content RF xerogels, at R/C ratio of : 100 (—), 300 (—), 400 (—), 500 (—), 600 (—) and 700 (—).

5.3 Thermal conductivity of RF xerogels via the physical properties

For determination, the thermal conductivity (TC) of the RF xerogels, the thermal diffusivities (a) were determined using the Laser Flash Analysis (LFA) in argon, and heat capacities (C_p) were measured using Differential Scanning Calorimetry (DSC) in N_2. As described in Section 3.7.4, the sampling requirement of the LFA apparatus indicates the xerogel composition and final forms. At high R/C ratios, the samples could not be moulded into a disc shape during preparation. Also, the low solids content gels showed similar behaviour, due to the narrow window of monolithic disc-shape, and the radial shrinkage (Figure 101) of xerogel samples; the formulations for analysis were, therefore, chosen as two R/C molar ratios of 400 and 1000 at different solids contents of 30 and 40%. The two solids contents for a solids content of 30 and 40% at R/C 400 were disc-shaped samples, while the same solids content at the higher R/C ratio of 1000 were ground to a fine powder. It has been observed that the disc-shaped samples for RF gels with lower than 30% solid contents result in brittle and cracked samples, so they were excluded from any further measurements.

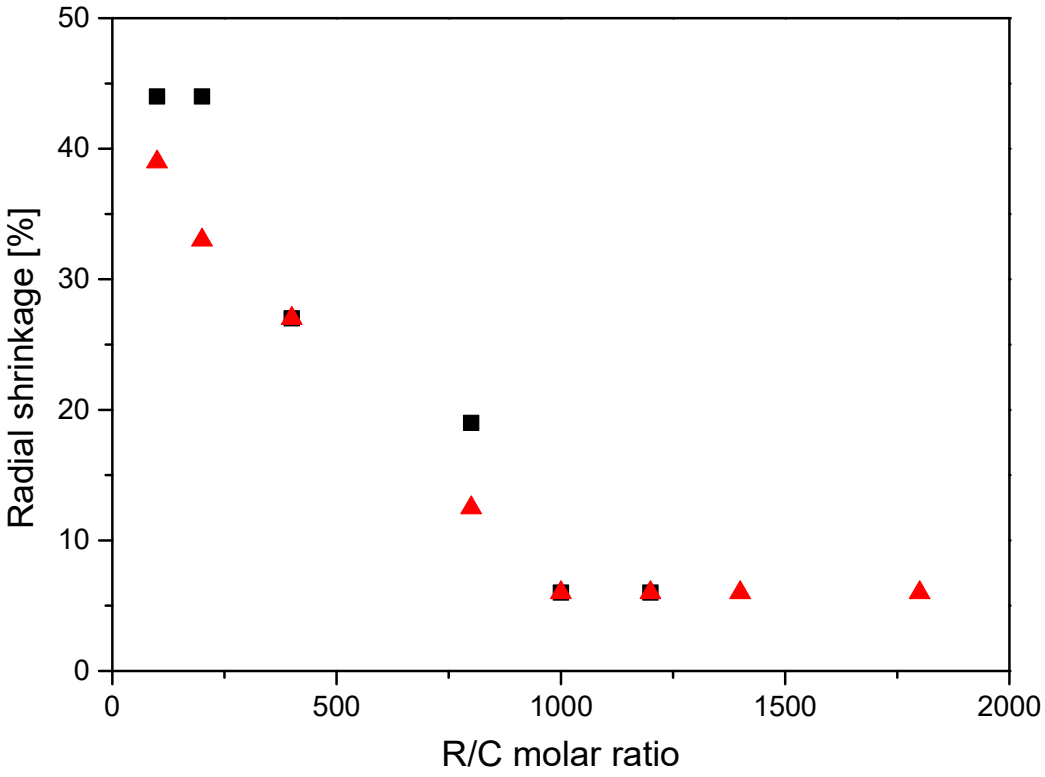

Figure 101: Dependence of the radial shrinkage rate of the monolithic RF xerogel on the catalyst concentration using solids percentage of 30% (■) and 40% (▲).

The total thermal conductivities (k) were estimated using the thermophysical properties; thermal diffusivity and specific heat capacity, and the bulk density through Equation 99 (Section 4.4.1).
The bulk densities (ρ) were calculated for disc-shaped and granulated RF xerogels (Table 15) using data obtained from the dimensions and mass, and water pycnometry, respectively.

It can be seen that the density of disc-shaped samples is lower than that of granulated gels. Therefore, the sampling condition can influence the total thermal conductivity of the RF gels obtained using this method. One-off measurement has been performed for each physical and thermophysical properties.

Table 15: Densities of selected samples of RF xerogels.

Sample R/C _ Solids%_Form	Density (kg m^{-3})
400_30_Disc	462
400_40_Disc	478
1000_30_Powder	1269
1000_40_Powder	1325

For the thermophysical properties, the measurements were conducted starting at room temperature (298 K) and heating up to approximately 473 K. Figure 102, and Figure 103 show the results obtained for these selected xerogel samples.

Figure 102 shows the heat capacity as a function of temperature for the four samples. It shows that at the same R/C ratio, the heat capacity tends to increase with decreasing solids content on a disc-shaped form and increase with the solids content of the powdered gels. As expected, the heat capacity increases with temperature. It can be noted that the heat capacity is influenced by the release of water vapour and residual acetone between the temperatures of 50 and 100 °C (323 and 373 K).

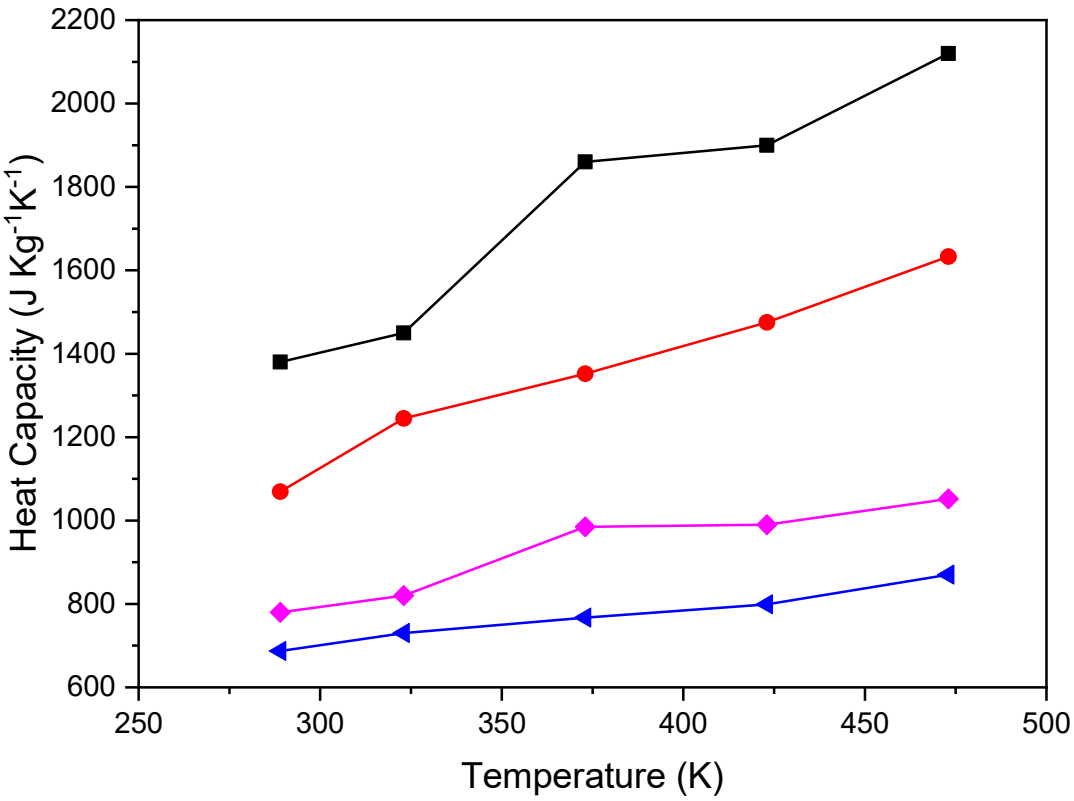

Figure 102: Heat capacity of RF xerogels prepared with different compositions and forms (R/C_% solids content_shape): 400_30_disc (■), 400_40_disc (●), 1000_30_powder (◀), and 1000_40_powder (◆).

The thermal diffusivity, as presented in Figure 103, increases with an increased solids content in the powdered material. At the same time, it remains relatively constant for both solids contents in the disc-shaped samples at the same R/C ratios. The diffusivity of the xerogels diverges with the results obtained by dos Santos *et al*. [353] study, as it increases within the reasonable range applied. A significant decrease in thermal diffusivity was reported with increasing the temperature from 20 to 100 °C for different polymeric materials (e.g. for polyvinyl chloride (PVC), the diffusivity declined from 1.36×10^{-7} to 0.97×10^{-7} m s^{-1} when the temperature was increased from 25 to 100 °C).

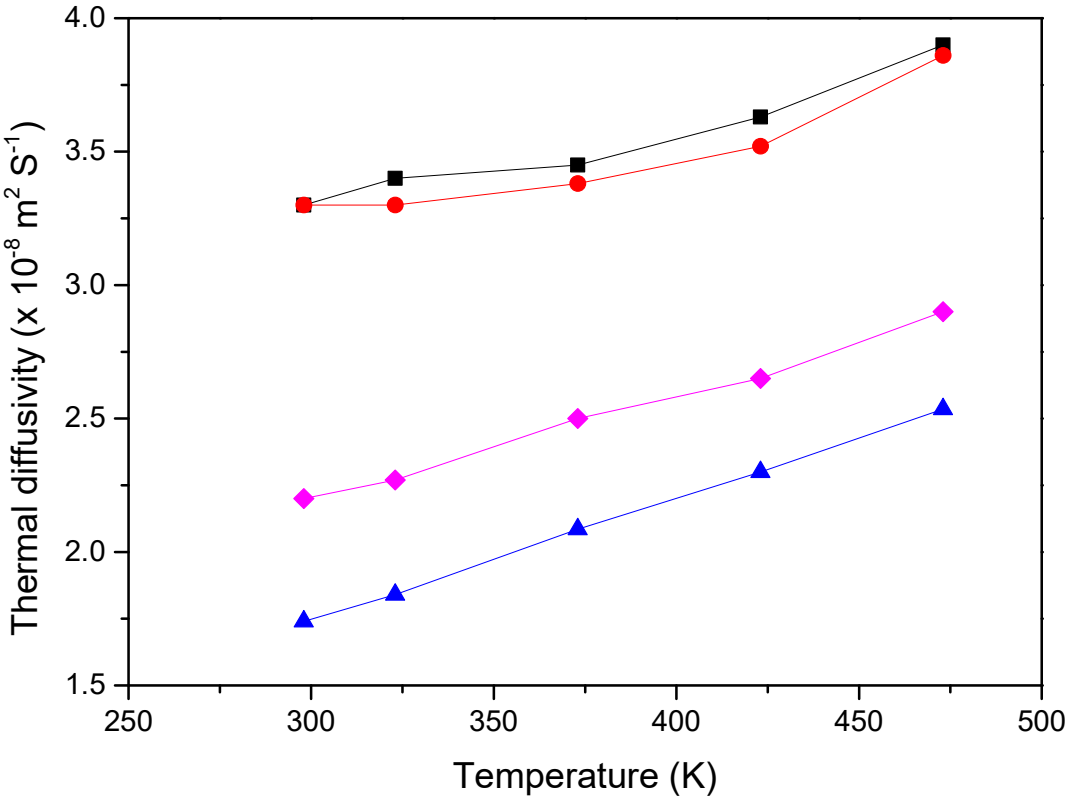

Figure 103: Thermal diffusivity of RF xerogels prepared with different compositions and forms (R/C_% solids content_shape): 400_30_disc (■), 400_40_disc (●), 1000_30_powder (◀), and 1000_40_powder (◆).

Figure 104 shows the plots of calculated thermal conductivity data; for the disc-shaped xerogels at a constant R/C molar ratio of 400, it can be seen that the thermal conductivities of the gels with a solids content of 40% are lower than in the sample with 30% solids content. However, in granular form, the higher R/C ratio of 1000, shows thermal conductivities that tend to decrease as solids content decreases. The values of thermal conductivity at 25 °C (298 K) are very low, which is due to the lower detected signals when using LFA and DSC measurements at room temperature. The methods used to determine thermal conductivity are affected by various factors, e.g. standard sampling requirements and moisture content of the samples examined.

Sample preparation for the different testing and measurement methods has a significant impact on the accuracy of the obtained thermal conductivity. For heat capacity, the observations indicated that the residual moisture could affect the heat capacity results. In contrast, the sampling procedure of the laser flash instrument could cause deviation in the obtained diffusivities.

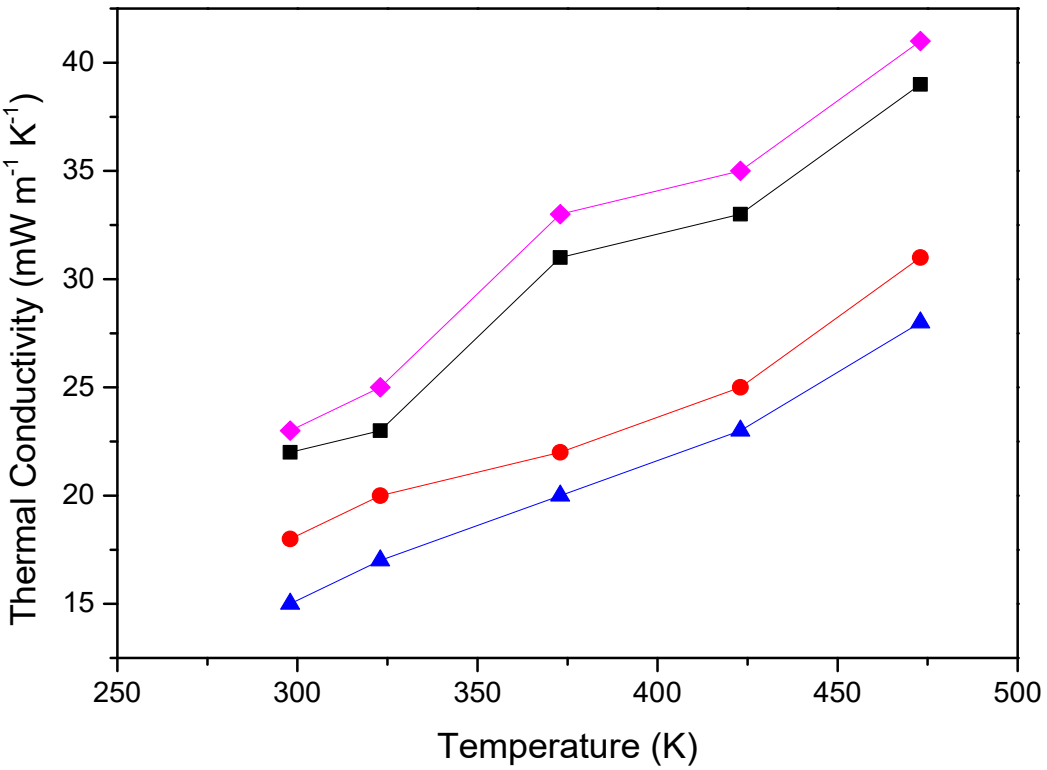

Figure 104: Thermal Conductivity of RF xerogels prepared with different compositions and forms (R/C_% solids content_shape): 400_30_disc (■), 400_40_disc (●), 1000_30_powder (◀), and 1000_40_powder (◆).

The shape of the sample could affect the results obtained using these methods. The powder characteristics, including particle shape, particle size distribution, and the tendency for segregation represent issues to be addressed when adapting the powder sampling procedure. During the measurement of powder samples, fine particles move as a result of the inrush of nitrogen gas into the sample container, causing instability in signals detected by the instrument; hence the accuracy of the final results. Also, handling the powder samples is another issue to be considered, as the potential of dust formation has health, safety, and environmental impacts.

5.4 Solid backbone density

As previously discussed (Section 1.5.5), the catalyst concentration and the solids content have a significant impact on the particle size and the number of clusters formed during the sol-gel transition process. Therefore, the skeletal density of materials can also be influenced by altering the xerogel composition, as presented in Figure 105. As can be seen, the solid backbone of the xerogels becomes denser with increasing R/C

ratio and changes slightly with the solids content of the initial RF sol. At low R/C ratios, small polymeric particles are formed with largely interconnected necks. On the other hand, high R/C ratios result in large particles with narrow, interconnected necks [43].

A previous study provided further insight into how the R/C ratio affects the solid backbone density, the work conducted by Taylor *et al*. [126] investigated the growth of particles during the RF sol-gel transition, using Dynamic Light Scattering (DLS). It was reported that lowering the R/C ratio led to high cluster number concentration and smaller pore sizes, while at the high R/C ratio, lower cluster number concentration and larger pore sizes formed. As demonstrated by Hsu *et al*. [354], the particle size significantly influences the interaction between the particles. The findings show that small particles tend to coagulate more than the larger particles. These all agree with the observation that of the density of the solid backbone of the xerogel changes as a function of the R/C ratio.

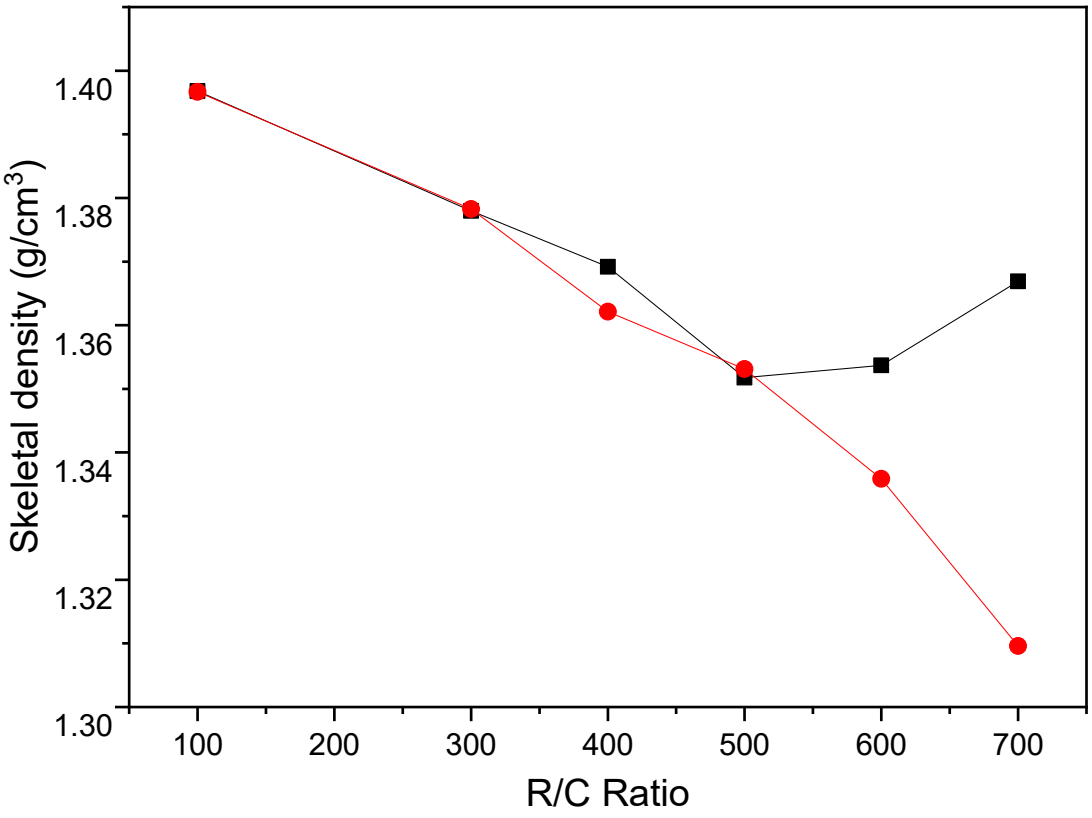

Figure 105: Skeletal density measured by helium pycnometer for RF xerogels at different compositions: 25 (■) and 30 % (●) solids content.

For the xerogels produced using an R/C level close to the gelation limit for the particular solids content, the skeletal density begins to rise as the R/C ratio increases (e.g. 25 % solids content series). One can see that the higher R/C ratios for xerogels at 30% solids content are stable event until R/C 700. Hence the solid density continues to decrease. It can also be noted that the micropore volume of the xerogels (Table 14) increases as the skeletal densities increase. The bulk and skeletal densities (ρ_b and ρ_s) of the material can be used to calculate its porosity (Π) as follows [29]:

$$\Pi = \frac{1/\rho_b - 1/\rho_s}{1/\rho_b} \qquad \textbf{Equation 114}$$

The total pore volume is inversely proportional to this form of density since the total pore volume can be obtained as [234]:

$$V_{Tot.\ pore} = \frac{1}{\rho_b} - \frac{1}{\rho_s} \qquad \textbf{Equation 115}$$

Hence, the porosity of RF xerogel can be estimated by combining the results obtained using physisorption analysis and pycnometer method. The total porosity is also expressed as the ratio of the total pore volume ($V_{Tot.Pore}$) to the specific total, or bulk volume of material (V_b) [355]:

$$\Pi = \frac{V_{Tot.Pore}}{V_b} \qquad \textbf{Equation 116}$$

The specific bulk volume (V_b) of material can be related to the bulk density, total pore volume and skeletal density [356]:

$$\frac{1}{\rho_b} = V_b = V_{Tot.Pore} + \frac{1}{\rho_s} \qquad \textbf{Equation 117}$$

The bulk density measured using the macroscopic methods (pycnometer), revealed a significant deviation in the calculated porosity of the studied RF xerogels. From the Table included in Appendix C, the specific bulk volumes are remarkably lower than the value of total pore volume derived by the physisorption analysis. Which could be due to the presence of adsorbed gases and trapped solvent within the closed pores; therefore, the density showed high values. Conversely, the specific bulk volume is much higher than the total pore volume, indicating that apart of sample pores is not accessible as described above, and insufficient equilibrium during the analysis [356].

The variation between the total pore volume derived from the BET analysis and the bulk density measured by other techniques can be observed in the results presented by Rey-Raap et al.[229] for RF xerogel materials.

As discussed previously (Section 3.7.1), the density of the porous materials influences their solid heat conduction properties, which contributes to the total thermal conductivity of the product. Therefore, the skeletal density has an impact on the thermal performance of the RF gels.

5.5 Thermal stability

Thermogravimetric analysis (TGA) and differential scanning calorimetry (DSC) was performed to examine the thermal stability of the RF xerogels at elevated temperatures. Figure 106 shows the results obtained from the TGA/DSC experiments for selected formulations of xerogel samples. All gel samples reveal relatively similar thermal behaviour.

The results of TGA indicated a total mass loss of about 40-45 % during heating of the samples in N_2. Based on the TG curves obtained, the thermal decomposition of the RF xerogel samples can be divided into three steps specified by the mass loss. In the first step, 2-3% of the initial mass loss was observed between 25 (298K) and 100 °C (373K), which occurred as a result of the release of the residual moisture and volatile compounds (e.g. acetone) and. Mass loss of about 10% occurred between 100 and 300 °C (573K), due to the release of unreacted species and residual moisture trapped into the pores of the dried xerogel. The third step determined the changes occurred between 300 and 500 °C (773K), which characterised by about 20% mass loss. During this stage, the percentage mass loss corresponds to the breakdown, release of the remaining unreacted monomers, and decomposition of the functional groups within the xerogel network. [87, 95, 152, 316]. The DSC results show no significant thermal peaks. However, the DSC curves indicated that a noticeable exothermic heat flow beginning at 200 °C. It can also be observed that the samples with lower R/C ratio were more stable at high temperatures.

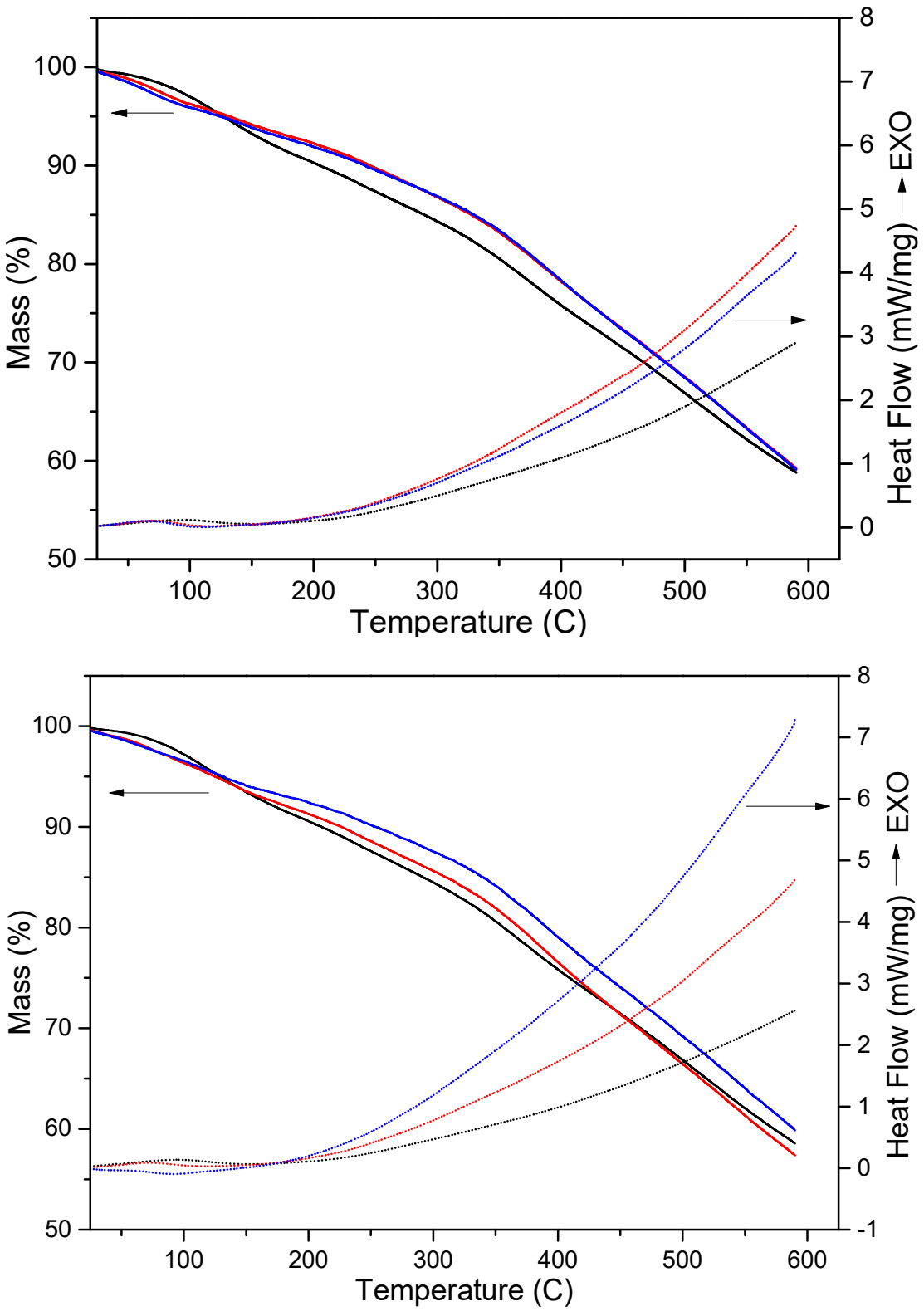

Figure 106: TG and DSC curves for (a) 25 % and (b) 30% solids content RF xerogels at R/C ratio of 100 (—), 300 (—) and 600 (—).

5.6 RF xerogel – summary of findings

The effect of synthesis parameters, on the final properties of RF xerogels, has been studied in detail, through the characterisation and analysis of gels prepared using various R/C ratios, solids contents, and different types of catalyst. N_2 adsorption-desorption method, FTIR spectroscopy and helium pycnometry ware utilised to characterise the nanostructure of the RF gels. The thermal efficiency of the gel, as an insulator, was evaluated using LFA and DSC techniques, while, the stability of the material was analysed using thermogravimetric methods.

In order to investigate the influence of R/C ratio on the porous structure of RF gels, a series of samples were prepared using sodium carbonate as a catalyst at R/C ratios of 100, 300, 400, 500, 600, 700, 800, and 900, depending on the level of constant solids content applied. Another suite of samples was based on the solids content as a processing variable, and the effect of 10, 20, 25, 30, and 35% solids content was examined at two different R/C ratios (300 and 500; these R/C ratios can be used at all chosen solids content). To further investigate the effect of synthesis conditions, alternative Group I catalysts were used to prepare gels. Potassium carbonate and sodium and potassium hydrogen-carbonates were utilised at a standard solids content of 20% (offering a material saving during gel production) and R/C ratios of 100, 300, 400, 500 and 600.

To summarise, the main findings from the studies of RF xerogels synthesised at varied conditions are:

- Average pore size and total pore volume typically increase with increasing R/C molar ratio at all solids content levels and for all catalyst types, with a corresponding decrease in micropore volume and specific surface area.
- R/C ratio significantly influences the skeletal density of RF gels, which affects the thermal conductivity via solid thermal conduction.
- Gelation times increased sharply with increasing R/C ratio, which affects the degree of crosslinking in the polymer network.
- At constant, relatively high R/C ratios, an increase in the solids content leads to an increase in pore size and total pore volume of the gels.

- Sodium and potassium hydrogen-carbonates show a similar trend at any given R/C. In contrast, potassium carbonate shows increased average pore size and total pore volume compared to the sodium counterpart.
- Results obtained from FTIR reveal that the functional groups are independent of the R/C ratio and solids content, except R/C 100.
- The OH group presents in the IR spectra indicates that trace water is still present within the gel structure of gels despite solvent exchange.
- The bulk materials at high R/C ratios were not suitable for the LFA measurement, because of their brittleness and high porosity.
- Thermal conductivities, calculated using the thermophysical properties of limited gel samples, show that the RF gels can be considered as promising insulating materials.
- Thermal decomposition of RF gels occurs at different stages, involving the release of water, solvent, and unreacted precursors, followed by removal of the hydrogen and oxygen atoms as CO_2, CH_4, and other organic forms.

Overall, RF xerogels can be prepared with a tuned pore size by systematic selection of R/C ratio, solids content, and a basic catalyst.

6 Result part 2 – Reinforcement (PET) characteristics

Air-bleeder polyester (AB 10) is a lightweight fibre with good all-around stretch. As mentioned above, this fibre matrix (PET nonwoven fabric) is used in an RF xerogel-type blanket as a reinforcement material. Physical properties of this material are provided in Table 16. The HFM 436 Lambda instrument measured the thermal conductivity of the PET fibre, as 39.5 mW/m.K. This value represents the highest thermal conductivity to which any RF gel blanket should perform. This result also shows that the reinforcement materials possess 50% higher thermal conductivity compared to the produced blankets. The high porosity of this PET fibre allows the percentage of the solids content of the gel with the blanket to be increased to 75%. Hence the total thermal conductivity of the blanket depends mainly on the thermal performance of the RF gel.

Table 16: Physical properties of PET non-woven polyester (AB10) [357, 358].

Maximum use temperature	**(K)**	478
Maximum cont. use temperature	**(K)**	343
Colour		white
Thickness (nominal, uncompressed)	**(mm)**	6
Tensile Strength	**(Mpa)**	2.5
Bulk density	**(kg/m^3)**	101
Thermal conductivity*	**(mW/m.K)**	39.5
Linear thermal expansion coefficient	**(K^{-1})**	70×10^{-6}
Melting point	**(K)**	523
Resistance to chemicals		Good

* Thermal conductivity at a mean temperature of 283K, 13.8 kPa compressions, and ambient pressure using HFM 436 Lambda.

6.1 Optical characterisation

Optical microscopic images of blank PET fibre show spaghetti-like strands of PET, as illustrated in Figure 107 at three different focus levels. It can be seen that the random three-dimension pattern of the strands was distributed in-plane. The observation shows that the structure of PET fibre exhibits several contact points between the strands, which provide additional adhesive nodes to incorporate the RF material.

SEM imaging of the blank non-woven PET fibre (Figure 108) confirmed the random distribution of the individual strands into the fabric plane, which is in agreement with the findings reported by Soltani et al.[359]. The images also showed relatively smooth strand surfaces with visible flacks and scratches, which could be related to the effect of impurities or resulted from the sampling procedure (e.g. cutting by scissors). It can also be observed that the fabric material reveals different contact points between the strands as described above.

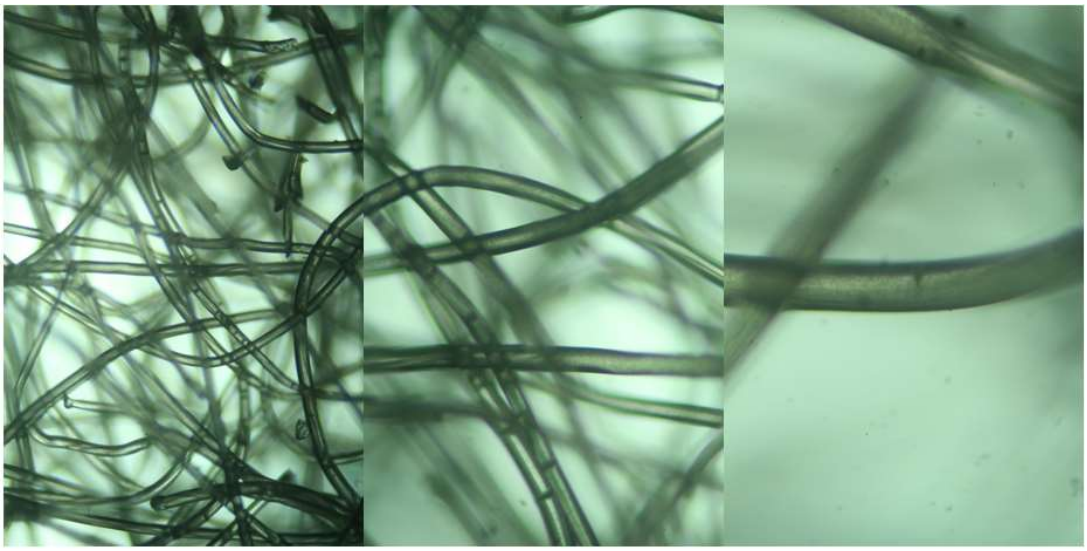

Figure 107: Optical micrographs of PET fibre used for RF composite blanket synthesis.

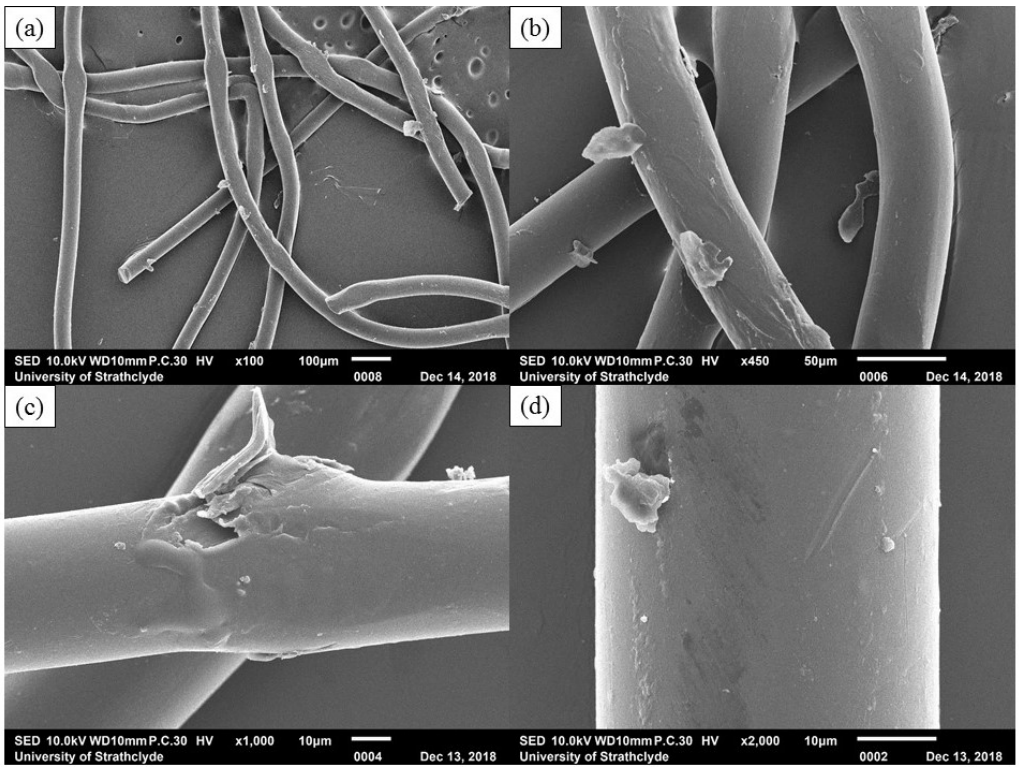

Figure 108: SEM images for blank PET fibre at different magnifications : (a) x100 , (b): x450, (c) x1000, and (d) x2000.

6.2 ATR-FTIR analysis

The ATR-FTIR spectra of the blank non-woven PET fibre are shown in Figure 109. The characteristic peaks of the PET fibre appeared at 1712, 1404, 1242, 1095 and 725 cm^{-1}. The energetic absorption band at 1712 cm^{-1} attributed to the stretching vibration of the carbonyl groups. The C – C interaction of the aromatic rings (phenyl) was observed as C = C stretching vibrations at a wavenumber of 1404 cm^{-1}, while the strong and most informative of the aromatic ring, resulted from out-of-plane C –H bending occurred at 725 cm^{-1}. There were two strong absorption bands at 1242 and 1095 cm^{-1}, indicating the common C – O stretch bonds in esters. Other peaks were observed at 2960, 1018 cm^{-1} come from the weak C – H and sharp C – C stretching vibrations. These results are consistent with the observations reported in the previous studies about the PET fibre [360-364].

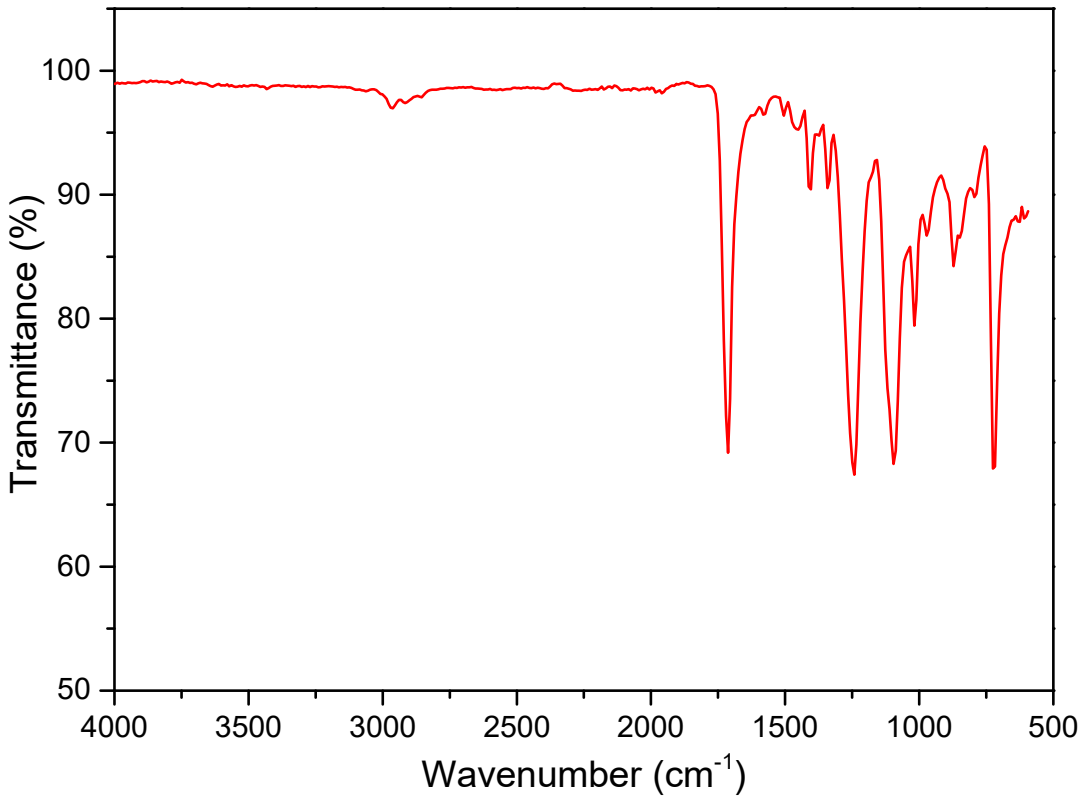

Figure 109: ATR-FTIR spectra of pure PET fibre.

6.3 Thermal degradation behaviour of PET fibre

Using simultaneous thermogravimetric (TG) and differential scanning calorimetry (DSC), a non-woven PET fibre was studied. Figure 110 shows the TG and DSC curves of PET fibre. Upon heating the sample to 600 °C (873 K), one mass-loss step of 86% was observed. This mass change occurred at 550 °C(823 K), with the decomposition was initiated at around 383 °C. The endothermic DSC peak at 256 °C (529 K) can be attributed to the melting of the PET sample, which is in agreement with the findings reported by Bozaci et al.[363]. On the other hand, the exothermic DSC is due to the decomposition of the functional groups, releasing gaseous products such as water, carbon monoxide, carbon dioxide or hydrocarbons [365, 366].

The plain PET fibre is thermally stable up to around 523 K, after that it begins to decompose, with mass loss of about 85% at 873 K. Therefore, the PET fibre can be used for thermal insulation where the service temperatures up to 473 K (200 °C).

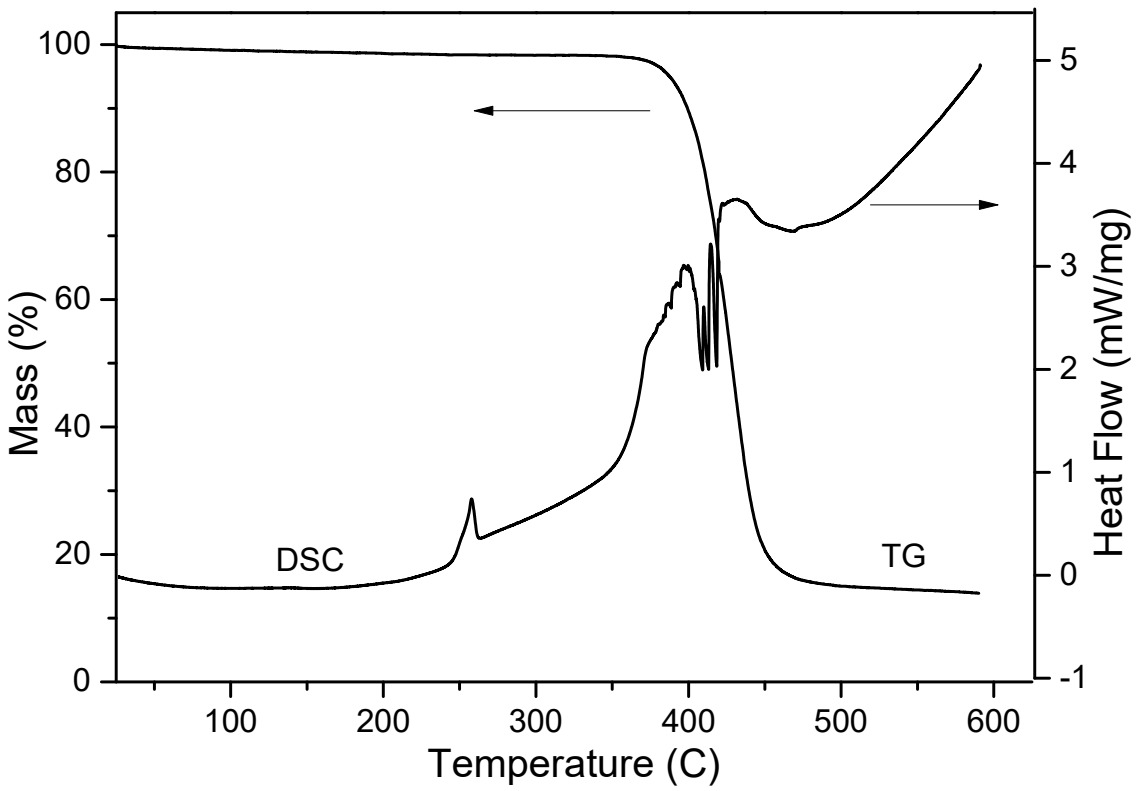

Figure 110: TG and DSC curves of non-woven blank PET fibre.

7 Results part 3 – Fabricated RF composite blanket

Formulations of RF blanket-type samples synthesised for the present work are outlined in Section 4.2. These were prepared at a size of 180 × 180 × 6 mm; using an appropriately scaled volume of sol-gel. The composition of the sol was systematically changed to obtain gel-blanket systems with different characteristics.

7.1 Blanket characterisation

The synthetic route of the sol, used in the construction of the composite, influences the morphology of the final material (blanket). An image (Figure 111) of representative RF blanket samples, produced with various R/C molar ratios at increased solids content, shows a discernible difference at the macro scale. As mentioned in Section 1.5, catalyst concentration is a dominant factor affecting the final properties of the RF gel. At the same time, the solids content could change the density of the gel and control the R/C ratio limiting point.

Figure 111: Samples of RF blanket-type xerogels synthesised using different R/C ratios and percentage solids contents from left to right: 400-20, 500-25, 300-30, 600-30, and 800-30, respectively.

In the manufacture of aerogel blankets, it has been suggested [230] that the reactant concentration of the initial solution is a very crucial parameter, which strongly affects the uptake of gel into the substrate, hence, the thermal performance of the blanket. Figure 112 demonstrates the effect of increasing the solids content of the RF reaction solution (sol) on the amount of gel incorporated into the fabricated blanket. It can be seen that the mass fraction of the RF gel within the blanket increases sharply as solids

content is increased from 10 to 20%, followed by a steady increase up to 35%. Where after higher solids content (>35%) results in a constant loading fraction.

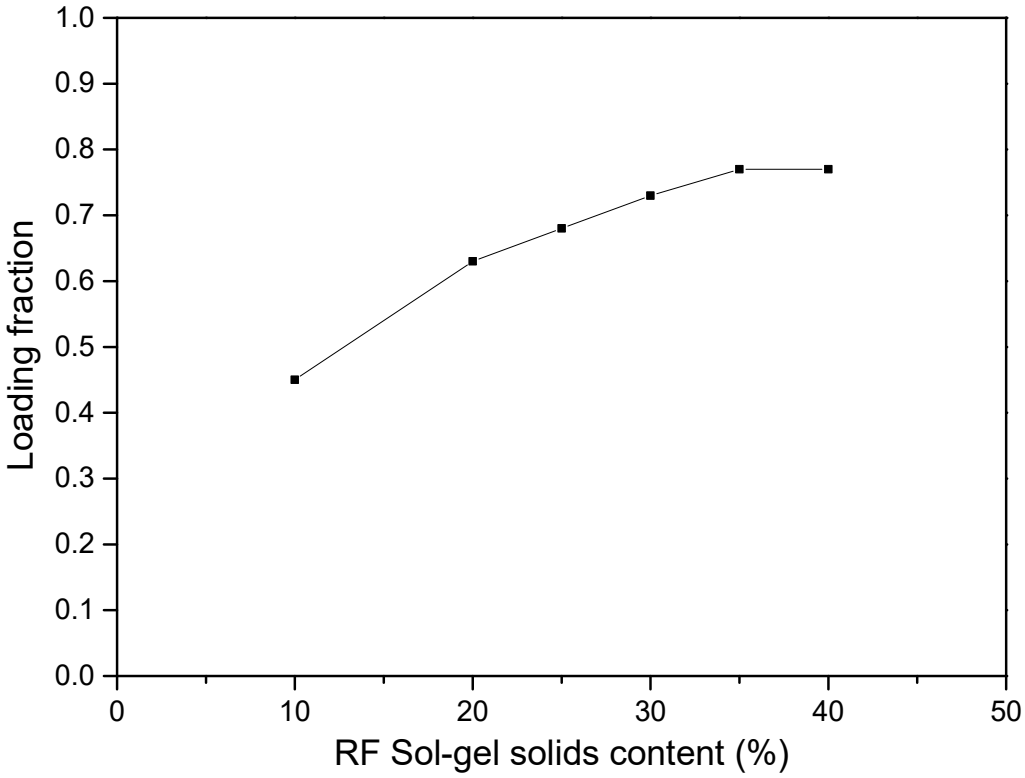

Figure 112: Influence of percentage solids content on the uptake of RF gel into fibrous PET.

RF blankets fabricated using RF sol at solids content higher than 30% solids, were excluded, because the products show adverse features, such as high rigidity, shrinkage and density (Figure 113).

Figure 113: RF blanket fabricated using an RF sol of 40% solids, showing a high level of shrinkage after gelation and curing stages.

When using R/C ratios lower than 300, the blankets subsequently obtained were also excluded due to the lack of flexibility, irregular surfaces, and high shrinkage. Figure 114 illustrates the effect of the low R/C ratio on the morphology of the blanket. Blankets with low R/C cannot be practically folded to insulate a pipeline or other cylindrical equipment. Also, they show lower thermal resistance compared with the higher R/C ratio based blankets (Section 5.2.1).

Figure 114: RF blanket prepared with a low R/C ratio (200) showing shrinkage and surface irregularities.

It is also notable that, at the higher R/C ratios, which are near to the gelation limiting value, dusty and brittle blanket structures are obtained.

7.1.1 Textural properties

Nitrogen sorption at 77 K (–196 °C) was applied to investigate the textural characteristics of RF-PET blankets. Porosity and surface area measurements were performed on each of the dried blankets. The structural characteristics of the dried RF-PET blankets (RFBs) compared to the parent RF xerogels (RFXs), including BET surface areas (S_{BET}), total pore volume (V_{Tot}), micropore volumes (V_{Mic}), and average pore diameters (d_p) are outlined in Table 17.

The data allow comparison between the various RF blankets prepared with different formulations of the RF sol-gel. As can be seen, a decrease in the concentration of the catalyst (Na_2CO_3) leads to an initial increase in the total pore volume and average pore diameter, before these parameters decrease at R/C ratios of 400 and 500 for the same solids content, respectively. It can also be seen that the micropore volume decreases as catalyst concentration decreases (higher R/C ratios), which strongly influences the specific surface area, which decreases. It can be observed that there is a substantial difference between the total pore volume and the micropore volume, which

corresponds to the contribution of the mesopore and macropore volume to the porous structure of the material. It would be expected that the total pore volume decreases as the average pore diameter increases; this means that not all of the porosity is detected when using nitrogen adsorption measurements. Alternative techniques can be used to probe these larger pore diameter (See Future Work).

Table 17: Textural properties of RF xerogels (RFXs) and blankets (RFBs) synthesised using a range of R/C ratios and percentage solids contents.

R/C	S_{BET} (m^2g^{-1})		V_{TOt} (cm^3g^{-1})		V_{Mic} (cm^3g^{-1})		d_p (nm)	
	RFXs	RFBs	RFXs	RFBs	RFXs	RFBs	RFXs	RFBs
				10% solids				
300	366.4	124.4	0.85	0.39	0.02	0.01	9	15
400	272.6	69.4	0.84	0.35	0.02	0.01	12	26
500	167.8	21.0	0.64	0.12	0.01	< 0.01	16	30
				20% solids				
300	477.1	181.2	0.92	0.52	0.04	0.02	8	13
400	406.6	142.0	0.98	0.70	0.04	0.01	11	23
500	345.3	82.0	1.09	0.43	0.04	< 0.01	14	27
600	274.8	13.9	1.00	0.05	0.03	< 0.01	18	21
				25% solids				
300	404.7	218.7	1.00	0.59	0.03	0.02	10	13
400	344.8	173.8	1.017	0.58	0.03	0.01	15	16
500	264.1	140.1	1.44	0.56	0.03	0.01	24	21
600	179.0	89.0	1.07	0.18	0.02	0.01	32	11
700	85.8	34.0	0.22	0.06	0.01	< 0.01	16	10
				30% solids				
300	479.0	249.2	1.08	0.68	0.04	0.02	9	13
400	395.3	203.8	1.31	0.98	0.04	0.02	15	26
500	329.7	168.2	1.54	0.49	0.04	0.02	24	16
600	248.4	136.1	1.17	0.28	0.03	0.02	28	12
700	164.9	78.2	0.34	0.15	0.02	0.01	14	11
800	100.5	23.6	0.17	0.04	00.01	< 0.01	13	10

Table 17 shows that the RF gel has a larger surface area and total pore volume than the gel materials contained in any of the RF blankets (RF-PET composites). In contrast, the average pore size is lower than that of the blanket, because of the low level of shrinkage and collapse within the reinforced gel structure.

7.1.1.1 Effect of R/C ratio on blanket structure

The N_2 adsorption isotherms and pore size distributions for RF blanket samples prepared using Na_2CO_3 as a catalyst at various initial solution R/C ratios and a solids content of either 25 or 30% are shown in Figures 115 and 116, respectively.

Type IV isotherms, categorised using the IUPAC classification scheme, are observed for N_2 adsorption on the xerogel blankets of the aerogel blankets; demonstrating the mesoporous nature of the materials by the presence of capillary condensation. The hysteresis character varies between H1 and H2 loops as R/C ratio increases. From Figure 110, it can be seen that the amounts of N_2 adsorbed on RF blankets synthesised with a solids content of 30% is consistently larger than for those blankets synthesised with 25 % solids.

Figures 115a and 115b, present the pore size distributions of the RF blankets synthesised with various R/C ratios at 25% and 30% solids contents, respectively. As shown in Figure 68, the mean pore size distribution varies from 5 to 50 nm in the mesopore range. For R/C ratios higher than 400, the blanket exhibits a combined meso-macropore structure with the pore size distribution shifting beyond 50nm.

The diameter peaks of the pore size distribution vary with the R/C and mass content, for the mass content of 25%, the width of peak sits at ~ 15 nm at an R/C of 300, in blankets prepared with a solids content of 30%, and R/C 400, the peak shifts to 25 nm. This deviation could be due to the effect of solids content on the solubility of the catalyst [84].

The effect of R/C ratios on the nitrogen sorption isotherms and pore size distributions of the RF blankets at other solids contents are displayed in Appendix D.

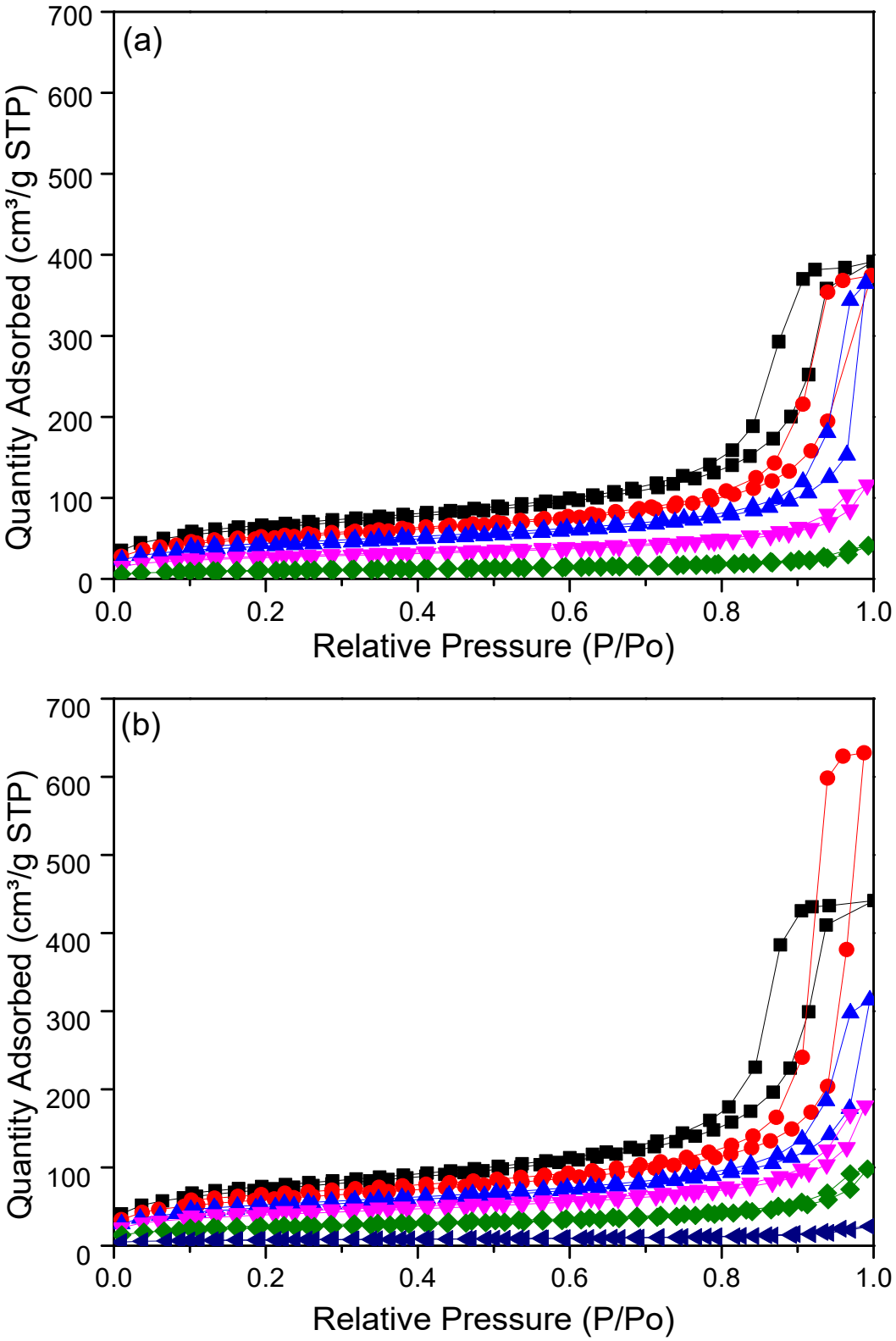

Figure 115: Nitrogen adsorption/desorption isotherms for (a) 25 % and (b) 30% solids content RF blankets, at R/C of: 300 (■), 400 (●), 500 (▲), 600 (▼), 700 (◆) and 800 (◄).

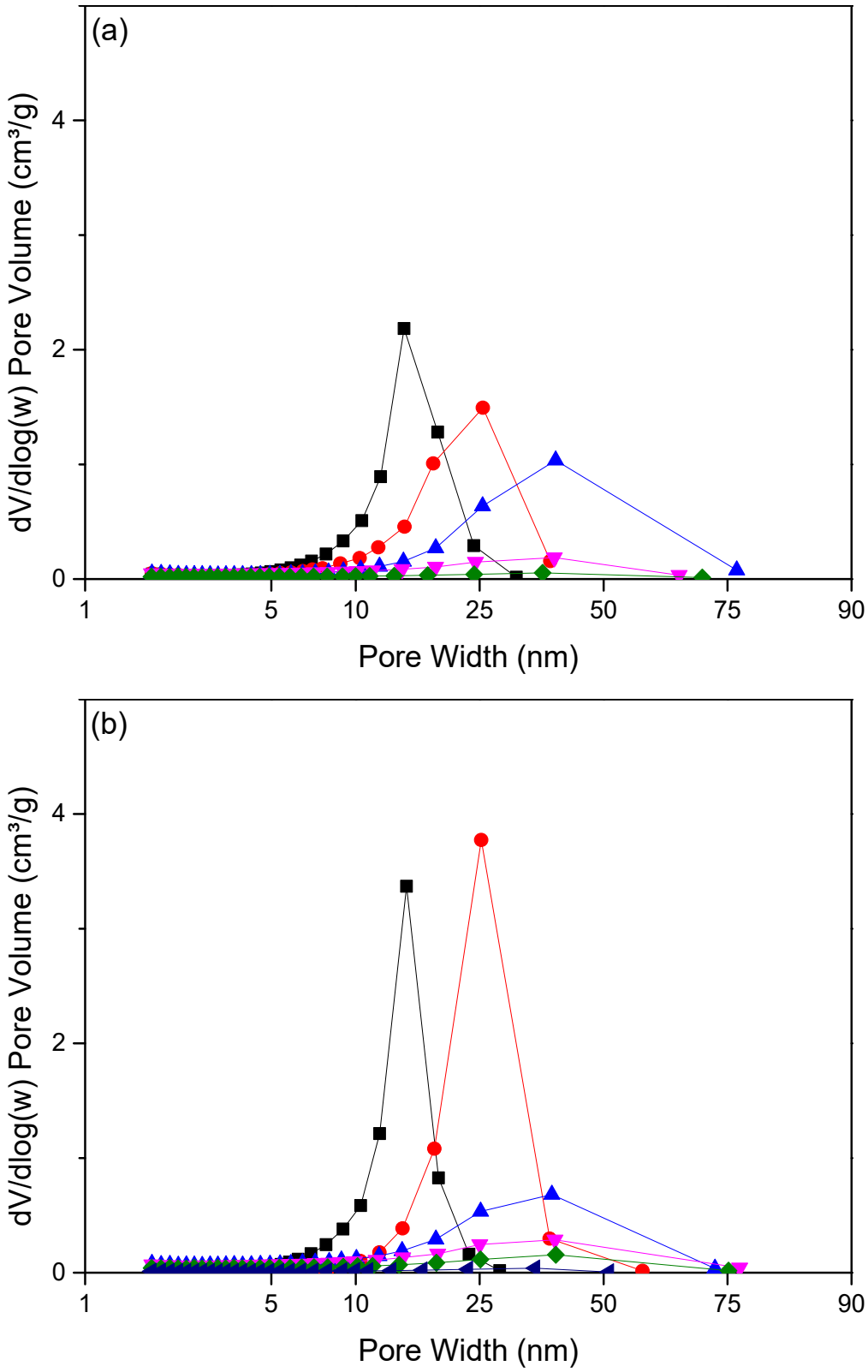

Figure 116: Pore size distributions for (a) 25 % and (b) 30% solids content RF blanket, at R/C of: 300 (■), 400 (●), 500 (▲), 600 (▼), 700 (◆) and 800 (◄).

7.1.1.2 Influence of reactants concentration (solids content)

The effect of solids content on the final structure of the RF blanket was examined at R/C ratios of 300 and 500. The results presented for the initial sol mass content, Figure 117 and 118, indicate that, although the concentration of the reactants is an essential parameter in determining final character, the RF-PET composite properties seem to be more dependent on the R/C molar ratio. As stated in Section 1.5.5, the solids content of the RF reaction solution (sol) influences the pore diameter and density of the RF gel. As shown in Table 17, for the same R/C ratio (300 or 500), the average pore diameter decreases with increasing solids content, which in turn, leads to increasing the surface area of the blanket.

Figure 117a shows that the RF blankets exhibit Type IV isotherms and the amount of N_2 adsorbed increases with increasing solids content at higher relative pressure. However, there is no significant effect from solids content at higher R/C ratios (low catalyst concentration) as depicted in Figure 117b, which is due to the limited catalysis of the high reactant concentration during the sol-gel reaction.

It can be observed that at 10% solids with an R/C ratio of 500, the blanket exhibits very low N_2 adsorption as a result of the weak, porous structure of the fabricated material. Pore size distributions of the blankets, synthesised using various solids contents are given in Figure 118. For the same R/C ratio of 300, the samples show a narrow pore size distribution. A shift towards smaller pore diameter is observed, which can be ascribed promotion of a higher number of the small particles, as a result of increased reactants concentration (see Section 1.5.5) in the presence of an alkaline media [126]. It can be seen that the pore width peak of 15 nm occurs at the highest solids content of 30%.

At low solids content, the RF blankets possess relatively high porous structure, which decreases the solid backbone thermal conductivity, resulting in lower total thermal conductivity. In contrast, low porosity (dense) RF blankets obtained via using higher solids content. Low porous blanket exhibits higher solid thermal conductance resulting from the increasing connectivity of the particles within the gel backbone. However, thermal insulating applications of the high porosity blanket could associate with some limitations such as poor mechanical properties and health issue (e.g. dust release).

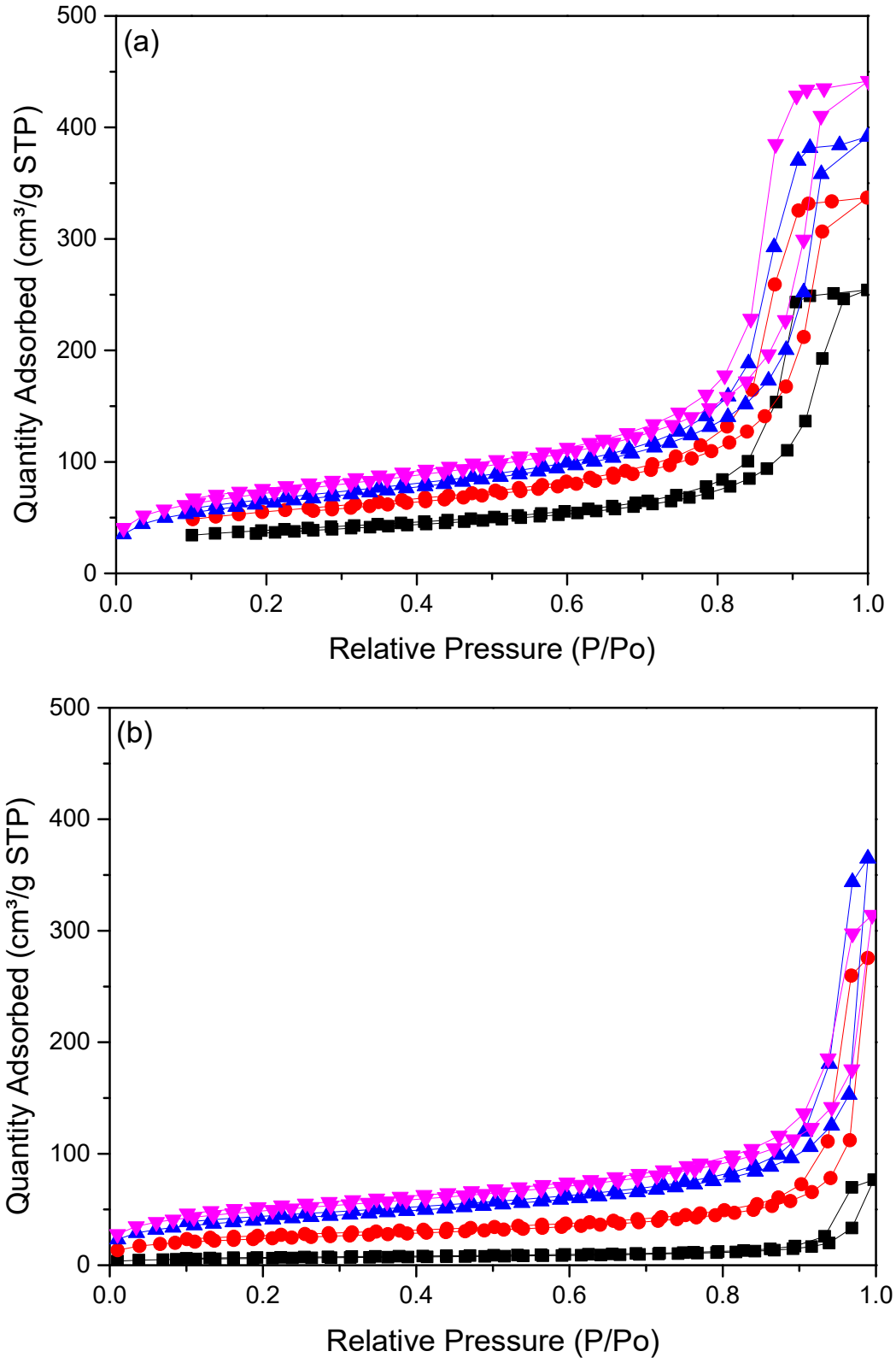

Figure 117: Nitrogen adsorption/desorption isotherms for (a) R/C of 300 and (b) 500 RF blankets, at 10% (■), 20% (●), 25% (▲) and 30% (▼) solids content.

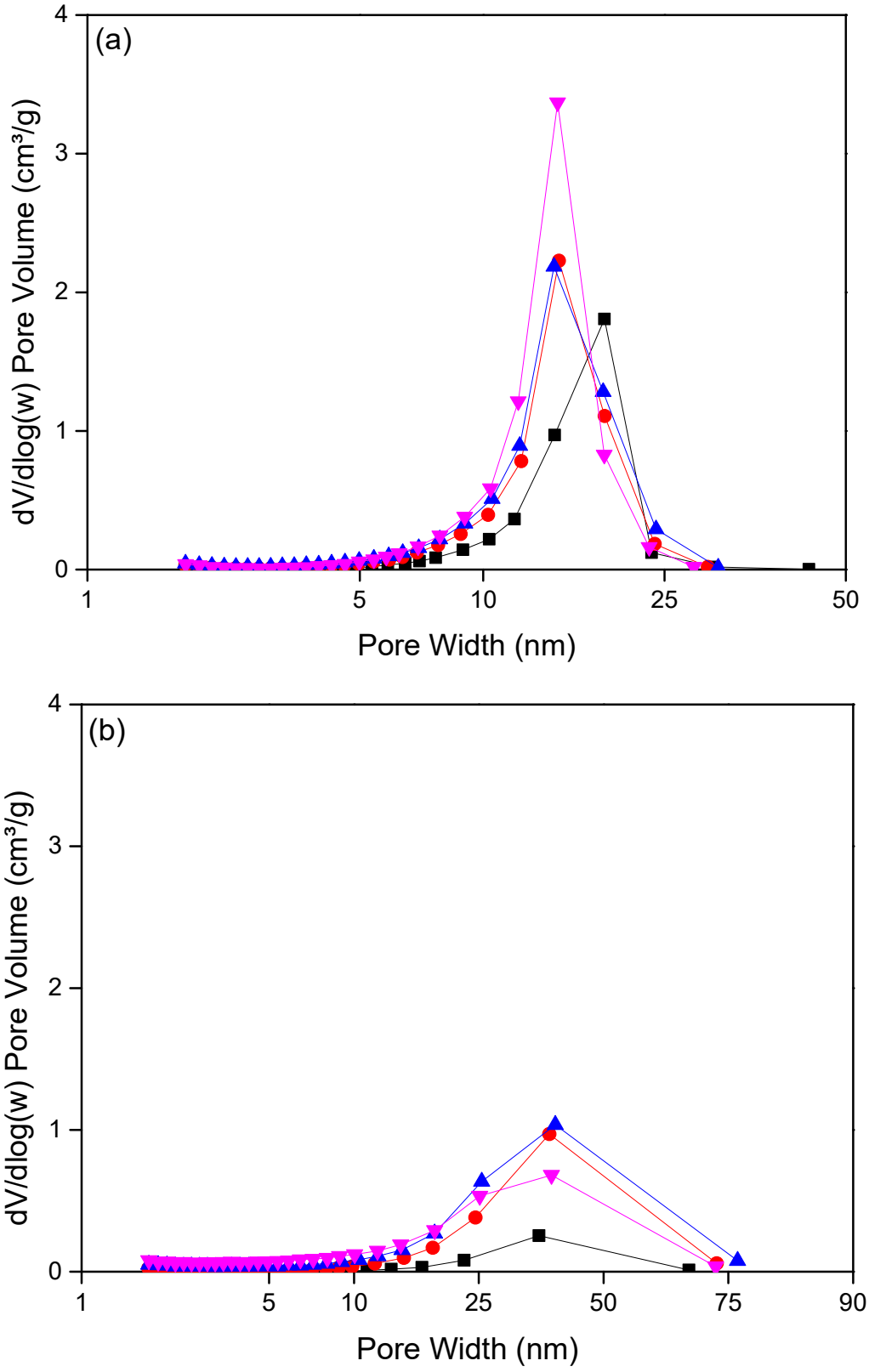

Figure 118: Pore size distributions for (a) R/C of 300 and (b) 500 RF blankets, at 10% (■), 20% (●), 25% (▲) and 30% (▼) solids content.

At higher R/C ratios, the pore size distribution shifts toward the larger pore diameters as a result of increasing the concentration of the RF reaction solution. With an insufficient amount of catalyst to activate the polycondensation reaction, large particles form, which leads to an increase in the pore diameter towards the macroporous scale. However, the largest pore diameter detected by N_2 adsorption is 76 nm, and additional modes may be required to characterise the macroporous properties of these materials fully.

Large pore structure, along with the hydroxyl groups on the gel surface influence the water adsorption on the RF blanket. Therefore, it is vital to coat or laminate the final product with water-resistant materials, to minimise the water intake by the blanket.

7.1.1.3 Type of Catalyst

K_2CO_3, $NaHCO_3$, and $KHCO_3$ were used as catalysts, in place of Na_2CO_3, to synthesise RF xerogel-type blankets. The properties of selected K_2CO_3 catalysed RF blankets are shown in Table 18. These blanket were prepared using an RF sol with 30% solids and different R/C molar ratios.

Table 18: Textural properties of RF - K_2CO_3-based catalyst xerogel blankets synthesised using various R/C ratios.

R/C	S_{BET} (m^2g^{-1})	V_{TOt} (cm^3g^{-1})	V_{Mic} (cm^3g^{-1})	d_p (nm)
		K_2CO_3		
400	171.8	0.87	0.02	22
500	131.1	0.28	0.01	16
600	78.7	0.19	< 0.01	14
700	13.1	0.03	< 0.01	13
		Na_2CO_3		
400	395.3	1.31	0.04	15
500	329.7	1.54	0.04	24
600	248.4	1.17	0.03	28
700	164.9	0.34	0.02	14

Type IV isotherms were observed for the produced blankets (Figure 119), typical for micro-mesoporous materials, except at the relatively high R/C ratio of 700, which

exhibited a Type II isotherm, corresponding to a macroporous material. As described above (Section 1.5.2), potassium salts contribute larger counter-ions (cations) than for sodium salts, which leads to an increase in gelation time. Hence the particle sizes formed are increased, producing a gel structure with a broader pore size distribution, as shown in Figure 120. It can also be seen that the pore size distributions shift towards larger pore diameters compared with those of the RF blankets catalysed with Na_2CO_3 (Figure 116b). The pore width peak can be seen at 25 nm for a relatively high catalyst concentration (R/C 400), while materials synthesised using the lower catalyst concentration show broader pore size distributions with pore width ranging from 2 to 73 nm.

By comparing the results of RF xerogels and RF blankets synthesised using K_2CO_3 as a catalyst, the isotherms obtained for the xerogels show higher N_2 adsorption capacities than for the blankets. At high R/C ratios, the blankets have broader PSDs than the xerogels. Again, this deviation indicates that the PET fibre contributes to altering the final structure of the RF blanket.

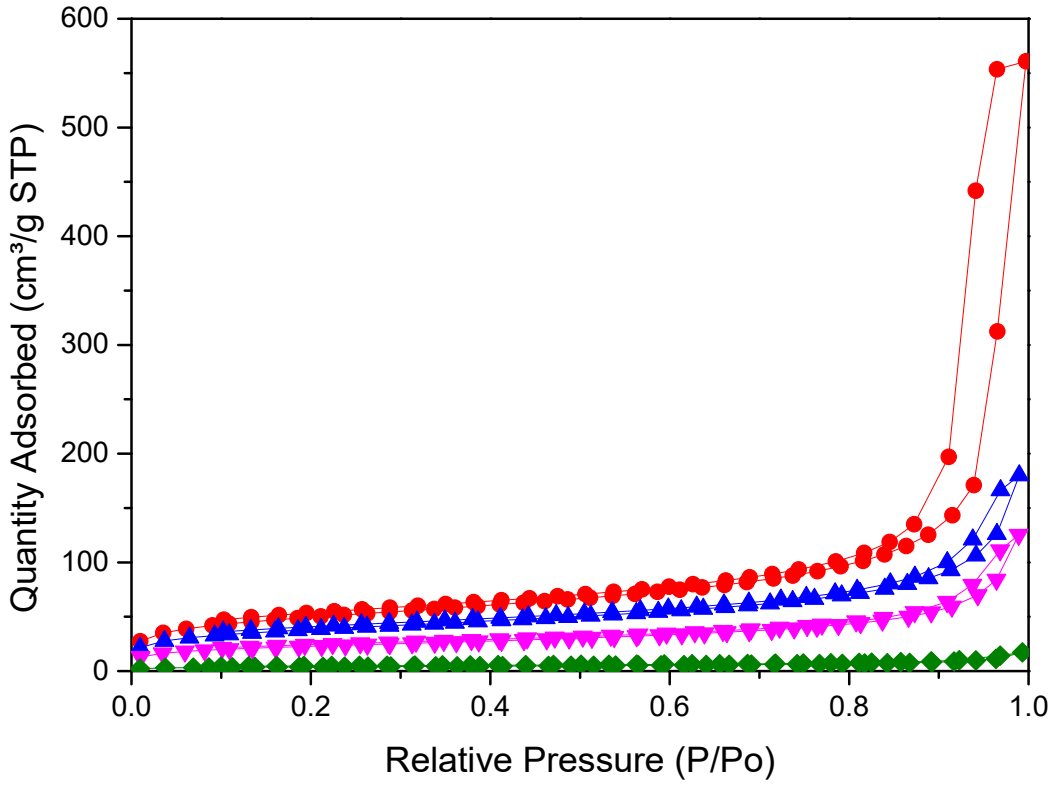

Figure 119: Adsorption and desorption isotherms of N_2 on RF xerogel blankets using an R/C ratio of: 400 (●), 500 (▲), 600 (▼), 700 (◆), K_2CO_3 used as catalyst.

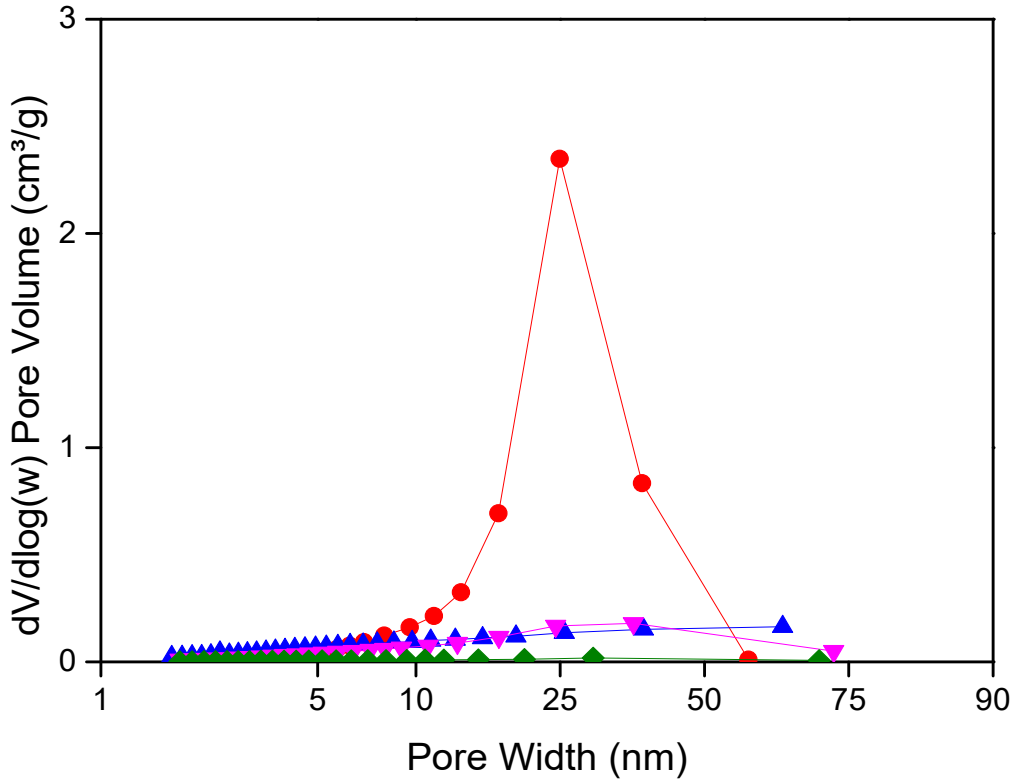

Figure 120: Pore size distribution of RF blanket prepared using RF solutions with 30% solids content at an R/C of: 400 (●), 500 (▲), 600 (▼), 700 (◆).

7.1.2 RF gel-Fibre interaction – SEM image

Scanning electron microscopy (SEM) shows the morphology of the RF xerogel-type blankets synthesised with different of both the R/C ratio and solids content (Figure 121). Observations confirmed that the RF gels had been adhered to the PET strands, as shown in Figure 121(b and c). At low R/C ratio of 300, the RF gel incorporated with the fibre strands as a bulk of gel on the surface fibre, while at the higher R/C ratio of 600, the blanket showed a lower amount of gel adhered to the fibre surface as layers or coating (Figure 121d). It can be seen that the amount of RF gel in the blanket increases as the solid contents increased (Figure 121b and c). As described in Section 6.1, the multiple contact points between the strands provided additional adhesion nodes for the RF gel, as shown in Figure 121c. However, the amount of gels between the fibre strands has been affected by the preparation procedure of this scanning method.

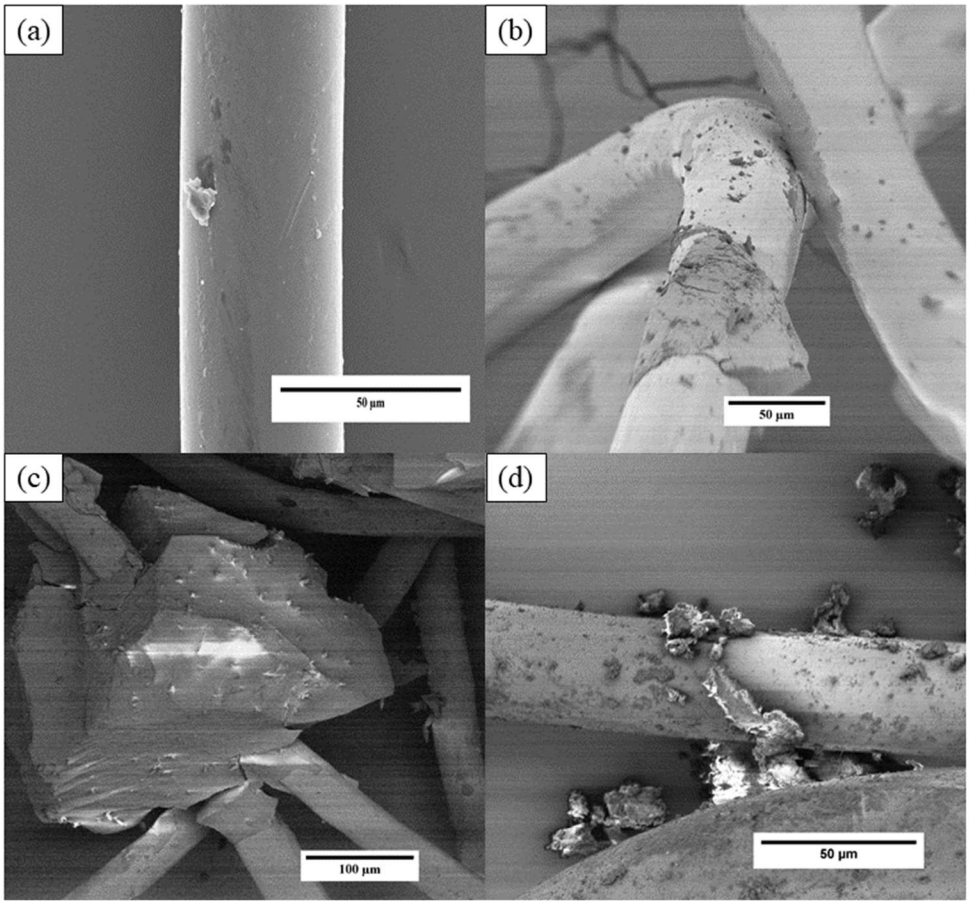

Figure 121: SEM images of RF blankets prepared using initial RF solutions with R/C – solids content of (a) Blank PET, (b) 300 – 20% and (c) 300 – 30% and (d) 600-30%.

7.2 Thermal performance of RF blankets

For samples of RF xerogel-type blankets prepared using a tuned composition of the initial RF reaction solutions, the thermal conductivities of blankets range between 0.023 and 0.032 $Wm^{-1}K^{-1}$, at standard atmospheric pressure and room temperature.

7.2.1 Influence of catalyst concentration and solids content on the effective thermal conductivity of RF xerogel blanket

As mentioned previously (Section 3.7), in porous solids, the thermal conductivity depends on four possible paths, which contribute to the total heat transport: conduction through the solid, conduction through the porous medium (gas molecules), convective transfer via the pore medium and radiative transfer from the solid surfaces. Therefore, the textural properties and the composition of RF xerogel-type blankets determine their thermal performance. The results obtained for the four series of blankets are shown in Figure 122, with values provided in Table 20.

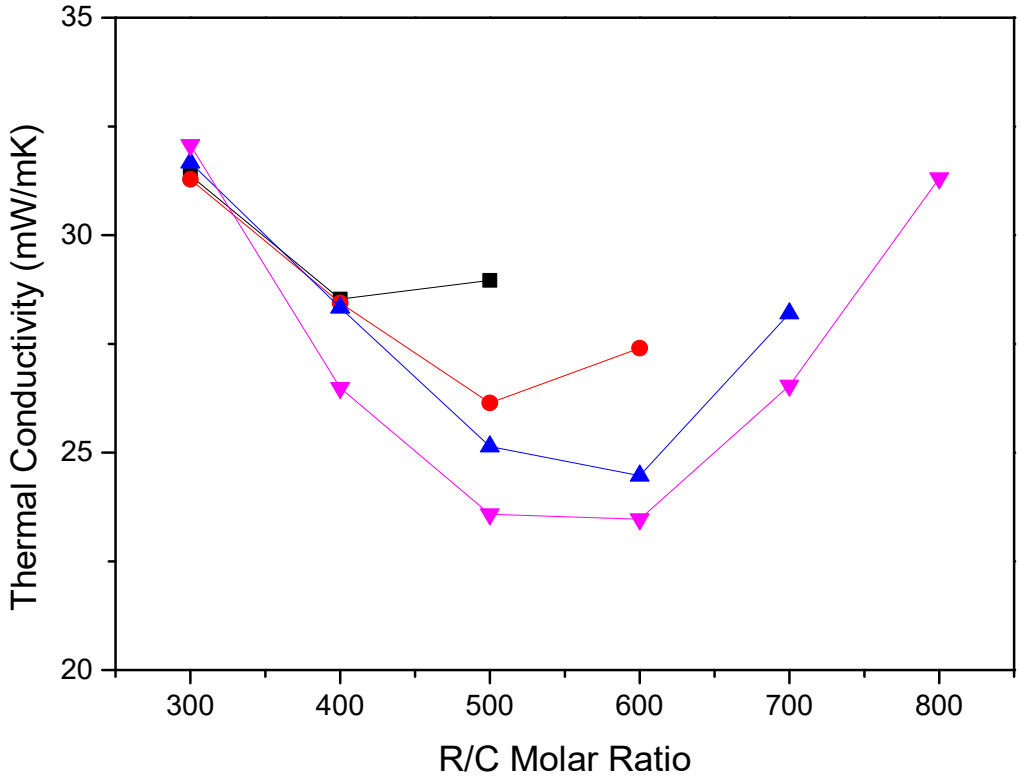

Figure 122: Thermal conductivity of RF blankets produced with different formulations: 10% (■), 20% (●), 25% (▲) and 30% (▼) solids content.

The pore size has a significant influence on the thermal conductivity by modifying the conductive and convective gas heat transfer processes, as these are dependent on the porous structure. It can be observed that the average pore diameter depends on both the R/C molar ratio and solids content (Table19). As the mean free path of the pore medium (air) is about 77 nm, it is essential to maintain an average pore diameter lower than this value. However, decreasing the pore size within the gel of the blanket leads to an increased density of the material, which contributes to increasing the total thermal conductivity.

Figure 122 shows that the RF blankets synthesised using RF sols with 30% solids at R/C 500 and 600 have the optimum thermal performance among these series of blankets. These formulations offer an average pore diameter, obtained by N_2 adsorption-desorption, in the range of 11 to 15 nm. Also, the mass fraction of the RF gel within the blanket has a significant effect on the thermal characteristics of this material (Section 5.1). Because of that, the solids content increases the uptake

percentage of the gel into the PET fibre, so the conductivity of the blanket can be reduced with increasing the solids content of the initial RF sol.

Table 19: Thermal conductivities of different series of RF xerogel blankets synthesised using various R/C ratios and percentage solids contents.

	Solids percentage			
	10%	20%	25%	30%
300	31.37	31.28	31.67	32.07
400	28.53	28.44	28.33	26.49
500	28.96	26.14	25.14	23.58
600		27.4	24.47	23.47
700			28.2	26.54
800				31.31

*Thermal conductivity at a mean temperature of 283K, 13.8 kPa compression, and ambient pressure using HFM436 Lambda

At lower R/C ratios, the thermal conductivity remains relatively constant with a slight increase at 30% solids, while ratios of 500 and 600, show a considerable decrease in conductivity with increasing solids content. For a further increase in the R/C ratio, the RF hydrogel blanket will lose some gel during the solvent exchange process reducing its mass fraction, which increases the thermal conductivity of the dried blanket.

7.2.2 Influence of resorcinol to formaldehyde molar ratio (R/F)

As described above (Section 1.5.1), the crosslinking of the RF gel could be enhanced by increasing the amount of formaldehyde within the polycondensation reaction. The promoted crosslinking can decrease the pore width of the RF gel to a micropore scale. To investigate the effect of altering the R/F molar ratio on the thermal properties of the blanket, RF blankets with various levels of this molar ratio were prepared and tested. For consistency during the comparison, the solids content and R/C ratio were held at constant values of 25% and 500, respectively. This composition was chosen to reduce the amount of formaldehyde used compared with 30% solids, as there is a small difference in performance but a significant potential saving in materials costs. The results are displayed in Figure 123, with corresponding values given in Table 20.

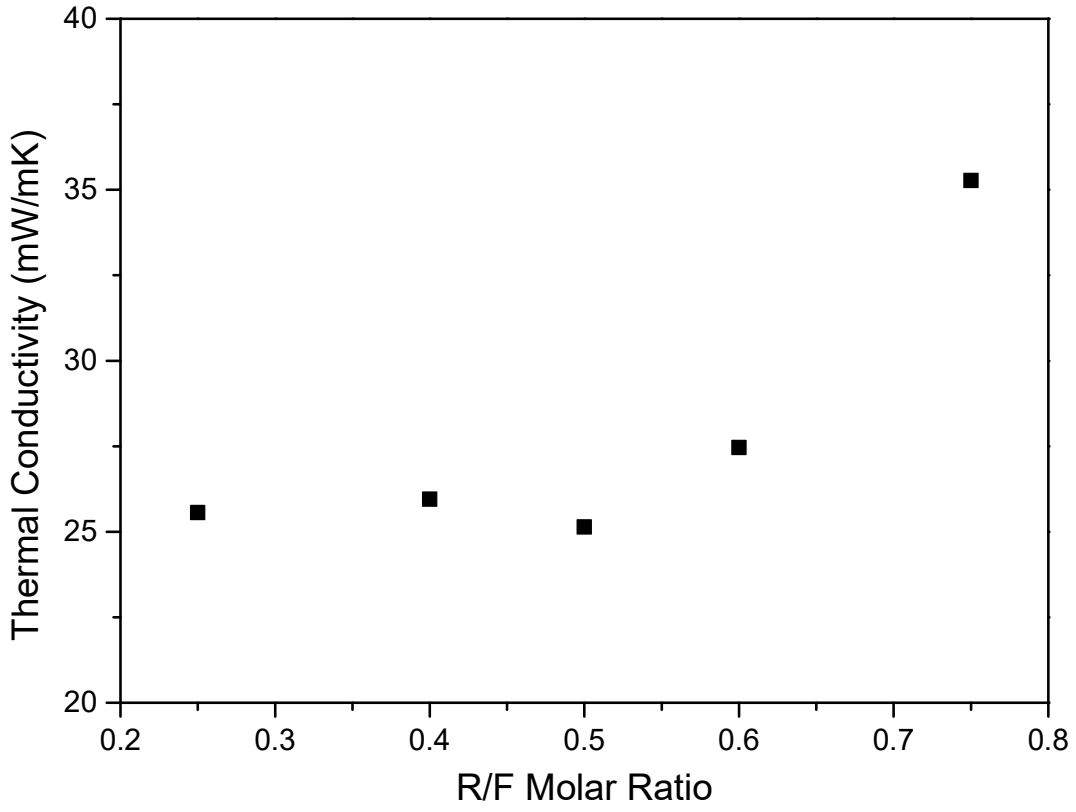

Figure 123: Thermal conductivity of RF xerogel blanket (25% solids and R/C 500) at various R/F molar ratio.

The modified formaldehyde content in the RF sol results in an increase in thermal conductivity (TC) with increasing R/F ratio, i.e. reduced quantity of formaldehyde, which relates to the weakness of the gel crosslinking as a result of the lack of formaldehyde to complete the reaction as the standard stoichiometric ratio is 0.5. In this case, large pores formed during synthesis lead to an increase in gaseous conductivity and hence increase the total TC.

Table 20: Thermal conductivity values of RF xerogel blanket (25% solids and R/C 500) synthesised using various R/F molar ratios.

	R/F molar ratio			
0.25	0.40	0.50	0.60	0.75
25.56	25.95	25.14	27.46	35.27

7.2.3 Influence of catalyst species

In order to further lower the thermal conductivity of the fabricated blankets, alternative metal carbonates were examined to catalyse the RF reaction. These metal carbonates include potassium carbonate (K_2CO_3), sodium hydrogen carbonate ($NaHCO_3$) and potassium hydrogen-carbonate ($KHCO_3$). For allowing comparison between all catalysts, used in this study, the overall solids content was kept constant at 30%. The results of this evaluation are presented in Figure 124. The actual values of TC are provided in Table 21.

As can be seen for samples prepared using sodium carbonates or hydrogen carbonates (Figure 124), the results obtained at R/C 500 or 600 are relatively identical. At the same time, at a ratio of 400 or 700, they are markedly different. For K_2CO_3, it can be observed that the TC of the blanket is only similar to those of blankets produced using Na_2CO_3 with R/C 500. The use of $KHCO_3$ as a catalyst at R/C 600, results in the blanket tending to behave thermally identical to of the blankets produced by sodium carbonate.

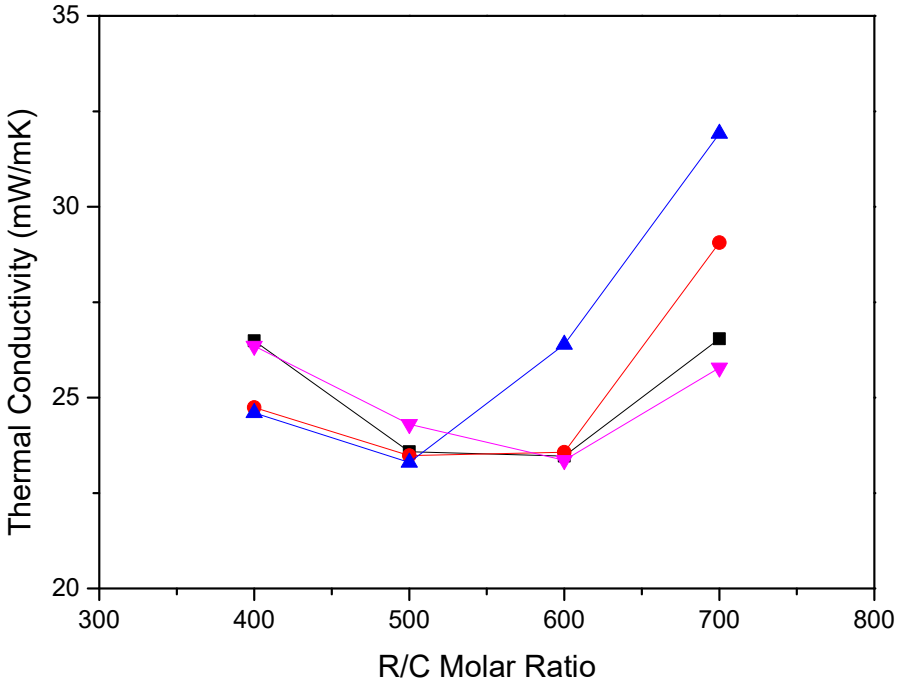

Figure 124: Thermal conductivity of RF xerogel-type blankets (30% solids) prepared with RF sol catalysed by: Na_2CO_3 (■), $NaHCO_3$ (●), K_2CO_3 (▲) and $KHCO_3$ (▼).

As described above, the counter-ion size influences the gelation time in sodium and potassium carbonates-based blankets. The difference in gelation time between these blankets has a significant impact on their final structures, thus their thermal efficiencies. The blankets produced by RF sol catalysed with low concentrations of potassium carbonate show cracks and brittle features, which might contribute to this deviation in their thermal performance (Figure 125).

Table 21: Thermal conductivity of RF xerogel-type blankets prepared using different catalyst species.

	R/C Molar ratio			
	400	500	600	700
Na_2CO_3	26.49	23.58	23.47	26.54
$NaHCO_3$	24.74	23.48	23.57	29.06
K_2CO_3	24.6	23.3	26.39	31.92
$KHCO_3$	26.35	24.3	23.36	25.78

Figure 125: RF blanket is showing the structural effects of using K_2CO_3 as a catalyst.

7.2.4 Influence of bulk density on blanket thermal performance

As illustrated above, the bulk density of the blanket can be affected by both the catalyst concentration and solids content of the initial RF solution. The bulk densities of the synthesised blankets were obtained from HFM measurements. For the parameter range studied, Figure 126 shows that the bulk density decreases with increasing the R/C molar ratio in the RF sol while maintaining a constant solids content. This tendency

differs if the solids content is modified at constant catalyst concentration, where density is found to increase with increasing the percentage of solids content. However, it can be seen that at low solids content values, the density of the blanket is influenced by the low mass fraction of the RF gel and limited gelation at higher R/C ratios. The densities of 40% solids blankets are significantly high compared to those of the super-insulating materials, i.e. silica aerogel blankets exhibit an extremely low density of < 150 kg m^{-3} [231].

For the two series of gels, presented in Figure 127, a decrease in thermal conductivity (from 32 to 24 mW/m.K) can be observed when the bulk density decrease from 328 to 280 kg m^{-3}. The thermal conductivity begins to rise as the density decreases beyond this value.

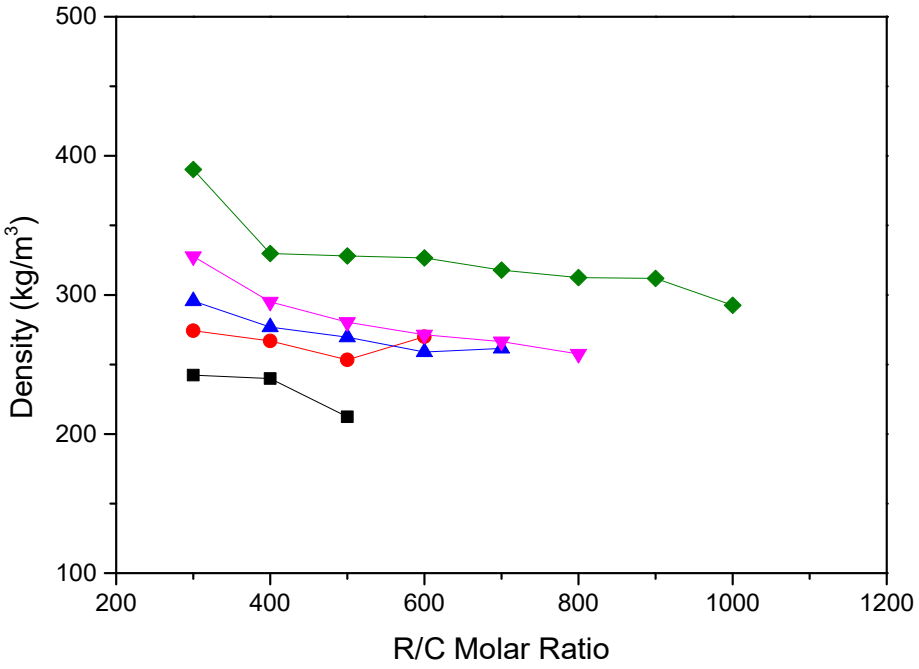

Figure 126: Effect of RF blanket composition on bulk density: 10% (■), 20% (●), 25% (▲), 30% (▼) and 40% (◆) solids content.

It can be seen that the thermal conductivity of RF blankets is not lowered further as the density decreases. However, the optimum density can be achieved at the minimum thermal conductivity value. Lu *et al*. [4] showed a similar trend for organic aerogels.

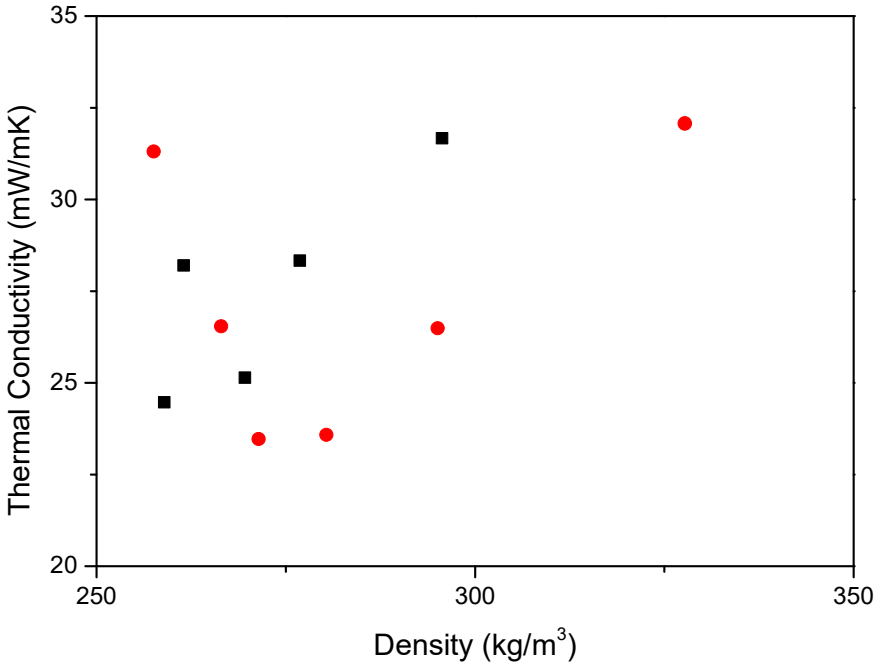

Figure 127: Total thermal conductivity as a function of density at 293 K (20 °C) for two series of RF blankets: 25% (■) and 30% (●) solids content.

7.3 Thermal stability

Thermal analyses were performed on selected RF blankets, to investigate the degradation behaviour and the temperature range in which the blanket can be used for insulation. Figure 128 shows the TG and DSC curves for both the RF composites and blank PET fibre. The phenolic thermosets are resistant to high temperature, which influences the formation of a high amount of char during pyrolysis [316].

The TG curves showed that the initial mass loss temperatures of various RF blanket samples are lower than that in the blank PET fibre, which could be due to the evaporation of the volatile materials (acetone). Above 523 K (250 °C), the DSC curve showed a melting point of the PET fibre within the composite blankets, which was confirmed by the similar thermal behaviour of the pure fabric material. At 773 K (500 °C), the weight percentage of the remaining RF-PET composites is about 27-45%, which is more than 15% PET. These results indicate that the RF gel exhibits relatively high thermal stability and intense interaction with the PET fibre.

For the blankets made with constant solids contents at different R/C ratios, the catalyst concentration could affect the thermal behaviour of the blanket. The findings revealed that the mass loss at low R/C is slightly higher than in the high R/C ratio, this figure

increased with increasing the solid content from 25 to 30% (w/v). The total mass loss of around 10 % was observed at 673 K (400 °C). The degradation phenomena of these blankets have one step up to 773 K (500 °C).

Above 673 K, the RF gel within the blanket begins to decompose with the release of water, carbon dioxide, methane and resorcinol derivatives, as illustrated in the heat flow change in the DSC curves. The significant decline in the mass of the material occurs at temperature ranges between 673-773 K.The final mass loss was recorded at 823 K (550 °C), and ranged between 55-70 %, for the tested RF blankets.

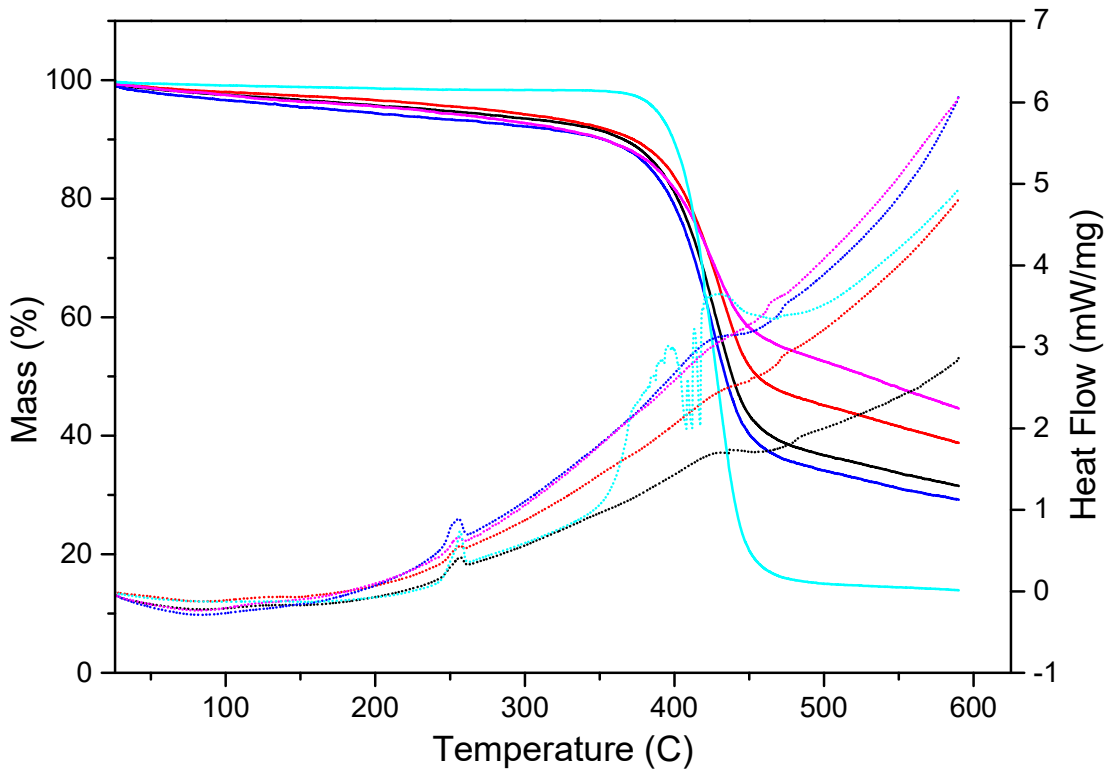

Figure 128: TG (solid line) and DSC (short dots) curves of blank PET fibre (—) and RF composite blankets prepared with various RF solutions of (R/C – percentage solids content): 300 – 25 (—),600 – 25 (—),300 – 30 (—) and 600 – 30 (—).

Since the physical properties of the blank PET fibre changed with increasing the temperature above 523 K (250 °C) in an inert gas (nitrogen), the RF-PET blankets could be used safely as thermal insulator up to 473 K (200 °C). It can be seen that the PET has enhanced the thermal stability of the RF blanket. This could be due to the effect of the fibre on the crosslinking of the gel network [43].

7.4 RF blankets – summary of findings

Several RF blankets were manufactured using various initial RF sol compositions. The synthesis parameters, including catalyst concentration (R/C), percentage solids content, resorcinol to formaldehyde (R/F) and type of catalyst were altered in a systematic pattern, to study their effects on the final properties of the blanket. For characterisation and testing these synthesised samples, methods and techniques such as N_2 sorption analysis, scanning electron microscopy (SEM), heat flow meter (HFM) and thermogravimetric analysis (TGA) were used.

The influence of R/C ratio on the structural properties of the blankets was examined through catalysed the samples, using Na_2CO_3 at an R/C of 300, 400, 600, 700 and 800 at a constant solids content. Whereas the effect of percentage solids content was investigated using different levels like 10, 20, 25, and 30% at the R/C ratio of 300 or 500. Another catalyst of K_2CO_3 was used in place of Na_2CO_3 with the R/C ratio of 400, 500,600, 700 at a solids content of 30%.

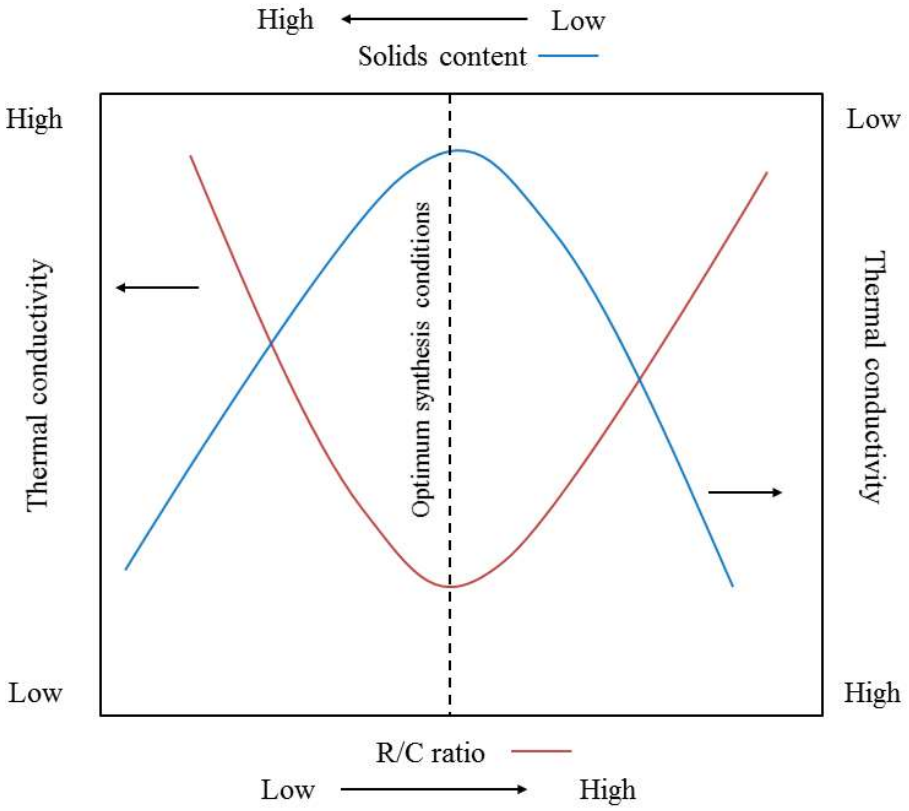

Figure 129: Effects of critical synthesis conditions on thermal conductivity of RF composite blanket.

The interaction between the RF gel and PET fibrous structure was characterised by analysing different samples: varied R/C at constant solids content and constant R/C at changed solids content. The thermal conductivities were measured for the blankets prepared using the similar formulations described above. Later, the thermal stability of both the plain PET fibre and fabricated RF blankets was analysed.

Based on the discussed results, it was found that:

- Average pore size increases with increasing R/C ratio at all percentage solids contents and the alternative alkaline used, with a corresponding decrease in micropore volume and specific surface area. However, near the limited gelation value, the pore size begins to decrease,
- Pore volume unexpectedly decreases at R/C 500 upwards; surprisingly, the pore size increases at R/C of 500, before decreasing as the value becomes close to the limited gelation,
- At constant relatively high R/C, an increase in the solids content leads to an increase the pore size and total pore volume of gels,
- Pore size decreases with increasing the percentage solids content at the same R/C ratio (300 or 500), while the pore volume increases with increasing the solids content at a constant R/C, before declining at the solids content of 30% upward,
- Potassium carbonate exhibits a different trend, the pore size/volume decrease with increasing the R/C ratio.
- Images obtained from an SEM show that the RF gels are well-interacted with the PET fibre,
- The morphology of gels on the blanket structure varies with an R/C value.
- The thermal conductivity of the blanket is strongly affected by an R/C ratio (Figure 129), with higher R/C giving low TC, but at value closes to their limited gelation, the conductivity begins to rise, while the increasing of percentage solids contents up to 30 %, at constant R/C, results in decreasing conductivity of the blanket,
- At a lower R/C ratio, there were no effects of increasing the solids content on the conductivity,

- The thermal conductivity remains relatively constant when an R/F decreases below the standard stoichiometric value of 0.5, while it increases with an increasing R/F ratio above this value,
- Sodium salts and potassium hydrogen-carbonate show very similar thermal conductivities for a given R/C at the same solids content of 30%,
- Potassium carbonate exhibits one of the lowest conductivity for the R/C 500; however, with further an increase in an R/C, the conductivity increases suddenly,
- The bulk density of the blankets is dependent on R/C ratio at a constant solids content, with lower catalyst concentrations giving a notable low bulk density.
- RF blanket exhibits the lowest thermal conductivity with a bulk density of around 280 kg m^{-3}, and
- Results from TGA showed that a small mass loss occurs as a result of releasing the water and acetone, while a higher degradation stage starts from the temperature of 673 K, reaching a mass loss of around 55-70% at 823 K.

8 Economic analysis of manufacturing RF blankets

Organic aerogels have received significant consideration with regards to their commercial development due to their fascinating thermal insulation properties [220]. Heat transfer phenomena within conventional resorcinol-formaldehyde gels have been investigated in detail. Other organic gel systems have also been described and discussed in the literature, including the investigation of their thermal properties. In general, aerogel materials can be utilised for a wide range of applications, with thermal and acoustic insulations representing around 8% of the global aerogel market in 2014 (Figure 130).

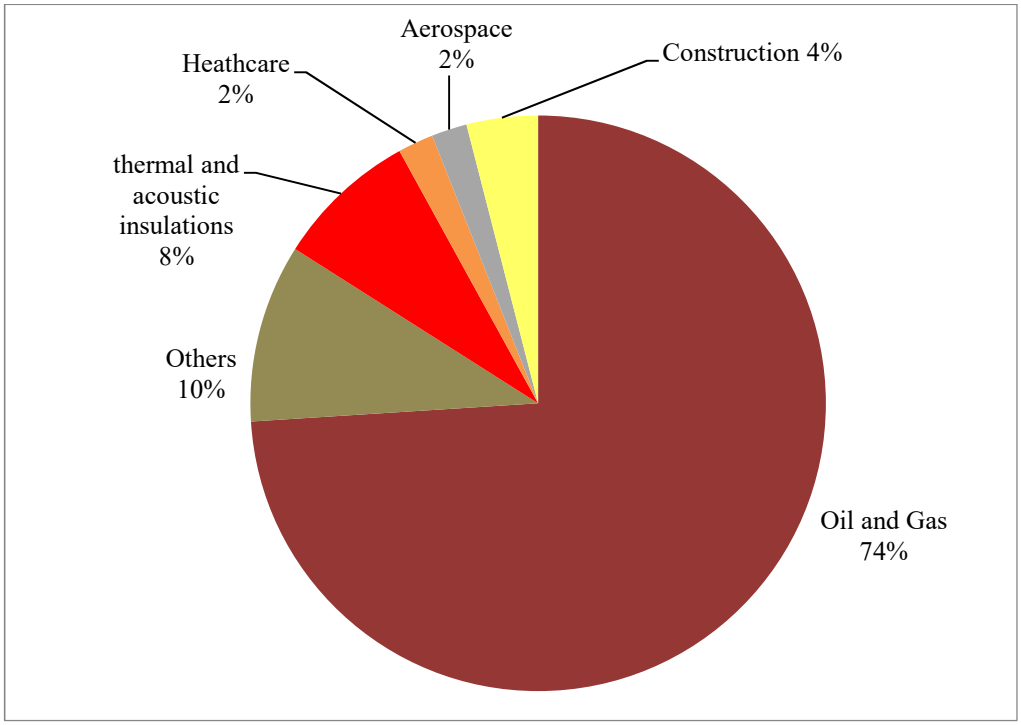

Figure 130: Global aerogel market sectors, by application, in 2014 [367].

Among the materials used in these applications, the aerogel blankets are novel high-performance materials, which can be used as thermal insulators for particular buildings and process pipelines. Aerogel blankets are synthesised as composites of an inorganic/organic aerogel and a fibrous reinforcing material, in order to enhance the mechanical properties of the final product [368]. It is crucial to perform an economic evaluation of the manufacturing process before commercialising these materials (RF blankets). As a consequence of some constraints associated with the synthesis processes used for RF gels, such as the operation method (batch), raw materials,

processing parameters, drying method and recycling, it is necessary to consider each of these issues before developing appropriate scale-up and marketing schemes. Thermal insulation aims to reduce heat loss, and consequently, a low conductivity or high resistance is the most critical property for insulating materials. The term 'R-Value' is applied, for commercial purposes, to measure the effectiveness of insulation. The R-value is a unit of thermal resistance for a single layer, of thickness *l* and thermal conductivity k, and given for flat insulation as [213]:

$$R = \frac{l}{k} \qquad \text{Equation 118}$$

8.1 Global demand for superinsulation

A higher R-value indicates better thermal insulating properties. The R-1 value is an SI standard expression, which equates to 1 m^2 K W^{-1}. This value means that the material has an R-value of 'X' when the temperature difference between two sides is 'X' degrees Kelvin and the heat flow rate through the material is given as 1 Wm^{-2} [213].

It has been realised that there was, and still is, a vital need to reduce global energy consumption and CO_2 emissions. The Chartered Institution of Building Services Engineers (CIBSE) investigated the energy efficiency of a wide range of buildings. The study reported that residential and industrial buildings (Figure 131) accounted for around half of the share of the total energy consumption of the UK in 2000. The report also indicated that burning extra fossil fuels contributes to environmental pollution via increasing CO_2 levels in the atmosphere [369]. Increased emissions, as well as limited fossil fuel supplies during conflicts and crises, coupled with an increased awareness of global climate change, has resulted in modern society developing energy strategies and policies to tackle these issues [368]. These strategies were described in detail in Section 1.7; where thermal insulation was highlighted as an essential short-term plan. Global demand for insulation has been estimated to rise 5% annually between 2013 and 2018. Table 22 illustrates the differences in global demand for insulation between 2008 and 2018 [370]

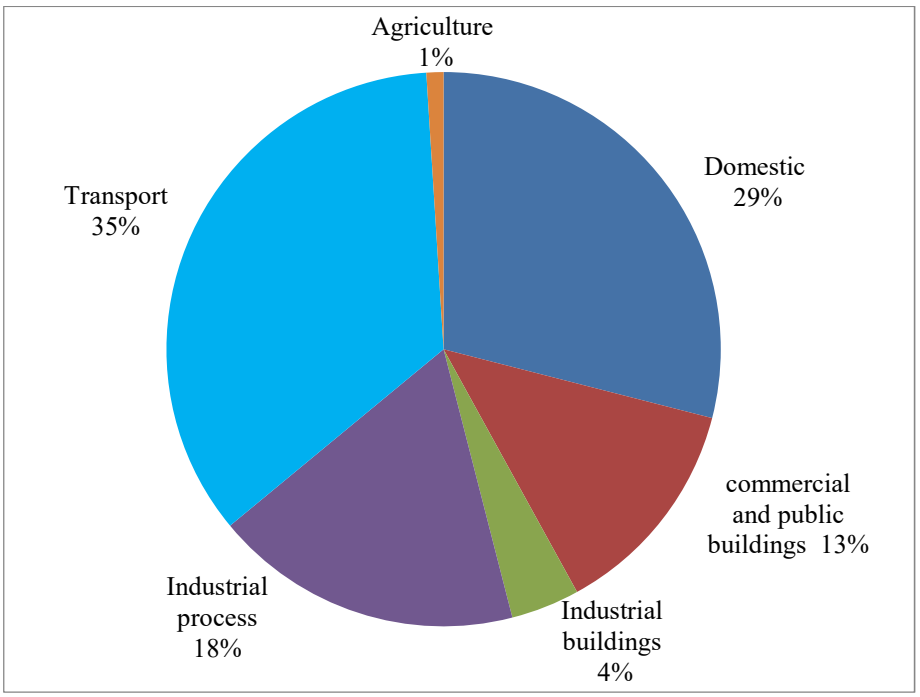

Figure 131: Total UK energy consumption by sector in 2000 [369].

As described previously (Section 1.7.3), traditional insulation materials can be classified into various types. Figure 132 shows the materials most commonly used within the insulation market. Considering significant types of insulations; mineral fibres constitute more than one of a third of the market, while foamy organic materials like polyurethane, expanded polystyrene (EPS) and extruded polystyrene (XPS) dominate the market of with a share of 44%. In 2013, the total value of the global insulation market reached ~ £22,500M [217, 370].

Table 22: World insulation demand (10^9 m^2 R-1) [370].

Item	2008	2013	2018	% Annual Growth 2008-2013	% Annual Growth 2013-2018
Insulation Demand	16430	19460	24850	3.4	5.0
North America	4578	4543	5845	-0.2	5.2
Western Europe	3934	3613	3955	-1.7	1.8
Asia/Pacific	5492	8612	11720	9.4	6.4
Central & South America	522	613	765	3.3	4.5
Eastern Europe	1005	1006	1165	-	3.0
Africa/Mideast	899	1073	1400	3.6	5.5

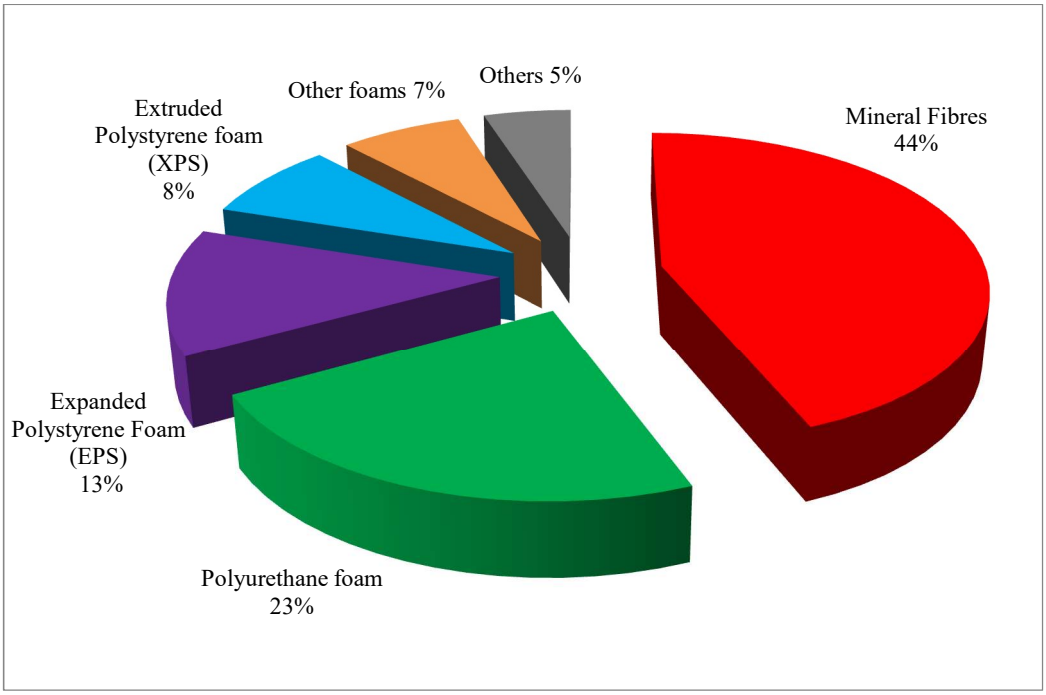

Figure 132: World insulation market by material [217].

For conventional insulating materials, thicker layers of the material need to be installed to perform effective thermal insulation, causing a space limitation. This leads to a reduction in building volumes for habitation or other purposes; hence, the demand for more effective thermally insulating materials, that are also space-saving, has led to superinsulation. Products of this type include novel technologies, such as aerogels [217, 368, 370]; however, the comparison between these insulating materials depends on material performance and cost of production concerning market share. Figure 133 shows that conventional insulating materials dominate the market as they offer an optimum rate of performance per cost; however, the expectations show a small increase in cost and a drop in market share. Low-cost products generally demonstrate poor performance and stability, and their situation will not markedly change. Contrastingly, super-insulating materials would lead the global market soon, as a result of their high performance, outstanding features and potentially reduced cost [217]. RF xerogel-based blankets exhibit insulating efficiencies that are slightly lower than that of superinsulation. Consequently, it is essential to perform strength, weaknesses, opportunities and threats (SWOT) analysis for RF blankets, before evaluation of the products at the industrial scale.

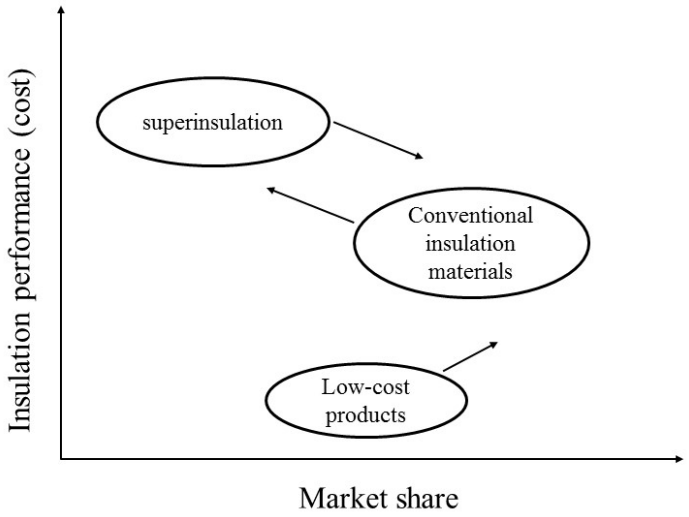

Figure 133: Correlation between cost/performance and market share in the insulation industry, arrows show expected future development of each category in future [210].

8.2 SWOT analysis

The SWOT analysis is the first stage in the evaluation of any process or business. It is a useful tool to understand the strengths and weaknesses of the process, and to identify both the opportunities and threats in the surroundings. This analysis includes the results of an internal appraisal, which determine the strengths and weaknesses of the process compared to competitors, and also from an external appraisal, which in turn determines the opportunities and threats of the process within the existing market [371, 372]. Once these factors are identified, strategies can be developed to enhance the aspects of the process before conducting detailed economic analysis.

Table 23: Comparison of performance for various thermal insulating materials [368].

Material	Thermal conductivity mW/m.K	Minimum improvement (reduction) in conductivity over brick or stone
Brick or stone	600 – 2500	-
Natural insulation materials	30 – 50	20
Mineral insulation	30 – 40	20
Layered foil	33 – 35	18
Organic insulation materials*	20 – 40	30
Aerogels	13 – 14	42
Vacuum-insulated panels	4 – 10	60

* RF xerogel blanket can be considered as an organic insulating material

SWOT analysis for the manufacture of RF xerogel blankets is shown in Figure 134. The results show one strength to be their high insulating performance (Table 23); however, a threat is an emergence of similarly performing competitive products (silica aerogel blanket) into the insulation market. Hence, further RF blanket developments are necessary before integrating this product into the market, where increasing global demand for super-insulating materials could open up opportunities for this product. The long production time is a weakness, which can be improved using controlled synthesis conditions, and subcritical drying can contribute to a reduction in processing time compared to existing processes. Other weaknesses, such as scarcity of scaled-up plants and previous experience on trade could be improved by using pilot plants and data from potential competitors. However, the safety issues such as the flammability and toxicity of the materials used in the synthesis of the RF blanket could represent potential hazards at the workplace.

STRENGTHS	WEAKNESSES
• Low thermal conductivity • Lightweight material • Good mechanical properties • No dust release • Cheap raw materials • Simple process equipment	• long processing time • Batch process • Low production • lack of previous trade experience • No scaled-up process • Some health and safety issues (e.g.Flammability, toxicity)
OPPORTUNITIES	**THREATS**
• Simple synthesis route • High demand for superinsulation • Social awareness about energy consumption and CO_2 emissions	• Integration into the market • Insulation market competition • Unstable economic • Resources of raw materials

Figure 134: Schematic SWOT analysis for the manufacture of RF xerogel blankets.

8.3 Production cost analysis of RF blanket

As mentioned above, the most critical barriers to commercialising RF blankets are the lack of scaled processes and the unpredictability of processing costs. As a result, the production cost of an RF blanket is estimated by considering the data available for the production costs of RF aerogels. However, the overall costs of processed RF xerogel blankets are expected to be much lower than those of RF aerogels, because of cheaper

drying methods used in the manufacture of blankets. Carlson *et al*.[86] conducted an economic analysis of the production costs of various aerogel materials. The study classified the cost analysis into five parts: raw materials, energy, utilities, workforce, and equipment. Their production costs analysis was applied to aerogels for thermal insulation applications. Therefore, their work has been adopted here to evaluate the essential areas of cost production for RF blankets.

Carlson and his co-workers simplified their assumptions for the cost estimation of the considered products. They applied a cylindrical steel autoclave for supercritical drying, and utilised volume was estimated as ~ 80% of the total internal volume of the vessel. Also, it was assumed that the plant would operate five days a week, with 22 days monthly as the standard, in a batch process. Finally, all produced materials were assumed to be free of defects [86]. The original study was conducted during the austerity period of the mid-1990s.

8.3.1 Raw materials

As per the adopted study, the costs of raw materials were based on the most substantial total quantity ordered (>10 tonnes), so the lowest cost that could be obtained. Table 24 shows the summary of raw material costs used by Carlson *et al.*; for supercritical extraction of solvent in an autoclave, methanol and carbon dioxide liquids were used to process silica and organic aerogels, respectively.

Table 24: Starting material costs, USA 1995 [86].

Material	Cost (£/kg)*
Methanol	0.22
Tetramethoxysilane (TMOS)	8.15
Tetraethoxysilane (TEOS)	2.99
Sodium silicate	0.59
Resorcinol	3.99
Formaldehyde	0.21
Phenol	0.68
Melamine – formaldehyde (R714)	2.14
furfural	1.12

* The cost was converted to the UK costs based on the exchange rate as at 1995 (January) [373].

It was assumed that the required volume of methanol was calculated as a sum of the utility volume of the autoclave plus the additional volume required to alter the final density of the product. On the other hand, carbon dioxide was used to extract the solvent from RF aerogels, as it is safer than methanol (due to flammability and health hazards of methanol). Other additional materials (e.g. wash solvents, catalysts, cooling water) required for the process were excluded in the original analysis [86].

8.3.2 Energy

Energy costs are expected to represent a considerable proportion of the aerogel production costs, as a result of the supercritical extraction process, which utilises the energy in three different areas: supercritical extraction of methanol, autoclave heating, and heat losses to the environment. For supercritical extraction, using methanol as a solvent, the study assumed that the energy consumed to pass 1 L of methanol into the autoclave is less than 2 MJ, with an energy cost of ~ £0.02/MJ; however, 50% of this value was required when CO_2 liquid was used as a solvent for organic aerogels. The energy required to heat the autoclave was based on the number of batches per day. The unit amount required by one batch per day is higher than that for two batches per day, etc. [86].

8.3.3 Workforce

Carlson and his group proposed that three shifts per day be estimated [86], with ten workers of people allocated over the three shifts. They assumed that the first shift was staffed by six persons, with subsequent shifts manned on a two-person basis. The total weekday costs were estimated to be ~ £1429.

8.3.4 Utility costs

Utility costs were estimated for lighting the industrial buildings with a monthly cost of ~ £650/month for a 600 m^2 property [86].

8.3.5 Equipment

Total fixed capital costs were estimated for the major equipment (autoclave) cost. Three different capacities of the cylindrical steel autoclave systems were selected: 856l, 1920l and 6849l. The cost estimates were £0.52M, £0.90M and £2.26M,

respectively. Amortisation, over five years with an annual interest rate of 10% gives daily costs of £500, £870 and £2180, respectively.

8.3.6 Cost distributions

The production cost areas can be fully appreciated by plotting the results obtained from Carlson's research [86]. The cost variables investigated were the cost of raw materials, major equipment size, number of shifts per day, product density, utility volume of the autoclave, and initial testing of alcohol recycling. Aerogel costs were calculated based on £/m^3 (all costs were converted to UK costs based on the rate of exchange as at January 1995) [373]. However, the costs of raw materials and workforce from different years are not straight comparable, as they are subjected to the rate of inflation. The most straightforward method to update the historical data is by using the cost indices, as given as [374]:

$$c_j = c_i \left(\frac{I_j}{I_i}\right) \quad \text{Equation 119}$$

where c_j and c_i indicate the costs in year j and i respectively, and I_j and I_i refer to the cost indices for the corresponding years.

The selected parameters were the small autoclave, three shifts per day, a density of 100 kg m^{-3} and 80% volume utility.

Cost distributions for the organic aerogels are shown in Figures 135 and 136. It can be seen that the phenol-furfural monomer results in a decreased contribution from the starting materials to the total costs.

Table 25: Aerogel estimated costs [86].

Material	Aerogel Cost (£/m^3)*
TMOS	2149
TEOS	1127
Sodium silicate	171
Resorcinol – Formaldehyde (RF)	364
Phenol-Formaldehyde (PF)	114
RF: PF (50:50)	242
Melamine – formaldehyde	310
Phenol – furfural	198

* The costs were converted to the UK costs based on the exchange rate as of 1995 (January) [373].

Table 25 shows a summary of the aerogel production costs per cubic metre with the following parameters: density of 100 kg m^{-3}, 90% solvent recycling, three shifts, large autoclave, 80% volume utilisation and 50% energy costs for organic aerogels. The costs for phenol-formaldehyde aerogels were estimated as the lowest value among all aerogels investigated in the study, which was based on the low costs of precursors, as illustrated in Table 25. From Table 25, the aerogel costs showed that materials made from less expensive raw materials are projected to be close to the price of the existing foamed polymers [86].

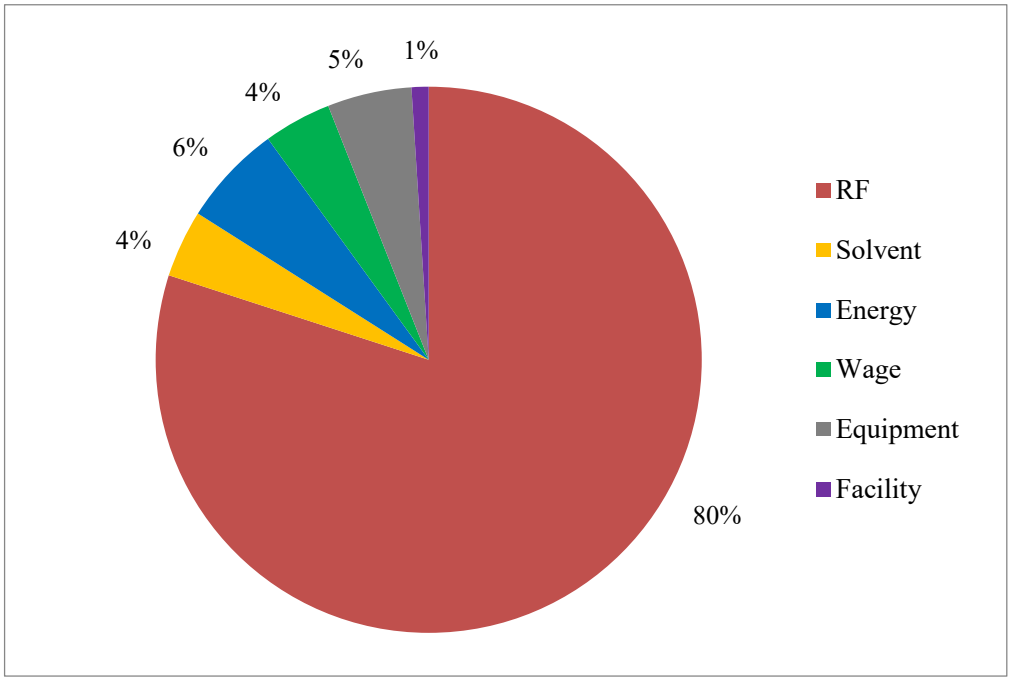

Figure 135: Cost distribution for organic aerogel to six variables, using resorcinol – formaldehyde as the precursor (relatively optimised costs) [86].

Carlson and his group performed this economic analysis for selected aerogel materials. The study was only a first estimation and omitted many parameters that could be involved in a more detailed analysis. It can be observed that the cost of the starting materials is the dominant factor in the cost of aerogel material, so the laboratory scale should be focused on less expensive raw materials. Also, the authors mentioned that, as a result of their low thermal conductivities, the aerogel materials are expected to be cost-effective in the future [86]; however, these materials require further development, and improved economic analysis, to evaluate the potential of taking the products to the market.

According to the report discussed above, RF xerogel-based blankets can be fabricated with a significant decrease in production costs, mainly due to the exclusion of expensive supercritical drying methods from the processing of the RF aerogel, hence, the cost estimate.

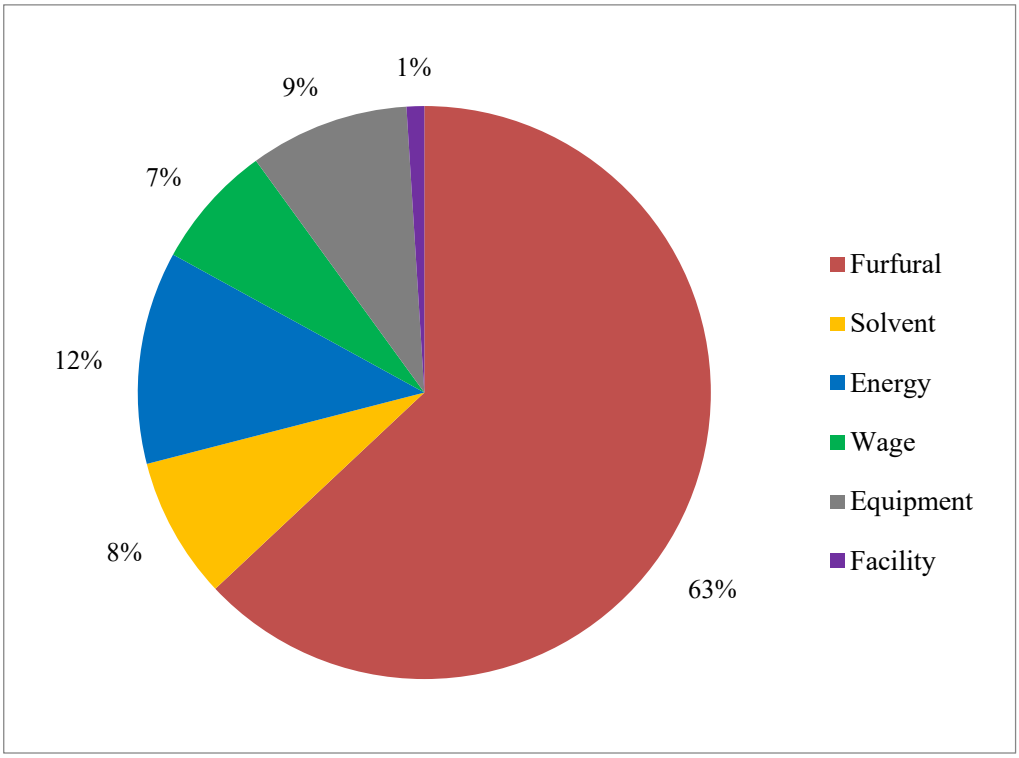

Figure 136: Cost distribution for organic aerogel for six variables using phenolic - furfural as the precursor (relatively optimised costs) [86].

8.3.7 Cost estimation of laboratory-scaled RF composite blanket

As it was not possible to find industrial-scale manufacture of RF composite blankets, laboratory-scale of these materials was studied in order to estimate their production cost. The produced samples were in the size of 18cm×18cm×0.6 cm, so the number of precursors used for the preparation of an RF solution was calculated from these dimensions. The estimation also includes the PET fibre mat, acetone used for solvent exchange, energy used for heating and drying, as well as packaging and waste disposal.

The synthesis conditions of an RF solution with solids content of 30%, Na_2CO_3 as a catalyst, and R/C ratio 600 were chosen. The cost estimation was performed for the individual parts, such as the raw materials and energy, as shown in Table 26 and Table 27. The total cost of the RF blanket sample was estimated by summation of these costs.

For energy consumption, the electricity running costs from the UK Power [375]was adapted. There were some assumptions for energy as:

- Mixing: electricity usage of the device assumed to be 100 W, with a working time of one hour,
- Heating: Oven electricity power used of 1000W, with a working time of 72 hours, and
- Vacuum drying: electricity usage assumed to be 2000W, with a working period of 16 hours.

The cost of packaging and waste disposal were not considered, as the cost of packaging (plastic bag) is minimal compared with the cost of raw material and energy consumed, while there was no data regarding waste disposal cost.

The data of the raw materials prices and suppliers are included in the Appendices (E).

Table 26: Total cost of raw material to synthesis lab-scale RF blanket.

Raw material	Amount (unit/sample)	Cost of raw material (£/unit raw material)	Cost £/sample
Resorcinol	34.91 g	0.08	2.80
Formaldehyde solution	47.20 ml	0.03	1.42
Sodium carbonate	0.07 g	0.10	~ 0.01
Acetone	600 ml	2×10^{-3}	1.2
PET Fibre	194.4 cm^3	6.08×10^{-5}	0.01
Deionised Water	156.20 ml	1×10^{-3}	0.16
Total	-	-	5.60

Table 27: Proposed energy consumption for lab-scale RF blanket.

Energy	Amount (kWh/sample)	Cost of energy (pence/kWh)	Cost £/sample
Mixing	0.1		0.15
Heating	72	14.899	10.73
Vacuum drying	32		4.77
Total	-	-	15.65

The total cost of a lab-scale RF blanket is about £ 21.25 per sample; however, for industrial-scale production, the cost of the raw material can be much lower than that of the lab-scale. Hart and Sommerfeld [376] proposed a methodology to predict bulk selling price using the laboratory-scale prices. They reported that chemical bulk prices could be much lower than the laboratory-scale prices. The implementation of the method in this study requires data for prices of different chemicals at both lab and bulk quantities.

8.4 Health and safety issues related to RF blanket production

Preparation of the RF xerogels and their composites involves using hazardous (e.g. toxic, flammable) substances. Hazards could arise as a result of exposure in the form of inhalation, ingestion or skin/eye contact, which may result in different consequences such as irritation, severe burns, or in the extreme case, cancer (in long term exposure). RF xerogels synthesis also comprises hazardous associated with the processing stages such as hot surfaces, electric appliances, sharp tools, and fragile glassware.
The substances used in this process are mainly resorcinol, formaldehyde, and acetone.

From a health and safety standpoint, resorcinol is more slightly toxic than phenol. Hazards could occur as a result of exposure to resorcinol through different routes such as oral, dermal or respiratory tract. Resorcinol is harmful if swallowed, an irritant to eyes and skin, and very toxic to aquatic life [377, 378]. The toxicological effects are related to dose, as presented in Table 28.

Table 28: Toxicity data for Resorcinol [378].

Route and measurement unit	
LD50 oral rat, mg/kg	510
LD50 dermal rabbit, mg/kg	2830
TWA* workplace exposure limit, mg/m^3 (ppm)	46 (10)
LC50 fish	29.5 mg/l – 96 Hours
EC50 Green Algea	> 97 mg/l – 72 Hours

* Basis in the UK. EH40 WEL- workplace exposure limit [379].

For handling resorcinol, appropriate personal protection equipment (PPE) and ventilation can significantly reduce the likelihood of the hazards associated with this substance. Due to the high toxicity of resorcinol to aquatic life, strict waste control policies must be adapted [380].

Formaldehyde is a flammable gas at room temperature but is usually supplied in solution (formalin), it is highly reactive, toxic (if swallowed), and an irritant for skin and eyes [381]. The toxicological effects of formaldehyde are listed in Table 29.

Table 29: Toxicity data for formaldehyde [381].

Route and measurement unit	
LD50 oral rat, mg/kg	800
LD50 dermal rabbit, mg/kg	270
TWA* workplace exposure limit, mg/m^3 (ppm)	2.5 (2)

* Basis in the UK. EH40 WEL- workplace exposure limit [379].

For handling formalin, appropriate personal protection equipment (PPE) and ventilation can significantly reduce the likelihood of the hazards associated with this substance. Release to the environment must be avoided.

Acetone is a flammable liquid, mainly irritant affecting the eyes and respiratory tracts. It has narcotic effects when inhaled or digested. Table 30 presents the toxicity data of acetone.

Table 30: Toxicity data for acetone [382].

Route and measurement unit	
LD50 oral rat, ml/kg	10.7
LD50 skin penetration rabbit, ml/kg	> 20
TWA* workplace exposure limit, mg/m^3 (ppm)	1210 (500)

* Basis in the UK. EH40 WEL- workplace exposure limit [379].

Acetone requires to be handled in a well-ventilated area. Vapour inhalation, eye and skin contact must be avoided. As this substance evaporates rapidly, it should be stored in a cool place and away from heat sources. Appropriate personal protection equipment (PPE) should be worn.

8.5 Methods toward low-cost RF blanket production

From the case study presented above and the SWOT analysis data obtained here, it is evident that an economic analysis of RF blanket synthesis needs to be conducted concerning different criteria:

(a) Raw material costs have a significant effect on the total cost of the product, so it is vital to consider inexpensive alternatives to prepare other blankets with comparable performances to RF based-composite blankets.

(b) The prolonged processing time could affect the costs of materials by increasing the number of shifts per day and, hence, the wage/salary rate of the staff. The very long manufacturing process could also influence the rate of production.

(c) The solvents used to represent an essential factor in the cost analysis.

(d) Energy consumption due to gelation/curing and drying of the hydrogel-PET blanket.

(e) Drying methods.

Some strategies can be assumed for the future development of cost-effective materials.

8.5.1 Using inexpensive alternative precursors

Costs of raw materials can be reduced by using alternative organic monomers that are cheaper than resorcinol. From the chemical viewpoint, resorcinol (R) has various prospective analogues, primarily phenolic compounds including phenol and cresols. Formulas of some hydroxybenzoles are given in Section 1.3.1.

Phenol is probably the most commonly used substance among the wide range of phenolic materials. It can undergo the polymerisation reactions typical of R, but its reactivity is much lower than that of resorcinol. To increase the rate of reaction, sodium hydroxide NaOH can be used as a catalyst in place of Na_2CO_3. The reactivity can also be modified by adding other precursors such as phloroglucinol [383]. Phenol can also be used with R to prepare RF: PF gels, in order to reduce the costs of raw materials [86].

Cresol or mixtures of cresol are other monomers used in the literature to synthesise organic gels [77]. These monomers are almost four times less expensive than R. The difference in synthesis parameters between cresol-formaldehyde (CF) and RF gels is in the catalyst used, NaOH for CF (as for PF), instead of Na_2CO_3. However, the solubility of cresol mixtures in water is lower than that of R. Using higher amounts of the basic catalyst is essential in increasing the solubility of these substituents in water [383].

Furfural-based aerogels could add some benefits of eliminating formaldehyde, as it can be produced from bio-fuel based method, thus reducing the level of the environmental impact associated with this process [86, 90].

8.5.2 Some approaches for shortening gelation and curing times

As discussed above (Section 6.1), the gelation time is mainly influenced by the solids content percentage and can be shortened at low R/C ratios. Different strategies can also be applied to shorten the gelation and curing times.

The gelation time can be drastically reduced by using an acid catalyst such as highly concentrated hydrochloric acid (HCl) [134, 384]. It has been reported that the synthesis process for RF gels can be accelerated by the further addition of acetic acid or Na_2CO_3 into pre-reacted RF sols [385]. Recently, a novel method has been developed to maintain the porosity of RF gels during drying. RF gels were synthesised using Na_2CO_3 as a catalyst and polydialyldimethylammonium chloride (PDADMAC) as a cationic polyelectrolyte. During this process, it was observed that the gelation and curing times were substantially shortened [386]. Another strategy used to reduce the gelation times is to perform the polycondensation step under ultrasonic waves. It has

been found that the ultrasound leads to an increased rate of reaction and decreases the gelation time [387, 388].

8.5.3 Solvent recycling

Acetone, used in the solvent exchange process, is a significant source of waste and costs in the synthesis of RF xerogels/blankets. On the industrial scale, waste acetone can be reused from the solvent exchange. The recovered solvent could be distilled using an automated commercial unit [389]. Considering the purity of the waste-acetone solvent, which could be reused directly within the process and as a cleaner for process equipment. Although the initial costs of the solvent recycling system are significant, due to the cost of the commercial recycling unit, the operating costs of this system are minimal compared to the other costs of production.

8.5.4 Alternative cheap drying methods

The drying process is one of the most critical steps in the preparation of RF aerogels because of its effect on the final porous structure of RF gels. For RF xerogels, subcritical methods are used to process these materials. A straightforward method can be utilised to dry the wet gel, which is based on the evaporation of the solvent at ambient conditions [383]. However, the porous structure will collapse, as a result of increased capillary forces (Section 1.5.10). The RF xerogel-based blankets were synthesised by reinforcing the RF gel using PET fibres, which could enhance the mechanical strength of the structure. Consequently, ambient drying could be used in manufacturing RF blankets with a lower rate of collapse within their final textures.

8.6 Life-cycle assessment of RF composite blankets as thermal insulation materials

Manufacturing, application, and disposal of materials, heavily contribute to curtailing resources and reserves, and to the other environmental issues such as climate change; which represents a significant issue to all species in recent decades. Awareness of the importance of environmental protection and impending issues associated with products both manufactured and used has raised the focus of the development of techniques to understand better and tackle these impacts. One of the methods being developed for this reason is life cycle assessment (LCA). It is a tool used to determine the potential environmental impacts of a given product over its entire life cycle (Figure

137). LCA involves considering and interpreting the material and energy inputs, as well as the environmental consequences of outputs, throughout a complete life cycle of the product from the acquisition of the raw materials to end of life [390-393].

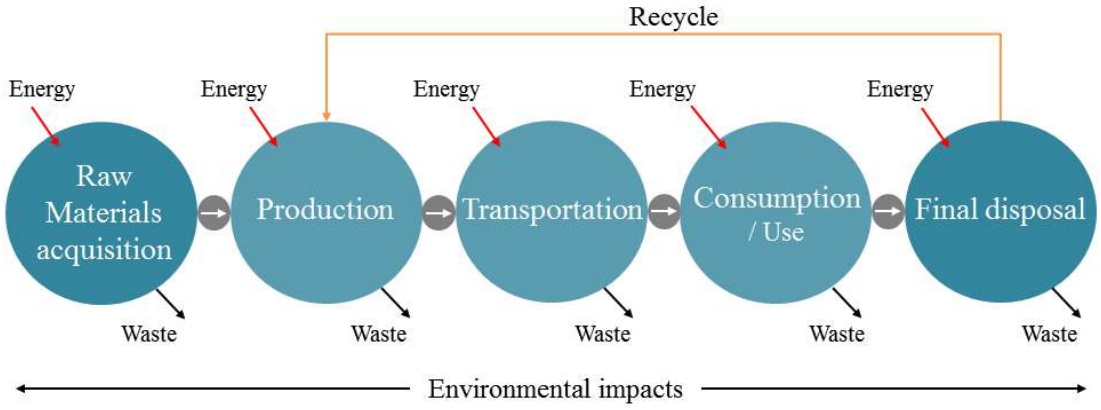

Figure 137: Typical Life-cycle of a product [391, 394].

It can also provide essential data on difficulties associated with the consumption of energy and raw materials, along with emissions to air, water and soil [394].

8.6.1 Life cycle assessment (LCA) analysis

LCA plays a vital role in environmental management, as it can be used to evaluate the environmental performance of products and services. The international organisation of standardisation (ISO) has formalised the methodological framework of LCA by producing ISO 14040 and 14044 standards [395, 396]. These standards describe the main phases of an LCA study [397]:

a) goal and scope definition,
b) inventory analysis (life cycle inventory),
c) impact assessment, and
d) interpretation.

8.6.1.1 Goal and scope definition

This initial phase elucidates the purpose of the study and the intended application. It also defines the functional unit, describes the system boundaries, and the method used to assess the impacts. In this phase, the system boundary determines which part of material processing should be included within the LCA. A broad LCA comprises all related stages of a product such as extraction or production of raw materials (raw

materials acquisition), processing of raw materials, manufacturing of products, transportation, and disposal or recycling methods. A cradle-to-gate boundary system considers the total life cycle of a product, while a gate-to-gate system covers only the manufacturing processes (production stage). The goal and scope definition describes the data collection and quality requirements, along with all assumptions and limitations of the LCA analysis [390, 398-400].

8.6.1.2 Inventory analysis

Inventory analysis identifies and records the quantities of all resources, emissions used and released during the production and life cycle related to the functional unit. This compilation of the input and output data is to set the life cycle inventory (LCI). Absence of appropriate data represents a challenge in conducting this phase. However, the LCI databases, combined with the LCA software tools, could offer detailed environmental and product data required. In this phase, it is necessary to make some assumptions in order to describe the complex systems. The outcomes from LCI could be, for example, obtaining natural resources or releasing hazardous substances [391, 398, 400].

8.6.1.3 Assessment of impacts

In the life cycle impact assessment (LCIA) phase, the emissions and resources data collected in the LCI stage, are evaluated regarding their magnitude and significance of the potential environmental impacts of the studied system. The assessment is based on different steps, and the findings can be demonstrated as single or several indicators. Classification, characterisation, normalisation and weighting are the common factors underpinning LCIA. In the first sub-phase, the classification, resource acquisition, pollutants and emissions are categorised concerning different environmental impacts. For example, the climate change category involves the emissions of greenhouse gases, like carbon dioxide and methane (CH_4). The characterisation factor indicates the relation between the level of an impact and the inventory data. During this sub-phase, a reference substance is used to quantify the contribution of the other substances grouped within a similar category. Normalisation interrelates the environmental impact caused by a system to the total impact load occurring in an area (region, country

or worldwide). The normalised impacts are further accumulated using the weighting factors [390, 398, 400].

8.6.1.4 Interpretation

The final phase of the LCA procedure is the life cycle interpretation, in which the results of the inventory analysis or impact assessment, or both, as well as the choices and assumptions made during the analysis, are assessed in terms of consistency and completeness. The main factors of this phase of LCA are evaluation and analysis of the results, in order to formulate and outline the conclusions and recommendations concerning the goal and scope of the study [390, 395].

8.6.2 Methodology of LCA analysis

There are several modelling tools available for LCA analysis, such as SimaPro, Ecoindicator, GaBi, and CCaLC software programmes [401-403]. In this study, the CCaLC2 version of this software was applied to evaluate the environmental impacts of the manufacturing of RF composite blankets.

The CCaLC tool has been developed to avoid the need to utilise sophisticated LCA software for a carbon footprint calculation. It allows the assessor to determine the carbon footprint-hot-spots in order to identify improvement opportunities. This LCA modelling tool also reduces the data collection effort by providing carbon footprint databases. It originated with comprehensive databases, including the Ecoinvent database. CCaLC contributes to achieving the carbon footprints magnitude under the PAS 2050 standards (specification for the assessment of the life cycle greenhouse gas emissions of goods and services) [403].

CCaLC2 enables estimation of different environmental impact categories. These impacts are characterised by equivalent references (as a standard measurement unit) as outlined [403]:

- Carbon footprint or global warming potential (GWP);
- Water footprint (WFP),
- Acidification potential (AP),
- Eutrophication potential (EP),
- Ozone depletion potential (ODP),

- Photochemical ozone creation (smog) potential (POCP), and
- Human toxicity potential (HTP)

8.6.2.1 Goal and scope of the study (RF composite blanket LCA analysis)

The main goal of this study is to propose an RF composite blanket LCA method, including the definition of the goal and scope of this insulation material, inventory analysis, impact analysis, and assessment interpretation (results).

A 1 m^3 blanket was defined as the functional unit based on the primary purpose to facilitate data application. For system boundary in the RF blanket LCA, the 'cradle-to-gate' system was assumed. The proposed boundary system includes all stages from in-ground resources to the RF blanket that also involves on-site inputs and emissions. As shown in Figure 138, the LCA stages mainly include:

- resources (raw materials and energy) extraction and production; and
- RF blanket production processes (mixing, impregnation, polymerisation (heating), solvent exchange, drying and packaging, and equipment washing).

As a result of the limitation in data availability, some part of the life cycle definitions and supply chain were not included in this study. These parts involve:

- transport of raw materials and wastes;
- final use application and carbon storage data of the product;
- transport of the intermediates within the production stages;
- benefits of carbon footprint reduction of the product; and
- waste recycling (solvent).

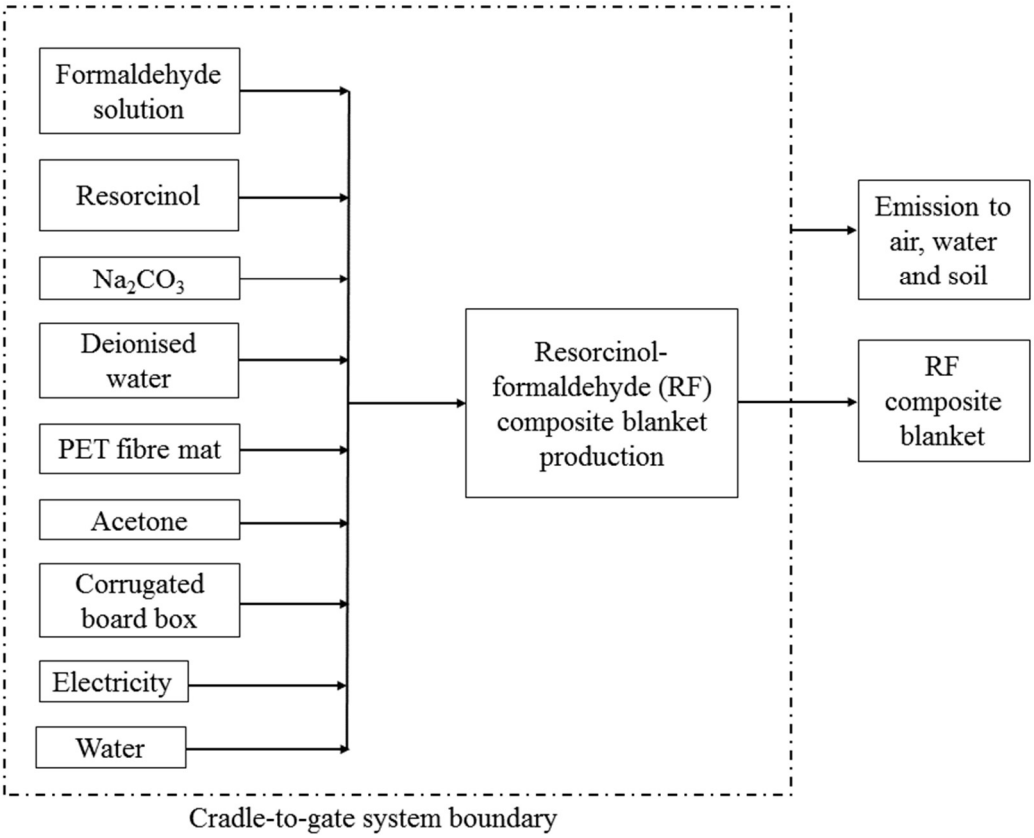

Figure 138: System boundary for RF composite blanket production.

Data collection and assumptions:

Those materials considered in the LCA analysis of resorcinol-formaldehyde composite blanket production included those stated in the system boundary (Figure 138). For quantities of the input materials, the existing data at the laboratory-scale have been utilised to produce 1 m^3 RF blanket as the functional unit (scale-up). Input and output data for modelling the production process were based on the data from the CCalC software and Ecoinvent database. The significant assumptions made for LCA of RF blanket production are summarised, as followed:

- Mass-based distribution was applied to assign the environmental loads to the blanket based on the system boundary;
- Life cycle inventory data for resorcinol production adapted from the dataset (CCalC2 software) of the phenol production process;
- Inventory data for formaldehyde solution was based on formaldehyde mixture as stated on the modelling programme used;

- Inventory data for PET fibre also adapted from the dataset (CCalC2 software) of the PET resin (amorphous);
- There are no on-site emissions of CO_2 and CO;
- Electricity from the wind-based power plant (3MW) of the UK selected as a source of energy;
- The transport distances in some life cycle stages were assumed to be as:
    a) transport of the product from process to storage: 0.30 km using tractor and trailer, and
    b) transport of the product from the site to the user: 10 km using < 3.5t van;
- Estimation of service water quantity for equipment cleaning purposes;
- The water footprint of the raw materials was assumed as the water used for zeolite process industry (Ecoinvent), and
- Packaging material selected as corrugate board box (15 kg weight);

8.6.2.2 Inventory analysis

The inventories used for this LCA study, including raw materials (chemicals, water, and packaging), and energy used for the composite blanket manufacturing, are listed in Table 31 and Table 33.

Table 31: Raw materials inventory for 1 m^3 RF composite blanket production.

Raw material	Quantity (tonne/functional unit)
Production stage	
Formaldehyde solution	26.50×10^{-2}
Resorcinol	18.00×10^{-2}
Sodium carbonate	2.88×10^{-4}
Deionised Water	80.30×10^{-2}
PET Fibre	5.50×10^{-2}
Acetone	23.52×10^{-1}
Equipment washing	
Service water	0.05
Packaging	
Corrugate board box	1.50×10^{-2}

Based on the RF composite blanket prepared on the laboratory-scale, these different raw materials required the molar ratios and other proportions to be considered in this study. These proportional criteria are presented in Table 32.

Table 32: Raw materials proportional criteria for RF composite blanket production.

	Molar ratio	wt./v %	Volume ratio
R: F	0.5		
R/C	600		
(R+F+C)/W		30	
RF solution/PET fibre			0.9259

For the energy inventory, electricity consumption by the process equipment in the production stage represented the main cost in this study. The electricity required for the oven adapted from data of an industrial oven, which has volume and temperature range meet this process requirement. This multi-purpose oven is designed by Airflow Group [404]. The mixer, with electricity load of 3 kW, was assumed to perform the agitation in 3 hours, while 7 kW was required for the vacuum heating dryer.

Table 33: Energy inventory for RF composite blanket production.

Energy	Amount (MJ/functional unit)
Production stage	
Mixing	
Electricity (3 kW Mixer, 1HR)	10.8
Heating (Polymerisation)	
Electricity (6 kW Oven, 72 HRS)	1555
Drying	
Electricity (7 kW vacuum dryer, 16 HRS)	403
Storage stage	
Electricity (120 W Lightening& ventilation, 120 HRS)	50

8.6.2.3 Environmental impact assessment method

According to ISO 14040/14044 standards, the classification and characterisation are mandatory impact assessment steps, while the normalisation and weighting steps could be optionally evaluated, based on the aim of the assessment [405-407].

The environmental impact assessment method used for the study is shown in Figure 139.

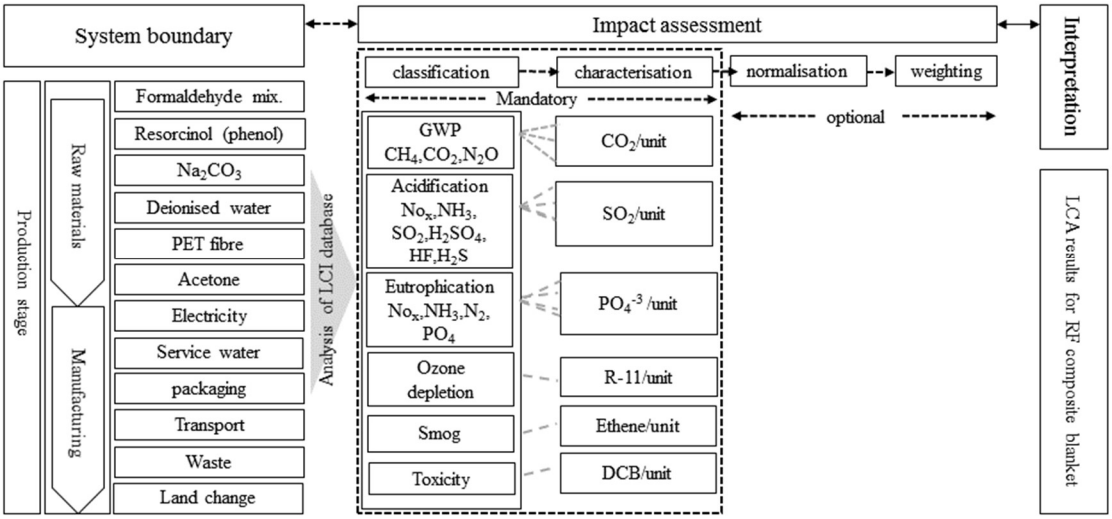

Figure 139: Life cycle impact assessment for RF composite blanket.

For the classification step, the life cycle inventory (LCI) results of the input and output factors, were assigned to impact categories, according to their potential environmental effect. For instance, the LCI of the formaldehyde mixture includes a dataset about the production of formaldehyde using the methanol oxidation process. It carries a part of the environmental effect load, as a result of the presence of precursors, ancillary materials and transport. The environmental effect of each inventory item within the production of formaldehyde is transformed into specific impact categories. Considering carbon footprint as an impact category, the steam used for the oxidation process could contribute to carbon dioxide emissions.

Carbon foot-print is referred to as the global warming potential GWP), because it is based on the CO_2 equivalent to the greenhouse gases (GHG). The GWP is utilised to quantify the contribution of the emission GHG to climate change. It measures the radiative efficiencies of different substances, as well as their life cycle in the atmosphere [408].

The LCI outputs (emissions) of the process might include some hazardous materials such as hydrogen fluoride (HF), nitrogen oxide (NO_x), sulphur dioxide (SO_2), ammonia (NH_3), and sulphuric acid. These substances can be classified as potential acidification impact, with SO_2 as reference material. For the characterisation, these inventory items are expressed in term of the reference material SO_2. This methodology is applied to the other considered impact categories.

8.6.2.4 Results and interpretation

Different environmental impacts (figures were assessed for the life cycle of 1 m^3 RF composite blanket, with cradle-to-gate system boundary conditions. The data reported in this study on such proposed insulation materials could form an underpinning basis for the further scientific evaluation of their environmental performance. The findings of this LCA demonstrate the contribution of each stage within the life cycle of the system to those environmental impacts. The main stages of the entire life cycle proposed by the CCalC tool involve raw materials, production, storage, and final use, as shown in Figure 140 and Appendices (E). Some of these essential stages comprise sub-stages or contents.

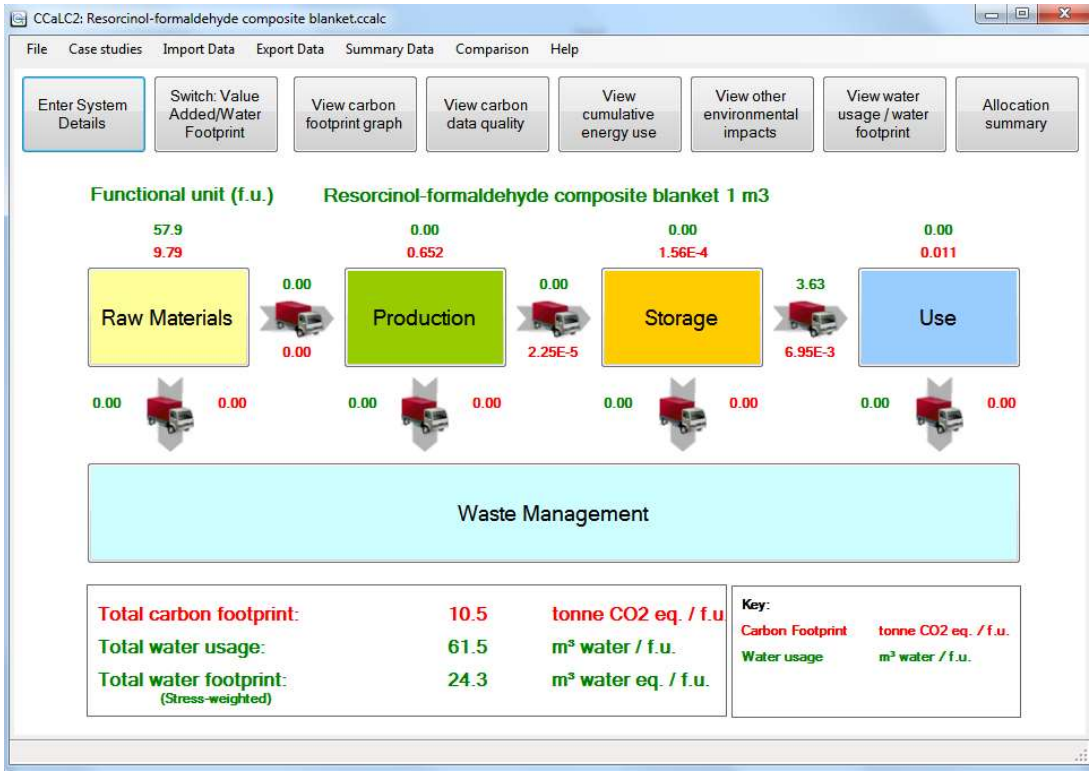

Figure 140: Life-cycle stages of RF composite blanket.

Carbon footprint (Global warming potential)

Carbon footprint (GWP) analysis results of RF composite blanket manufacturing, as modelled in CCaLC2, are presented in Figures 141 and 142. The total footprint is ~ 10.5 tonnes CO_2 eq., per $1m^3$ of the blanket. It can be seen that the raw materials stage gives the significant contribution (more than 93%) along the supply chain of the RF composite blanket production (Figure 141), which is mainly because of the consumption of different substances (precursors) and also land-use change effects.

On the other hand, the production stage emissions are due to energy used during the sub-stages, such as heating and drying. Figure 142 shows that the acquisition of the substance contributed significantly to this figure of GHG emissions. At the same time, the land-use change represents more than one-third of the carbon footprint amount emitted in the raw materials stage. The land-use change effects can be influenced by the land area utilised for the production of the raw materials.

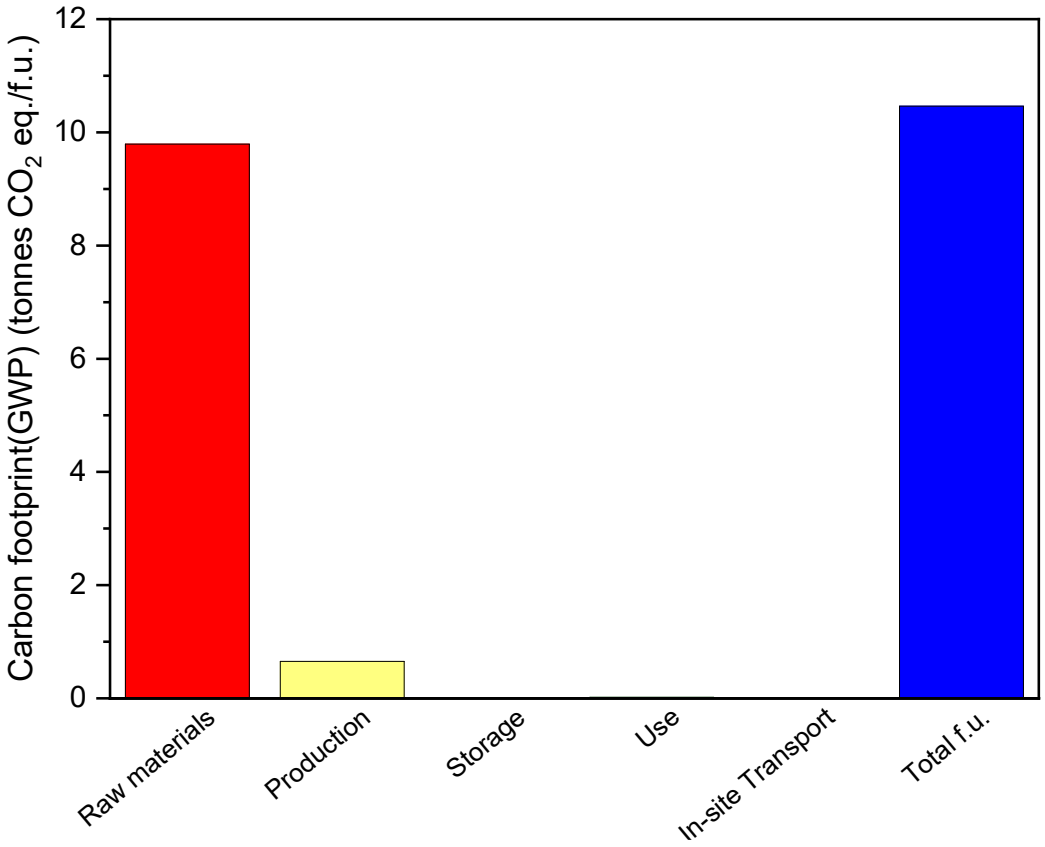

Figure 141: Contribution of life cycle stages on total carbon footprint.

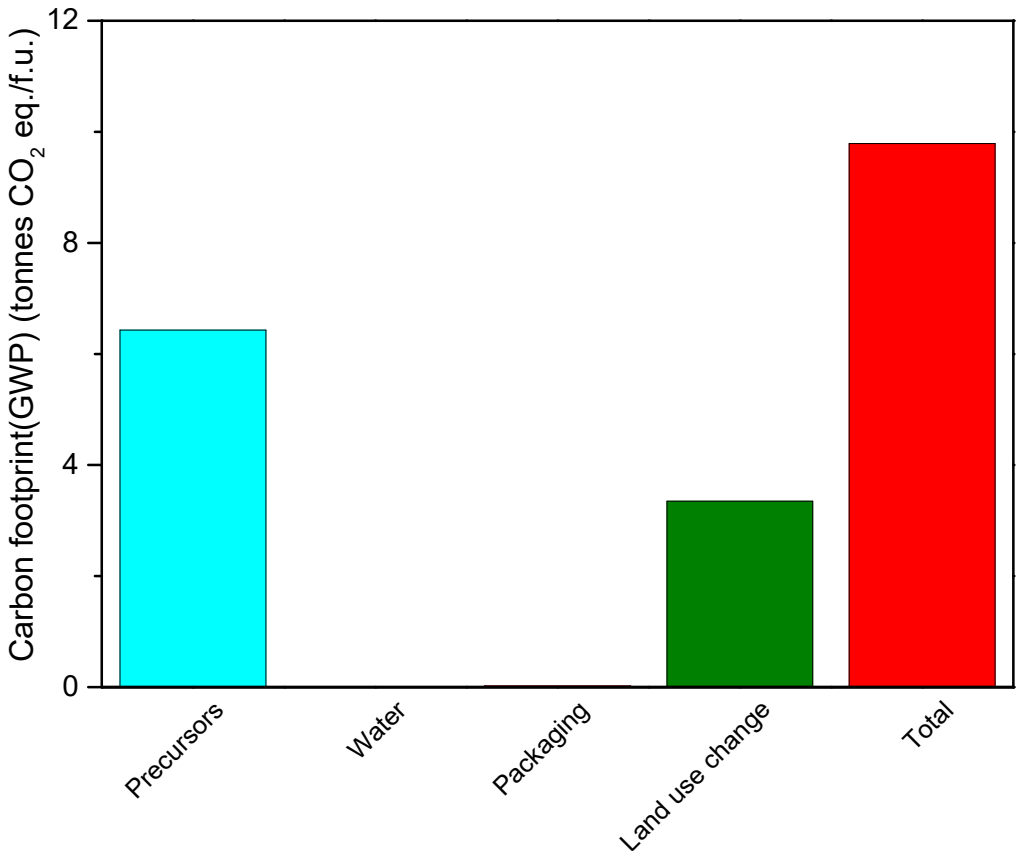

Figure 142: Carbon footprint of raw materials sub-stages.

The production of the raw material acetone emits the highest amounts of CO_2 among the precursors (Figure 143). Acetone production contributes to climate change, with around 50% of the total carbon footprints. The other constituents, such as phenol (resorcinol), formaldehyde mixture, and PET fibre, release small CO_2 amounts of ~ 0.70, 0.30, and 0.20 tonnes per functional unit, respectively.

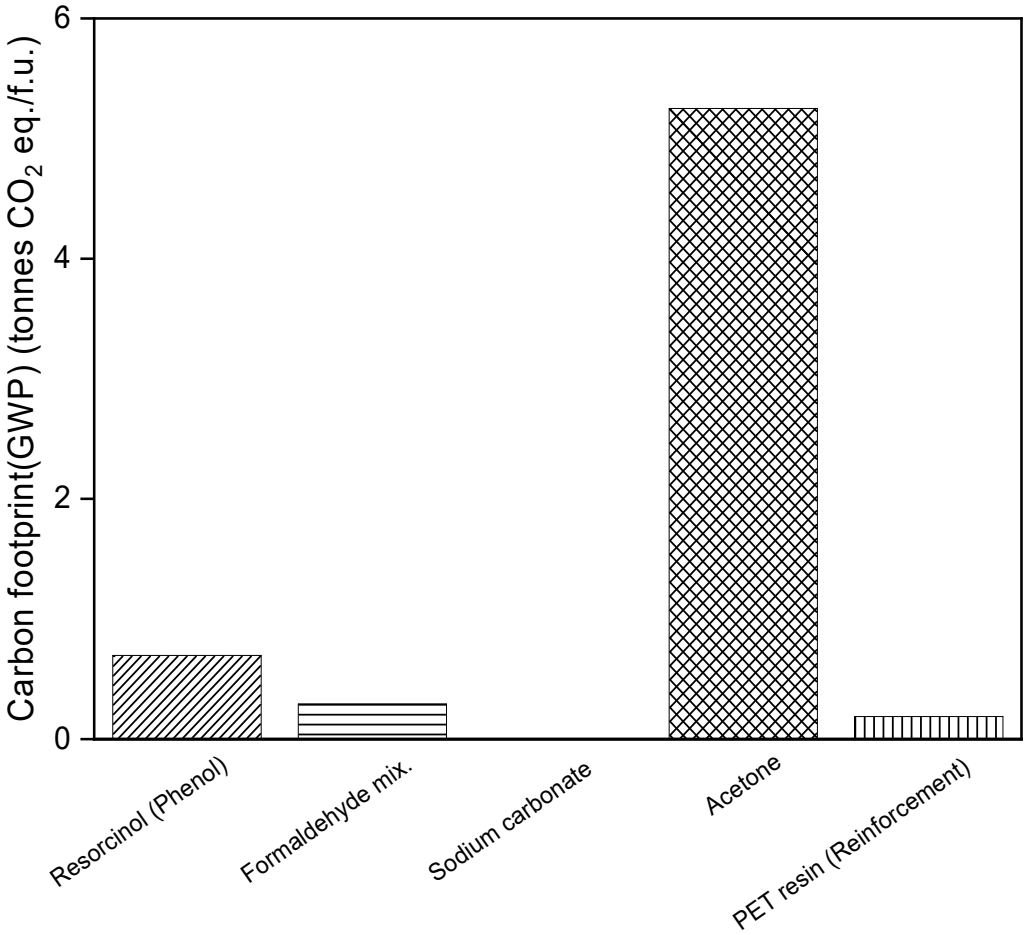

Figure 143: Contribution of raw materials production on carbon footprints

Acidification potential (AP)

The contribution to acidification potential of the RF blanket production was shown to be around 30 kg SO_2 eq/m^3 (Figure 144). The raw materials stage possessed the most significant impact on acidification (more than 96%). The production stage was observed to contribute acidification of 0.7 kg SO_2 eq/m^3, which reflected about 2.3 % of the total emissions to the atmosphere. As shown in Figure 145, acetone was found to have a value of 25 kg SO_2 eq/m^3, which represented more than 83% of the total, while phenol (resorcinol) and formaldehyde solution accounted 7.5% and 2% of the total SO_2 equivalents, respectively.

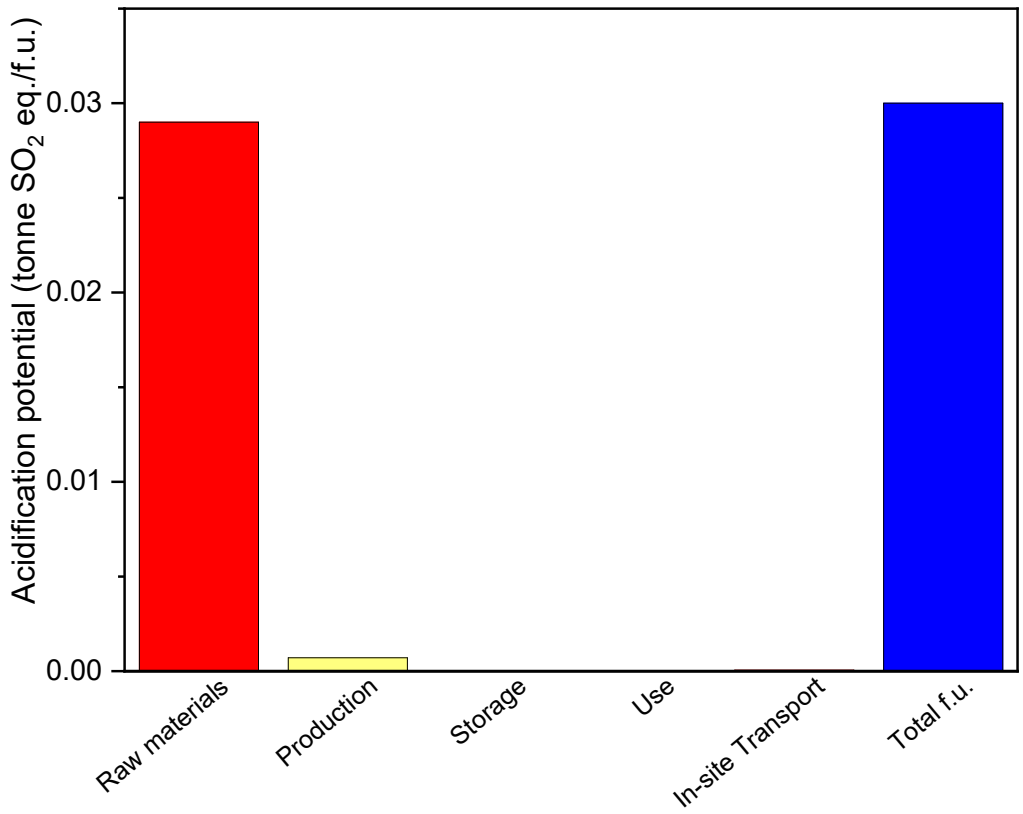

Figure 144: Contribution of life cycle stage of RF composite blanket to total acidification potential.

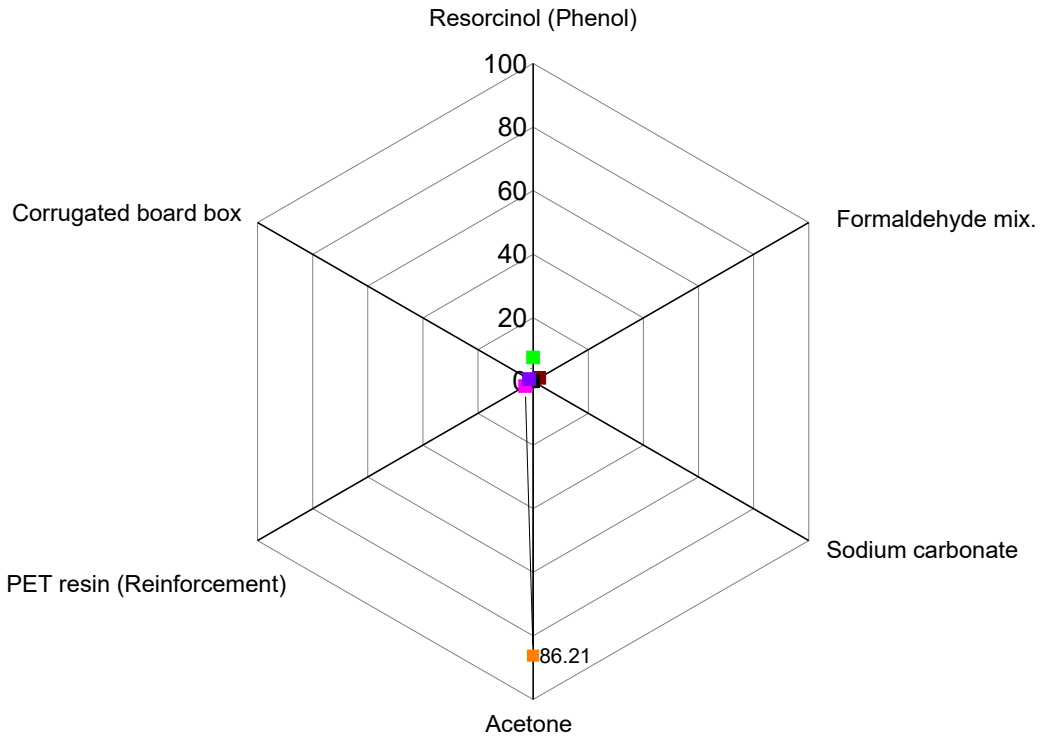

Figure 145: Acidification potential percentage for precursors.

Eutrophication potential (EP)

Assessing the eutrophication potential from the system using the CCaLC2 model has shown (Figure 146) that the total nutrients load is ~ 4 kg phosphate (PO_4^{-3}) eq. per functional unit. The raw materials stage is the major hot spot along the life cycle stages of this system. Contribution of the production stage to EP is much smaller compared with the raw materials; it had about 7% of the total load.

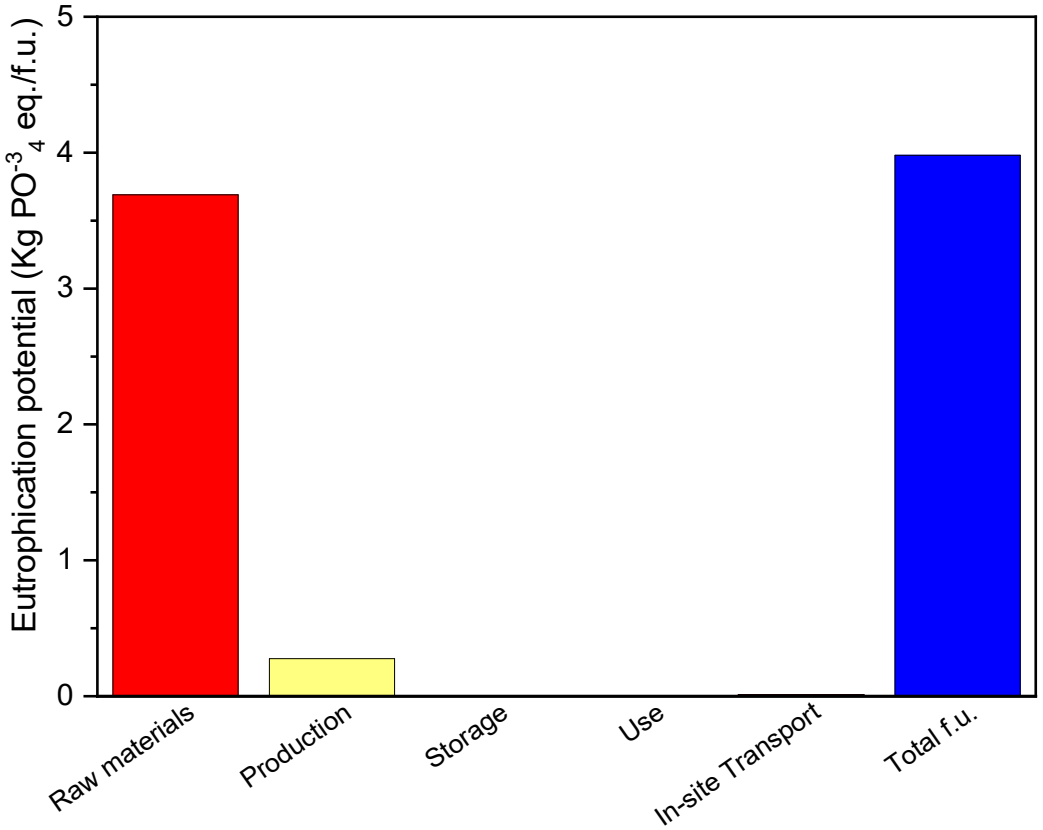

Figure 146: Contribution of life cycle stages of RF blanket to total eutrophication potential

Figure 147 illustrates that the acetone exhibited the value of the height of nutrient effluent into the ecosystem; it represented around 70% of the total raw materials impact. Phenol and formaldehyde solution accounted for about 20.5 and 8% of the total raw materials impact, respectively.

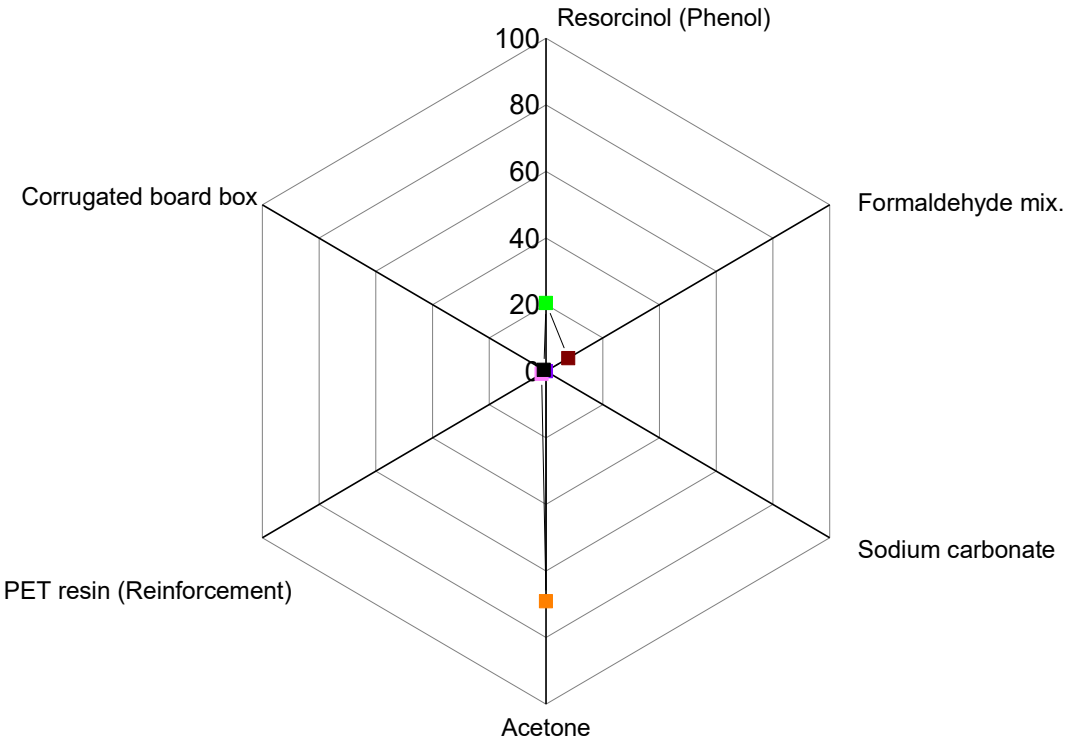

Figure 147: Contribution to eutrophication of raw materials in raw materials stage (percentage).

Ozone depletion potential (ODP)

The results of ozone depletion potential analysis of the RF blanket manufacturing as assessed by the CCaLC2 method are presented in Figure 148. The contribution to the ODP of the life cycle stages was shown to be 4.84×10^{-3} kg trichlorofluoromethane (R-11) eq. per m^3 RF blanket. The ozone depletion potential of the production stage was 4.65×10^{-3} kg R-11 eq. per m^3 RF blanket, which represented 96 % of the total. This is mainly due to the emissions from the energy (electricity) consumption during the sub-stages of the production. It can be observed that the electricity source of the wind-powered plant has a crucial role in the reduction of this value.

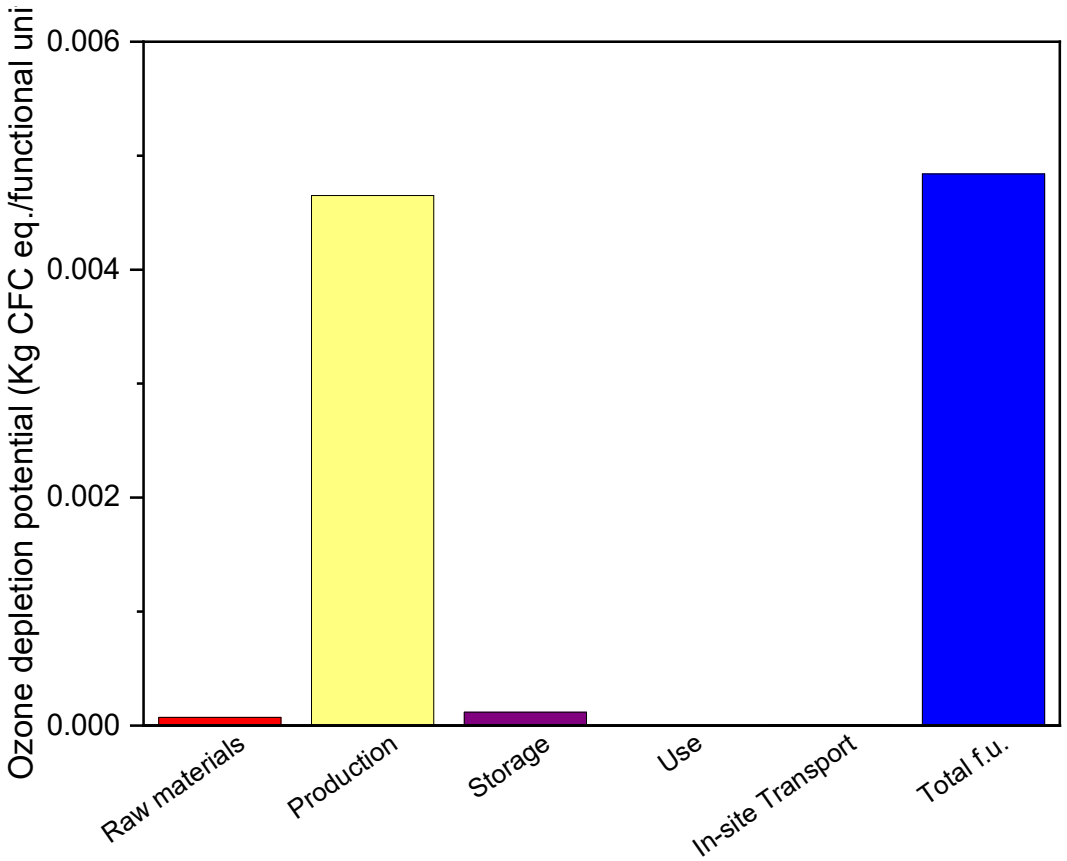

Figure 148: Contribution of life cycle stages of RF blanket to ozone depletion potential.

Photochemical ozone creation potential (POCP)

Figure 149 presents the results of the category "photochemical ozone creation potential" or "photochemical smog". The photochemical ozone condition occurs in the atmosphere as a result of degradation of the light organic compounds in the presence of solar radiation and nitrogen oxide (NO_x). The observations indicated that the contribution of this process to POCP is about 2.33 kg ethane (C_2H_4) eq. per functional unit. The main impact caused by the raw materials stage, which reflected about 85% of the total value. Contributions of the different raw material inputs to the POCP for the RF blanket are shown in Figure 150. It can be seen that acetone and phenol accounted for about 58% and 32%, respectively, of the total raw materials impact, while the PET fibre and formaldehyde had lesser effects, with around 6.5% and 3.5%, respectively.

Production stage also has effects on this impact category, as the direct emissions of formaldehyde mixture and acetone contributed mainly to the total value assigned for this life cycle stage.

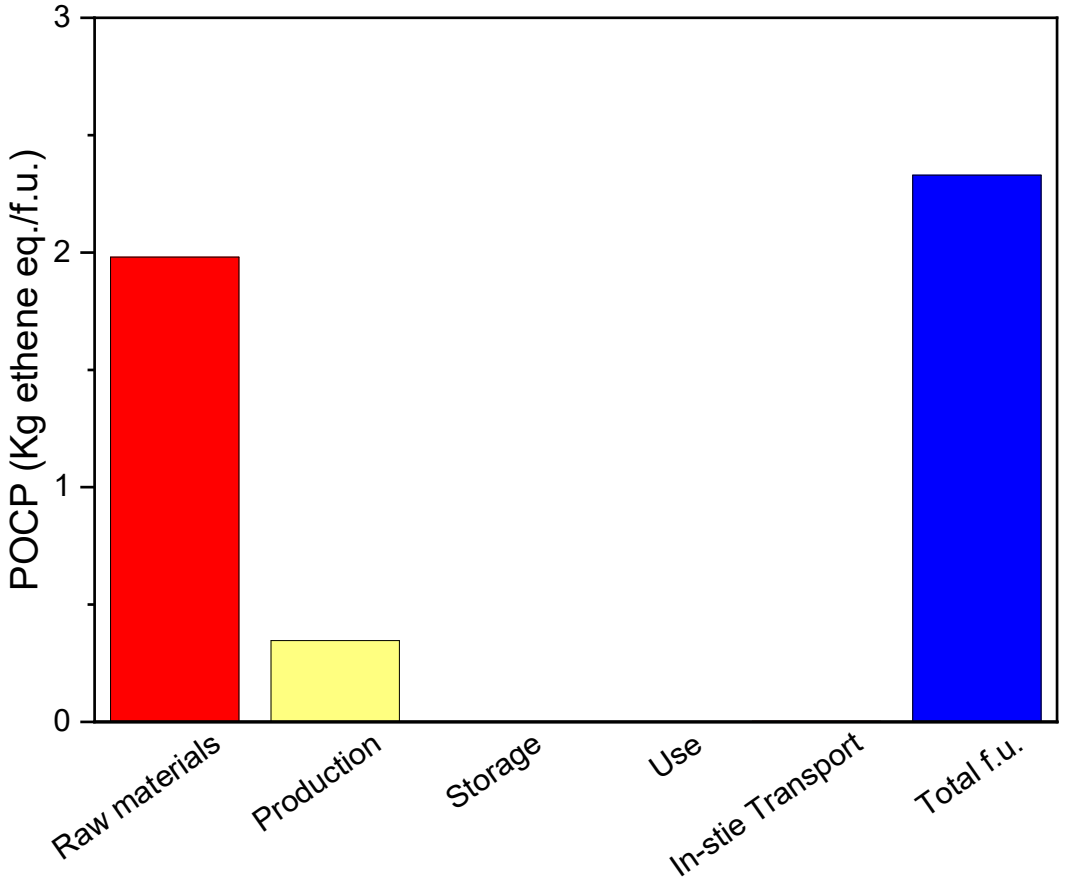

Figure 149: Contribution of life cycle stages of RF blanket to photochemical ozone creation potential.

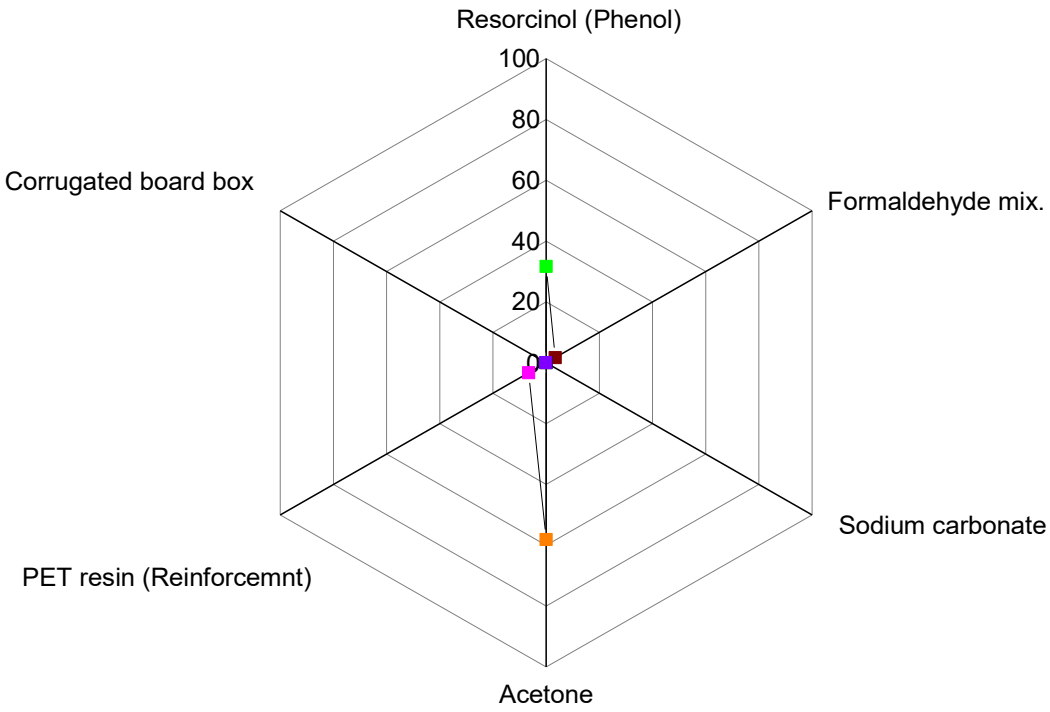

Figure 150: Photochemical ozone creation potential (percentages) for raw materials in raw material stage.

Human toxicity potential (HTP)

The results of the impact assessment of the RF blanket, as modelled by the CCaLC2 tool, are shown in Figure 151. Life cycle stages of RF blanket contribute to the category of human toxicity with 2.83 tonnes dichlorobenzene (DCB) eq. per $1m^3$ of the studied material. As for the other impact categories, the acquisition of raw materials is the main factor (reflecting more than 98%).

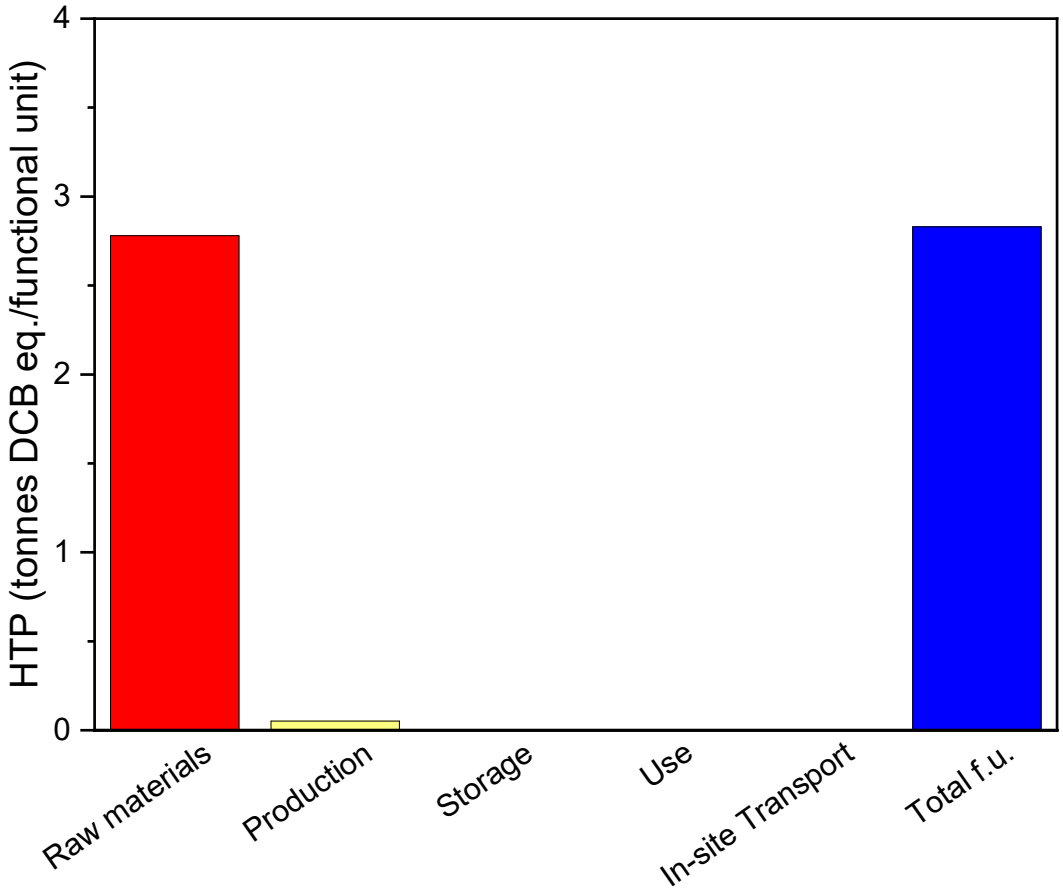

Figure 151: Contribution of life cycle of RF blanket to human toxicity potential.

As shown in Figure 152, phenol (representing the resorcinol precursor) was observed to contribute health toxicity of about 83% of the total raw material impact. In contrast, the other substances showed relatively lower effects.

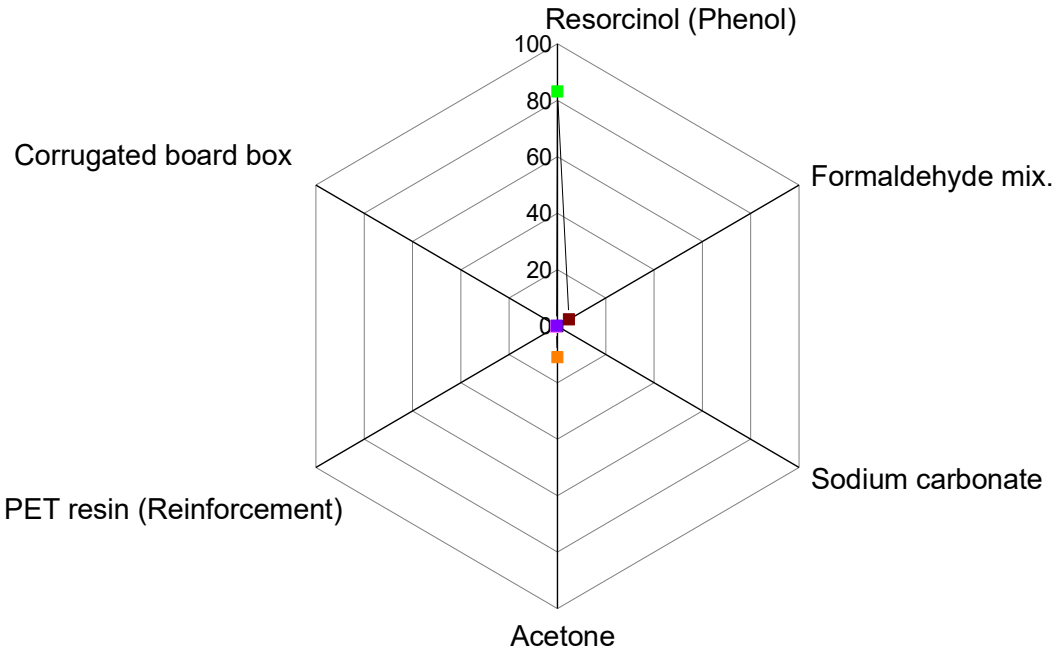

Figure 152: Human toxicity potential of raw materials in the raw material stage (percentage).

Water footprint potential

The results of the LCA of RF composite blanket showed that the total water footprint (stress-weighted) was about 24.3m^3 water eq. per functional unit, while the total water usage was 61.5 m^3 water per functional unit. These values were based on the assumptions stated earlier (Section 8.6.2.1).

Fossil depletion

Table 31 (Section 8.5.2.2) depicts the contribution of raw material inputs to fossil depletion. The production of raw materials such as resorcinol, formaldehyde, and acetone represents the most considerable contribution to fossil depletion among the life cycle of the RF blanket. However, some processes reveal an indirect contribution to fossil depletion, such as steam generation for the production of formaldehyde from the oxidation of methanol. The applied CCaLC2 tool has no evaluation facility for fossil depletion, which is considered as one of the critical environmental issues.

For this life cycle assessment study, it was not possible to obtain a comprehensive database regarding RF composite materials. Therefore, the LCA results showed in this research are innovative, as no life cycle data have as yet conducted for similar products.

8.7 Summary

RF xerogel blankets have some additional advantages compared with traditional insulation materials, as the synthetic route does not involve harmful blowing agents, such as chlorofluorocarbons (CFC) or hydrochlorofluorocarbons (HCFC), and less volume (thickness) of the material is required because of the higher resistance. Furthermore, furfural-derived gels have eliminated the need for formaldehyde, hence shortening the process and reducing the environmental impact.

The blankets can be made from less expensive starting materials to be close in cost to the currently used insulation materials. For reduction in the manufacturing time, different approaches can be adapted to decrease the gelation time; working at low R/C ratios, using alternative acid catalysts, the addition of a cationic polyelectrolyte, or performing the polycondensation reaction under ultrasonic waves.

Another critical factor is the use of acetone as a solvent to exchange the water inside the gel pores. Solvent recycling has a significant impact on the cost of production and reduces waste disposal issues. Although the price of the recycling unit is relatively high, the operation costs are low.

As the RF/PET structure seems to be stronger than the parent gel, inexpensive methods can be applied to dry the wet RF blanket. Ambient drying methods can be incorporated into the cost reduction strategy by excluding the necessity for pumping facilities; hence, reducing the energy consumption of this process.

LCA of the blanket reported that the significant contribution to different environmental impacts is the acquisition of raw materials, particularly acetone, which can be recycled using an appropriate waste solvent treatment method. Karlisch et al.[409] indicated that considering the environmental impact, distillation is a superior process for waste-solvent recovery.

The improved insulation properties and low-cost of production for RF blankets mean that they can be considered as a potential material for thermal insulation in buildings and industry.

9 Conclusions

In order to study and investigate the effectiveness of RF xerogel used in the blanket form as promising next-generation super-insulating materials, several samples of both RF xerogel and its blanket with varying sol-gel parameters were prepared. The porous structure of xerogels and blankets was characterised using low-temperature nitrogen adsorption-desorption analysis. The resulting textural properties were then correlated to the measured thermal conductivity of the products. The thermal stability of these materials also was monitored at elevated temperatures.

9.1 RF xerogels

The effect of synthesis conditions on the porous structure and thermal conductivity of the parent RF xerogel was experimentally investigated. RF xerogels were prepared by altering the R/C ratio, the percentage of solids content and catalyst type in making the RF hydrogels. The same nitrogen adsorption analysis was performed on the parent gels. Other methods were employed to analyse and test the material such as FTIR, helium pycnometer, thermogravimetric analysis (TGA) and laser flash analysis.

The textural characteristics varied with R/C ratios at constant solids content using sodium carbonates as a catalyst. It was found that the xerogels have significantly large pore sizes/volume, and thus low densities at high R/C ratios. The low-density texture contributes to the lower thermal conductivity of the gel through decreasing of heat transport via the solid backbone. However, at R/C ratios, which are near to the gelation limit value, the density appears to be increased as a result of the structure collapse. The gelation time was also influenced by the catalyst concentrations, where it was noticed that the high catalyst levels in the initial RF solution led to a decrease the gelation time.

On the other hand, the increase of the solids content at relatively high R/C ratios resulted in increasing the pore sizes/volume and provided further stability of the RF hydrogel at higher R/C ratios. The alternative catalysts used in place of sodium carbonates were potassium and sodium hydrogen carbonate, and potassium carbonates. All these catalysts showed similar trends as the standards catalyst (sodium carbonates), except the potassium carbonates which exhibit larger pore sizes/volume at a given R/C, this because the potassium has larger counter-ions (cations) than for

sodium, which leads to an increase in gelation time. Hence the particle sizes formed are increased, producing a gel structure with wider pore widths.

The infrared spectra obtained for the dried RF xerogels indicated that the functional groups are independent of R/C. It was also observed that the presence of – OH group which provides information about the water moisture within the gel structure. The thermal conductivity increases with increasing the water content of the gel, so it is essential to carry out the drying process properly. The results obtained for limited samples showed that the thermal conductivity of the RF xerogel was extremely low compared with the traditional insulating materials. However, the measuring methods comprise uncertainties regarding the sampling requirements and release of water and volatile components during the heating of the samples. TGA profile indicated that the RF xerogels initially start to decompose by releasing the water, acetone and unreacted materials, followed by the removal of hydrogen and oxygen atoms. These results were consistent with the literature.

9.2 RF xerogel based blankets

RF blankets were synthesised in subsequent processes, using RF solution embedded in a PET fibre as starting material. The first series of blankets to be tested were those catalysed using sodium carbonate at R/C ratios between 300 and 800 with an altered solids content percentage from 10 to 40%. For the initial RF sols, samples prepared at higher solids contents of 35 and 40%, were excluded; because the blankets showed undesirable trends of the visual flexibility, density and regularity.

The R/C ratio dramatically influences the thermal conductivity; as the conductivity decreases with increasing the R/C ratio to near the limited gelation value. It was found that at a constant relatively high R/C ratio, the thermal conductivity of the blanket decreases with increasing the solids content up to the percentage of 30%. Also, there was no a significant effect of altering the R/F ratio on the thermal performance of the blanket, unless at higher than standards value of 0.5, which leads to an increase the conductivity. Also, three alkaline catalysts ($NaHCO_3$, K_2CO_3 and $KHCO_3$) were employed in place of sodium carbonate. These catalysts presented no remarkable influence on the conductivity of the material. The results also indicate that higher RF

gel uptake within the blanket structure reduces the thermal conductivity of these composites.

These findings can be correlated to the textural properties obtained through nitrogen sorption measurement, where low catalyst concentrations led to a mesopore structure and lower density material; hence lower thermal conductivity. While high catalyst concentrations resulted in microporous and dense material revealing high thermal conductivity. The solids content influenced the conductivity via increasing the gel uptake into the final blanket structure and also improved the stability of the RF gels at higher R/C ratios.

In general, the thermal conductivity components are linked to the bulk density and the blanket structure as modified by the R/C ratio. The interconnected particles and the density govern the solid thermal conductivity, while the R/C ratio and thus the resultant pore width control the gas conduction within the porous structure.

When RF blankets were compared to the traditional insulating materials, it showed a thermal conductivity reduction of about 30%. Also, these novel materials exhibit extremely low dust release.

9.3 RF blanket commercialisation

Although only an initial economic analysis is available in the literature, the cost of raw materials has been reported as the critical factor in the total cost of the production of RF blankets. The analysis has shown that the manufacturing cost can be lowered by using inexpensive precursors such as phenol and cresols. It was found that using furfural based gels can reduce the hazards associated with the process. The cost of production can also be reduced by shortening the gelation time, solvent recycling, and using ambient drying methods. Raw materials production represents the main source of undesired environmental emissions. The need is for effective reuse strategy of the waste materials associated with such products. Further development and economic analysis are necessary to assess the possibility of emerging these materials into the thermal insulation market.

10 Future work

Some of the results presented in this work appear extraordinarily encouraging, and further investigation into several areas is recommended.

10.1 RF xerogels

The nanostructure of the RF xerogels is key to their effectiveness as thermal insulation materials. The proposed work to further develop these materials is based on the following actions:

- Investigation of the influence of a decrease in the temperatures of gelation and curing on the gels prepared at high solids contents.
- Examination of the effect of using alternative catalysts, such as Li2CO3 and CaCO3 on the final properties of xerogels synthesised at the high solids contents.
- Utilisation of MIP to determine pore volumes of gels obtained using high R/C ratio formulations.
- Determination of the effect of drying on gel structure collapse; this would be affected by using vacuum drying via two consecutive different temperature profiles: gradual heating to 60 ℃ for the first day, then heating at 120 °C for the second day.
- Studying the effect of Shortening the time taken for the solvent exchange to only two days by using an increased volume of solvent.
- Post thermal treatment can also be performed to reduce the presence of hydroxyl groups within the final structure of the gel, thereby reducing water content.
- As stated in the section for the future development of RF blankets, it is vital to apply alternative methods for the validity of thermal conductivity measurements.
- Development of RF gels in powdered form as thermal insulators for vacuum insulation systems.

10.2 RF blankets

Based on the results obtained from thermal conductivity and textural properties measurements (Chapter 5) suggested that future work would take a form of:

- A finer grain investigation of the effect of solids content percentages between 25 and 30% at R/C ratios in the range of 500-600 on thermal conductivity, allowing determining the accurate optimum composition of the initial RF solution required to achieve the lowest thermal conductivity product; hence minimising the amount of raw material used to fabricate a blanket
- Extension of the catalyst substitution work started here, by studying the effect of other catalysts such as lithium carbonate (Li_2CO_3) and calcium carbonate ($CaCO_3$) on the structural characteristics and conductivity of these materials.
- Process optimisation, by decreasing the gelation/curing times for RF blankets synthesised using low R/C, thus reducing the production duration for current formulations.
- Examining the influence of alternative reinforcement materials, other than PET, on the thermal conductivity of produced blankets; this could include polypropylene non-woven fabrics, electrospun polyvinylidene fluoride (PVDF), and cellulose.
- Introducing a post-heat treatment stage to remove trace moisture from the blanket structure. An initial suggestion would involve heating the sample to 125 °C, at ambient pressure for a day; however, this does represent an additional parameter for optimisation.
- Encapsulation of the blanket [20] in an appropriate material, and combined with pressure reduction to vacuum pressure, in order to minimise conductivity via reduction or elimination of gaseous conduction within the pores.
- Additional porosity measurements could be performed out using mercury intrusion porosimetry (MIP), to cover the pore size distributions range above that probed by nitrogen sorption measurements. This method also allows pore volumes due to the presence of larger pore widths to be determined.
- Alternative techniques could be trailed for the measurement of thermal conductivity in order to validate the results presented here. The proposed

methods include transient pulse (C-therm analyser) and laser comb conductimetry.

- Measurement of water taken up each blanket, using a climate chamber, would provide information on water sorption characteristics at different environmental conditions for various formulations.

10.3 Economic analysis of production of RF blankets

In order to conduct a comprehensive economic analysis of this process, it is essential to divide the synthesis method into separate segments to scale up the lab-produced materials. These segments could present a practical approach to establishing a pilot plant. Each segment of the manufacturing process can be considered a unit of operation. Capital investment should be estimated for the pilot plant; after which it can be scaled up to a mass-production unit. The additional SWOT analysis for the new pilot plant could provide an overview of the economic aspects associated with this process. Further development of alternative, inexpensive raw materials is essential in accelerating the integration of RF blankets into the commercial marketplace.

11 Appendices

Appendix A – Standard hydrogel formulations

This Appendix presents the masses of resorcinol and formaldehyde, as well as, metal carbonate required for each of the RF hydrogels synthesised in this study.

A1 Sodium carbonate – Na_2CO_3

Table 34: Na_2CO_3_100_0.5_10% composition

	Equivalent Moles	Equivalent Mass (g)	Percentage Mass %	Required Mass (g)
Resorcinol	1.0000	110.1100	64.3082	3.8585
Formaldehyde	2.0000	60.0524	35.0728	2.1044
Catalyst	0.0100	1.0599	0.6190	0.0371
Totals		171.2223	100.0000	6.0000

Table 35: Na_2CO_3_300_0.5_10% composition

	Equivalent Moles	Equivalent Mass (g)	Percentage Mass %	Required Mass (g)
Resorcinol	1.0000	110.1100	64.5747	3.8745
Formaldehyde	2.0000	60.0524	35.2181	2.1131
Catalyst	0.0033	0.3533	0.2072	0.0124
Totals		170.5157	100.0000	6.0000

Table 36: Na_2CO_3_400_0.5_10% composition

	Equivalent Moles	Equivalent Mass (g)	Percentage Mass %	Required Mass (g)
Resorcinol	1.0000	110.1100	64.6082	3.8765
Formaldehyde	2.0000	60.0524	35.2364	2.1142
Catalyst	0.0025	0.2650	0.1555	0.0093
Totals		170.4274	100.0000	6.0000

Table 37: Na_2CO_3_500_0.5_10% composition

	Equivalent Moles	Equivalent Mass (g)	Percentage Mass %	Required Mass (g)
Resorcinol	1.0000	110.1100	64.6283	3.8777
Formaldehyde	2.0000	60.0524	35.2473	2.1148
Catalyst	0.0020	0.2120	0.1244	0.0075
Totals		170.3744	100.0000	6.0000

Table 38: Na_2CO_3_100_0.5_20% composition

	Equivalent Moles	Equivalent Mass (g)	Percentage Mass %	Required Mass (g)
Resorcinol	1.0000	110.1100	64.3082	7.7170
Formaldehyde	2.0000	60.0524	35.0728	4.2087
Catalyst	0.0100	1.0599	0.6190	0.0743
Totals		171.2223	100.0000	12.0000

Table 39: Na_2CO_3_300_0.5_20% composition

	Equivalent Moles	Equivalent Mass (g)	Percentage Mass %	Required Mass (g)
Resorcinol	1.0000	110.1100	64.5747	7.7490
Formaldehyde	2.0000	60.0524	35.2181	4.2262
Catalyst	0.0033	0.3533	0.2072	0.0249
Totals		170.5157	100.0000	12.0000

Table 40: Na_2CO3_400_0.5_20% composition

	Equivalent Moles	Equivalent Mass (g)	Percentage Mass %	Required Mass (g)
Resorcinol	1.0000	110.1100	64.6082	7.7530
Formaldehyde	2.0000	60.0524	35.2364	4.2284
Catalyst	0.0025	0.2650	0.1555	0.0187
Totals		170.4274	100.0000	12.0000

Table 41: Na_2CO_3_500_0.5_20% composition

	Equivalent Moles	Equivalent Mass (g)	Percentage Mass %	Required Mass (g)
Resorcinol	1.0000	110.1100	64.6283	7.7554
Formaldehyde	2.0000	60.0524	35.2473	4.2297
Catalyst	0.0020	0.2120	0.1244	0.0149
Totals		170.3744	100.0000	12.0000

Table 42: Na_2CO_3_600_0.5_20% composition

	Equivalent Moles	Equivalent Mass (g)	Percentage Mass %	Required Mass (g)
Resorcinol	1.0000	110.1100	64.6417	7.7570
Formaldehyde	2.0000	60.0524	35.2546	4.2306
Catalyst	0.0017	0.1767	0.1037	0.0124
Totals		170.3391	100.0000	12.0000

Table 43: Na_2CO_3_100_0.5_25% composition

	Equivalent Moles	Equivalent Mass (g)	Percentage Mass %	Required Mass (g)
Resorcinol	1.0000	110.1100	64.3082	9.6462
Formaldehyde	2.0000	60.0524	35.0728	5.2609
Catalyst	0.0100	1.0599	0.6190	0.0929
Totals		171.2223	100.0000	15.0000

Table 44: Na_2CO_3_300_0.5_25% composition

	Equivalent Moles	Equivalent Mass (g)	Percentage Mass %	Required Mass (g)
Resorcinol	1.0000	110.1100	64.5747	9.6862
Formaldehyde	2.0000	60.0524	35.2181	5.2827
Catalyst	0.0033	0.3533	0.2072	0.0311
Totals		170.5157	100.0000	15.0000

Table 45: Na_2CO_3_400_0.5_25% composition

	Equivalent Moles	Equivalent Mass (g)	Percentage Mass %	Required Mass (g)
Resorcinol	1.0000	110.1100	64.6082	9.6912
Formaldehyde	2.0000	60.0524	35.2364	5.2855
Catalyst	0.0025	0.2650	0.1555	0.0233
Totals		170.4274	100.0000	15.0000

Table 46: Na_2CO_3_500_0.5_25% composition

	Equivalent Moles	Equivalent Mass (g)	Percentage Mass %	Required Mass (g)
Resorcinol	1.0000	110.1100	64.6283	9.6942
Formaldehyde	2.0000	60.0524	35.2473	5.2871
Catalyst	0.0020	0.2120	0.1244	0.0187
Totals		170.3744	100.0000	15.0000

Table 47: Na_2CO_3_600_0.5_25% composition

	Equivalent Moles	Equivalent Mass (g)	Percentage Mass %	Required Mass (g)
Resorcinol	1.0000	110.1100	64.6417	9.6963
Formaldehyde	2.0000	60.0524	35.2546	5.2882
Catalyst	0.0017	0.1767	0.1037	0.0156
Totals		170.3391	100.0000	15.0000

Table 48: Na_2CO_3_700_0.5_25% composition

	Equivalent Moles	Equivalent Mass (g)	Percentage Mass %	Required Mass (g)
Resorcinol	1.0000	110.1100	64.6512	9.6977
Formaldehyde	2.0000	60.0524	35.2599	5.2890
Catalyst	0.0014	0.1514	0.0889	0.0133
Totals		170.3138	100.0000	15.0000

Table 49: Na_2CO_3_100_0.5_30% composition

	Equivalent Moles	Equivalent Mass (g)	Percentage Mass %	Required Mass (g)
Resorcinol	1.0000	110.1100	64.3082	11.5755
Formaldehyde	2.0000	60.0524	35.0728	6.3131
Catalyst	0.0100	1.0599	0.6190	0.1114
Totals		171.2223	100.0000	18.0000

Table 50: Na_2CO_3_300_0.5_30% composition

	Equivalent Moles	Equivalent Mass (g)	Percentage Mass %	Required Mass (g)
Resorcinol	1.0000	110.1100	64.5747	11.6234
Formaldehyde	2.0000	60.0524	35.2181	6.3393
Catalyst	0.0033	0.3533	0.2072	0.0373
Totals		170.5157	100.0000	18.0000

Table 51: Na_2CO_3_400_0.5_30% composition

	Equivalent Moles	Equivalent Mass (g)	Percentage Mass %	Required Mass (g)
Resorcinol	1.0000	110.1100	64.6082	11.6295
Formaldehyde	2.0000	60.0524	35.2364	6.3425
Catalyst	0.0025	0.2650	0.1555	0.0280
Totals		170.4274	100.0000	18.0000

Table 52: Na_2CO_3_500_0.5_30% composition

	Equivalent Moles	Equivalent Mass (g)	Percentage Mass %	Required Mass (g)
Resorcinol	1.0000	110.1100	64.6283	11.6331
Formaldehyde	2.0000	60.0524	35.2473	6.3445
Catalyst	0.0020	0.2120	0.1244	0.0224
Totals		170.3744	100.0000	18.0000

Table 53: Na_2CO_3_600_0.5_30% composition

	Equivalent Moles	Equivalent Mass (g)	Percentage Mass %	Required Mass (g)
Resorcinol	1.0000	110.1100	64.6417	11.6355
Formaldehyde	2.0000	60.0524	35.2546	6.3458
Catalyst	0.0017	0.1767	0.1037	0.0187
Totals		170.3391	100.0000	18.0000

Table 54: Na_2CO_3_700_0.5_30% composition

	Equivalent Moles	Equivalent Mass (g)	Percentage Mass %	Required Mass (g)
Resorcinol	1.0000	110.1100	64.6512	11.6372
Formaldehyde	2.0000	60.0524	35.2599	6.3468
Catalyst	0.0014	0.1514	0.0889	0.0160
Totals		170.3138	100.0000	18.0000

Table 55: Na_2CO_3_800_0.5_30% composition

	Equivalent Moles	Equivalent Mass (g)	Percentage Mass %	Required Mass (g)
Resorcinol	1.0000	110.1100	64.6584	11.6385
Formaldehyde	2.0000	60.0524	35.2638	6.3475
Catalyst	0.0013	0.1325	0.0778	0.0140
Totals		170.2949	100.0000	18.0000

Table 56: Na_2CO_3_1000_0.5_30% composition

	Equivalent Moles	Equivalent Mass (g)	Percentage Mass %	Required Mass (g)
Resorcinol	1.0000	110.1100	64.6685	11.6403
Formaldehyde	2.0000	60.0524	35.2693	6.3485
Catalyst	0.0010	0.1060	0.0622	0.0112
Totals		170.2684	100.0000	18.0000

Table 57: Na_2CO_3_100_0.5_35% composition

	Equivalent Moles	Equivalent Mass (g)	Percentage Mass %	Required Mass (g)
Resorcinol	1.0000	110.1100	64.3082	13.5047
Formaldehyde	2.0000	60.0524	35.0728	7.3653
Catalyst	0.0100	1.0599	0.6190	0.1300
Totals		171.2223	100.0000	21.0000

Table 58: Na_2CO_3_300_0.5_35% composition

	Equivalent Moles	Equivalent Mass (g)	Percentage Mass %	Required Mass (g)
Resorcinol	1.0000	110.1100	64.5747	13.5607
Formaldehyde	2.0000	60.0524	35.2181	7.3958
Catalyst	0.0033	0.3533	0.2072	0.0435
Totals		170.5157	100.0000	21.0000

Table 59: Na_2CO_3_400_0.5_35% composition

	Equivalent Moles	Equivalent Mass (g)	Percentage Mass %	Required Mass (g)
Resorcinol	1.0000	110.1100	64.6082	13.5677
Formaldehyde	2.0000	60.0524	35.2364	7.3996
Catalyst	0.0025	0.2650	0.1555	0.0326
Totals		170.4274	100.0000	21.0000

Table 60: Na_2CO_3_500_0.5_35% composition

	Equivalent Moles	Equivalent Mass (g)	Percentage Mass %	Required Mass (g)
Resorcinol	1.0000	110.1100	64.6283	13.5719
Formaldehyde	2.0000	60.0524	35.2473	7.4019
Catalyst	0.0020	0.2120	0.1244	0.0261
Totals		170.3744	100.0000	21.0000

Table 61: Na_2CO_3_600_0.5_35% composition

	Equivalent Moles	Equivalent Mass (g)	Percentage Mass %	Required Mass (g)
Resorcinol	1.0000	110.1100	64.6417	13.5748
Formaldehyde	2.0000	60.0524	35.2546	7.4035
Catalyst	0.0017	0.1767	0.1037	0.0218
Totals		170.3391	100.0000	21.0000

Table 62: Na_2CO_3_700_0.5_35% composition

	Equivalent Moles	Equivalent Mass (g)	Percentage Mass %	Required Mass (g)
Resorcinol	1.0000	110.1100	64.6512	13.5768
Formaldehyde	2.0000	60.0524	35.2599	7.4046
Catalyst	0.0014	0.1514	0.0889	0.0187
Totals		170.3138	100.0000	21.0000

Table 63: Na_2CO_3_800_0.5_35% composition

	Equivalent Moles	Equivalent Mass (g)	Percentage Mass %	Required Mass (g)
Resorcinol	1.0000	110.1100	64.6584	13.5783
Formaldehyde	2.0000	60.0524	35.2638	7.4054
Catalyst	0.0013	0.1325	0.0778	0.0163
Totals		170.2949	100.0000	21.0000

Table 64: Na_2CO_3_900_0.5_35% composition

	Equivalent Moles	Equivalent Mass (g)	Percentage Mass %	Required Mass (g)
Resorcinol	1.0000	110.1100	64.6640	13.5794
Formaldehyde	2.0000	60.0524	35.2668	7.4060
Catalyst	0.0011	0.1178	0.0692	0.0145
Totals		170.2802	100.0000	21.0000

Table 65: Na_2CO_3_400_0.5_40% composition

	Equivalent Moles	Equivalent Mass (g)	Percentage Mass %	Required Mass (g)
Resorcinol	1.0000	110.1100	64.6082	15.5060
Formaldehyde	2.0000	60.0524	35.2364	8.4567
Catalyst	0.0025	0.2650	0.1555	0.0373
Totals		170.4274	100.0000	24.0000

Table 66: Na_2CO_3_1000_0.5_40% composition

	Equivalent Moles	Equivalent Mass (g)	Percentage Mass %	Required Mass (g)
Resorcinol	1.0000	110.1100	64.6685	15.5204
Formaldehyde	2.0000	60.0524	35.2693	8.4646
Catalyst	0.0010	0.1060	0.0622	0.0149
Totals		170.2684	100.0000	24.0000

Table 67: Na_2CO_3_500_0.25_25% composition

	Equivalent Moles	Equivalent Mass (g)	Percentage Mass %	Required Mass (g)
Resorcinol	1.0000	110.1100	47.7852	7.1678
Formaldehyde	4.0000	120.1048	52.1228	7.8184
Catalyst	0.0020	0.2120	0.0920	0.0138
Totals		230.4268	100.0000	15.0000

Table 68: Na_2CO_3_500_0.4_25% composition

	Equivalent Moles	Equivalent Mass (g)	Percentage Mass %	Required Mass (g)
Resorcinol	1.0000	110.1100	59.3945	8.9092
Formaldehyde	2.5000	75.0655	40.4911	6.0737
Catalyst	0.0020	0.2120	0.1143	0.0172
Totals		185.3875	100.0000	15.0000

Table 69: Na_2CO_3_500_0.6_25% composition

	Equivalent Moles	Equivalent Mass (g)	Percentage Mass %	Required Mass (g)
Resorcinol	1.0000	110.1100	68.6614	10.2992
Formaldehyde	1.6667	50.0447	31.2064	4.6810
Catalyst	0.0020	0.2120	0.1322	0.0198
Totals		160.3667	100.0000	15.0000

Table 70: Na_2CO_3_500_0.75_25% composition

	Equivalent Moles	Equivalent Mass (g)	Percentage Mass %	Required Mass (g)
Resorcinol	1.0000	110.1100	73.2329	10.9849
Formaldehyde	1.3333	40.0339	26.6261	3.9939
Catalyst	0.0020	0.2120	0.1410	0.0211
Totals		150.3559	100.0000	15.0000

A2 Potassium carbonate – K_2CO_3

Table 71: K_2CO_3_100_0.5_20% composition

	Equivalent Moles	Equivalent Mass (g)	Percentage Mass %	Required Mass (g)
Resorcinol	1.0000	110.1100	64.1874	7.7025
Formaldehyde	2.0000	60.0524	35.0069	4.2008
Catalyst	0.01	1.3821	0.8057	0.0967
Totals		171.5445	100.0000	12.0000

Table 72: K_2CO_3_300_0.5_20% composition

	Equivalent Moles	Equivalent Mass (g)	Percentage Mass %	Required Mass (g)
Resorcinol	1.0000	110.1100	64.5341	7.7441
Formaldehyde	2.0000	60.0524	35.1959	4.2235
Catalyst	0.0033	0.4607	0.2700	0.0324
Totals		170.6231	100.0000	12.0000

Table 73: K_2CO_3_400_0.5_20% composition

	Equivalent Moles	Equivalent Mass (g)	Percentage Mass %	Required Mass (g)
Resorcinol	1.0000	110.1100	64.5776	7.7493
Formaldehyde	2.0000	60.0524	35.2197	4.2264
Catalyst	0.0025	0.3455	0.2026	0.0243
Totals		170.5079	100.0000	12.0000

Table 74: K_2CO_3_500_0.5_20% composition

	Equivalent Moles	Equivalent Mass (g)	Percentage Mass %	Required Mass (g)
Resorcinol	1.0000	110.1100	64.6038	7.7525
Formaldehyde	2.0000	60.0524	35.2340	4.2281
Catalyst	0.0020	0.2764	0.1622	0.0195
Totals		170.4388	100.0000	12.0000

Table 75: K_2CO_3_600_0.5_20% composition

	Equivalent Moles	Equivalent Mass (g)	Percentage Mass %	Required Mass (g)
Resorcinol	1.0000	110.1100	64.6213	7.7546
Formaldehyde	2.0000	60.0524	35.2435	4.2292
Catalyst	0.0017	0.2303	0.1352	0.0162
Totals		170.3927	100.0000	12.0000

Table 76: K_2O_3_400_0.5_30% composition

	Equivalent Moles	Equivalent Mass (g)	Percentage Mass %	Required Mass (g)
Resorcinol	1.0000	110.1100	64.5776	11.6240
Formaldehyde	2.0000	60.0524	35.2197	6.3395
Catalyst	0.0025	0.3455	0.2026	0.0365
Totals		170.5079	100.0000	18.0000

Table 77: K_2CO_3_500_0.5_30% composition

	Equivalent Moles	Equivalent Mass (g)	Percentage Mass %	Required Mass (g)
Resorcinol	1.0000	110.1100	64.6038	11.6287
Formaldehyde	2.0000	60.0524	35.2340	6.3421
Catalyst	0.0020	0.2764	0.1622	0.0292
Totals		170.4388	100.0000	18.0000

Table 78: K_2CO_3_600_0.5_30% composition

	Equivalent Moles	Equivalent Mass (g)	Percentage Mass %	Required Mass (g)
Resorcinol	1.0000	110.1100	64.6213	11.6318
Formaldehyde	2.0000	60.0524	35.2435	6.3438
Catalyst	0.0017	0.2303	0.1352	0.0243
Totals		170.3927	100.0000	18.0000

Table 79: K_2CO_3_700_0.5_30% composition

	Equivalent Moles	Equivalent Mass (g)	Percentage Mass %	Required Mass (g)
Resorcinol	1.0000	110.1100	64.6338	11.6341
Formaldehyde	2.0000	60.0524	35.2503	6.3451
Catalyst	0.0014	0.1974	0.1159	0.0209
Totals		170.3598	100.0000	18.0000

A3 Sodium hydrogen-carbonate – $NaHCO_3$

Table 80: $NaHCO_3$_50_0.5_20% composition

	Equivalent Moles	Equivalent Mass (g)	Percentage Mass %	Required Mass (g)
Resorcinol	1.0000	110.1100	64.0761	7.6891
Formaldehyde	2.0000	60.0524	34.9462	4.1935
Catalyst	0.0200	1.6802	0.9778	0.1173
Totals		171.8426	100.0000	12.0000

Table 81: $NaHCO_3$_150_0.5_20% composition

	Equivalent Moles	Equivalent Mass (g)	Percentage Mass %	Required Mass (g)
Resorcinol	1.0000	110.1100	64.4965	7.7396
Formaldehyde	2.0000	60.0524	35.1755	4.2211
Catalyst	0.0067	0.5601	0.3281	0.0394
Totals		170.7225	100.0000	12.0000

Table 82: $NaHCO_3$_200_0.5_20% composition

	Equivalent Moles	Equivalent Mass (g)	Percentage Mass %	Required Mass (g)
Resorcinol	1.0000	110.1100	64.5494	7.7459
Formaldehyde	2.0000	60.0524	35.2043	4.2245
Catalyst	0.0050	0.4201	0.2462	0.0295
Totals		170.5825	100.0000	12.0000

Table 83: $NaHCO_3$_250_0.5_20% composition

	Equivalent Moles	Equivalent Mass (g)	Percentage Mass %	Required Mass (g)
Resorcinol	1.0000	110.1100	64.5812	7.7497
Formaldehyde	2.0000	60.0524	35.2217	4.2266
Catalyst	0.0040	0.3360	0.1971	0.0237
Totals		170.4984	100.0000	12.0000

Table 84: $NaHCO_3$_300_0.5_20% composition

	Equivalent Moles	Equivalent Mass (g)	Percentage Mass %	Required Mass (g)
Resorcinol	1.0000	110.1100	64.6025	7.7523
Formaldehyde	2.0000	60.0524	35.2332	4.2280
Catalyst	0.0033	0.2800	0.1643	0.0197
Totals		170.4424	100.0000	12.0000

Table 85: $NaHCO_3$_200_0.5_30% composition

	Equivalent Moles	Equivalent Mass (g)	Percentage Mass %	Required Mass (g)
Resorcinol	1.0000	110.1100	64.5494	11.6189
Formaldehyde	2.0000	60.0524	35.2043	6.3368
Catalyst	0.0050	0.4201	0.2462	0.0443
Totals		170.5825	100.0000	18.0000

Table 86: $NaHCO_3$_250_0.5_30% composition

	Equivalent Moles	Equivalent Mass (g)	Percentage Mass %	Required Mass (g)
Resorcinol	1.0000	110.1100	64.5812	11.6246
Formaldehyde	2.0000	60.0524	35.2217	6.3399
Catalyst	0.0040	0.3360	0.1971	0.0355
Totals		170.4984	100.0000	18.0000

Table 87: $NaHCO_3$_300_0.5_30% composition

	Equivalent Moles	Equivalent Mass (g)	Percentage Mass %	Required Mass (g)
Resorcinol	1.0000	110.1100	64.6025	11.6284
Formaldehyde	2.0000	60.0524	35.2332	6.3420
Catalyst	0.0033	0.2800	0.1643	0.0296
Totals		170.4424	100.0000	18.0000

Table 88: $NaHCO_3$_350_0.5_30% composition

	Equivalent Moles	Equivalent Mass (g)	Percentage Mass %	Required Mass (g)
Resorcinol	1.0000	110.1100	64.6176	11.6312
Formaldehyde	2.0000	60.0524	35.2415	6.3435
Catalyst	0.0029	0.2400	0.1409	0.0254
Totals		170.4024	100.0000	18.0000

A4 Potassium hydrogen-carbonate – $KHCO_3$

Table 89: $KHCO_3$_50_0.5_20% composition

	Equivalent Moles	Equivalent Mass (g)	Percentage Mass %	Required Mass (g)
Resorcinol	1.0000	110.1100	63.9562	7.6747
Formaldehyde	2.0000	60.0524	34.8808	4.1857
Catalyst	0.0200	2.0023	1.1630	0.1396
Totals		172.1647	100.0000	12.0000

Table 90: $KHCO_3$_150_0.5_20% composition

	Equivalent Moles	Equivalent Mass (g)	Percentage Mass %	Required Mass (g)
Resorcinol	1.0000	110.1100	64.4560	7.7347
Formaldehyde	2.0000	60.0524	35.1533	4.2184
Catalyst	0.0067	0.6674	0.3907	0.0469
Totals		170.8298	100.0000	12.0000

Table 91: $KHCO_3$_200_0.5_20% composition

	Equivalent Moles	Equivalent Mass (g)	Percentage Mass %	Required Mass (g)
Resorcinol	1.0000	110.1100	64.5190	7.7423
Formaldehyde	2.0000	60.0524	35.1877	4.2225
Catalyst	0.005	0.5006	0.2933	0.0352
Totals		170.6630	100.0000	12.0000

Table 92: $KHCO_3$_250_0.5_20% composition

	Equivalent Moles	Equivalent Mass (g)	Percentage Mass %	Required Mass (g)
Resorcinol	1.0000	110.1100	64.5568	7.7468
Formaldehyde	2.0000	60.0524	35.2084	4.2250
Catalyst	0.004	0.4005	0.2348	0.0282
Totals		170.5629	100.0000	12.0000

Table 93: $KHCO_3$_300_0.5_20% composition

	Equivalent Moles	Equivalent Mass (g)	Percentage Mass %	Required Mass (g)
Resorcinol	1.0000	110.1100	64.5821	7.7499
Formaldehyde	2.0000	60.0524	35.2222	4.2267
Catalyst	0.0033	0.3337	0.1957	0.0235
Totals		170.4961	100.0000	12.0000

Table 94: $KHCO_3$_200_0.5_30% composition

	Equivalent Moles	Equivalent Mass (g)	Percentage Mass %	Required Mass (g)
Resorcinol	1.0000	110.1100	64.5190	11.6134
Formaldehyde	2.0000	60.0524	35.1877	6.3338
Catalyst	0.005	0.5006	0.2933	0.0528
Totals		170.6630	100.0000	18.0000

Table 95: $KHCO_3$_250_0.5_30% composition

	Equivalent Moles	Equivalent Mass (g)	Percentage Mass %	Required Mass (g)
Resorcinol	1.0000	110.1100	64.5568	11.6202
Formaldehyde	2.0000	60.0524	35.2084	6.3375
Catalyst	0.004	0.4005	0.2348	0.0423
Totals		170.5629	100.0000	18.0000

Table 96: $KHCO_3$_300_0.5_30% composition

	Equivalent Moles	Equivalent Mass (g)	Percentage Mass %	Required Mass (g)
Resorcinol	1.0000	110.1100	64.5821	11.6248
Formaldehyde	2.0000	60.0524	35.2222	6.3400
Catalyst	0.0033	0.3337	0.1957	0.0352
Totals		170.4961	100.0000	18.0000

Table 97: $KHCO_3$_350_0.5_30% composition

	Equivalent Moles	Equivalent Mass (g)	Percentage Mass %	Required Mass (g)
Resorcinol	1.0000	110.1100	64.6002	11.6280
Formaldehyde	2.0000	60.0524	35.2320	6.3418
Catalyst	0.0029	0.2860	0.1678	0.0302
Totals		170.4484	100.0000	18.0000

Appendix B – Standard Hydrogel calculated reaction volumes

Appendix B presents the volumes of both formalin and additional deionised water required for each of the hydrogel compositions detailed in Appendix A.

B1 Sodium carbonate – Na_2CO_3

Table 98: Na_2CO_3 volumes required for R/F 0.5 and 10% solids content hydrogels

R/C	100	300	400	500
Volume of Formalin (ml)	5.22	5.24	5.24	5.24
Volume due to F (ml)	2.58	2.59	2.59	2.59
Volume due to H_2O/MeOH (ml)	2.64	2.65	2.65	2.65
Volume of H_2O (ml)	7.36	7.35	7.35	7.35

Table 99: Na_2CO_3 volumes required for R/F 0.5 and 20% solids content hydrogels

R/C	100	300	400	500	600
Volume of Formalin (ml)	10.44	10.48	10.48	10.49	10.49
Volume due to F (ml)	5.17	5.19	5.19	5.19	5.19
Volume due to H_2O/MeOH (ml)	5.27	5.29	5.29	5.30	5.30
Volume of H_2O (ml)	4.73	4.71	4.71	4.70	4.70

Table 100: Na_2CO_3 volumes required for R/F 0.5 and 25% solids content hydrogels

R/C	100	300	400	500	600	700
Volume of Formalin (ml)	13.05	13.10	13.11	13.11	13.11	13.11
Volume due to F (ml)	6.45	6.48	6.49	6.49	6.49	6.49
Volume due to H_2O/MeOH (ml)	6.60	6.62	6.62	6.62	6.62	6.62
Volume of H_2O (ml)	3.40	3.38	3.38	3.38	3.38	3.38

Table 101: Na_2CO_3 volumes required for R/F 0.5 and 30% solids content hydrogels

R/C	100	300	400	500	600	700	800	1000
Volume of Formalin (ml)	15.65	15.72	15.73	15.73	15.73	15.74	15.74	15.74
Volume due to F (ml)	7.74	7.78	7.78	7.78	7.78	7.79	7.79	7.79
Volume due to H_2O/MeOH (ml)	7.91	7.94	7.95	7.95	7.95	7.95	7.95	7.95
Volume of H_2O (ml)	2.09	2.06	2.05	2.05	2.05	2.05	2.05	2.05

Table 102: Na_2CO_3 volumes required for R/F 0.5 and 35% solids content hydrogels

R/C	100	300	400	500	600	700	800	900
Volume of Formalin (ml)	18.26	18.34	18.35	18.35	18.36	18.36	18.36	18.36
Volume due to F (ml)	9.03	9.08	9.08	9.08	9.09	9.09	9.09	9.09
Volume due to H_2O/MeOH (ml)	9.23	9.26	9.27	9.27	9.27	9.27	9.27	9.27
Volume of H_2O (ml)	0.77	0.74	0.73	0.73	0.73	0.73	0.73	0.73

Table 103: Na_2CO_3 volumes required for R/F 0.5 and 40% solids content hydrogels

R/C	400	1000
Volume of Formalin (ml)	20.96	20.99
Volume due to F (ml)	10.38	10.39
Volume due to H_2O/MeOH (ml)	10.59	10.60
Volume of H_2O (ml)	- 0.59*	- 0.60*

* Minus value means that volume required to be reduced from 50 ml initial volume of H_2O

Table 104: Na_2CO_3 volumes required for R/C 500 and 25% solids content hydrogels

R/F	0.25	0.40	0.60	0.75
Volume of Formalin (ml)	19.39	15.06	11.61	9.90
Volume due to F (ml)	9.60	7.45	5.75	4.90
Volume due to H_2O/MeOH (ml)	9.79	7.61	5.86	5.00
Volume of H_2O (ml)	0.79	2.39	4.14	5.00

B2 Potassium carbonate – K_2CO_3

Table 105: K_2CO_3 volumes required for R/F 0.5 and 20% solids content hydrogels

R/C	100	300	400	500	600
Volume of Formalin (ml)	10.42	10.47	10.48	10.48	10.49
Volume due to F (ml)	5.15	5.18	5.19	5.19	5.19
Volume due to H_2O/MeOH (ml)	5.27	5.29	5.29	5.29	5.30
Volume of H_2O (ml)	4.73	4.71	4.71	4.71	4.70

Table 106: K_2CO_3 volumes required for R/F 0.5 and 30% solids content hydrogels

R/C	400	500	600	700
Volume of Formalin (ml)	15.72	15.73	15.73	15.73
Volume due to F (ml)	7.78	7.78	7.78	7.78
Volume due to H_2O/MeOH (ml)	7.94	7.95	7.95	7.95
Volume of H_2O (ml)	2.06	2.05	2.05	2.05

B3 Sodium hydrogen-carbonate – $NaHCO_3$

Table 107: $NaHCO_3$ volumes required for R/F 0.5 and 20% solids content hydrogels

R/C	50	150	200	250	300
Volume of Formalin (ml)	10.40	10.47	10.47	10.48	10.48
Volume due to F (ml)	5.15	5.18	5.18	5.19	5.19
Volume due to H_2O/MeOH (ml)	5.25	5.29	5.29	5.29	5.29
Volume of H_2O (ml)	4.75	4.71	4.71	4.71	4.71

Table 108: $NaHCO_3$ volumes required for R/F 0.5 and 30% solids content hydrogels

R/C	200	250	300	350
Volume of Formalin (ml)	15.71	15.72	15.73	15.73
Volume due to F (ml)	7.77	7.78	7.78	7.78
Volume due to H_2O/MeOH (ml)	7.94	7.94	7.95	7.95
Volume of H_2O (ml)	2.06	2.06	2.05	2.05

B4 Potassium Hydrogen-carbonate – $KHCO_3$

Table 109: $KHCO_3$ volumes required for R/F 0.5 and 20% solids content hydrogels

R/C	50	150	200	300	350
Volume of Formalin (ml)	10.38	10.46	10.47	10.48	10.48
Volume due to F (ml)	5.14	5.18	5.18	5.19	5.19
Volume due to H_2O/MeOH (ml)	5.24	5.28	5.29	5.29	5.29
Volume of H_2O (ml)	4.76	4.72	4.71	4.71	4.71

Table 110: $KHCO_3$ volumes required for R/F 0.5 and 30% solids content hydrogels

R/C	200	250	300	350
Volume of Formalin (ml)	15.71	15.71	15.72	15.73
Volume due to F (ml)	7.77	7.77	7.78	7.78
Volume due to H_2O/MeOH (ml)	7.94	7.94	7.94	7.95
Volume of H_2O (ml)	2.06	2.06	2.06	2.05

Appendix C – Additional results related to RF xerogels

C1 Uncertainty in repeated measurements

Average (Mean)

$$\bar{x} = \frac{\sum x_i}{N} \qquad \text{Equation 120}$$

N = number of observations, x_i

Standard deviation

$$S = \sqrt{\frac{\sum(\bar{x} - x_i)^2}{N}} \qquad \text{Equation 121}$$

Standard deviation of the mean (standard error)

$$\sigma_{\bar{x}} = \frac{S}{\sqrt{N}} \qquad \text{Equation 122}$$

The above equations are available in the literature [410].

Error bars

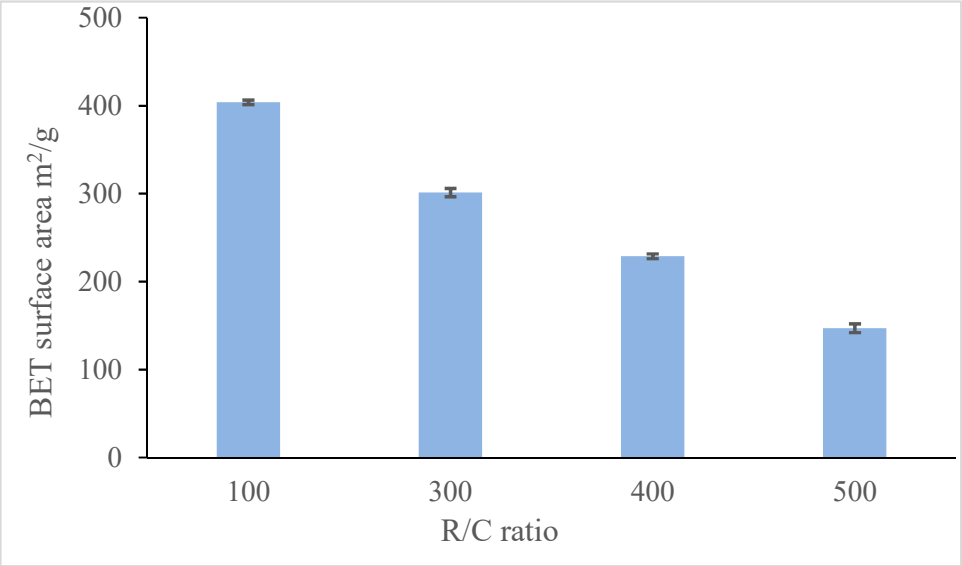

Figure 153: Error bar for BET surface area of RF xerogel (solids content 10%)

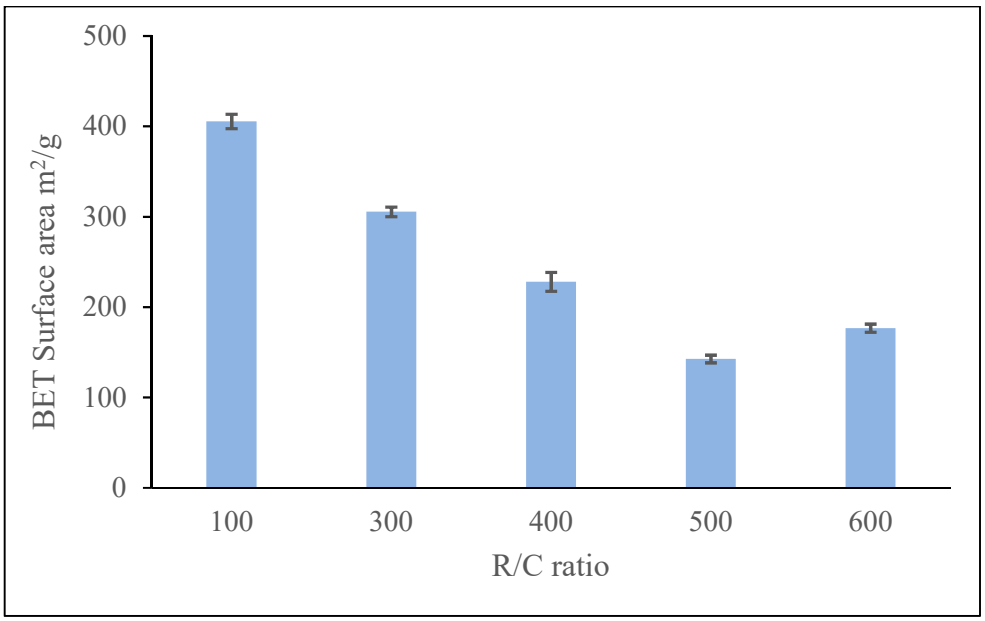

Figure 154: Error bar for BET surface area of RF xerogels (solids content 20%).

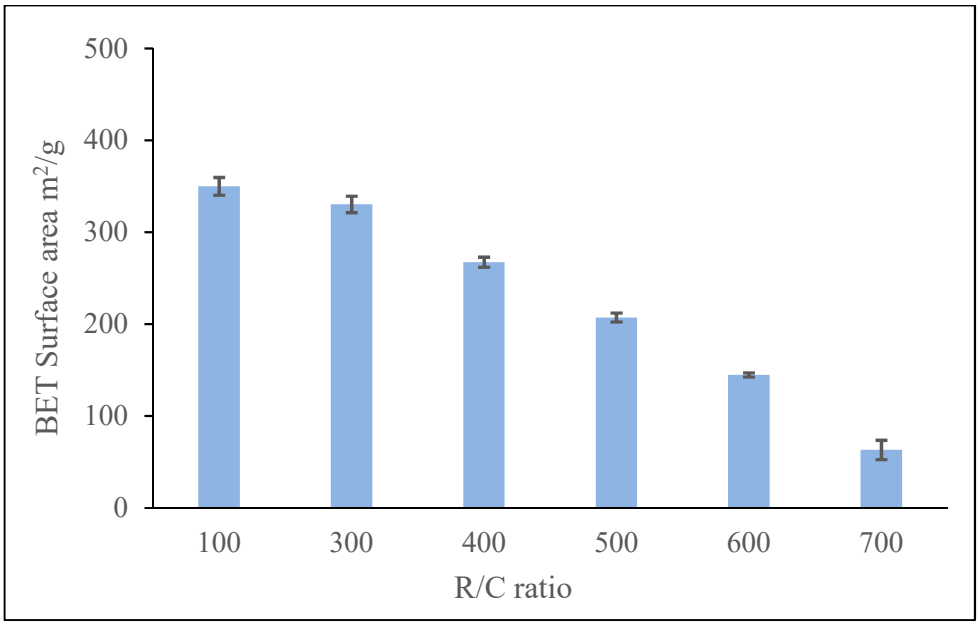

Figure 155: Error bars for BET surface area of RF xerogels (solids content 25%).

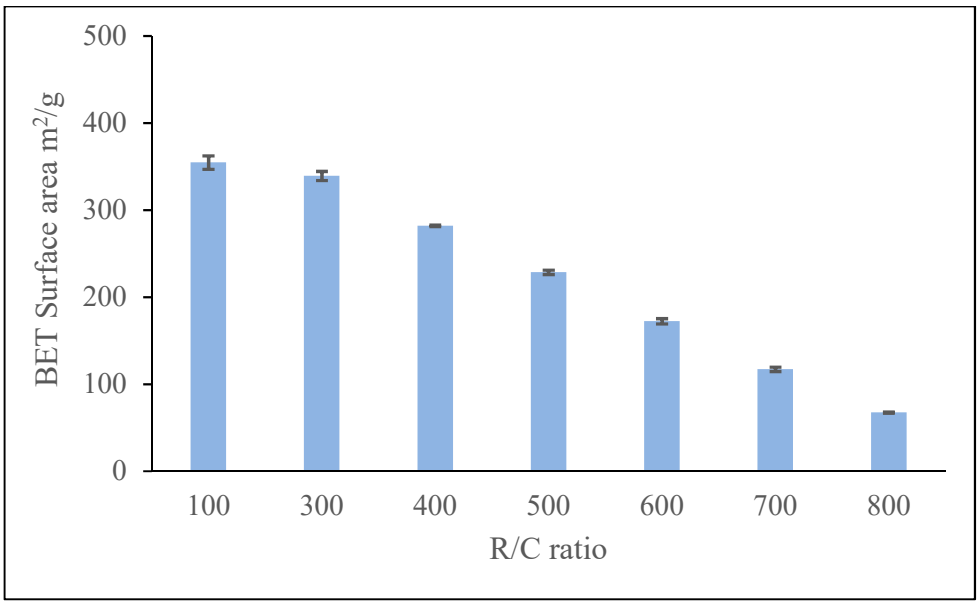

Figure 156: Error bar for BET surface area of RF xerogels (solids content 30%).

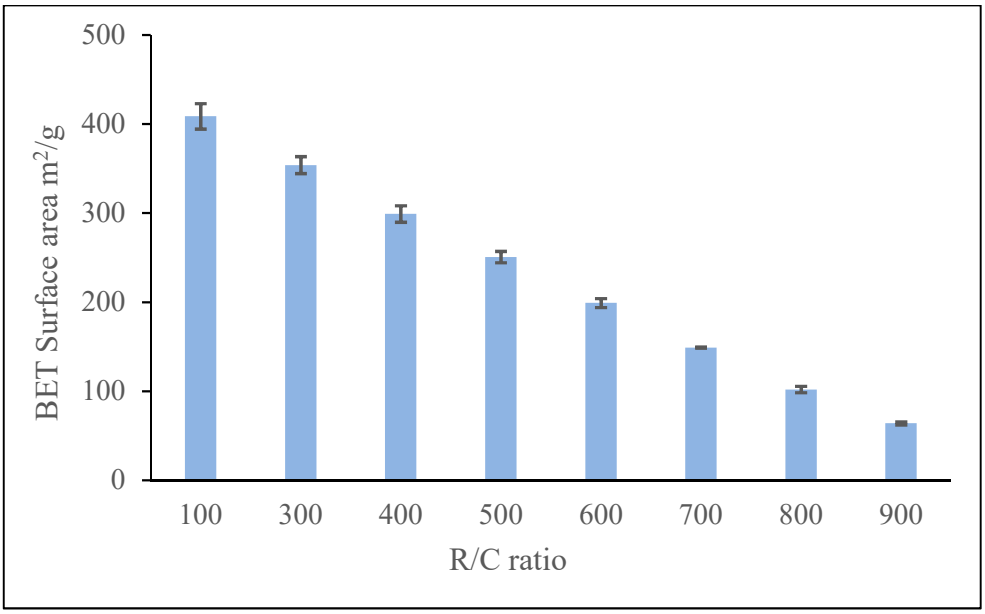

Figure 157: Error bars for BET surface area of RF xerogels (solids content 35%).

C2 Structural properties

It contains additional nitrogen adsorption/desorption isotherms and pore size distributions for RF xerogel samples, prepared using Na_2CO_3 as a catalyst.

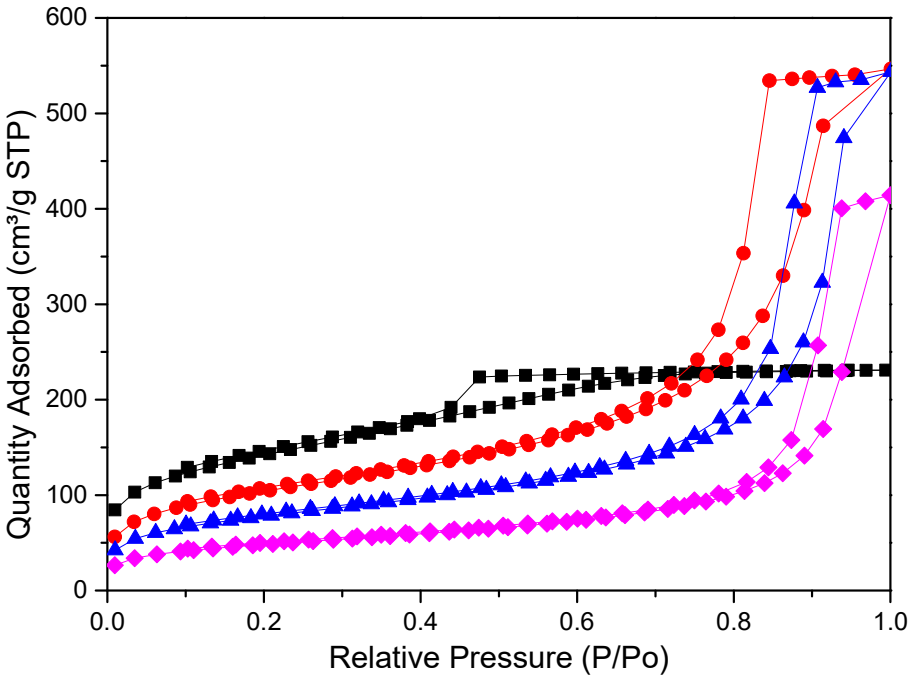

Figure 158: Nitrogen adsorption/desorption isotherms for 10% solids content RF xerogels, at R/C ratio of: 100 (■), 300 (●), 400 (▲) and 500 (◆).

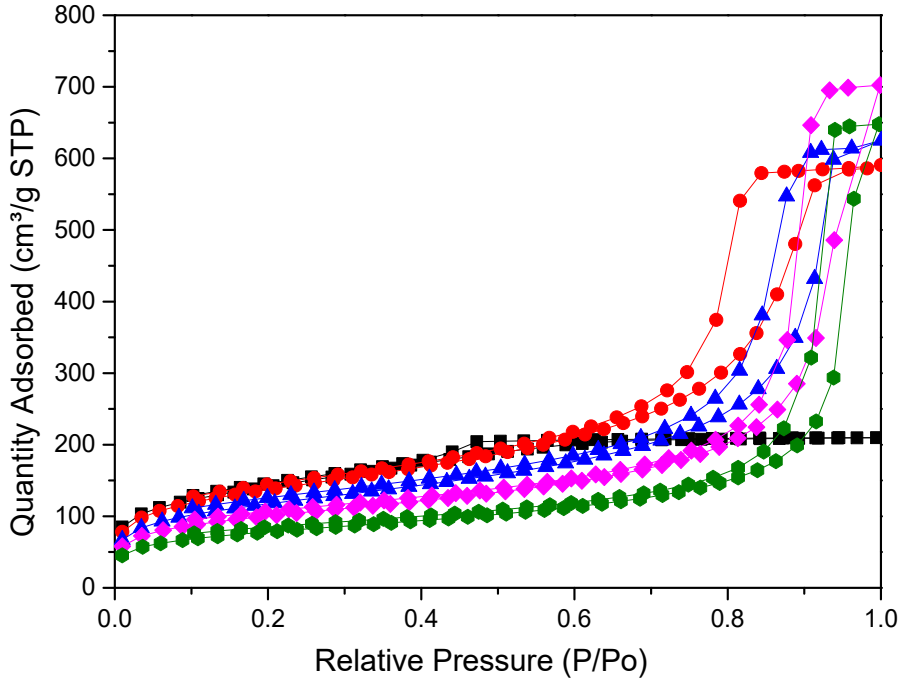

Figure 159: Nitrogen adsorption/desorption isotherms for 20% solids content RF xerogels, at R/C ratio of: 100 (■), 300 (●), 400 (▲), 500 (◆) and 600 (⬢).

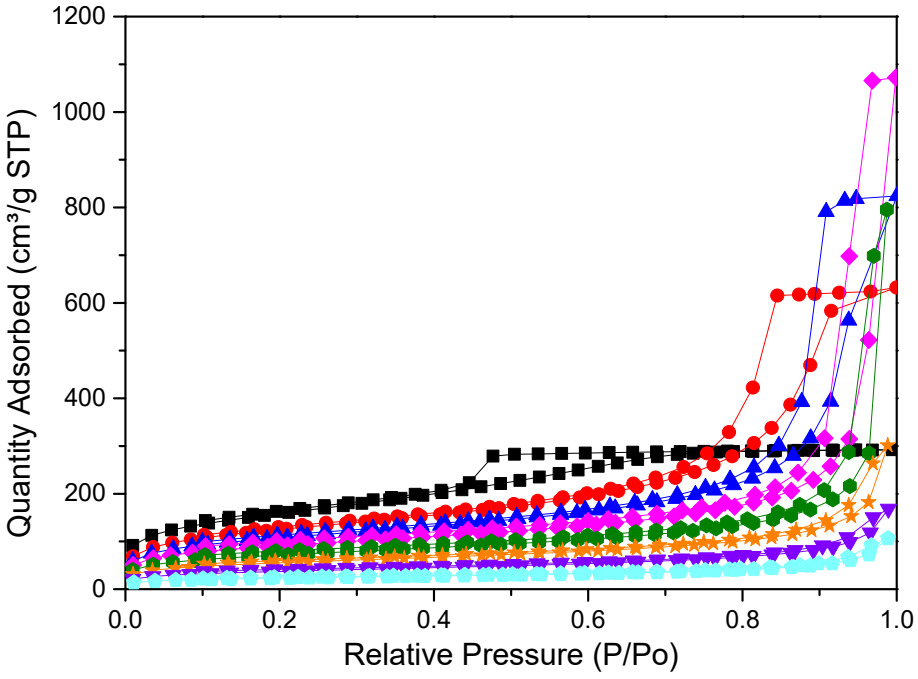

Figure 160: Nitrogen adsorption/desorption isotherms for 35% solids content RF xerogels, at R/C ratio of: 100 (■), 300 (●), 400 (▲), 500 (◆), 600 (⬢), 700 (★), 800 (▼) and 900 (⬟).

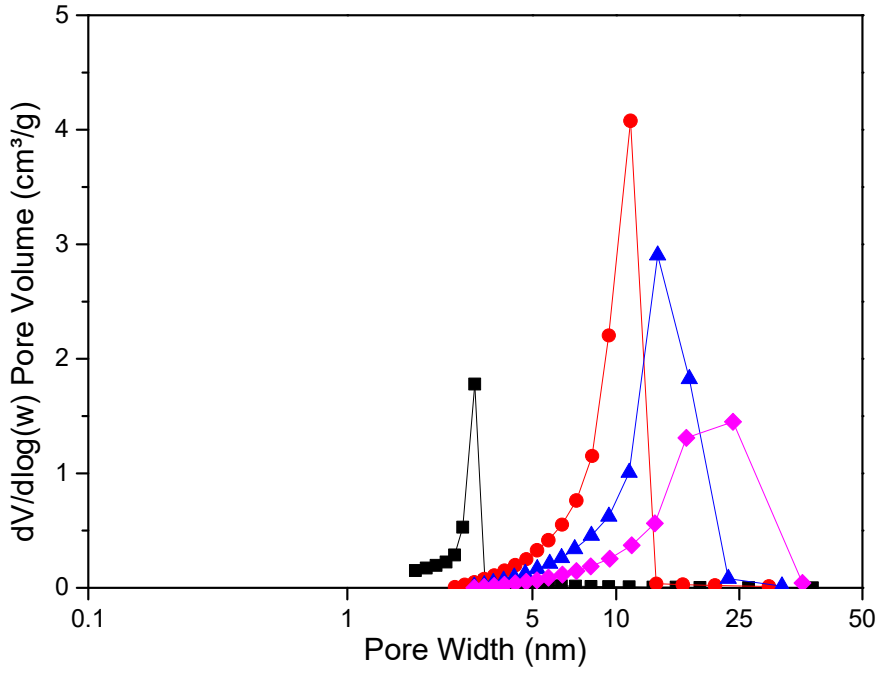

Figure 161: Pore size distributions for 10% solids content RF xerogels, at R/C ratio of: 100 (■), 300 (●), 400 (▲) and 500 (◆).

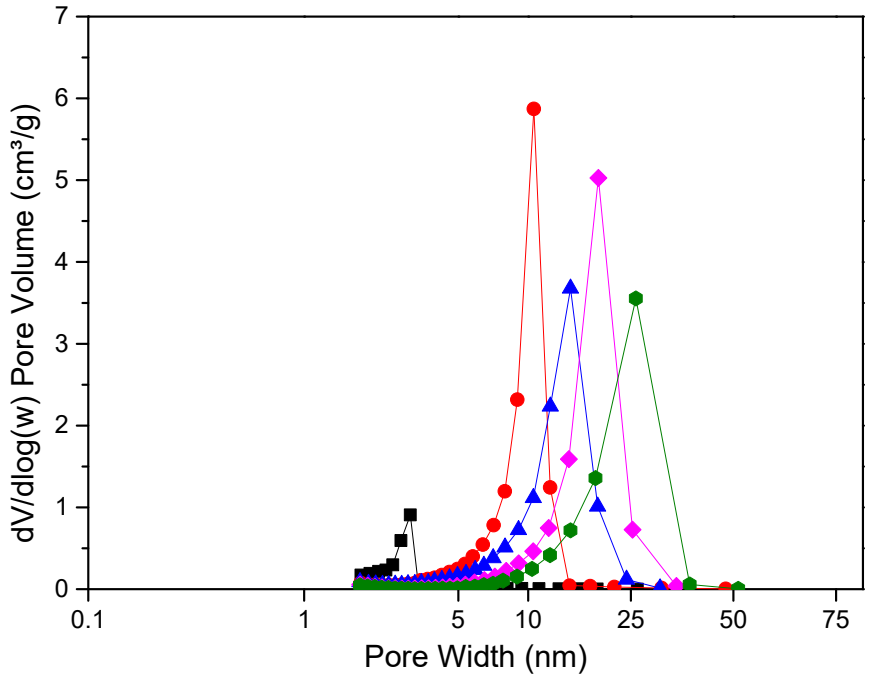

Figure 162: Pore size distributions for 20% solids content RF xerogels, at R/C ratio of: 100 (■), 300 (●), 400 (▲), 500 (◆) and 600 (⬢).

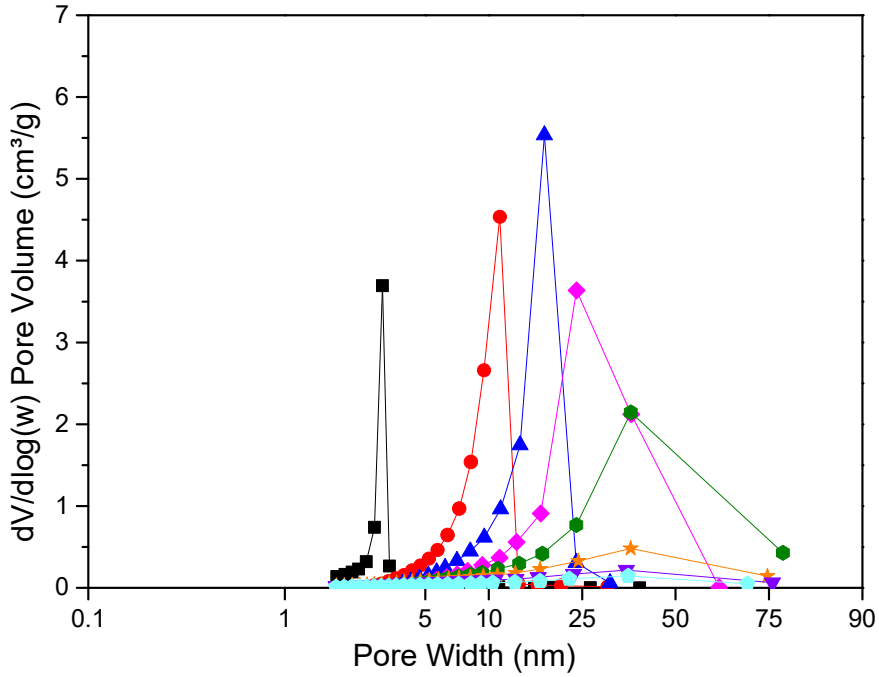

Figure 163: Pore size distributions for 35% solids content RF xerogels, at R/C ratio of: 100 (■), 300 (●), 400 (▲), 500 (◆), 600 (⬢), 700 (★), 800 (▼) and 900 (⬟).

C3 Thermal conductivity

This part of Appendix D details the thermal diffusivities, heat capacities, densities used in calculations of thermal conductivity for selected RF xerogel samples. It contains three measurements for each property, which were used to estimate the average value for the final thermal conductivity.

Table 111: Thermophysical properties used in the calculation of thermal conductivity for disc-shaped RF xerogel prepared using R/C ratio of 400 at 30% solids content.

Temperature °C	Half time ($t_{0.5}$) s	Thickness $\times 10^{-3}$ m	Diffusivity $\times 10^{-8}$ m^2s^{-1}	C_p $J\,kg^{-1}K^{-1}$	Density $kg\,m^{-3}$	Thermal Conductivity $Wm^{-1}K^{-1}$
25	13.59	1.8	3.31	1380	478	0.022
25	13.67	1.8	3.29	1380	478	0.022
25	13.59	1.8	3.31	1380	478	0.022
50	13.51	1.8	3.33	1450	478	0.023
50	13.46	1.8	3.34	1450	478	0.023
50	13.51	1.8	3.33	1450	478	0.023
100	12.92	1.8	3.48	1860	478	0.031
100	12.92	1.8	3.48	1860	478	0.031
100	12.92	1.8	3.48	1860	478	0.031
150	12.39	1.8	3.63	1900	478	0.033
150	12.39	1.8	3.63	1900	478	0.033
150	12.39	1.8	3.63	1900	478	0.033
200	11.13	1.8	4.04	2120	478	0.041
200	11.68	1.8	3.85	2120	478	0.039
200	11.68	1.8	3.85	2120	478	0.039

Table 112: Thermophysical properties used in the calculation of thermal conductivity for disc-shaped RF xerogel prepared using R/C ratio of 400 at 40% solids content.

Temperature °C	Half time ($t_{0.5}$) s	Thickness $\times 10^{-3}$ m	Diffusivity $\times 10^{-8}$ m^2s^{-1}	C_p $J\,kg^{-1}K^{-1}$	Density $kg\,m^{-3}$	Thermal Conductivity $Wm^{-1}K^{-1}$
25	11.12	1.66	3.44	1069	462	0.017
25	10.51	1.66	3.64	1069	462	0.018
25	10.51	1.66	3.64	1069	462	0.018
50	10.48	1.66	3.65	1245	462	0.021
50	11.59	1.66	3.30	1245	462	0.019
50	11.00	1.66	3.48	1245	462	0.020
100	11.38	1.66	3.36	1352	462	0.021
100	10.86	1.66	3.52	1352	462	0.022
100	10.86	1.66	3.52	1352	462	0.022
150	10.42	1.66	3.67	1475	462	0.025
150	10.42	1.66	3.67	1475	462	0.025
150	10.86	1.66	3.52	1475	462	0.024
200	9.96	1.66	3.84	1633	462	0.029
200	9.31	1.66	4.11	1633	462	0.031
200	9.31	1.66	4.11	1633	462	0.031

Table 113: Thermophysical properties used in the calculation of thermal conductivity for powdered RF xerogel prepared using R/C ratio of 1000 at 30% solids content.

Temperature °C	Half time ($t_{0.5}$) s	Thickness $\times 10^{-3}$ m	Diffusivity $\times 10^{-8}$ m^2s^{-1}	C_p $J\ kg^{-1}K^{-1}$	Density $kg\ m^{-3}$	Thermal Conductivity $Wm^{-1}K^{-1}$
25	3.38	0.65	1.74	687	1269	0.015
25	3.34	0.65	1.75	687	1269	0.015
25	3.39	0.65	1.71	687	1269	0.015
50	3.18	0.65	1.84	730	1269	0.017
50	3.19	0.65	1.84	730	1269	0.017
50	3.16	0.65	1.85	730	1269	0.017
100	2.81	0.65	2.08	767	1269	0.020
100	2.80	0.65	2.09	767	1269	0.020
100	2.79	0.65	2.09	767	1269	0.020
150	2.54	0.65	2.30	799	1269	0.023
150	2.54	0.65	2.31	799	1269	0.023
150	2.53	0.65	2.31	799	1269	0.023
200	2.30	0.65	2.55	870	1269	0.028
200	2.32	0.65	2.52	870	1269	0.028
200	2.32	0.65	2.52	870	1269	0.028

Table 114: Thermophysical properties used in the calculation of thermal conductivity for powdered RF xerogel prepared using R/C ratio of 1000 at 40% solids content.

Temperature °C	Half time ($t_{0.5}$) s	Thickness $\times 10^{-3}$ m	Diffusivity $\times 10^{-8}$ m^2s^{-1}	C_p $J\ kg^{-1}K^{-1}$	Density $kg\ m^{-3}$	Thermal Conductivity $Wm^{-1}K^{-1}$
25	2.66	0.65	2.20	780	1325	0.023
25	2.69	0.65	2.18	780	1325	0.023
25	2.69	0.65	2.18	780	1325	0.023
50	2.59	0.65	2.27	820	1325	0.025
50	2.59	0.65	2.27	820	1325	0.025
50	2.57	0.65	2.28	820	1325	0.025
100	2.35	0.65	2.50	985	1325	0.033
100	2.35	0.65	2.50	985	1325	0.033
100	2.34	0.65	2.50	985	1325	0.033
150	2.22	0.65	2.64	990	1325	0.035
150	2.23	0.65	2.63	990	1325	0.034
150	2.23	0.65	2.63	990	1325	0.035
200	2.00	0.65	2.90	1053	1325	0.041
200	19.97	0.65	2.93	1053	1325	0.041
200	2.00	0.65	2.93	1053	1325	0.041

C4 Density of RF xerogel suing pycnometer method

Table 115: Density of different RF xerogels measured by pycnometer method.

R/C	Bulk density g/cm^3
Solids 10%	
100	1.705
300	1.500
400	1.428
500	2.103
Solids 20%	
100	0.991
300	1.048
400	2.056
500	1.907
600	1.513
Solids 25%	
100	1.661
300	1.442
400	1.241
500	1.340
600	1.606
700	1.675
Solids 30%	
100	1.815
300	1.219
400	1.113
500	0.952
600	0.837
700	0.625
800	0.762
Solids 35%	
100	0.979
300	0.866
400	0.831
500	0.806
600	0.637
700	0.590
800	0.394
900	0.560

Appendix D – Additional results related to RF xerogel blankets

This Appendix displays the results cited in Chapter 5, but not presented in the main text.

It contains additional nitrogen adsorption/desorption isotherms and pore size distributions for RF blanket samples, prepared using Na_2CO_3 as a catalyst.

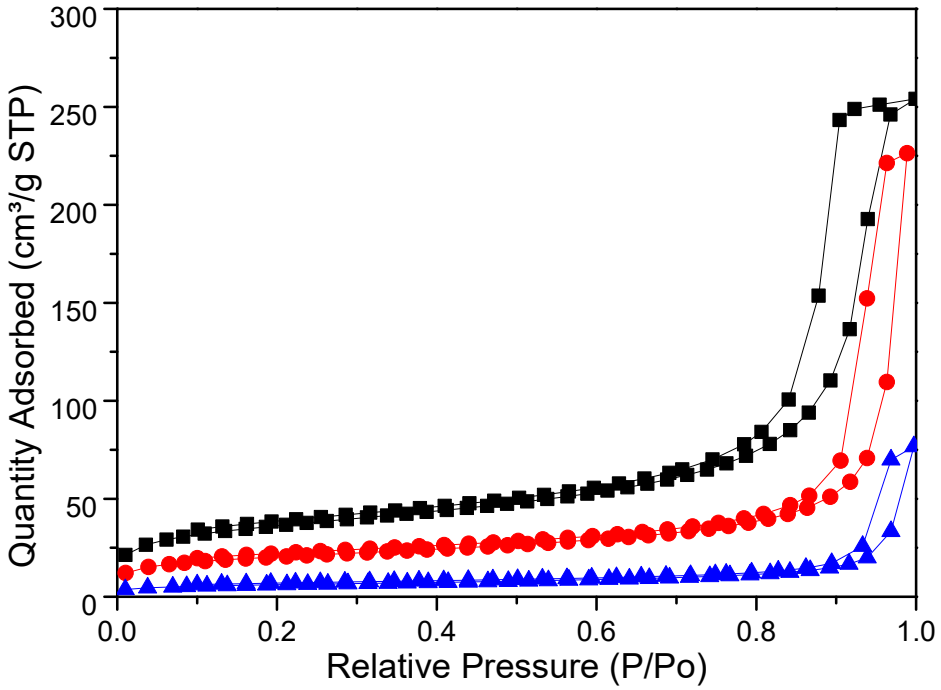

Figure 164: Nitrogen adsorption/desorption isotherms for 10% solids content RF blankets, at R/C of: 300 (■), 400 (●) and 500 (▲).

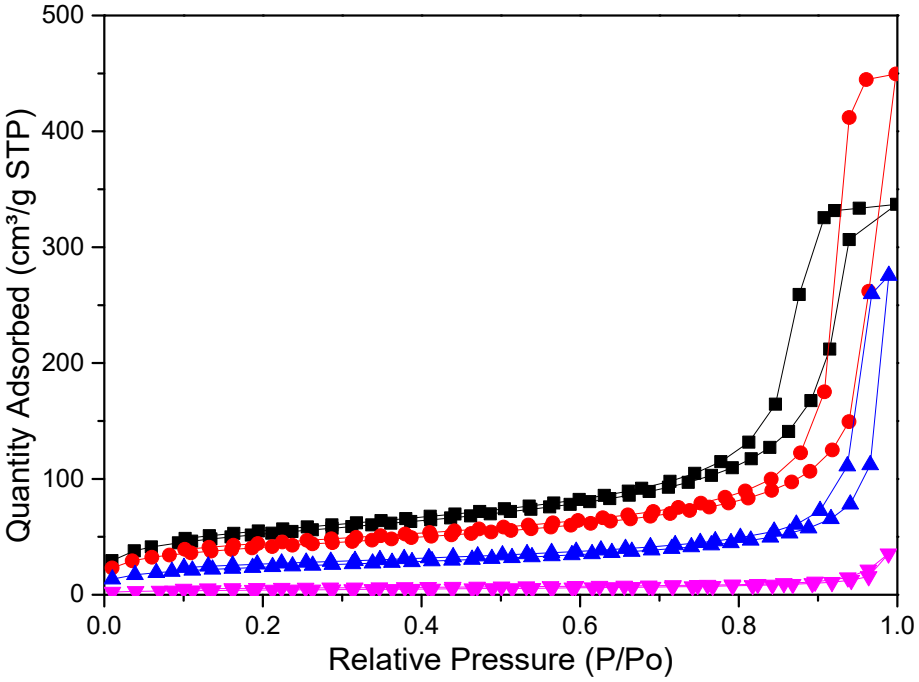

Figure 165: Nitrogen adsorption/desorption isotherms for 20 % solids content RF blankets, at R/C of: 300 (■), 400 (●), 500 (▲) and 600 (▼).

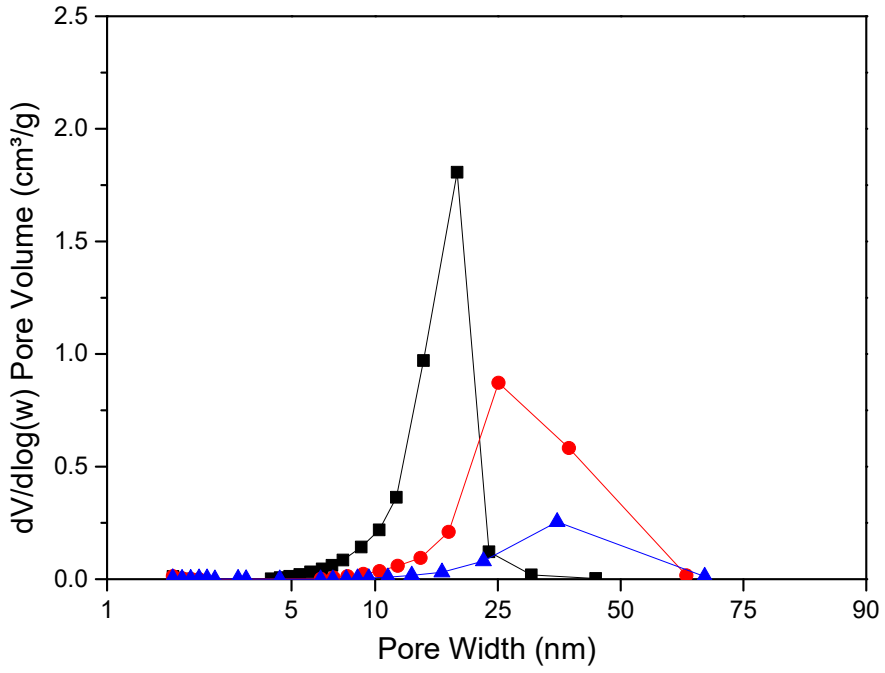

Figure 166: Pore size distributions for 10% solids content RF blanket, at R/C of: 300 (■), 400 (●) and 500 (▲).

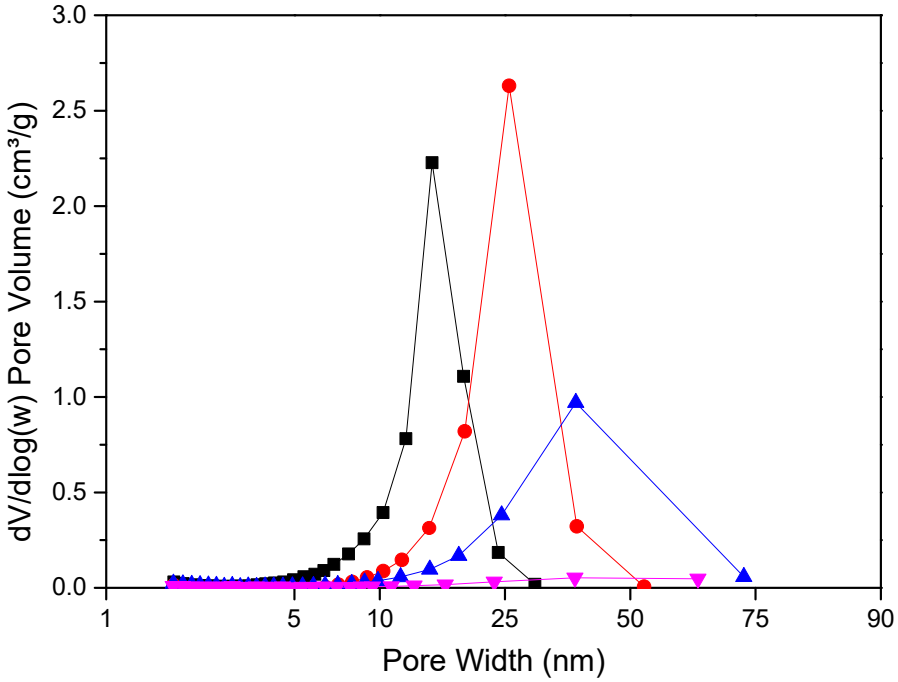

Figure 167: Pore size distributions for 20% solids content RF blanket, at R/C of: 300 (■), 400 (●), 500 (▲), and 600 (▼).

Appendix E – Life cycle assessment: 1 m^3 Resorcinol – formaldehyde composite blanket

Table 116: Prices of raw material used for lab-scale RF synthesis.

Product	CAS Number	Supplier	Pack size	Pack price £	Unit price £/unit
Resorcinol	108-46-3	Merck	1 Kg	76.40	76.40 £/Kg
Formaldehyde solution	50-00-0	Merck	1 L	24.60	24.60 £/L
Sodium carbonate	497-19-8	Merck	0.5 Kg	50.30	100.60 £/kg
Acetone	67-64-1	VWR International	2.5 L	3.99	1.6 £/L
PET Fibre		Cytec	20m Length× 68.5cm×0.6 cm	49.99	60.82 £/m^3

Table 117: LCA summary for 1 m^3 RF composite blanket.

Environmental impacts by stage						
Analysis name:					Functional unit	
Resorcinol-formaldehyde composite blanket					1 m3	
	Carbon footprint	Acidification potential	Eutrophication potential	Ozone layer depletion potential	Photochemical smog potential	Human toxicity potential
	tonne CO2 eq./f.u.	tonne SO2 eq./f.u.	tonne phosphate eq./f.u.	tonne R11 eq./f.u.	tonne ethene eq./f.u.	tonne DCB eq./f.u.
Raw Materials	9.79	0.029	3.69E-3	7.23E-8	1.98E-3	2.78
Mixing	4.67E-5	3.45E-7	2.50E-7	3.54E-8	1.53E-4	5.52E-4
Impregnation	0.00	0.00	0.00	0.00	1.53E-4	2.45E-4
Heating	4.84E-3	3.58E-5	2.59E-5	3.67E-6	2.58E-10	0.032
Solvent exchange	0.196	4.64E-4	1.71E-4	1.02E-9	2.47E-5	8.03E-3
Drying	0.082	2.01E-4	7.74E-5	9.51E-7	1.02E-5	0.012
Stage 6	0.00	0.00	0.00	0.00	0.00	0.00
Stage 7	0.00	0.00	0.00	0.00	0.00	0.00
Stage 8	0.00	0.00	0.00	0.00	0.00	0.00
Equipment washing	1.21E-4	3.46E-6	1.30E-6	1.10E-11	6.32E-6	6.84E-5
Packging	0.00	0.00	0.00	0.00	0.00	0.00
Storage	1.56E-4	1.15E-6	8.34E-7	1.18E-7	8.28E-12	1.02E-3
Use	0.011	0.00	0.00	0.00	0.00	0.00
Transport	6.98E-3	2.63E-5	8.78E-6	9.82E-10	2.58E-6	3.42E-3
Total per f.u.	10.1	0.029	3.98E-3	4.84E-6	2.33E-3	2.83
Co-products	0.00	0.00	0.00	0.00	0.00	0.00
Total inc. co-products	10.1	0.029	3.98E-3	4.84E-6	2.33E-3	2.83
Environmental impact by category						
Raw materials	6.43	0.029	3.66E-3	7.08E-8	1.98E-3	2.77
Energy	6.29E-3	7.06E-4	2.77E-4	4.77E-6	3.50E-5	0.053
Direct Emissions	0.00	0.00	0.00	0.00	3.12E-4	4.99E-4
Packaging	0.013	4.29E-5	3.22E-5	1.44E-9	2.57E-6	8.52E-3
Transport	6.98E-3	2.63E-5	8.78E-6	9.82E-10	2.58E-6	3.42E-3
Waste	0.288	0.00	0.00	0.00	0.00	0.00
Land use change	3.35	0.00	0.00	0.00	0.00	0.00
Carbon storage	0.00	0.00	0.00	0.00	0.00	0.00
Total per f.u.	10.1	0.029	3.98E-3	4.84E-6	2.33E-3	2.83
Co-products	0.00	0.00	0.00	0.00	0.00	0.00
Total inc. co-products	10.1	0.029	3.98E-3	4.84E-6	2.33E-3	2.83

References

1. Brabazon, D., *Nanostructured Materials*, in *Reference Module in Materials Science and Materials Engineering*. 2016, Elsevier.

2. Fricke, J. and A. Emmerling, *Aerogels—Recent Progress in Production Techniques and Novel Applications.* Journal of Sol-Gel Science and Technology, 1998. **13**(1): p. 299-303.

3. Brinker, C.J. and G.W. Scherer, *Sol-gel science: the physics and chemistry of sol-gel processing*. 1990, San Diego: Academic press.

4. Hench, L.L. and J.K. West, *The Sol-Gel process.* Chemical Reviews, 1990. **90**(1): p. 33-72.

5. Graham, T., *Liquid Diffusion Applied to Analysis.* Philosophical Transactions of the Royal Society of London, 1861. **151**(0): p. 183-224.

6. Graham, T., *XXXV.-On the properties of silicic acid and other analogous colloidal substances.* Journal of the Chemical Society, 1864. **17**(0): p. 318-327.

7. Schubert, U., *Chemistry and Fundamentals of the Sol–Gel Process*, in *The Sol–Gel Handbook: Synthesis, Characterization, and Applications*, D. Levy and M. Zayat, Editors. 2015, Wiley-VCH Verlag GmbH & Co. KGaA: Weinheim Germany.

8. Pierre, A.C. and G.M. Pajonk, *Chemistry of aerogels and their applications.* Chemical Reviews, 2002. **102**(11): p. 4243-4266.

9. Calvo, E.G., J.Á. Menéndez, and A. Arenillas, *Designing nanostructured carbon xerogels*, in *Nanomaterials*. 2011, InTech.

10. Maleki, H., L. Durães, and A. Portugal, *An overview on silica aerogels synthesis and different mechanical reinforcing strategies.* Journal of Non-Crystalline Solids, 2014. **385**: p. 55-74.

11. Gesser, H.D. and P.C. Goswami, *Aerogels and related porous materials.* Chemical Reviews, 1989. **89**(4): p. 765-788.

12. Ayen, R.J. and P.A. Iacobucci, *Metal Oxide Aerogel Preparation by Supercritical Extraction*, in *Reviews in Chemical Engineering*. 1988. p. 157.

13. Hüsing, N. and U. Schubert, *Aerogels—Airy Materials: Chemistry, Structure, and Properties.* Angewandte Chemie International Edition, 1998. **37**(1-2): p. 22-45.

14. Schmidt, M. and F. Schwertfeger, *Applications for silica aerogel products.* Journal of Non-Crystalline Solids, 1998. **225**: p. 364-368.

15. Pajonk, G.M., *Some applications of silica aerogels.* Colloid and Polymer Science, 2003. **281**(7): p. 637-651.

16. Rao, A.V., et al., *Synthesis and Characterization of Hydrophobic Silica Aerogels Using Trimethylethoxysilane as a Co-Precursor.* Journal of Sol-Gel Science and Technology, 2003. **27**(2): p. 103-109.

17. Soleimani Dorcheh, A. and M.H. Abbasi, *Silica aerogel; synthesis, properties and characterization.* Journal of Materials Processing Technology, 2008. **199**(1): p. 10-26.

18. Ye, L., et al., *Synthesis and Characterization of Silica/Carbon Composite Aerogels.* Journal of the American Ceramic Society, 2010. **93**(4): p. 1156-1163.

19. Du, A., et al., *A Special Material or a New State of Matter: A Review and Reconsideration of the Aerogel.* Materials, 2013. **6**(3): p. 941-968.

20. Berthon-Fabry, S., et al., *Evaluation of lightweight and flexible insulating aerogel blankets based on Resorcinol-Formaldehyde-Silica for space applications.* European Polymer Journal, 2017. **93**: p. 403-416.

21. Sachithanadam, M. and S.C. Joshi, *Silica Aerogel Composites*. Engineering materials 2016, Singapore: Springer.

22. Tillotson, T.M. and L.W. Hrubesh. *Transparent ultralow-density silica aerogels prepared by a two-step sol-gel process*. 1991. United States.

23. Coasne, B., et al., *Adsorption, intrusion and freezing in porous silica: the view from the nanoscale.* Chemical Society Reviews, 2013. **42**(9): p. 4141-4171.

24. Saoud, K.M., et al., *Fabrication of strong and ultra-lightweight silica-based aerogel materials with tailored properties.* Journal of Porous Materials, 2017.

25. Heinrich, T., U. Klett, and J. Fricke, *Aerogels—Nanoporous materials part I: Sol-gel process and drying of gels.* Journal of Porous Materials, 1995. **1**(1): p. 7-17.

26. Iler, R.K., *The chemistry of silica : solubility, polymerization, colloid and surface properties, and biochemistry*. 1979, New York: New York : Wiley.

27. Norris, P.M. and S. Shrinivasan, *Aerogels: Unique material, fascinating properties and unlimited applications*, in *Annual review of heat transfer* G. Chen, V. Prasad, and Y. Jaluria, Editors. 2005, begell: New York. p. 385-408.

28. Fricke, J., et al. *Thermal properties of silica aerogels.* Le Journal de Physique Colloques, 1989. **50**(C4): p. C4-87-C4-97.

29. Capadona, L.A., et al., *Flexible, low-density polymer crosslinked silica aerogels.* Polymer, 2006. **47**(16): p. 5754-5761.

30. Gurav, J.L., et al., *Silica Aerogel: Synthesis and Applications.* Journal of Nanomaterials, 2010. **2010**: p. 11.

31. Leventis, N., et al., *Nanoengineering Strong Silica Aerogels.* Nano Letters, 2002. **2**(9): p. 957-960.

32. Bheekhun, N., A.R. Abu Talib, and M.R. Hassan, *Aerogels in Aerospace: An Overview.* Advances in Materials Science and Engineering, 2013. **2013**: p. 18.

33. Maleki, H., *Recent advances in aerogels for environmental remediation applications: A review.* Chemical Engineering Journal, 2016. **300**(Supplement C): p. 98-118.

34. NASA. *Aerogel photo*. STARDUST 2007 [cited 2017 19th September]; Available from: https://stardust.jpl.nasa.gov/photo/aerogel1.html.

35. Pekala, R.W., *Organic aerogels from the polycondensation of resorcinol with formaldehyde.* Journal of Materials Science, 1989. **24**(9): p. 3221-3227.

36. Pekala, R. and F.M. Kong, *A synthetic route to organic aerogels-mechanism, structure, and properties.* Le Journal de Physique Colloques, 1989. **50**(C4): p. C4-33-C4-40.

37. Elkhatat, A. and S.A. Al-Muhtaseb, *Advances in Tailoring Resorcinol-Formaldehyde Organic and Carbon Gels*, in *Adv. Mater.* 2011. p. 2887-2903.

38. Job, N., et al., *Rheological determination of the sol–gel transition during the aqueous synthesis of resorcinol-formaldehyde resins.* Colloids and Surfaces A: Physicochemical and Engineering Aspects, 2007. **293**(1): p. 224-228.

39. Laskowski, J., B. Milow, and L. Ratke, *Subcritically dried resorcinol–formaldehyde aerogels from a base–acid catalyzed synthesis route.* Microporous and Mesoporous Materials, 2014. **197**: p. 308-315.

40. Schaefer, D.W., R.W. Pekala, and G. Beaucage, *Origin of porosity in resorcinol-formaldehyde aerogels.* Journal of Non-Crystalline Solids, 1995. **186**: p. 159-167.

41. Gross, J., et al., *Elastic properties of crosslinked Resorcinol-Formaldehyde gels and aerogels.* Journal of Non-Crystalline Solids, 1997. **211**(1): p. 132-142.

42. Yoo, K.-P., et al., *Synthesis, characterisation, and thermal conductivity of resorcinol-formaldehyde aerogel.* HIGH TEMPERATURES HIGH PRESSURES, 2001. **33**(4): p. 441-446.

43. Al-Muhtaseb, S.A. and J.A. Ritter, *Preparation and Properties of Resorcinol–Formaldehyde Organic and Carbon Gels.* Advanced Materials, 2003. **15**(2): p. 101-114.

44. Mirzaeian, M. and P. Hall, *The control of porosity at nano scale in resorcinol formaldehyde carbon aerogels.* J Mater Sci, 2009. **44**(10): p. 2705-2713.

45. Schwan, M. and L. Ratke, *Flexibilisation of resorcinol–formaldehyde aerogels.* Journal of Materials Chemistry A, 2013. **1**(43): p. 13462-13468.

46. Alshrah, M., et al., *Nanostructure to thermal property relationship of resorcinol formaldehyde aerogels using the fractal technique.* Nanoscale, 2018. **10**(22): p. 10564-10575.

47. Prostredný, M., et al., *Process variable optimization in the manufacture of resorcinol–formaldehyde gel materials.* 2018.

48. Mulik, S. and C. Sotiriou-Leventis, *Resorcinol–Formaldehyde Aerogels*, in *Aerogels Handbook*, M.A. Aegerter, N. Leventis, and M.M. Koebel, Editors. 2011, Springer: New York. p. 215-234.

49. Dressler, H., *Resorcinol: its uses and derivatives*. Topics in applied chemistry, ed. A.R. Katritzky and G.J. Sabongi. 1994, Monroeville, USA: Springer Science & Business Media.

50. Dunky, M. and A. Pizzi, *Wood adhesives*, in *Adhesion Science and Engineering: Surface, Chemistry and Applications*, D.A. Dillard, A.V. Pocius, and M. Chaudhury, Editors. 2002, Elsevier Science B.V.: Amsterdam. p. 1039-1103.

51. Durairaj, R.B., *Resorcinol Based Resins and Applications*, in *Resorcinol : chemistry, technology, and applications*, Springerlink, Editor. 2005, Springer: Berlin. p. 179-261.

52. McMurry, J., *Organic chemistry*. 7th ed.. ed. 2008, Belmont, CA: Belmont, CA : Thomson Brooks/Cole.

53. Ouellette, R.J. and J.D. Rawn, *Electrophilic Aromatic Substitution*, in *Organic Chemistry*, R.J. Ouellette and J.D. Rawn, Editors. 2014, Elsevier: Boston. p. 417-451.

54. Dewick, P.M., *Essentials of organic chemistry : for students of pharmacy, medicinal chemistry and biological chemistry*. 2006, Chichester, England

J. Wiley.

55. Roberts, J.D. and M.C. Caserio, *Basic principles of organic chemistry*. 2nd ed. 1977: WA Benjamin, Inc.

56. Clayden, J., N. Greeves, and S.G. Warren, *Organic chemistry*. 2nd ed.. ed. 2012, Oxford: Oxford University Press.

57. Werstler, D.D., *Quantitative 13C n.m.r. characterization of aqueous formaldehyde resins: 2. Resorcinol-formaldehyde resins.* Polymer, 1986. **27**(5): p. 757-764.

58. Ingram, A.R., *Electronic interpretation of the uncatalyzed reaction between resorcinol and formaldehyde in alcohols and dioxane.* Canadian Journal of Chemistry, 1951. **29**(10): p. 863-870.

59. Gardziella, A., L.A. Pilato, and A. Knop, *Phenolic resins: chemistry, applications, standardization, safety and ecology*. 2 ed. 2013: Springer Science & Business Media.

60. Pilato, L., *Phenolic resins: a century of progress*. 2010: Springer.

61. Šebenik, A., U. Osredkar, and I. Vizovišek, *Study of the reaction between resorcinol and formaldehyde.* Polymer, 1981. **22**(6): p. 804-806.

62. Kim, M.G., L.W. Amos, and E.E. Barnes, *Investigation of a resorcinol–formaldehyde resin by 13C-NMR spectroscopy and intrinsic viscosity measurement.* Journal of Polymer Science Part A: Polymer Chemistry, 1993. **31**(7): p. 1871-1877.

63. Christiansen, A.W., *Resorcinol-formaldehyde reactions in dilute solution observed by carbon-13 NMR spectroscopy.* Journal of Applied Polymer Science, 2000. **75**(14): p. 1760-1768.

64. Moudrakovski, I.L., et al., *Nuclear Magnetic Resonance Studies of Resorcinol−Formaldehyde Aerogels.* The Journal of Physical Chemistry B, 2005. **109**(22): p. 11215-11222.

65. Gaca, K.Z., J.A. Parkinson, and J. Sefcik, *Kinetics of early stages of resorcinol-formaldehyde polymerization investigated by solution-phase nuclear magnetic resonance spectroscopy.* Polymer, 2017. **110**: p. 62-73.

66. Li, T., et al., *Mechanism of base-catalyzed resorcinol-formaldehyde and phenol-resorcinol-formaldehyde condensation reactions: A theoretical study.* Polymers, 2017. **9**(9).

67. Ouellette, R.J. and J.D. Rawn, *Aldehydes and Ketones: Nucleophilic Addition Reactions*, in *Organic Chemistry*, R.J. Ouellette and J.D. Rawn, Editors. 2014, Elsevier: Boston. p. 629-657.

68. Gaca, K.Z., *Kinetics and mechanisms of early stages of resorcinol-formaldehyde polmerization*, in *Department of Chemical and Process Engineering*. 2012, University of Strathclyde: Glasgow.

69. Hasse, H. and G. Maurer, *Kinetics of the Poly(oxymethylene) Glycol Formation in Aqueous Formaldehyde Solutions.* Industrial and Engineering Chemistry Research, 1991. **30**(9): p. 2195-2200.

70. Hahnenstein, I., et al., *NMR Spectroscopic and Densimetric Study of Reaction Kinetics of Formaldehyde Polymer Formation in Water, Deuterium Oxide, and Methanol.* Industrial & Engineering Chemistry Research, 1995. **34**(2): p. 440-450.

71. Winkelman, J.G.M., et al., *Kinetics and chemical equilibrium of the hydration of formaldehyde.* Chemical Engineering Science, 2002. **57**(19): p. 4067-4076.

72. Gaca-Zając, K.Z., et al., *Investigation of IR and Raman spectra of species present in formaldehyde-water-methanol systems.* Vibrational Spectroscopy, 2018. **97**: p. 44-54.

73. Gaca, K.Z., et al., *Equilibrium Speciation in Moderately Concentrated Formaldehyde–Methanol–Water Solutions Investigated Using 13C and 1H Nuclear Magnetic Resonance Spectroscopy.* Industrial & Engineering Chemistry Research, 2014. **53**(22): p. 9262-9271.

74. Lewicki, J.P., C.A. Fox, and M.A. Worsley, *On the synthesis and structure of resorcinol-formaldehyde polymeric networks – Precursors to 3D-carbon macroassemblies.* Polymer, 2015. **69**: p. 45-51.

75. Pekala, R.W., et al., *New organic aerogels based upon a phenolic-furfural reaction.* Journal of Non-Crystalline Solids, 1995. **188**(1): p. 34-40.

76. Li, W. and S. Guo, *Preparation of low-density carbon aerogels from a cresol/formaldehyde mixture.* Carbon, 2000. **38**(10): p. 1520-1523.

77. Li, W., G. Reichenauer, and J. Fricke, *Carbon aerogels derived from cresol–resorcinol–formaldehyde for supercapacitors.* Carbon, 2002. **40**(15): p. 2955-2959.

78. Scherdel, C. and G. Reichenauer, *Carbon xerogels synthesized via phenol-formaldehyde gels.* Microporous and Mesoporous Materials, 2009. **126**(1): p. 133-142.

79. Ghiloufi, I., L. Khezami, and L. El Mir, *Nanoporous activated carbon for fast uptake of heavy metals from aqueous solution.* Desalination and Water Treatment, 2015. **55**(4): p. 935-944.

80. Bhatt, R.R. and B.A. Shah, *Sorption studies of heavy metal ions by salicylic acid–formaldehyde–catechol terpolymeric resin: Isotherm, kinetic and thermodynamics.* Arabian Journal of Chemistry, 2015. **8**(3): p. 414-426.

81. Fiege, H., et al., *Phenol Derivatives*, in *Ullmann's Encyclopedia of Industrial Chemistry*. 2000, Wiley-VCH Verlag GmbH & Co. KGaA.

82. Wang, M., M. Leitch, and C. Xu, *Synthesis of phenol-formaldehyde resol resins using organosolv pine lignins.* European Polymer Journal, 2009. **45**(12): p. 3380-3388.

83. Paju, J., T. Pehk, and P. Christjanson *Structure of phenol-formaldehyde polycondensates*. Polymer Science, 2009. **58**, 45-52 DOI: 10.3176/proc.2009.1.08.

84. Scherdel, C., et al., *Organic and carbon xerogels derived from sodium carbonate controlled polymerisation of aqueous phenol-formaldehyde solutions.* Journal of Porous Materials, 2011. **18**(4): p. 443-450.

85. Shitta-Bey, G., M. Mirzaeian, and P. Hall, *Effect of composition, solvent exchange liquid and drying method on the porous structure of phenol-formaldehyde gels.* J Sol-Gel Sci Technol, 2011. **57**(2): p. 178-184.

86. Carlson, G., et al., *Aerogel commercialization: technology, markets and costs.* Journal of Non-Crystalline Solids, 1995. **186**: p. 372-379.

87. El Mir, L., et al., *Synthesis and characterization of electrical conducting nanoporous carbon structures.* Physica B: Condensed Matter, 2007. **395**(1): p. 104-110.

88. Garro–Galvez, J.M. and B. Riedl, *Pyrogallol–formaldehyde thermosetting adhesives.* Journal of Applied Polymer Science, 1997. **65**(2): p. 399-408.

89. Wu, D., R. Fu, and Z. Yu, *Organic and carbon aerogels from the NaOH-catalyzed polycondensation of resorcinol–furfural and supercritical drying in ethanol.* Journal of Applied Polymer Science, 2005. **96**(4): p. 1429-1435.

90. Mariscal, R., et al., *Furfural: a renewable and versatile platform molecule for the synthesis of chemicals and fuels.* Energy & Environmental Science, 2016. **9**(4): p. 1144-1189.

91. Mohammed, J., J., *Kinetics Study of(Phenol-Resorcinol-Formaldehyde) Resin.* Basrah journal of science, 2011. **29**(1C): p. 101-109.

92. Gaca, K.Z. and J. Sefcik, *Mechanism and kinetics of nanostructure evolution during early stages of resorcinol–formaldehyde polymerisation.* Journal of Colloid and Interface Science, 2013. **406**: p. 51-59.

93. Kinnertová, E. and V. Slovák, *Kinetics of resorcinol–formaldehyde polycondensation by DSC.* Journal of Thermal Analysis and Calorimetry, 2018. **134**(2): p. 1215-1222.

94. Stedry, P.J., *Resorcinol-Formaldehyde Reaction - Observed by Ultraviolet Absorption Measurements.* Industrial & Engineering Chemistry, 1951. **43**(10): p. 2372-2375.

95. Job, N., et al., *Porous carbon xerogels with texture tailored by pH control during sol–gel process.* Carbon, 2004. **42**(3): p. 619-628.

96. Job, N., et al., *Synthesis optimization of organic xerogels produced from convective air-drying of resorcinol–formaldehyde gels.* Journal of Non-Crystalline Solids, 2006. **352**(1): p. 24-34.

97. Alonso-Buenaposada, I.D., et al., *Acid-based resorcinol-formaldehyde xerogels synthesized by microwave heating.* Journal of Sol-Gel Science and Technology, 2017. **84**(1): p. 60-69.

98. Lin, C. and J.A. Ritter, *Effect of synthesis pH on the structure of carbon xerogels.* Carbon, 1997. **35**(9): p. 1271-1278.

99. Matos, I., et al., *The effect of surfactants on the porosity of carbon xerogels.* Microporous and Mesoporous Materials, 2006. **92**(1): p. 38-46.

100. Borchardt, H.J. and F. Daniels, *The Application of Differential Thermal Analysis to the Study of Reaction Kinetics.* Journal of the American Chemical Society, 1957. **79**(1): p. 41-46.

101. Reed, R.L., L. Weber, and B.S. Gottfried, *Differential Thermal Analysis and Reaction Kinetics.* Industrial & Engineering Chemistry Fundamentals, 1965. **4**(1): p. 38-46.

102. Šebenik, A., I. Vizovišek, and S. Lapanje, *Determination of kinetic parameters for the reaction between phenol and formaldehyde by differential scanning calorimetry.* European Polymer Journal, 1974. **10**(3): p. 273-278.

103. Malhotra, H. and V. Kumar, *Kinetics of the alkali-catalyzed o-cresol-formaldehyde reaction.* Journal of Macromolecular Science—Chemistry, 1979. **13**(1): p. 143-152.

104. Mulik, S., L. Sotiriou-Leventis, and N. Leventis, *Acid-catalyzed time-efficient synthesis of resorcinol-formaldehyde aerogels and crosslinking with isocyanates.* 2006.

105. Pekala, R.W., *Low density, resorcinol-formaldehyde aerogels*. 1989, Google Patents.

106. Rey-Raap, N., A. Arenillas, and J. Menéndez, *Carbon Gels and Their Applications: A Review of Patents*, in *Submicron Porous Materials*. 2017, Springer. p. 25-52.

107. Ruben, G.C., et al., *Imaging aerogels at the molecular level.* Journal of Materials Science, 1992. **27**(16): p. 4341-4349.

108. Tamborini, L., et al., *Production of Porous Carbons from Resorcinol-Formaldehyde Gels: Applications.* Handbook of Composites from Renewable Materials, Design and Manufacturing, 2017. **2**: p. 175.

109. Rey-Raap, N., J. Angel Menéndez, and A. Arenillas, *RF xerogels with tailored porosity over the entire nanoscale.* Microporous and Mesoporous Materials, 2014. **195**: p. 266-275.

110. Mulik, S., C. Sotiriou-Leventis, and N. Leventis, *Time-Efficient Acid-Catalyzed Synthesis of Resorcinol−Formaldehyde Aerogels.* Chemistry of Materials, 2007. **19**(25): p. 6138-6144.

111. Raff, R.A.V. and B.H. Silverman, *Kinetics of the Uncatalyzed Reactions between Resorcinol and Formaldehyde.* Industrial & Engineering Chemistry, 1951. **43**(6): p. 1423-1427.

112. Anderson, L., *The effect of the catalyst on the formation of RF xerogels*, in *Department of Chemical and Process Engineering*. 2014, University of Strathclyde: Glasgow.

113. Wu, D., et al., *Low-density organic and carbon aerogels from the sol–gel polymerization of phenol with formaldehyde.* Journal of Non-Crystalline Solids, 2005. **351**(10): p. 915-921.

114. Yamamoto, T., et al., *Interpretation of structure formation during the sol-gel transition of a resorcinol-formaldehyde solution by population balance.* Journal of Colloid And Interface Science, 2003. **264**(2): p. 532-537.

115. Berthon, S., et al., *DLS and SAXS investigations of organic gels and aerogels.* Journal of Non-Crystalline Solids, 2001. **285**(1): p. 154-161.

116. Kakunuri, M. and C.S. Sharma, *Resorcinol-formaldehyde derived carbon xerogels: A promising anode material for lithium-ion battery.* Journal of Materials Research, 2017. **33**(9): p. 1074-1087.

117. Gommes, C.J. and A.P. Roberts, *Structure development of resorcinol-formaldehyde gels: Microphase separation or colloid aggregation.* Physical Review E, 2008. **77**(4): p. 041409.

118. Bergna, H.E., *Colloid chemistry of silica: An overview*. 1994, ACS Publications.

119. Yamamoto, T., et al., *Dynamic and static light scattering study on the sol-gel transition of resorcinol-formaldehyde aqueous solution.* J Colloid Interface Sci, 2002. **245**(2): p. 391-6.

120. Yamamoto, T., et al., *Control of mesoporosity of carbon gels prepared by sol-gel polycondensation and freeze drying.* Journal of Non-Crystalline Solids, 2001. **288**(1): p. 46-55.

121. Tamon, H. and H. Ishizaka, *SAXS Study on Gelation Process in Preparation of Resorcinol–Formaldehyde Aerogel.* Journal of Colloid and Interface Science, 1998. **206**(2): p. 577-582.

122. Feinle, A., M.S. Elsaesser, and N. Hüsing, *Sol-gel synthesis of monolithic materials with hierarchical porosity.* Chemical Society Reviews, 2016. **45**(12): p. 3377-3399.

123. Xue, L., J. Zhang, and Y. Han, *Phase separation induced ordered patterns in thin polymer blend films.* Progress in Polymer Science, 2012. **37**(4): p. 564-594.

124. Gebert, M.S. and R.W. Pekala, *Fluorescence and light-scattering studies of sol-gel reactions.* Chemistry of Materials, 1994. **6**(2): p. 220-226.

125. Pekala, R.W. and D.W. Schaefer, *Structure of organic aerogels. 1. Morphology and scaling.* Macromolecules, 1993. **26**(20).

126. Taylor, S.J., et al., *Gelation Mechanism of Resorcinol-Formaldehyde Gels Investigated by Dynamic Light Scattering.* Langmuir, 2014. **30**(34): p. 10231-10240.

127. Lambert, S.M., et al., *Low-Density-FoamShells*, in *ICF Annual Report*, J. Lindl and D. Correll, Editors. 1997, Lawrence Livermore National Laboratory p. 22-30.

128. Kraiwattanawong, K., H. Tamon, and P. Praserthdam, *Influence of solvent species used in solvent exchange for preparation of mesoporous carbon xerogels from resorcinol and formaldehyde via subcritical drying.* Microporous and Mesoporous Materials, 2011. **138**(1): p. 8-16.

129. Wang, B., et al., *Progress in Drying Technology for Nanomaterials.* Drying Technology, 2005. **23**(1-2): p. 7-32.

130. Metzger, T., et al., *Understanding and Preventing Structural Changes during Drying of Gels*, in *Modern Drying Technology*, E. Tsotsas and A.S. Mujumdar, Editors. 2011, Wiley-VCH Verlag & Co. KGaA,: Weinheim, Germany.

131. Smith, D.M., et al., *Preparation of low-density xerogels at ambient pressure.* Journal of Non-Crystalline Solids, 1995. **186**: p. 104-112.

132. Czakkel, O., et al., *Influence of drying on the morphology of resorcinol–formaldehyde-based carbon gels.* Microporous and Mesoporous Materials, 2005. **86**(1): p. 124-133.

133. Scherer, G.W., *Theory of Drying.* Journal of the American Ceramic Society, 1990. **73**(1): p. 3-14.

134. Reuß, M. and L. Ratke, *Subcritically dried RF-aerogels catalysed by hydrochloric acid.* Journal of Sol-Gel Science and Technology, 2008. **47**(1): p. 74-80.

135. Alonso-Buenaposada, I.D., et al., *Acid-based resorcinol-formaldehyde xerogels synthesized by microwave heating.* Journal of Sol-Gel Science and Technology, 2017.

136. Mathieu, B., et al., *Freeze-dried resorcinol-formaldehyde gels.* Journal of Non-Crystalline Solids, 1997. **212**(2): p. 250-261.

137. Hu, L., et al., *Carbon Aerogel for Insulation Applications: A Review.* International Journal of Thermophysics, 2019. **40**(4): p. 39.

138. Şahin, İ., et al., *Kinetics of supercritical drying of gels.* Gels, 2018. **4**(1): p. 3.

139. Pakowski, Z., *Modern methods of drying nanomaterials.* Transport in porous media, 2007. **66**(1-2): p. 19-27.

140. Ren, H., et al., *Hydrophobicity control by a supercritical drying technique in a sol-gel process with hybrid materials.* Materials Research Bulletin, 2015. **70**: p. 87-92.

141. Czakkel, O., et al., *Drying of resorcinol–formaldehyde gels with CO2 medium.* Microporous and Mesoporous Materials, 2012. **148**(1): p. 34-42.

142. Szczurek, A., et al., *Porosity of resorcinol-formaldehyde organic and carbon aerogels exchanged and dried with supercritical organic solvents.* Materials Chemistry and Physics, 2011. **129**(3): p. 1221-1232.

143. Rojas-Cervantes, M.L., *Some strategies to lower the production cost of carbon gels.* Journal of Materials Science, 2015. **50**(3): p. 1017-1040.

144. Yamamoto, T., et al., *Effect of drying method on mesoporosity of Resorcinol-Formaldehyde drygel and Carbon gel* Drying Technology, 2001. **19**(7): p. 1319-1333.

145. Shen, J. and D.Y. Guan, *Preparation and Application of Carbon Aerogels*, in *Aerogels Handbook*, M.A. Aegerter, N. Leventis, and M.M. Koebel, Editors. 2011, Springer New York: New York, NY. p. 813-831.

146. Zhang, L., et al., *Structure and electrochemical properties of resorcinol–formaldehyde polymer-based carbon for electric double-layer capacitors.* Carbon, 2007. **45**(7): p. 1439-1445.

147. Zhu, Y., et al., *Resorcinol-formaldehyde based porous carbon as an electrode material for supercapacitors.* Carbon, 2007. **45**(1): p. 160-165.

148. Rey-Raap, N., J. Angel Menéndez, and A. Arenillas, *Simultaneous adjustment of the main chemical variables to fine-tune the porosity of carbon xerogels.* Carbon, 2014. **78**(Supplement C): p. 490-499.

149. Calvo, E.G., et al., *Exploring New Routes in the Synthesis of Carbon Xerogels for Their Application in Electric Double-Layer Capacitors.* Energy & Fuels, 2010. **24**(6): p. 3334-3339.

150. Zubizarreta, L., et al., *Development of microporous carbon xerogels by controlling synthesis conditions.* Journal of Non-Crystalline Solids, 2008. **354**(10): p. 817-825.

151. Sharma, C.S., et al., *Synthesis of carbon xerogel particles and fractal-like structures.* Chemical Engineering Science, 2009. **64**(7): p. 1536-1543.

152. Awadallah-F, A., A. Elkhatat, and S. Al-Muhtaseb, *Impact of synthesis conditions on meso- and macropore structures of resorcinol–formaldehyde xerogels.* J Mater Sci, 2011. **46**(24): p. 7760-7769.

153. Morales-Torres, S., et al., *Textural and mechanical characteristics of carbon aerogels synthesized by polymerization of resorcinol and formaldehyde using alkali carbonates as basification agents.* Phys. Chem. Chem. Phys., 2010. **12**(35): p. 10365-10372.

154. Job, N., et al., *Effect of the counter-ion of the basification agent on the pore texture of organic and carbon xerogels.* Journal of Non-Crystalline Solids, 2008. **354**(40): p. 4698-4701.

155. Horikawa, T., et al., *Controllability of pore characteristics of resorcinol–formaldehyde carbon aerogel.* Carbon, 2004. **42**(8): p. 1625-1633.

156. Calvo, E.G., J.A. Menéndez, and A. Arenillas, *Influence of alkaline compounds on the porosity of resorcinol-formaldehyde xerogels.* Journal of Non-Crystalline Solids, 2016. **452**: p. 286-290.

157. Merzbacher, C.I., et al., *Carbon aerogels as broadband non-reflective materials.* Journal of Non-Crystalline Solids, 2001. **285**(1): p. 210-215.

158. Brandt, R., et al., *Acetic Acid Catalyzed Carbon Aerogels.* Journal of Porous Materials, 2003. **10**(3): p. 171-178.

159. Brandt, R. and J. Fricke, *Acetic-acid-catalyzed and subcritically dried carbon aerogels with a nanometer-sized structure and a wide density range.* Journal of Non-Crystalline Solids, 2004. **350**(Supplement C): p. 131-135.

160. Barbieri, O., et al., *Small-angle X-ray scattering of a new series of organic aerogels.* Journal of Non-Crystalline Solids, 2001. **285**(1): p. 109-115.

161. Pekala, R.W., et al., *Aerogels derived from multifunctional organic monomers.* Journal of Non-Crystalline Solids, 1992. **145**: p. 90-98.

162. Lu, X., et al., *Correlation between structure and thermal conductivity of organic aerogels.* Journal of Non-Crystalline Solids, 1995. **188**(3): p. 226-234.

163. Bock, V., A. Emmerling, and J. Fricke, *Influence of monomer and catalyst concentration on RF and carbon aerogel structure.* Journal of Non-Crystalline Solids, 1998. **225**: p. 69-73.

164. Tamon, H., et al., *Porous structure of organic and carbon aerogels synthesized by sol-gel polycondensation of resorcinol with formaldehyde.* Carbon, 1997. **35**(6): p. 791-796.

165. Zanto, E.J., S.A. Al-Muhtaseb, and J.A. Ritter, *Sol−Gel-Derived Carbon Aerogels and Xerogels: Design of Experiments Approach to Materials Synthesis.* Industrial & Engineering Chemistry Research, 2002. **41**(13): p. 3151-3162.

166. Qin, G. and S. Guo, *Preparation of RF organic aerogels and carbon aerogels by alcoholic sol-gel process.* Carbon, 2001. **39**(12): p. 1935-1937.

167. Fairén-Jiménez, D., F. Carrasco-Marín, and C. Moreno-Castilla, *Inter- and Intra-Primary-Particle Structure of Monolithic Carbon Aerogels Obtained with Varying Solvents.* Langmuir, 2008. **24**(6): p. 2820-2825.

168. Najeh, I., et al., *Synthesis and characterization of electrical conducting porous carbon structures based on resorcinol–formaldehyde.* Solid State Sciences, 2009. **11**(10): p. 1747-1751.

169. Najeh, I., et al., *Electrical Properties of Partial Carbonized Nanoporous Resin Based on Resorcinol-Formaldehyde.* Sensors & Transducers, 2014. **27**: p. 285-289.

170. Ellingboe, J.L. and J.H. Runnels, *Solubilities of Sodium Carbonate and Sodium Bicarbonate in Acetone-Water and Methanol-Water Mixtures.* Journal of Chemical & Engineering Data, 1966. **11**(3): p. 323-324.

171. ThermoFisher, *Acetone*, in *Material Safety Data Sheet*. 2009: Online.

172. Lee, H.-J., J.-H. Song and J.-H. Kim, *Synthesis of resorcinol/formaldehyde gel particles by the sol- emulsion–gel technique.* Materials Letters, 1998. **37**(4): p. 197-200.

173. Schwan, M., R. Tannert, and L. Ratke, *New soft and spongy resorcinol–formaldehyde aerogels.* The Journal of Supercritical Fluids, 2016. **107**: p. 201-208.

174. Tamon, H. and H. Ishizaka, *Porous characterization of carbon aerogels.* Carbon, 1998. **36**(9): p. 1397-1399.

175. Tamon, H. and H. Ishizaka, *Influence of Gelation Temperature and Catalysts on the Mesoporous Structure of Resorcinol–Formaldehyde Aerogels.* Journal of Colloid And Interface Science, 2000. **223**(2): p. 305-307.

176. Despetis, F., et al., *Effect of Aging on Mechanical Properties of Resorcinol-Formaldehyde Gels.* Journal of Sol-Gel Science and Technology, 2000. **19**(1): p. 829-831.

177. Job, N., et al., *Carbon aerogels, cryogels and xerogels: Influence of the drying method on the textural properties of porous carbon materials.* Carbon, 2005. **43**(12): p. 2481-2494.

178. Pekala, R., C. Alviso, and J. LeMay, *Organic aerogels: microstructural dependence of mechanical properties in compression.* Journal of non-crystalline solids, 1990. **125**(1-2): p. 67-75.

179. Deng, Z., et al., *High strength SiO 2 aerogel insulation* Journal of Non-Crystalline Solids, 1998. **225**: p. 101-104.

180. Léonard, A., et al., *Evolution of mechanical properties and final textural properties of resorcinol–formaldehyde xerogels during ambient air drying.* Journal of Non-Crystalline Solids, 2008. **354**(10): p. 831-838.

181. Yang, J., et al., *Compressive behaviors and morphological changes of resorcinol–formaldehyde aerogel at high strain rates.* Microporous and Mesoporous Materials, 2010. **133**(1): p. 134-140.

182. Yang, X., et al., *Experimental investigation on mechanical properties of a fiber-reinforced silica aerogel composite.* Materials Science and Engineering: A, 2011. **528**(13–14): p. 4830-4836.

183. Alshrah, M., et al., *Development of high-porosity resorcinol formaldehyde aerogels with enhanced mechanical properties through improved particle necking under CO2 supercritical conditions.* Journal of Colloid And Interface Science, 2017. **485**: p. 65-74.

184. Mullins, M.J., D. Liu, and H.J. Sue, *Mechanical properties of thermosets* in *Thermosets: Structure, properties and applications*, Q. Guo, Editor. 2012, Woodhead Publishing: Oxford. p. 28-61.

185. Schwan, M., et al., *From hard to rubber-like: mechanical properties of resorcinol–formaldehyde aerogels.* Journal of Materials Science, 2015. **50**(16): p. 5482-5493.

186. Frackowiak, E. and F. Béguin, *Carbon materials for the electrochemical storage of energy in capacitors.* Carbon, 2001. **39**(6): p. 937-950.

187. Frackowiak, E., *Carbon materials for supercapacitor application.* Physical chemistry chemical physics, 2007. **9**(15): p. 1774-1785.

188. Li, X. and B. Wei, *Supercapacitors based on nanostructured carbon.* Nano Energy, 2013. **2**(2): p. 159-173.

189. Mirzaeian, M. and P.J. Hall, *Preparation of controlled porosity carbon aerogels for energy storage in rechargeable lithium oxygen batteries.* Electrochimica Acta, 2009. **54**(28): p. 7444-7451.

190. Moreno-Castilla, C. and F.J. Maldonado-Hódar, *Carbon aerogels for catalysis applications: An overview.* Carbon, 2005. **43**(3): p. 455-465.

191. Machado, B.F., et al., *Carbon xerogel supported noble metal catalysts for fine chemical applications.* Catalysis Today, 2010. **149**(3): p. 358-364.

192. Pirard, S.L., et al., *Kinetics and diffusional limitations in nanostructured heterogeneous catalyst with controlled pore texture.* Catalysis Communications, 2011. **12**(6): p. 441-445.

193. Fricke, J. and T. Tillotson, *Aerogels: production, characterization, and applications.* Thin Solid Films, 1997. **297**(1): p. 212-223.

194. Prakash, C.T. and S. Kirti, *Aerogels as Promising Thermal Insulating Materials: An Overview.* Journal of Materials, 2014. **2014**.

195. Hrubesh, L., *Aerogel applications.* J. Non-Cryst. Solids, 1998. **225**(1-3): p. 335-342.

196. Ebert, H.P., *Functional materials for energy-efficient buildings.* EPJ Web of Conferences, 2015. **98**.

197. Caps, R., et al., *Thermal transport in monolithic silica aerogel.* Le Journal de Physique Colloques, 1989. **50**(C4): p. C4-113-C4-118.

198. Fricke, J., et al., *Optimization of monolithic silica aerogel insulants.* International Journal of Heat and Mass Transfer, 1992. **35**(9): p. 2305-2309.

199. Liu, Z.-H., et al., *Thermal insulation material based on SiO2 aerogel.* Construction and Building Materials, 2016. **122**: p. 548-555.

200. Kabbour, H., et al., *Toward New Candidates for Hydrogen Storage: High-Surface-Area Carbon Aerogels.* Chemistry of Materials, 2006. **18**(26): p. 6085-6087.

201. Tian, H.Y., et al., *A synthesis method for cobalt doped carbon aerogels with high surface area and their hydrogen storage properties.* International Journal of Hydrogen Energy, 2010. **35**(24): p. 13242-13246.

202. de la Casa-Lillo, M.A., et al., *Hydrogen Storage in Activated Carbons and Activated Carbon Fibers.* The Journal of Physical Chemistry B, 2002. **106**(42): p. 10930-10934.

203. Gadiou, R., et al., *The Influence of Microporosity on the Hydrogen Storage Capacity of Ordered Mesoporous Carbons.* Adsorption, 2005. **11**(1): p. 823-827.

204. Jordá-Beneyto, M., et al., *Advanced activated carbon monoliths and activated carbons for hydrogen storage.* Microporous and Mesoporous Materials, 2008. **112**(1): p. 235-242.

205. Querejeta, N., et al., *Carbon Monoliths in Adsorption-based Post-combustion CO2 Capture.* Energy Procedia, 2017. **114**(Supplement C): p. 2341-2352.

206. Zheivot, V.I., et al., *Carbon xerogels: Nano- and adsorption textures, chemical nature of the surface and gas chromatography properties.* Microporous and Mesoporous Materials, 2010. **130**(1): p. 7-13.

207. Sánchez-Polo, M., et al., *Ag-doped carbon aerogels for removing halide ions in water treatment.* Water Research, 2007. **41**(5): p. 1031-1037.

208. Oyedoh, E.A., et al., *Preparation of controlled porosity resorcinol formaldehyde xerogels for adsorption applications.* Chemical Engineering Transactions, 2013. **32**: p. 1651-1656.

209. Bahadori, A., *Thermal insulation handbook for the oil, gas, and petrochemical industries*, ed. Elsevier. 2014, Amsterdam: Amsterdam : Elsevier.

210. Koebel, M.M., A. Rigacci, and P. Achard, *Aerogels for Superinsulation: A Synoptic View*, in *Aerogels Handbook*, M.A. Aegerter, N. Leventis, and M.M. Koebel, Editors. 2011, Springer New York. p. 607-633.

211. (EIA), T.U.S.E.I.A., *International energy outlook 2017*. 20.12.2017: https://www.eia.gov/outlooks/ieo/.

212. Riffat, S.B. and G. Qiu, *A review of state-of-the-art aerogel applications in buildings.* International Journal of Low-Carbon Technologies, 2013. **8**(1): p. 1-6.

213. Çengel, Y.A., *Heat Transfer: A Practical Approach*. 2003: McGraw-Hill.

214. Başoğul, Y., C. Demircan, and A. Keçebaş, *Determination of optimum insulation thickness for environmental impact reduction of pipe insulation.* Applied Thermal Engineering, 2016. **101**: p. 121-130.

215. Kalyon, M. and A.Z. Sahin, *Application of optimal control theory in pipe insulation* Numerical Heat Transfer, Part A: Applications, 2002. **41**(4): p. 391-402.

216. Papadopoulos, A.M., *State of the art in thermal insulation materials and aims for future developments.* Energy and Buildings, 2005. **37**(1): p. 77-86.

217. Cuce, E., et al., *Toward aerogel based thermal superinsulation in buildings: a comprehensive review.* Renewable and Sustainable Energy Reviews, 2014. **34**: p. 273-299.

218. Zhao, S., et al., *Aerogels*, in *The Sol-Gel Handbook*, D. Levy and M. Zayat, Editors. 2015, Wiley-VCH Verlag GmbH & Co. KGaA: Weinheim, Germany. p. 519-574.

219. Jelle, B.P., *Traditional, state-of-the-art and future thermal building insulation materials and solutions – Properties, requirements and possibilities.* Energy & Buildings, 2011. **43**(10): p. 2549-2563.

220. Ebert, H.-P., *Thermal properties of aerogels*, in *Aerogels Handbook*, M.A. Aegerter, N. Leventis, and M.M. Koebel, Editors. 2011, Springer: New York. p. 537-564.

221. Kistler, S. and A. Caldwell, *Thermal conductivity of silica aerogel.* Industrial & Engineering Chemistry, 1934. **26**(6): p. 658-662.

222. White, J.F., *Silica aerogel effect of variables on Its thermal conductivity.* Industrial & Engineering Chemistry, 1939. **31**(7): p. 827-831.

223. Rubin, M. and C.M. Lampert, *Transparent silica aerogels for window insulation.* Solar Energy Materials, 1983. **7**(4): p. 393-400.

224. Buttner, D. and J. Fricke, *Thermal Conductivity of Evacuated Highly Transparent Silica Aerogel.* International Journal of Solar Energy, 1985. **3**(2): p. 89-94.

225. Nilsson, O., Å. Fransson, and O. Sandberg, *Thermal properties of silica aerogel*, in *Aerogels*, J. Fricke, Editor. 1986, Springer: Berlin. p. 121-126.

226. Coffman, B.E., et al., *Aerogel blanket insulation materials for cryogenic applications.* AIP Conference Proceedings, 2010. **1218**(1): p. 913-920.

227. Biesmans, G., et al. *Polyurethane-based organic aerogels' thermal performance.* Journal of Non-Crystalline Solids, 1998. **225**: p. 36-40.

228. Caps, R. and J. Fricke, *Aerogels for Thermal Insulation*, in *Sol-Gel Technologies for Glass Producers and Users*, M.A. Aegerter and M. Mennig, Editors. 2004, Springer US: Boston, MA. p. 349-353.

229. Rey-Raap, N., et al., *Exploring the potential of resorcinol-formaldehyde xerogels as thermal insulators.* Microporous and Mesoporous Materials, 2017. **244**: p. 50-54.

230. Razzaghi, M., H.R.H. Raeisi, and A.R. Bahramian, *Improvement of Polyester Blanket Thermal Insulator Properties Using Phenolic Aerogel.* Procedia Materials Science, 2015. **11**: p. 522-526.

231. Berthon-Fabry, S., C. Hildenbrand, and P. Ilbizian, *Lightweight superinsulating Resorcinol-Formaldehyde-APTES benzoxazine aerogel blankets for space applications.* European Polymer Journal, 2016. **78**: p. 25-37.

232. Lu, X., et al., *Thermal conductivity of monolithic organic aerogels.* Science, 1992. **255**(5047): p. 971-972.

233. Hrubesh, L.W. and R.W. Pekala, *Thermal properties of organic and inorganic aerogels.* Journal of Materials Research, 1994. **9**(3): p. 731-738.

234. Tannert, R., M. Schwan, and L. Ratke, *Reduction of shrinkage and brittleness for resorcinol-formaldehyde aerogels by means of a pH-controlled sol–gel process.* The Journal of Supercritical Fluids, 2015. **106**(Supplement C): p. 57-61.

235. Schwan, M., B. Milow, and L. Ratke, *Novel superflexible resorcinol–formaldehyde aerogels and combining of them with aramid honeycombs.* MRS Communications, 2014. **4**(4): p. 177-181.

236. Alshrah, M., H.E. Naguib, and C.B. Park, *Reinforced resorcinol formaldehyde aerogel with Co-assembled polyacrylonitrile nanofibers and graphene oxide nanosheets.* Materials & Design, 2018. **151**: p. 154-163.

237. Rouquerol, J., et al. *Recommendations for the characterization of porous solids (Technical Report).* Pure and Applied Chemistry, 1994. **66**(8): p. 1739-1758.

238. Anderson, L., *The effect of the catalyst on the formation of RF xerogels*, C. University of Strathclyde. Dept. of and E. Process, Editors. 2014, Thesis [Ph. D] -- University of Strathclyde, 2014.

239. Dąbrowski, A., *Adsorption - From theory to practice.* Advances in Colloid and Interface Science, 2001. **93**(1-3): p. 135-224.

240. Richardson, J.F., J.H. Harker, and J.R. Backhurst, *Adsorption*, in *Chemical Engineering : Particle Technology and Separation Processes*. 2002, Butterworth-Heinemann: Oxford. p. 970-1052.

241. Abbas, S. and N. Jawad Jalob, *Gas Solid Separation*. 2016, The National University of Malaysia: Malaysia. p. 1-15.

242. Atkins, P.W., *Atkins' physical chemistry*. 8th ed.. ed. Physical chemistry, ed. J. De Paula. 2006, Oxford: Oxford University Press.

243. Gregg, S.J., *Adsorption, surface area, and porosity*. [U.S. ed.].. ed, ed. K.S.W. Sing. 1967, London and New York: Academic Press.

244. Micormeritics, *Gas AdsorptionTheory* in *http://www.micromeritics.com/Repository/Files/Gas_Adsorption_Theory_poster.pdf*. 2017, MicromeriticsInstrumentCorporation.

245. Thommes, M., et al., *Physisorption of gases, with special reference to the evaluation of surface area and pore size distribution (IUPAC Technical Report)*, in *Pure and applied chemistry*. 2015, IUPAC.

246. Leofanti, G., et al., *Surface area and pore texture of catalysts.* Catalysis Today, 1998. **41**(1–3): p. 207-219.

247. Rouquerol, F., et al., *Introduction*, in *Adsorption by Powders and Porous Solids* 2014, Academic Press: Oxford. p. 1-24.

248. Ksw, S., et al., *Reporting physisorption data for gas/solid systems with special reference to the determination of surface area and porosity (Recommendations 1984).* Pure Appl. Chem., 1985. **57**(4).

249. Sing, K.S.W., *Physisorption of nitrogen by porous materials.* Journal of Porous Materials, 1995. **2**(1): p. 5-8.

250. Sing, K.S.W., et al., *Reporting Physisorption Data for Gas/Solid Systems with Special Reference to the Determination of Surface Area and Porosity.* Pure and Applied Chemistry, 1985. **57**(4): p. 603-619.

251. J., R., et al. *Recommendations for the Chararcterization of Porous Solids.* Pure Appl. Chem., 1994. **66**(8): p. 1739-1758

252. Ksw, S., *Assessment of Surface Area by Gas Adsorption*, in *Adsorption by Powders and Porous Solids*, R. F., et al., Editors. 2014, Elsevier, Academic Press: Oxford.

253. L., A., *The effect of the catalyst on the formation of RF xerogels*, in *Chemical and Process Engineering*. 2014, University of Strathclyde Glasgow: University of Strathclyde Glasgow. p. i-308.

254. S., B., E. E., and T. E., *Adsorption of gases in multimolecular layers.* Journal of the American Chemical Society, 1938. **60**(2): p. 309-319

255. Sing, K.S.W., F. Rouquerol, and J. Rouquerol, *Classical Interpretation of Physisorption Isotherms at the Gas-Solid Interface*, in *Adsorption by Powders and Porous Solids (Second Edition)*. 2014, Academic Press: Oxford. p. 159-189.

256. Sing, K.S., *Reporting physisorption data for gas/solid systems with special reference to the determination of surface area and porosity (Recommendations 1984).* Pure and applied chemistry, 1985. **57**(4): p. 603-619.

257. Ksw, S., et al., *Assessment of Mesoporosity*, in *Adsorption by Powders and Porous Solids: Principles, Methodology and Applications*, R. F., et al., Editors. 2014, Elsevier, Academic Press: Oxford.

258. P., B.E., J.L. G., and H.P. P., *The determination of pore volume and area distributions in porous substances. I. Computations from nitrogen isotherms.* Journal of the American Chemical Society, 1951. **73**(1): p. 373-380

259. Sing, K.S.W., et al., *Assessment of Mesoporosity*, in *Adsorption by Powders and Porous Solids (Second Edition)*. 2014, Academic Press: Oxford. p. 269-302.

260. Do, D.D., *Adsorption Analysis: Equilibria and Kinetics*. Vol. 2. 1998: World Scientific.

261. Siminiceanu, I., et al., *Textural characterization of a new iron-based ammonia synthesis catalyst.* Chemical Buletin, 2008. **53**: p. 1-2.

262. Lippens, B.C., B.G. Linsen, and J.H.d. Boer, *Studies on pore systems in catalysts I. The adsorption of nitrogen; apparatus and calculation.* Journal of Catalysis, 1964. **3**(1): p. 32-37.

263. Strickland, M.L., *Physical adsorption theory: Basic concepts and models*, in *Small particles*. 2012, Micromeritics Instrument Corp.: Norcross, USA.

264. Ayral, A., J. Phalippou, and T. Woignier, *Skeletal density of silica aerogels determined by helium pycnometry.* Journal of Materials Science, 1992. **27**(5): p. 1166-1170.

265. Tamari, S. and A. Aguilar-Chávez, *Optimum design of gas pycnometers for determining the volume of solid particles.* Journal of Testing and Evaluation, 2005. **33**(2): p. 135-138.

266. Semel, F.J. and D.A. Lados, *Porosity analysis of PM materials by helium pycnometry.* Powder Metallurgy, 2006. **49**(2): p. 173-182.

267. Harwood, L.M., *Introduction to organic spectroscopy*, ed. T.D.W. Claridge. 1997, Oxford

Oxford University Press.

268. Yadav, L.D.S., *Introduction to Spectroscopy* in *Organic Spectroscopy*. 2005, Springer Netherlands: Dordrecht. p. 1-6.

269. Hof, M. and R. Machan, *Basics of Optical Spectroscopy*, in *Handbook of spectroscopy*, T. Vo-Dinh and G.T. Gauglitz, Editors. 2014, Wiley-VCH: Cambridge. p. 31-38.

270. Levine, I.N., *Physical chemistry*. 4th ed.. ed. 1995, New York: New York: McGraw-Hill.

271. Pavia, D.L., et al., *Introduction to spectroscopy*. 4th ed. 2009, Belmont, The USA: Brooks/Cole

CENGAGE Learning.

272. Smith, B.C., *Fundamentals of Fourier transform infrared spectroscopy*. 2nd ed. 2011, New York: CRC press.

273. Masood, T.M., et al., *Fourier-transform infrared spectroscopy/attenuated total reflectance analysis for the degree of conversion and shear bond strength of Transbond XT adhesive system.* Clinical, cosmetic and investigational dentistry, 2018. **10**: p. 275-280.

274. Elliott, D.A., et al., *Radiation Therapy*, in *Oral, Head and Neck Oncology and Reconstructive Surgery*, R.B. Bell, R.P. Fernandes, and P.E. Andersen, Editors. 2018, Elsevier. p. 268-290.

275. Martucci, A., *Characterization Methods*, in *Sol-Gel Nanocomposites*, M. Guglielmi, G. Kickelbick, and A. Martucci, Editors. 2014, Springer: New York. p. 83-108.

276. Baker, M.J., C.S. Hughes, and K.A. Hollywood, *Infrared spectroscopy*, in *Biophotonics: Vibrational Spectroscopic Diagnostics*. 2016, Morgan & Claypool Publishers. p. 2-1-2-14.

277. Christy, A., Y. Ozaki, and V. Gregorio, *Modern Fourier Transform Infrared Spectroscopy*. Comprehensive Analytical Chemistry, ed. D. Barceló. Vol. 35. 2002, Amsterdam: Elsevier.

278. Stuart, B., *Infrared Spectroscopy*, in *Kirk-Othmer Encyclopedia of Chemical Technology*, Kirk-othmer, Editor. 2015, John Wiley & Sons, Inc (Ed.). p. 1-18.

279. Yadav, L.D.S., *Infrared (IR) Spectroscopy*, in *Organic spectroscopy* L.D.S. Yadav, Editor. 2005, Springer, Dordrecht: Dordrecht. p. 52-105.

280. Griffiths, P.R. and J.A. de Haseth, *Introduction to Vibrational Spectroscopy*, in *Fourier Transform Infrared Spectrometry*. 2006, John Wiley & Sons, Inc., Publication: New Jersey. p. 1-18.

281. Sablinskas, V., G. Steiner, and M. Hof, *Applications*, in *Handbook of Spectroscopy*, G.T. Gauglitz and T. Vo-Dinh, Editors. 2005, Wiley-VCH: Cambridge.

282. Sablinskas, V., *Instrumentation*, in *Handbook of Spectroscopy*, G.T. Gauglitz and T. Vo-Dinh, Editors. 2005, Wiley-VCH: Cambridge. p. 48-69.

283. Stuart, B., *Infrared Spectroscopy: Fundamentals and Applications*. 1st ed. Analytical Techniques in the Sciences, ed. D.J. Ando. 2004, Chichester, The UK: John Wiley & Sons, Ltd 15-44.

284. Steiner, G., *Measurement Techniques*, in *Handbook of Spectroscopy*, G.T. Gauglitz and T. Vo-Dinh, Editors. 2005, Wiley-VCH: Cambridge. p. 70-88.

285. Leng, Y., *Vibrational Spectroscopy for Molecular Analysis*, in *Materials Characterization: Introduction to Microscopic and Spectroscopic Methods*. 2008, John Wiley & Sons: Singapore. p. 253-300.

286. Kuzmany, H., *Solid-State Spectroscopy: An Introduction*. 2nd ed. 2009, Berlin: Springer.

287. Gunzler, H. and H.-U. Gremlich, *IR Spectroscopy: An Introduction*. 2002, Weinheim: Wiley-VCH.

288. Griffiths, P.R. and J.A. de Haseth, *Attenuated Total Reflection*, in *Fourier Transform Infrared Spectrometry*. 2006, John Wiley & Sons, Inc., Publication

New Jersey. p. 321-348.

289. Bruker-Optics, *Attenuated Total Reflection (ATR) Mode Advantages for FTIR Spectroscopy.* AZO Materials, 2012.

290. Derrick, M.R., D. Stulik, and J.M. Landry, *Infrared Spectroscopy in Conservation Science*. Scientific Tools for Conservation ed. T.G.C. Institute. 1999, Los Angeles: The J. Paul Getty Trust

291. Czichos, H., T. Saito, and L. Smith, *Springer handbook of materials measurement methods*. Vol. 978. 2006: Springer Berlin.

292. Ul-Hamid, A., *Introduction*, in *A Beginners' Guide to Scanning Electron Microscopy*. 2018, Springer Cham, Switzerland. p. 1-14.

293. Kalantar-Zadeh, K. and B. Fry, *Nanotechnology-enabled sensors*. 2008, New York: Springer Science & Business Media.

294. Leng, Y., *Scanning Electron Microscopy*, in *Materials Characterization: Introduction to Microscopic and Spectroscopic Methods*. 2008, Wiley-VCH Verlag GmbH & Co. KGaA: Singapore. p. 127-161.

295. Hilal, A.A., *Microstructure of Concrete*, in *High Performance Concrete Technology and Applications*, S. Yilmaz and H.B. Ozmen, Editors. 2016, InTech: Rijeka. p. Ch. 01.

296. Lyman, C.E., et al., *Scanning electron microscopy, X-ray microanalysis, and analytical electron microscopy: a laboratory workbook*. 1990, New York Springer Science & Business Media.

297. Goldstein, J.I., et al., *Scanning electron microscopy and X-ray microanalysis*. 3rd ed. 2003, New York: Kluwer Academic/Plenum Publishers.

298. Monospektra. *Drives and Positioning Systems for Electron Microscopes*. 2018 10th March 2018]; Available from http://www.monospektra.com/positioning/applications/drives-positioning-systems-electron-microscopes/.

299. Zumbrunnen, D.A., R. Viskanta, and F.P. Incropera, *Heat transfer through porous solids with complex internal geometries.* International Journal of Heat and Mass Transfer, 1986. **29**(2): p. 275-284.

300. Banji, U., *Preparation and characterization of hydrophobic aerogels using inorganic precursor by ambient pressure drying*, in *Department of physics*. 2010, Shivaji University Maharashtra (India). p. 165.

301. Tien, C.L. and G.R. Cunnington, *Cryogenic Insulation Heat Transfer*, in *Advances in Heat Transfer*, T.F. Irvine and J.P. Hartnett, Editors. 1973, Elsevier. p. 349-417.

302. Gross, J., J. Fricke, and L. Hrubesh, *Sound propagation in SiO2 aerogels.* The Journal of the Acoustical Society of America, 1992. **91**(4): p. 2004-2006.

303. Ebert, H.-P., *High-Performance Insulation Materials*, in *Nearly Zero Energy Building Refurbishment: A Multidisciplinary Approach*, F. Pacheco Torgal, et al., Editors. 2013, Springer London. p. 457-481.

304. Kistler, S.S., *The Calculation of the Surface Area of Microporous Solids from Measurements of Heat Conductivity.* The Journal of Physical Chemistry, 1942. **46**(1): p. 19-31.

305. Reichenauer, G., U. Heinemann, and H.P. Ebert, *Relationship between pore size and the gas pressure dependence of the gaseous thermal conductivity.* Colloids and Surfaces A: Physicochemical and Engineering Aspects, 2007. **300**(1): p. 204-210.

306. Zhang, H., et al., *The influence of gaseous heat conduction to the effective thermal conductivity of nano-porous materials.* International Communications in Heat and Mass Transfer, 2015. **68**: p. 158-161.

307. Caps, R. and J. Fricke, *Radiative heat transfer in silica aerogel*, in *Aerogels*. 1986, Springer. p. 110-115.

308. Ratna, D., *Thermal properties of thermosets* in *Thermosets*, Q. Guo, Editor. 2012, Woodhead Oxford. p. 62-91.

309. Chen, H., et al., *Thermal conductivity of polymer-based composites: Fundamentals and applications.* Progress in Polymer Science, 2016. **59**: p. 41-85.

310. Netzsch, *Heat Flow Meter - HFM 436 Lambda*, in *https://dcyd0ggl1hia3.cloudfront.net/media/thermal-analysis/brochures/HFM_436_Lambda_en_web.pdf?1487611442*. 2016: Internet.

311. Smith, D., et al. *Thermal conductivity of porous materials.* Journal of Materials Research, 2013. **28**(17): p. 2260-2272.

312. Yüksel, N. *The review of some commonly used methods and techniques to measure the thermal conductivity of insulation materials*. Insulation Materials in Context of Sustainability, InTech 2016 [18-12-2017]]; Available from: http://www.intechopen.com/books/insulation-materials-in-context-of-

sustainability/the-review-of-some-commonly-used-methods-and-techniques-to-measure-the-thermal-conductivity-of-insul

313. ASTM, I., *Standard Test Method for Steady-State Thermal Transmission Properties by Means of the Heat Flow Meter Apparatus*. 2017. p. 1-16.

314. Lian, T.-W., et al., *Rapid thermal conductivity measurement of porous thermal insulation material by laser flash method.* Advanced Powder Technology, 2016. **27**(3): p. 882-885.

315. Wunderlich, B., *Introduction*, in *Thermal Analysis*. 1990, Academic Press. p. 1-36.

316. Frollini, E., C.G. Silva, and E.C. Ramires, *Phenolic resins as a matrix material in advanced fiber-reinforced polymer (FRP) composites A2 - Bai, Jiping*, in *Advanced Fibre-Reinforced Polymer (FRP) Composites for Structural Applications*. 2013, Woodhead Publishing. p. 7-43.

317. Le Parlouër, P., *Thermal Analysis and Calorimetry Techniques for Catalytic Investigations*, in *Calorimetry and Thermal Methods in Catalysis*, A. Auroux, Editor. 2013, Springer Berlin Heidelberg: Berlin. p. 51-101.

318. Kasap, S., J. Málek, and R. Svoboda, *Thermal Properties and Thermal Analysis: Fundamentals, Experimental Techniques and Applications*, in *Springer Handbook of Electronic and Photonic Materials*, S. Kasap and P. Capper, Editors. 2017, Springer International Publishing: Cham, Switzerland. p. 1-1.

319. Thomas, L.C. *An introduction to the techniques of differential scanning calorimetry (DSC) and modulated DSC*. in *International Seminar: Thermal Analysis and Rheology*. 2005. Ferrol, Spain: Universidade da Coruña, Servizo de Publicacións.

320. Wunderlich, B., *Thermal analysis of polymeric materials*. 2005: Springer Science & Business Media.

321. Menczel, J.D., et al., *Differential Scanning Calorimetry (DSC)*, in *Thermal Analysis of Polymers: Fundamentals and Applications*, J.D. Menczel and R.B. Prime, Editors. 2008, John Wiley & Sons, Inc: New Jersey. p. 7-239.

322. Kodre, K., et al., *Differential Scanning Calorimetry: A Review.* Research & Reviews: Journal of Pharmaceutical Analysis, 2014. **3**(3): p. 11-22.

323. Xu, W., et al. *Fundamentals of TGA and SDT*. in *International Seminar: Thermal Analysis and Rheology* 2005. Ferrol, Spain: Universidade da Coruña, Servizo de Publicacións.

324. Prime, R.B., et al., *Thermogravimetric Analysis (TGA)*, in *Thermal Analysis of Polymers: Fundamentals and Applications*, J.D. Menczel and R.B. Prime, Editors. 2008, John Wiley & Sons, Inc.: New jersey. p. 241-317.

325. Taylor, S.J., *Monitoring the gelation mechanism of resorcinol-formaldehyde xerogels*, in *Department of Chemical and Process Engineering*. 2014, University of Strathclyde: Glasgow.

326. Principe, I.A., *Development of nitrogen doped resorcinol-formaldehyde gels for carbon capture*, in *Department of Chemical Process Engineering*. 2017, University of Strathclyde.

327. Obhielo, E., *Synthesis, characterisation and optimisation of novel adsorbents for CO2 capture*, in *Department of Chemical and Process Engineering*. 2015, University of Strathclyde: Glasgow.

328. JSC. *Hanna Easy-Use Basic pH Benchtop Meter*. 2019; Available from https://www.jjstech.com/ph20-01.html.

329. Bai, J., *Introduction*, in *Advanced Fibre-Reinforced Polymer (FRP) Composites for Structural Applications*. 2013, Woodhead Publishing. p. 1-4.

330. Miskolczi, N., *Polyester resins as a matrix material in advanced fibre-reinforced polymer (FRP) composites A2 - Bai, Jiping*, in *Advanced Fibre-Reinforced Polymer (FRP) Composites for Structural Applications*. 2013, Woodhead Publishing. p. 44-68.

331. Coronado, P.R. and J.F. Poco, *Flexible aerogel composite for mechanical stability and process of fabrication*. 1999, Google Patents.

332. Russell, S.J., *Handbook of Nonwovens*. Woodhead publishing in textiles, ed. T.t. Insitute. 2006, Cambridge, UK: Woodhead Publishing Limited.

333. MicromeriticsInstrumentCorporation. *Micromeritics ASAP 2420 Product-showcase* 18th Febrauary 2018]; Available from: http://www.micromeritics.com/Product-Showcase/ASAP-2420.aspx.

334. MicromeriticsInstrumentCorporation. *Micromeritics BET Surface area and porosity analyzer ASAP 2020* [cited 19 February 2018; Available from https://borch.agsci.colostate.edu/files/2016/02/BET-Analyzer-Generalized-SOP.pdf.

335. Smith, B.C., *A process for successful infrared spectral interpretation.* Spectroscopy: Solutions for Materials Analysis, 2016. **31**(1): p. 14-21.

336. Cole-Parmer, *Laboratory Supplies*, in *https://www.coleparmer.co.uk/c/mortars-and-pestles*, M.a. Petsles, Editor. 2019, Cole-Parmer.

337. ASTMInternational, *ASTM E1461-13 Standard Test Method for Thermal Diffusivity by the Flash Method*. 2013: West Conshohocken, PA.

338. Kim, S.-K. and Y.-J. Kim, *Determination of apparent thickness of graphite coating in flash method.* Thermochimica Acta, 2008. **468**: p. 6-9.

339. O'Neill, M.J., *Measurement of Specific Heat Functions by Differential Scanning Calorimetry.* Analytical Chemistry, 1966. **38**(10): p. 1331-1336.

340. Höhne, G., W. Hemminger, and H.J. Flammersheim, *Differential scanning calorimetry: an introduction for practitioners*. 1996, Berlin: Springer-Verlag.

341. Netzsch, *STA 449 F3 Jupiter* O. Instructions, Editor. 2008, Netzsch: Selb, Germany.

342. International, A., *Standard Test Method for Temperature Calibration of Thermogravimetric Analyzers*. 2017, ASTM International: ASTM COMPASS Web page.

343. International, A., *Standard Test Method for Mass Scale Calibration of Thermogravimetric Analyzers*. 2104, ASTM International: ASTM COMPASS Web page.

344. Wendlandt, W.W. and P.K. Gallagher, *Instrumentation*, in *Thermal Characterization of Polymeric Materials*, E.A. Turi, Editor. 1981, Academic Press: London. p. 1-90.

345. Bottom, R., *Thermogravimetric Analysis*, in *Principles and applications of thermal analysis*, P. Gabbott, Editor. 2008, Blackwell Publishing: Oxford.

346. Speyer, R.F., *Thermal analysis of materials*. 1994, New York: Marcel Dekker.

347. Hwang, S.-W. and S.-H. Hyun, *Capacitance control of carbon aerogel electrodes.* Journal of Non-Crystalline Solids, 2004. **347**(1): p. 238-245.

348. O'Neil, M.J., *The Merck index: an encyclopedia of chemicals, drugs, and biologicals*. 2013, UK: RSC Publishing.

349. Poljanšek, I. and M. Krajnc, *Characterization of phenol-formaldehyde prepolymer resins by in line FT-IR spectroscopy.* Acta Chimica Slovenica, 2005. **52**(3): p. 238-244.

350. Giwa, A.-R., et al., *Kinetics and Thermodynamics of Ternary Dye System Adsorption on to Melon (Citrillus lanatus) Seed Husk.* American Chemical Science Journal, 2015. **7**: p. 7-25.

351. Pelletier, M.J. and C.C. Pelletier, *Spectroscopic Theory for Chemical Imaging*, in *Raman, Infrared, and Near-Infrared Chemical Imaging*, S. Šašić and Y. Ozaki, Editors. 2011.

352. Obhielo, E., *Synthesis, characterisation and optimisation of novel adsorbents for CO_2 capture*. 2015, University of Strathclyde: Glasgow.

353. Nunes Dos Santos, W., P. Mummery, and A. Wallwork, *Thermal diffusivity of polymers by the laser flash technique.* Polymer Testing, 2005. **24**(5): p. 628-634.

354. Hsu, J.-P. and B.-T. Liu, *Effect of Particle Size on Critical Coagulation Concentration.* Journal of Colloid and Interface Science, 1998. **198**(1): p. 186-189.

355. Lawrence, M. and Y. Jiang, *Porosity, pore size distribution, micro-structure*, in *Bio-aggregates Based Building Materials*, S. Amziane and F. Collet, Editors. 2017, Springer: Dordrecht. p. 39-71.

356. Reichenauer, G., *Structural Characterization of Aerogels*, in *Aerogels Handbook*, M.A. Aegerter, N. Leventis, and M.M. Koebel, Editors. 2011, Springer New York: New York, NY. p. 449-498.

357. BPF. *Polyesters (Thermoplastic) PETP, PBT, PET*. Plastipedia 2018 [cited 14th January 2018; Available from http://www.bpf.co.uk//plastipedia/polymers/Polyesters.aspx.

358. Aerovac. *Technical datasheets*. 2017 [cited 3rd November 2017; Available from http://www.novia.hu/downloads/download.php?file=../admin_upload/katalog_item_docs/373_p_CatalogueEnglish.pdf.

359. Soltani, P., M.S. Johari, and M. Zarrebini, *3D fibre orientation characterization of nonwoven fabrics using X-ray micro-computed tomography.* World J Text Eng Technol, 2015. **1**: p. 41-47.

360. Bhattacharya, S. and D.S. Chaudhari, *Study on Structural, Mechanical and Functional Properties of Polyester Silica Nanocomposite Fabric.* International Journal of Pure and Applied Sciences and Technology, 2014. **21**: p. 43-52.

361. Huang, Z., et al., *Effects of dimethylolpropionic acid modification on the characteristics of polyethylene terephthalate fibers.* Molecular Medicine Reports, 2012. **6**(4): p. 709-715.

362. Parvinzadeh, M. and I. Ebrahimi, *Influence of atmospheric-air plasma on the coating of a nonionic lubricating agent on polyester fibre.* Radiation Effects and Defects in Solids, 2011. **166**(6): p. 408-416.

363. Bozaci, E., et al. *Potential use of new methods for identification of hollow polyester fibres.* Tekstil ve Konfeksiyon, 2012. **22**: p. 317-323.

364. Aflori, M. and M. Drobota, *Modification of Polyethylene Terephthalate*, in *Poly(Ethylene Terephthalate) Based Blends, Composites and Nanocomposites*, P.M. Visakh and M. Liang, Editors. 2015, William Andrew Publishing: Oxford. p. 15-39.

365. Liu, X., et al., *Fabricating conductive poly(ethylene terephthalate) nonwoven fabrics using an aqueous dispersion of reduced graphene oxide as a sheet dyestuff.* RSC Advances, 2014. **4**(45): p. 23869-23875.

366. Turnbull, L., J.J. Liggat, and W.A. MacDonald, *Thermal degradation chemistry of poly(ethylene naphthalate) – A study by thermal volatilisation analysis.* Polymer Degradation and Stability, 2013. **98**(11): p. 2244-2258.

367. Probst, L., et al., *Aerogels, getting their second wind*, in *Advanced Materials*, BIO, Editor. 2015, EU: Luxembourg. p. 1-14.

368. Venkataraman, M., et al., *Aerogels for thermal insulation in high-performance textiles.* Textile Progress, 2016. **48**(2): p. 55-118.

369. CIBSE, *Guide F: Energy efficiency in buildings*, in *CIBSE Guides*. 2004, Chartered Institution of Building Service Engineers: London.

370. Blackburn, A., *The demand for insulation: a look at trends and the forecast for insulation throughout the world*. 2015, Freedonia Group: http://bi.galegroup.com/global/article/GALE%7CA400956335/209cbaae89ddff f7d24ea42d3371d6df?u=ustrath.

371. Dyson, R.G., *Strategic development and SWOT analysis at the University of Warwick.* European Journal of Operational Research, 2004. **152**(3): p. 631-640.

372. Víctor-Román, S., et al., *CNF-reinforced polymer aerogels: Influence of the synthesis variables and economic evaluation.* Chemical Engineering Journal, 2015. **262**: p. 691-701.

373. PoundSterlingLive. *Historical spot exchange rates*. 2018 12th February 2018]; Available from https://www.poundsterlinglive.com/bank-of-england-spot/historical-spot-exchange-rates/gbp/.

374. Lemmens, S., *Cost Engineering Techniques and Their Applicability for Cost Estimation of Organic Rankine Cycle Systems.* Energies, 2016. **9**(7): p. 485.

375. UKPower. *Electricity Running Costs Calculator*. [cited 2019 4th March]; Available from https://www.ukpower.co.uk/tools/running_costs_electricity.

376. Hart, P.W. and J.T. Sommerfeld, *Cost estimation of speciality chemicals from laboratory-scale prices.* Cost Engineering, 1997. **39**(3): p. 31.

377. Krumenacker, L., et al., *Encyclopedia of Chemical Technology*. 4th ed, ed. Kirk-Othmer. Vol. 13. 2001.

378. Ltd, S.-A.C., *Resorcinol*. 2018: Online.

379. HSE, *EH40/2005 Workplace exposure limits*. 2018, TSO: HSE. p. 1-63.

380. Euan, M., *Effects of Secondary Sodium Carbonate Addition on the Porous Structure or Resorcinol-Formaldehyde Organic Xerogels*, in *Pure and Applied Chemistry*. 2012, University of Strathclyde: Glasgow.

381. Abdollahi, M. and A. Hosseini, *Formaldehyde*, in *Encyclopedia of Toxicology*, P. Wexler, et al., Editors. 2014, Elsevier Inc.: Amsterdam, Boston , Heidelberg, and London. p. 653-656.

382. Kalapos, M.P., *Acetone*, in *Encyclopedia of Toxicology*, P. Wexler, et al., Editors. 2014, Elsevier Inc.: Amsterdam, Boston , Heidelberg, and London

p. 36-39.

383. Rojas-Cervantes, M. *Some strategies to lower the production cost of carbon gels.* J Mater Sci, 2015. **50**(3): p. 1017-1040.

384. Fairén-Jiménez, D., F. Carrasco-Marín, and C. Moreno-Castilla, *Porosity and surface area of monolithic carbon aerogels prepared using alkaline carbonates and organic acids as polymerization catalysts.* Carbon, 2006. **44**(11): p. 2301-2307.

385. Feng, Y.N., et al., *Effects of further adding of catalysts on nanostructures of carbon aerogels.* Materials Science and Engineering: B, 2008. **148**(1): p. 273-276.

386. Bruno, M.M., et al., *A novel way to maintain resorcinol–formaldehyde porosity during drying: Stabilization of the sol–gel nanostructure using a cationic polyelectrolyte.* Colloids and Surfaces A: Physicochemical and Engineering Aspects, 2010. **362**(1): p. 28-32.

387. Suslick, K.S. and G.J. Price, *Applications of ultrasound to materials chemistry.* Annual Review of Materials Science, 1999. **29**(1): p. 295-326.

388. Siyasukh, A., et al., *Preparation of a carbon monolith with hierarchical porous structure by ultrasonic irradiation followed by carbonization, physical and chemical activation.* Carbon, 2008. **46**(10): p. 1309-1315.

389. Seyler, C., et al., *Waste-Solvent Management as an Element of Green Chemistry: A Comprehensive Study on the Swiss Chemical Industry.* Industrial & Engineering Chemistry Research, 2006. **45**(22): p. 7700-7709.

390. Messmer, A. and A. Chaudhary, *Life cycle assessment of adhesives used in wood constructions*. 2015, Institute of Ecological System Design

ETH Zürich: Zürich.

391. Clark, C.E., *Considerations in Conducting a Life-Cycle Inventory*, in *Fundamentals of Materials for Energy and Environmental Sustainability*, D.S. Ginley and D. Cahen, Editors. 2012, Cambridge University Press: Cambridge, The UK.

392. Silvestre, J., J. Brito, and M. Pinheiro, *Life-Cycle Assessment of Thermal Insulation Materials for External Walls of Buildings*, in *International*

Conference of Constructions - Towards a Better Built Environment. 2011, ResearchGate: Innsbruck, Austria.

393. Nie, Z.-r., et al., *Recent progress and application of materials life cycle assessment in China.* Progress in Natural Science: Materials International, 2011. **21**(1): p. 1-11.

394. Islam, S.u. and A. Kumar, *Life Cycle Assessment of Rubber Dam*, in *Hydraulic Rubber Dam*, S. Thomas, et al., Editors. 2019, William Andrew Publishing. p. 99-122.

395. Guinée, J., et al., *Handbook on Life Cycle Assessment, operational guide to the ISO standards*. ECO-Efficiency in Industry and Science ed. A. Tukker. Vol. 7. 2002, Dordrecht: KLUWER ACADEMIC PUBLISHERS.

396. Finkbeiner, M., et al., *The New International Standards for Life Cycle Assessment: ISO 14040 and ISO 14044.* The International Journal of Life Cycle Assessment, 2006. **11**(2): p. 80-85.

397. BSI, *BS EN ISO 14044:2006+A1- Environmental management-Life cycle assessment-Requirements and guidelines*. 2018, BSI: Online.

398. Finnveden, G., et al., *Recent developments in Life Cycle Assessment.* Journal of environmental management, 2009. **91**: p. 1-21.

399. Wilson, J., *Life-cycle inventory of formaldehyde-based resins used in wood composites in terms of resources, emissions, energy and carbon.* Wood and Fiber Science, 2010. **42**.

400. Frischknecht, R., R. Steiner, and N. Jungbluth, *The Ecological Scarcity Method-Eco-factors 2006: A method for impact assessment in LCA*, in *Environmental studies*. 2009, Federal Office for the Environment (FOEN) Bern.

401. Dylewski, R. and J. Adamczyk, *Life cycle assessment (LCA) of building thermal insulation materials*, in *Eco-efficient Construction and Building Materials*, F. Pacheco-Torgal, et al., Editors. 2014, Woodhead Publishing. p. 267-286.

402. Turconi, R., et al., *Life cycle assessment of waste incineration in Denmark and Italy using two LCA models.* Waste Management & Research, 2011. **29**(10_suppl): p. S78-S90.

403. Morgan, A., H. Stichnothe, and A. Azapagic, *Carbon Calculations over the Life Cycle of Industrial Activities (CCaLC)*, in *Environmental Informatics and Industrial Environmental Protection: Concepts, Methods and Tools*, V. Wohlgemuth, B. Page, and K. Voigt, Editors. 2009, Shaker Verlag, Aachen: Berlin. p. 25-34.

404. *Multi - Purpose Ovens*. [cited 2019 10th September]; brochure]. Available from: https://www.airflow-group.com/pdfs/airflow-multi-purpose-ovens-brochure.pdf.

405. Kim, T.H. and C.U. Chae, *Environmental Impact Analysis of Acidification and Eutrophication Due to Emissions from the Production of Concrete.* Sustainability, 2016. **8**(6): p. 578.

406. Margni, M. and M.A. Curran, *Life Cycle Impact Assessment*, in *Life Cycle Assessment Handbook- A Guide for Environmentally*

Sustainable Products, M.A. Curran, Editor. 2012, Scrivener Publishing LLC

Wiley & Sons, Inc: New York. p. 67-103.

407. Rosenbaum, R.K., et al., *Life Cycle Impact Assessment*, in *Life Cycle Assessment: Theory and Practice*, M.Z. Hauschild, R.K. Rosenbaum, and S.I. Olsen, Editors. 2018, Springer International Publishing: Cham. p. 167-270.

408. IPCC, *Climate change 2013: The physical science basis*, T.F. Stocker, et al., Editors. 2013, WMO&UNEP: Cambridge and New York.

409. Kralisch, D., D. Ott, and D. Gericke, *Rules and benefits of Life Cycle Assessment in green chemical process and synthesis design: a tutorial review.* Green Chemistry, 2015. **17**(1): p. 123-145.

410. Baird, D.C., *Experimentation: An Introduction to Measurement Theory and Experiment Design*. 3rd ed. 1995, Englewood Cliffs: Prentice Hall, New York.

gels

MDPI

Article

Process Variable Optimization in the Manufacture of Resorcinol–Formaldehyde Gel Materials

Martin Prostredný, Mohammed G. M. Abduljalil, Paul A. Mulheran and Ashleigh J. Fletcher *

Department of Chemical and Process Engineering, University of Strathclyde, Glasgow G1 1XJ, UK; martin.prostredny@strath.ac.uk (M.P.); mohammed.abduljalil@strath.ac.uk (M.G.M.A.); paul.mulheran@strath.ac.uk (P.A.M.)

* Correspondence: ashleigh.fletcher@strath.ac.uk; Tel.: +44-(0)-141-548-2431

Received: 15 December 2017; Accepted: 12 April 2018; Published: 17 April 2018

check for updates

Abstract: Influence of process parameters of resorcinol–formaldehyde xerogel manufacture on final gel structure was studied, including solids content, preparation/drying temperature, solvent exchange, and drying method. Xerogels produced using a range of solids content between 10 and 40 w/v% show improved textural character up to 30 w/v% with a subsequent decrease thereafter. Preparation/drying temperature shows a minimal threshold temperature of 55 °C is required to obtain a viable gel structure, with minimal impact on gel properties for further thermal increase. Improving the solvent exchange method by splitting the same amount of acetone used in this phase over the period of solvent exchange, rather than in a single application, shows an increase in total pore volume and average pore diameter, suggesting less shrinkage occurs during drying when using the improved method. Finally, comparing samples dried under vacuum and at ambient pressure, there seems to be less shrinkage when using vacuum drying compared to ambient drying, but these changes are insubstantial. Therefore, of the process parameters investigated, improved solvent exchange seems the most significant, and it is recommended that, economically, gels are produced using a solids content of 20 w/v% at a minimum temperature of 55 °C, with regular solvent replenishment in the exchange step, followed by ambient drying.

Keywords: xerogel; Brunauer-Emmett-Teller theory; Barrett-Joyner-Halenda analysis; temperature; solids content; drying; solvent exchange

1. Introduction

Resorcinol–formaldehyde (RF) aerogels are a family of porous materials, first discovered in 1989 [1] by Pekala, and which have seen extensive application, due to their tailorable textural properties, in a range of applications, including as catalyst supports [2–4], in gas storage systems [5,6] and gas separation devices [7,8], in the fabrication of fuel cells [9,10], and as a core component in insulation [11,12]. The control of the porous character of these materials underpins their vast applicability, allowing tailored synthesis in terms of surface area, pore volume and pore size; however, the mechanism by which these gel materials form is not completely understood and there is significant scope for materials and process optimization.

It is generally accepted that the sol-gel polycondensation reaction of resorcinol (R) and formaldehyde (F) proceeds as shown in Figure 1; the reaction is also usually performed at above ambient temperatures. The reaction can be seen to proceed via an initial addition reaction between R and F, forming a hydroxymethyl derivative species, which undergoes self-condensation to create oligomeric chains that form clusters, and finally, a cross-linked 3D gel network. Our previous work, utilizing light scattering techniques, has provided insight into the mechanism of cluster growth, whereby, in a system with fixed reaction parameters, thermodynamics controls the size of growing

clusters, while there is kinetic control of cluster population [13]. The reaction is promoted by the presence of a metal salt, known within the field as a catalyst. The most commonly used catalyst is sodium carbonate (Na_2CO_3), as originally used by Pekala, and the role of the metal carbonate is thought to be two-fold. While the carbonate is known to act as a base, promoting the initial reaction between resorcinol and formaldehyde through proton abstraction, the metal ion is thought to stabilise the colloidal suspension involved in development of clusters dispersed within the solvent matrix [14]. Hence, many studies have previously focused on the use of different catalytic species to control the final gel material [13–19]. However, it should be noted that the polycondensation reaction can also be influenced by a variety of other synthesis parameters, resulting in a modification of the porous character of the final aerogel product [20,21]. This includes synthesis parameters such as resorcinol to carbonate molar ratio (R/C) and the mass of solids dissolved within a fixed volume of solvent (deionised water) [22], as well as process variables, which can also affect the end material. Recent research has shown that both the time allowed for the reaction mixture to be stirred before heating [23], and the shape of the mould used to form the RF aerogel [24], can also have a significant effect on the internal structure of the gel product. The post-synthetic processing of RF gels is also subject to significant variation, in terms of solvent exchange and drying methods used, the former is usually selected to enhance the latter. Drying methods include supercritical drying, freeze drying or ambient temperature drying, with or without vacuum.

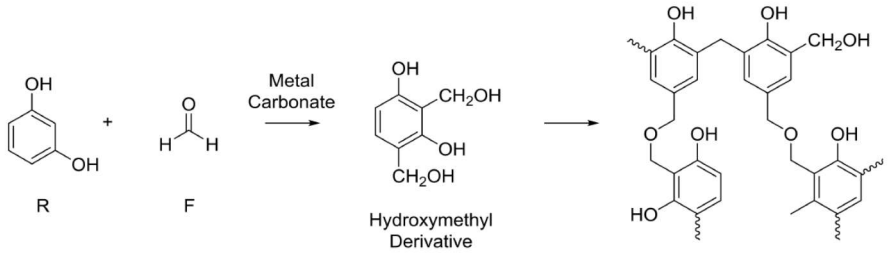

Figure 1. General reaction mechanism proposed in the reaction of resorcinol and formaldehyde. R: resorcinol; F: formaldehyde.

Kistler was instrumental in developing the first aerogels from silica based materials, and in his work, he had observed that evaporative drying results in destructive forces acting on the pore walls as a consequence of surface tension, and subsequent collapse of the gel [25]; he also established that, due to the high critical temperature and pressure of H_2O [26], and its poor solubility in supercritical solvents [27], the water entrained within the gel first had to be exchanged with a solvent that was completely miscible with the supercritical solvent. Following this work, the Lawrence Berkeley Laboratory [28] discovered that supercritical CO_2 could be used as a direct solvent replacement in the drying of silica aerogels [28], presenting a safer route to gel production. Pekala subsequently used this discovery, in conjunction with previous knowledge on RF resins to prepare organic aerogels [1,29]. Further studies, since then, discovered that other drying methods can be used, e.g., conventional evaporative drying to form xerogels [30] and freeze drying to form cryogels [31–34]. Czakkel et al. [32] compared the effects of evaporative drying in an inert atmosphere, freeze drying and supercritical drying, on the textural properties of RF gels, and found that the cryogels exhibited the highest pore volumes and surface areas due to the improved solvent quality of t-butanol; the evaporative samples showed less developed structures due to increased shrinkage arising from the formation of a liquid–vapour interface and resultant surface tension [20]. This indicates that the final drying step is critical to retention of porous character; however, Jabeen also demonstrated that exchanging entrained water with a solvent of lower surface tension reduced gel shrinkage and, as a result, increased pore volume [35]. The results indicate that, even in the event of a prolonged solvent exchange, residual water is retained within the pores of the gel, resulting in increased surface tension during drying,

and impacting on the porous structure obtained. Another way to avoid liquid–vapour interfaces is to use freeze-drying [12–15]. It has been noted, in previous studies, that supercritical drying and freeze-drying are expensive to perform, and require specialist knowledge [34,36]; hence, a route to gel production that avoids such methods would be economically beneficial.

These previous works have established a base from which most researchers work to produce RF gels but, to date, there has been no overarching study that has investigated process optimization holistically, which is essential for the scaled production of these materials. Hence, the aim of this current work is to optimise synthesis parameters and process variables to provide tailored production of selected textural characteristics in the final material. This involves determination of the impact of the solvent exchange method, total solids content, and drying method used, with respect to with varying R/C ratio. This optimal system was then studied further by altering the temperature at which the steps of synthesis, curing and drying were all set, to determine the validity of the widely accepted temperature of 85 °C in the synthetic procedure, as this has potential impact on the basis of both economics and safety. Low temperature nitrogen sorption measurements were used to characterise the textural properties of the synthesised aerogels, allowing changes in the internal structure of the xerogel to be monitored and quantified.

2. Results and Discussion

2.1. Effect of Solvent Exchange Method

Gels, produced as outlined above, generally undergo solvent exchange for a period of three days with only an initial volume of acetone added to the drained, cured gel; however, this may not be the most appropriate method to retain the porous structure developed during synthesis. Due to the high surface tension value for water, over the synthetic temperature range used to produce RF gels, the process of drying hydrogels leads to significant shrinkage of the material, as a consequence of the resulting high stresses that act on the pore walls. Therefore, it is desirable to replace the water, entrained within the pores, with a liquid that exhibits a lower surface tension, and preferably a lower boiling point, than water, within the temperature range of interest. The surface tension of water is high, even at elevated temperatures, e.g., 67.94 N/m at 50 °C [37], and a number of alternative solvents, with reduced surface tensions e.g., amyl acetate, acetone, t-butanol and isopropanol [20,38], have been proposed for solvent exchange in previous studies; however, acetone offers an excellent combination of a reduction in surface tension (19.65 N/m at 50 °C [39]) and relatively low cost compared to alternative solvents. Hence, acetone was used for solvent exchange within this study.

Replacement of the liquid within the pores is driven by diffusion, although agitation is often used to enhance contact of the material and fresh solvent; hence, sufficient time is required for full exchange to occur. Another factor that is potentially important, in maximizing the level of exchange, is the water concentration gradient between the pore liquid and the bulk solvent surrounding the sample. To investigate the effect of the solvent exchange method used, three batches of gels, individually of 60 mL total liquid volume, were synthesised, each of which, after curing, were washed with acetone, drained and, subsequently, agitated in acetone for three days. The key difference was that the first two batches were used to investigate the effect of a different volume of acetone used in one application and were processed by adding the entire volume of acetone at the beginning of the three days, namely 180 or 240 mL, and the sample was left without further handling for the whole solvent exchange period, while the third batch was treated with a fresh volume of acetone each day for three successive days with the total volume of acetone used adding up to 240 mL, thus maintaining the same total volume of acetone as the second batch but splitting the total volume over multiple days.

The data obtained for the pore size distributions of the three batches of gels are shown in Figure 2, and it can be seen that changing the acetone bath daily has a more pronounced positive effect on the total pore volume of the RF gel samples compared to just increasing the total acetone volume without changing the bath daily, especially for samples with lower R/C ratios. Improving the solvent exchange

method, by increasing the concentration gradient daily, leads to pores with larger average diameter (Table 1). This, coupled with the increase in pore volume, is ascribed to a reduction in shrinkage during the drying stage. If the acetone bath is replaced daily, the water concentration gradient is renewed every day, thus there is an increased driving force, which removes more water from the pores. This leads to lower stresses being exerted on the pore walls during the drying stage, due to the lower surface tension of acetone compared to water. However, for samples with higher R/C ratios exhibiting a weaker gel structure, the improved method does not seem to have the same pronounced positive effect observed for the lower R/C gels with smaller average pore diameter. A possible explanation is that when the acetone bath is exchanged daily, the replenishment step slightly damages the softer structure, resulting in lower values of surface area and pore size. The findings from this section of work suggest that there is significant advantage in using an improved solvent exchange method for most of the samples, hence, all samples in the following sections were prepared using daily replenishment of acetone within the solvent exchange stage, with the intention of maintaining the gel structure as close to the original hydrogel structure as possible, without the need to use cryogenic or supercritical processing steps. It is important to note that, in order to obtain improved gel characteristics, it is not necessary to increase the amount of acetone used during the solvent exchange, rather it is imperative to split this amount over the exchange period.

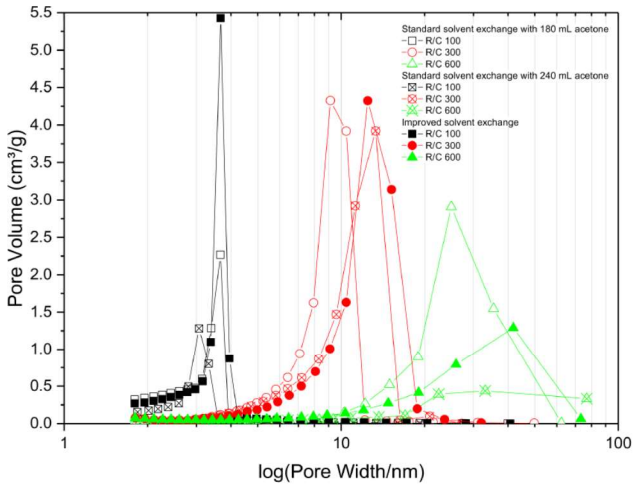

Figure 2. Effect of solvent exchange method on pore size distribution for resorcinol–formaldehyde xerogels with varied resorcinol:carbonate (R/C) molar ratio.

Table 1. Textural properties of resorcinol–formaldehyde xerogels prepared with standard and improved solvent exchange.

R/C	S_{BET} (m^2/g)			V_T (cm^3/g)			V_μ (cm^3/g)			$\overline{\varphi}$ (nm)		
	Acetone Exchange Method			Acetone Exchange Method			Acetone Exchange Method			Acetone Exchange Method		
	Standard		Improved	Standard		Improved	Standard		Improved	Standard		Improved
	180 mL	240 mL		180 mL	240 mL		180 mL	240 mL		180 mL	240 mL	
100	480	470	580	0.33	0.33	0.46	0.052	0.046	0.059	3	3	3
200	470	530	500	0.54	0.71	0.73	0.040	0.056	0.052	5	5	6
300	420	430	470	0.78	0.93	1.05	0.043	0.052	0.060	8	10	11
400	370	300	220	0.97	0.95	0.99	0.046	0.035	0.033	12	14	24
500	300	220	230	0.97	0.96	1.17	0.039	0.033	0.034	16	24	29
600	230	110	220	1.01	0.44	0.81	0.036	0.019	0.036	24	27	22

S_{BET}—surface area from Brunauer-Emmett-Teller (BET) analysis; V_T—total pore volume determined from adsorption at p/p° ~1; V_μ—micropore volume determined using t-plot method; $\overline{\varphi}$—average pore width from Barrett-Joyner-Halenda (BJH) analysis. Errors are omitted from the table as all values are reported to an accuracy less than the largest error for each variable.

2.2. Effect of Changing Solids Content

There is a tendency within the literature to use solids contents of ~20 w/v% in the production of RF gels [13,14,40,41]; however, the amount of solid material within the reaction volume would be expected to affect the solid:liquid ratio, hence, the final gel characteristics. Here, RF gels were synthesised over the range of solids content between 10 and 40 w/v%, using R/C ratios of 100, 300 and 600. Note that these samples were prepared at 85 °C, using improved solvent exchange (see Section 2.1) and vacuum drying (see Section 2.3). For the samples synthesised using a solids content of 10 w/v%, gelation was unsuccessful for R/C ratios greater than 600, hence, the range used in this study, but it should be noted that R/C ratio can be increased as the solids content increases but would not allow a direct comparison within this work, thus R/C 600 was the highest value studied here. For solids contents ≥20 w/v%, some of the samples exhibited cracking during the drying stage, which affected their final characteristics.

From Table 2, it can be observed that, at constant R/C molar ratio, there is no significant change in specific surface area as mass content changes; however, the total pore volume is seen to increase with solids content, up to ≤30 w/v%, after which point, the pore volume is slightly reduced at low R/C but still increases at higher R/C values. This can be ascribed to interplay between R/C ratio, i.e., particle nucleation number, and solids content, i.e., available material for particle growth; this means that the higher R/C ratios are more greatly affected by the additional mass available, due to the lower number of particles formed. The decrease at low R/C may be attributable to inhomogeneity during the gelation process, when no active agitation is applied, or possibly due to the increased mass per unit volume, which increases the relative density and reduces the void space available. Similarly, at constant R/C molar ratio, the average pore size increases with increasing solids content, again to 30 w/v%, whereupon it decreases steadily with increasing reactant concentration. Increasing the mass of reactants at a fixed R/C ratio, increases both the monomer concentration and that of sodium carbonate, as the catalyst, which leads to an increase in the number of particles formed during gelation; this could result in the observed decrease in average pore size. It should be noted that the pore diameters determined for R/C 100 are constant at three nanometers; however, differentiation at this level is hindered by the size of the probe molecule, which only allows integer values to be reported.

Table 2. Textural properties of resorcinol–formaldehyde xerogels prepared using different percentage solids contents.

w/v% Solids	S_{BET} (m^2/g)			V_T (cm^3/g)			V_μ (cm^3/g)			$\overline{\varphi}$ (nm)		
	R/C Ratio			R/C Ratio			R/C Ratio			R/C Ratio		
	100	300	600	100	300	600	100	300	600	100	300	600
10	500	370	-	0.36	0.85	-	0.057	0.037	-	3	9	-
20	500	490	280	0.32	0.91	1.00	0.065	0.064	0.046	3	8	18
25	550	410	190	0.42	1.00	1.07	0.054	0.042	0.030	3	10	32
30	570	490	260	0.46	1.08	1.17	0.055	0.064	0.045	3	9	28
35	570	450	260	0.45	0.98	1.23	0.051	0.050	0.038	3	9	27
40	540	550	330	0.44	1.07	1.53	0.048	0.077	0.056	3	9	29

S_{BET}—surface area from BET analysis; V_T—total pore volume determined from adsorption at p/p° ~1; V_μ—micropore volume determined using t-plot method; $\overline{\varphi}$—average pore width from BJH analysis. Errors are omitted from the table as all values are reported to an accuracy less than the largest error for each variable.

Figure 3 shows the pore size distribution of RF gel samples prepared at a constant R/C molar ratio of 300, and using different percentage solids contents. It can be seen that there is no significant change in the pore size distribution as the reactant concentration changes; however, it can be observed that RF gels with solids contents of 25 and 30 w/v% exhibit the narrowest distribution, with a sharp peak at ~15 nm. From Figure 4, meanwhile, it is obvious that altering the solids content has no major effect on overall shape of the adsorption–desorption isotherm of N_2, with all samples exhibiting Type IV isotherms [42]. The quantity of N_2 adsorbed increases with increasing relative pressure and a solids

content of 30 w/v% shows the highest adsorption capacity of all levels tested. The combination of a discrete pore size distribution and high pore volume (Table 2) indicates that the selection of 20 w/v% in the synthetic matrix is in line with process optimization.

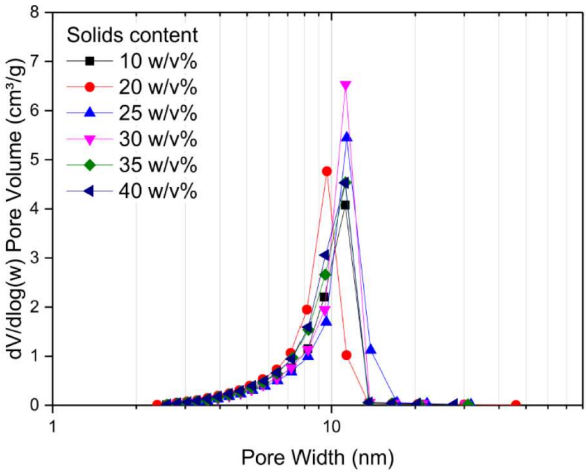

Figure 3. Pore size distribution obtained for resorcinol–formaldehyde xerogels synthesised using a resorcinol:cataylst molar ratio of 300 and varied percentage solids contents.

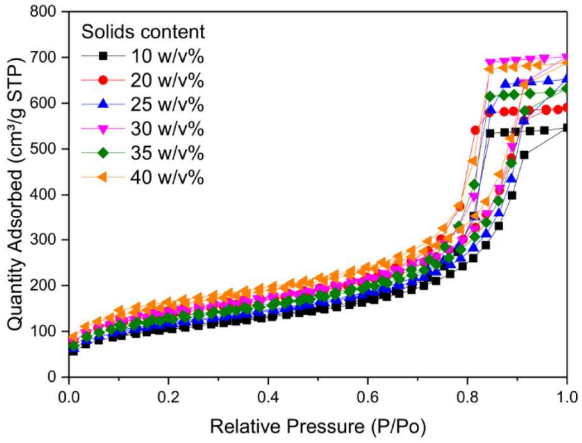

Figure 4. Nitrogen adsorption-desorption isotherms obtained for resorcinol–formaldehyde xerogels using a resorcinol:cataylst molar ratio of 300 and varied percentage solids content.

2.3. Ambient Pressure vs. Vacuum Drying

The final stage of gel preparation is drying of solvent exchanged gels, which, in this case, involves subcritical drying of the gels to remove acetone. The gels prepared in this way exhibit a higher degree of shrinkage; however, it is much easier to implement, and more economical, when compared to supercritical drying with CO_2. Usually, in order to make the drying process faster, and to ensure that the final materials have been dried thoroughly, vacuum drying is utilised. Maintaining a vacuum during drying is also not inexpensive, so it would be beneficial if RF gels could be dried under ambient pressure at elevated temperature, while retaining their final properties. Therefore, a series of gel samples were prepared, where the gel sample was divided in two halves post improved solvent exchange. This ensured that any effects observed within the final structure only resulted from the

selected drying procedure. One half of the sample was dried for two days under vacuum at 85 °C, while the other half was dried under ambient pressure at 85 °C for one day and subsequently moved to the vacuum oven with the other sample half for one day of further drying, this time sub-atmospherically. Most of the drying process occurs during the first day; while the second day is used to remove the final traces of acetone remaining in the pores.

Table 3 shows the textural properties obtained for the gels prepared as outlined above. It can be observed that even though the gels dried under vacuum tend to have higher surface areas, pore volumes, micropore volumes, and larger average pore widths, the differences are insubstantial. This means that, if the requirements for the final material are not too strict, it should be possible to initially dry RF gels at ambient pressure, potentially even in the same oven as is used for gelation, since the temperatures are equivalent. From an industrial perspective, this could result in significant cost savings associated with the drying process of RF gels, and the handling of materials between unit operations, and could make such materials potentially cost-effective for new applications.

Table 3. Textural properties of resorcinol–formaldehyde gels dried at ambient pressure and under vacuum.

R/C	S_{BET} (m^2/g)		V_T (cm^3/g)		V_μ (cm^3/g)		$\overline{\varphi}$ (nm)	
	Drying Method		Drying Method		Drying Method		Drying Method	
	Ambient	Vacuum	Ambient	Vacuum	Ambient	Vacuum	Ambient	Vacuum
100	510	600	0.45	0.47	0.037	0.064	4	3
300	380	460	1.11	1.12	0.044	0.064	13	12
600	90	120	0.31	0.54	0.014	0.023	19	30

S_{BET}—surface area from BET analysis; V_T—total pore volume determined from adsorption at p/p° ~1; V_μ—micropore volume determined using t-plot method; $\overline{\varphi}$—average pore width from BJH analysis. Errors are omitted from the table as all values are reported to an accuracy less than the largest error for each variable.

2.4. Influence of Synthetic and Processing Temperature

In light of the three previous steps, it seems reasonable that the preparation of gels using 20 w/v% solids content, with an improved solvent exchange step and either ambient or vacuum drying should yield reasonably optimal materials. The constraint of several process variables also indicates that it should be possible to obtain materials with a high degree of reproducibility; however, this is dependent on control of one significant parameter, which can have significant impact on the overall process costs, i.e., temperature. The first stages of resorcinol–formaldehyde (RF) gel formation, immediately after mixing the components, are gelation and curing, which are usually carried out at elevated temperatures, and the final processing steps of gel production also include the use of a raised temperature during drying. Hence, the final parameter studied here was the influence of temperature within the manufacturing process. In all previous experiments, 85 °C was selected as the gelation and curing temperature as gels previously obtained at this temperature have exhibited a viable structure, and it is also a commonly used value in the literature, allowing further comparisons to be made to previously reported results [20,43,44]. It has, however, been shown that RF cluster particles begin to grow once the solution reaches a temperature of at least 55 °C [13], which indicates a minimum threshold for investigation; since water is used as the solvent, in the synthesis outlined above, the upper temperature limit is, therefore, set by the boiling point of water. Thus, the chosen temperature range studied was 45–95 °C, with 10 °C intervals. This allowed the region both above and below the temperature necessary for cluster growth to be probed to determine whether a viable gel structure can be established and maintained at temperatures approaching both (i) the boiling point of water and (ii) lower, less energy demanding, temperatures. R/C ratio was varied, as required, but all other synthesis parameters were kept constant as stated above; the only other change was that of oven temperature during the gelation and drying stages. Due to the enhanced performance observed above, improved solvent exchange was used exclusively, and the drying temperature, used in the vacuum

stage, matched the gelation and curing temperatures, in order to restrict any post gelation changes in structure caused by exposure to a higher temperature during drying.

Table 4 shows the textural properties for gels synthesised at different temperatures, obtained from nitrogen adsorption analysis. Gels prepared at lower temperatures either did not gel or exhibited a very weak structure that did not withstand the drying process; this led to materials with a low degree of porosity or even to non-porous materials. The effect of temperature can be seen more clearly in Figure 5, where the influence of gel preparation temperature, and R/C ratio, on Brunauer-Emmett-Teller (BET) surface area is shown. It can be seen that, at low temperatures (45 and 55 °C), the surface areas obtained are very low, and are essentially independent of the R/C ratio used. At higher temperatures, the BET surface area seems to be only slightly dependent on temperature, and the effect of catalyst concentration dominates as the major factor in determining the final gel structure properties. These results are in disagreement with results from Tamon and Ishizaka [45] who reported that gelation temperature had no influence on the final gel structure. The difference is likely ascribed to the fact that their gelation step at either 25 or 50 °C was followed by a curing period of five days at 90 °C. Thus, the influence of the lower temperature gelation stage would have been masked by subsequent exposure to the same higher temperature during the curing stage.

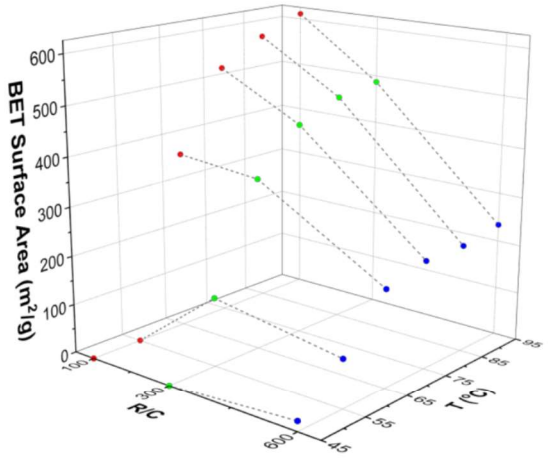

Figure 5. Dependence of BET surface area on resorcinol–formaldehyde xerogel preparation temperature and resorcinol:catalyst (R/C) molar ratio.

Table 4. Textural properties of resorcinol–formaldehyde xerogels prepared at different temperatures.

T (°C)	S_{BET} (m^2/g)			V_T (cm^3/g)			V_μ (cm^3/g)			$\overline{\varphi}$ (nm)		
	R/C Ratio			R/C Ratio			R/C Ratio			R/C Ratio		
	100	300	600	100	300	600	100	300	600	100	300	600
45	-	<1	20	-	-	0.07	-	-	0.002	-	-	9
55	<1	140	100	-	0.14	0.48	-	0.010	0.011	-	4	22
65	370	350	200	0.22	0.52	0.82	0.054	0.036	0.027	3	6	20
75	530	440	220	0.37	0.77	0.82	0.064	0.052	0.030	3	8	21
85	580	470	220	0.46	1.05	0.81	0.059	0.060	0.036	3	11	22
95	610	490	230	0.52	1.18	0.92	0.057	0.064	0.038	4	12	24

S_{BET}—surface area from BET analysis; V_T—total pore volume determined from adsorption at p/p° ~1; V_μ—micropore volume determined using t-plot method; $\overline{\varphi}$—average pore width from BJH analysis. Errors are omitted from the table as all values are reported to an accuracy less than the largest error for each variable.

Pore size distributions for the suites of samples prepared using different temperatures, and R/C ratio 300, are presented in Figure 6, and the results show that the pore size distribution shifts towards

larger pore diameters with increasing gelation temperature. This implies that gels prepared at higher temperatures develop stronger crosslinkages, which leads to a lower degree of shrinkage during the drying stage. It can also be observed that the total pore volume, which is given by the area under the pore size distribution curves, increases with increasing temperature, further supporting the theory that shrinkage is reduced within the stronger structures created at higher temperatures. The gels prepared at 45 °C exhibited such low porosity that the values are not even discernible in Figure 6, and are overlapped by other points; specific values are presented in Table 4.

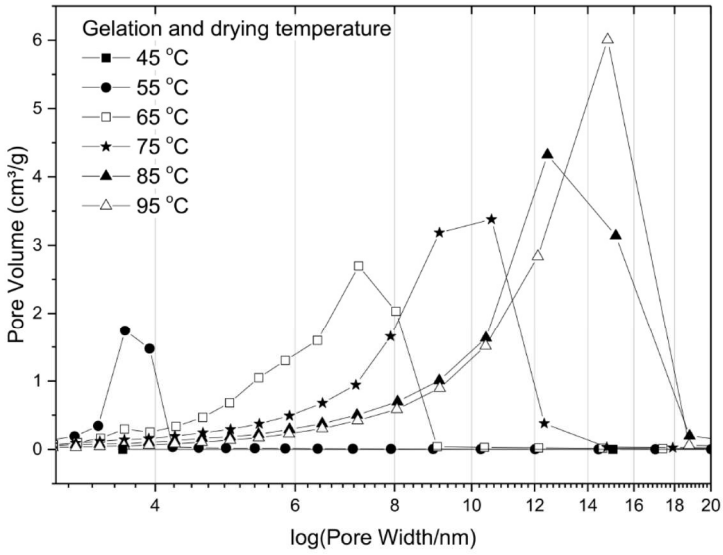

Figure 6. Effect of gelation temperature on pore size distributions for resorcinol–formaldehyde xerogels prepared using resorcinol:catalyst molar ratio of 300 and 20 w/v% solids content.

Morphological images of xerogel samples synthesised at 45 and 85 °C, with R/C ratios 100 and 600, are shown in Figure 7. It can be observed that the samples prepared with R/C ratio 100 do not show any significant textural features at this macroscopic level, which is expected considering the results from nitrogen sorption measurements. The pore size for these samples is below the limit at this magnification and due to the porous nature of the samples, it was not possible to achieve higher magnifications without using a higher thickness of gold coating, which would obscure any fine textural features. By contrast, there is a clear difference in morphology between the samples prepared with R/C 600 at different temperatures. The xerogel prepared at 85 °C (Figure 7d) exhibits a typical porous structure, composed of RF clusters crosslinked into a 3D network with some of the macropores clearly visible. While there are visible differences between samples prepared at 85 °C (Figure 7b,d), the xerogels prepared at 45 °C (Figure 7a,c) exhibit a very similar structure independent of catalyst amount. This agrees with the textural data obtained from nitrogen sorption measurements.

It is evident from these results that, in order to obtain a viable gel structure capable of enduring the drying process, the gelation temperature must be in excess of 55 °C, as suggested by Taylor et al. [13]; however, increasing the temperature further does not seem to have a significant impact on the surface area obtained. The other textural variables are affected slightly and it may be required to use elevated temperatures to optimise a particular variable or enhance the crosslinking within the final gel. This information could be used in process optimization of RF gel manufacture to reduce the heating costs associated with the gelation and drying processes for a specific set of required textural characteristics, as defined by a selected application.

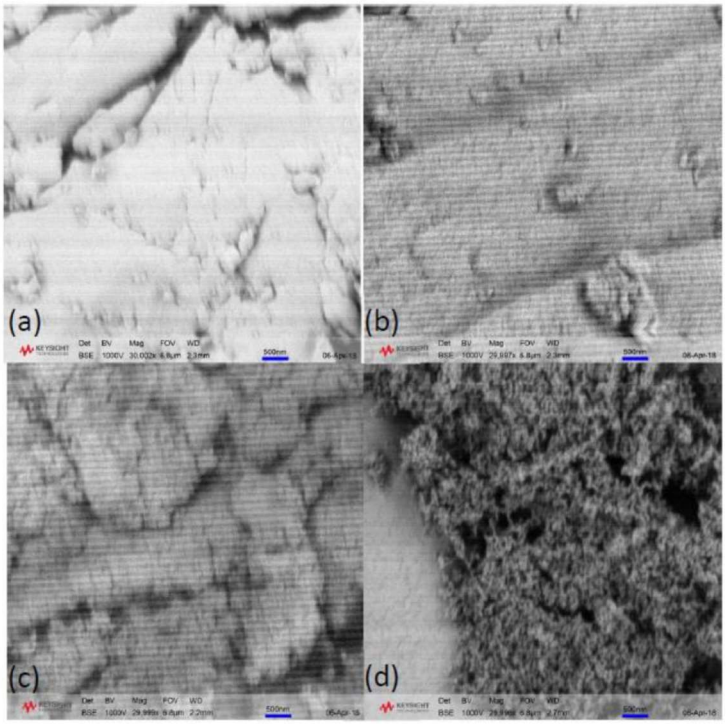

Figure 7. SEM micrographs of resorcinol–formaldehyde xerogels prepared at (**a**) 45 °C with resorcinol:catalyst molar ratio of 100, (**b**) 85 °C with resorcinol:catalyst molar ratio of 100, (**c**) 45 °C with resorcinol:catalyst molar ratio of 600, and (**d**) 85 °C with resorcinol:catalyst molar ratio of 600 at 30,000× magnification.

3. Conclusions

The work presented here demonstrates the need to carefully control the synthesis and process parameters used in RF gel production, in order to obtain the optimal material for a given application. Solids content is integral to gel viability, with low solids contents resulting in weaker structures that fail to gel at higher R/C ratios, and very high solids contents resulting in increased densification of the material and a reduction in porosity. It was observed that 30 w/v% represents an upper bound for solids content in the systems studied here, and such materials exhibited the highest accessible pore volume; however, surface area was unaffected by increased mass, at constant R/C. It is suggested that the increased mass of reactants (both monomer and catalyst) increased particle number and decreased average pore size. Within the systems studied, those gels created using solids contents of 20–30 w/v% exhibited the narrowest distribution; thus, the combination of discrete pore size distribution and high pore volume, with lower reactant costs, indicates 20 w/v% is optimal for gel production. In line with previous studies, a minimum temperature of 55 °C was shown to be critical in viable gel formation; gels prepared at lower temperatures either did not gel or exhibited a very weak structure with low or negligible porosity, independent of R/C. Gels prepared at higher temperatures showed insignificant changes in surface area with temperature, with the effect of catalyst concentration dominating gel formation; while pore diameter increases with increasing gelation temperature, due to stronger crosslinkages, hence, a lower degree of shrinkage during processing. This indicates that, while the gelation temperature must be in excess of 55 °C, increasing the temperature further has little impact on the final surface area, allowing a lower temperature to be used for gel synthesis if this is a key measure of gel performance. Post-synthesis, the regular replacement of the solvent exchange fluid has

a marked positive effect on total pore volume, leading to pores with larger average diameters, which is ascribed to a reduction in shrinkage during the drying stage, due to the increased driving force for water removal, hence, lower stresses being exerted on the pore walls during processing. It is, therefore, not necessary to increase the amount of solvent used within the exchange but it is imperative to increase the number of solvent changes over the exchange period. Finally, the differences between gels dried at atmospheric and sub-atmospheric pressure show little difference in their textural character, hence, it may be possible to dry RF gels at ambient pressure, potentially even in the same oven as gelation, to reduce both heating and pump costs. Combined, these results provide guidance to reduce the costs of RF gel manufacture, without impinging on the desired qualities of the materials produced.

4. Materials and Methods

4.1. Sample Preparation

Unless otherwise stated, all resorcinol–formaldehyde (RF) gel samples were prepared using an analogous procedure, excepting for the specific parameter investigated in each section of the study. All chemicals were used as received from the supplying company, and deionised water was produced in-house (Millipore Elix® 5 with Progard® 2 (Merck, Watford, UK)). Firstly, the appropriate amount of resorcinol (Sigma Aldrich, Gillingham, UK, ReagentPlus, 99%) was added to a premeasured volume of deionized water in a jar containing a magnetic stirrer bar. Upon dissolution of all of the added resorcinol, a corresponding amount of sodium carbonate (Sigma Aldrich, anhydrous, ≥99.5%), on a molar basis, was weighed out and added to the solution. As outlined above, sodium carbonate acts as a catalyst, by a combination of increasing the solution pH in the basic region via hydrolysis of the carbonate ion, and by the introduction of sodium ions, which, it has been suggested, assist in the addition of formaldehyde to resorcinol [46]. Catalyst concentration is expressed as resorcinol/catalyst molar ratio (R/C) and the range studied here is R/C 100–600. After all solids were dissolved, the required amount of formaldehyde, in the form of formalin solution (Sigma Aldrich, 37 wt % formaldehyde in water, containing 10–15 wt % methanol as a polymerization inhibitor), was added, and the solution was stirred in a closed jar for 30 min. All samples were prepared with 20 w/v% solids content, unless otherwise stated, and the total volume used was 60 mL, made up of water and methanol, contributed by the formalin solution used. At the end of the period of agitation, stirrer bars were removed from the solution, and the jar lid was hand-tightened, before moving the jar to an oven (Memmert UFE400, Schwabach, Germany) preheated to 85 °C, unless otherwise stated. Samples formed during this study gelled within 1–2 h [13]; however, samples were left to cure for three days in order to ensure sufficient time for crosslinking to occur. After three days, the jars containing the gels were removed from the oven and left to cool to room temperature. The formed gels were cut into smaller pieces before washing and solvent exchange with acetone (Sigma Aldrich, ≥99.5%). Standard solvent exchange involved addition of ~180 or ~240 mL of acetone to the drained gel, before resealing the lid and, in order to minimise acetone losses, wrapping with paraffin film. Sealed jars were put on a shaker unit (VWR 3500 Analog Orbital Shaker, Lutterworth, UK) and agitated for three days. In the improved solvent exchange method, the exchanged acetone was drained and replaced with 80 mL of fresh solvent on each successive day for three days. After three days of either solvent exchange method, the gel was drained and placed in a vacuum oven (Townson and Mercer 1425 Digital Vacuum Oven, Stretford, UK), preheated to 85 °C (or, in the case of the temperature study samples, the drying temperature was set to match the curing temperature), to dry for two days. Finally, the sample was transferred to a labelled sample tube for storage.

4.2. Sample Characterisation

Nitrogen adsorption-desorption measurements were used to obtain textural properties for the RF gel samples prepared in this study. Nitrogen sorption was performed at −196 °C using a Micromeritics ASAP 2420 (Hexton, UK) surface area and porosity analyser. Prior to analysis, samples were outgassed

under vacuum below 10 μmHg at 50 °C for 30 min and then at 110 °C for 2 h; except for samples where the influence of temperature was investigated, for these samples, outgassing temperatures matched the gelation and drying temperatures used, and the time for outgassing was adjusted accordingly to ensure removal of all volatile contaminant species. Samples were analysed using a 40 pressure point adsorption and 30 pressure point desorption cycle. All samples were characterised for surface area (m^2/g), using Brunauer-Emmett-Teller (BET) theory [47], and the Rouquerol correction for microporous samples [42]; total pore volume (cm^3/g); micropore volume (cm^3/g) from the t-plot method [48]; and average pore size (nm) from the Barrett-Joyner-Halenda method [49].

Scanning electron microscopy (SEM) micrographs were recorded in backscattered mode at 1000 V using a Field Emission Scanning Electron Microscope (Keysight, U9320B, Wokingham, UK) at magnification 30,000×. Prior to analysis, samples were ground into a fine powder, coated with a 10 nm gold layer using an EM ACE 200 sputter-coater (Leica Inc., Milton Keynes, UK), and attached to aluminium stubs with carbon tape.

Acknowledgments: Martin Prostredný thanks the University of Strathclyde and the Department of Chemical and Process Engineering for financial support. Mohammed G. M. Abduljalil thanks the Libyan Government for financial support. The authors would also like to acknowledge that the SEM analysis was carried out in the CMAC (Continuous Manufacturing and Crystallisation) National Facility, housed within the University of Strathclyde's Technology and Innovation Centre, and funded with a UKRPIF (UK Research Partnership Institute Fund) capital award, SFC (Scottish Funding Council) ref. H13054, from the Higher Education Funding Council for England (HEFCE).

Author Contributions: Martin Prostredný, Mohammed G. M. Abduljalil, Paul A. Mulheran and Ashleigh J. Fletcher contributed equally to conceiving and designing the experiments, analysing the data and writing and revising the manuscript. Martin Prostredný and Mohammed G. M. Abduljalil performed the experiments.

Conflicts of Interest: The authors declare no conflict of interest.

References

1. Pekala, R.W. Organic aerogels from the polycondensation of resorcinol with formaldehyde. *J. Mater. Sci.* **1989**, *24*, 3221–3227. [CrossRef]
2. Marie, J.; Berthon-Fabry, S.; Chatenet, M.; Chaînet, E.; Pirard, R.; Cornet, N.; Achard, P. Platinum supported on resorcinol–formaldehyde based carbon aerogels for PEMFC electrodes: Influence of the carbon support on electrocatalytic properties. *J. Appl. Electrochem.* **2007**, *37*, 147–153. [CrossRef]
3. Job, N.; Marie, J.; Lambert, S.; Berthon-Fabry, S.; Achard, P. Carbon xerogels as catalyst supports for PEM fuel cell cathode. *Energy Convers. Manag.* **2008**, *49*, 2461–2470. [CrossRef]
4. Smirnova, A.; Dong, X.; Hara, H.; Vasiliev, A.; Sammes, N. Novel carbon aerogel-supported catalysts for PEM fuel cell application. *Int. J. Hydrogen Energy* **2005**, *30*, 149–158. [CrossRef]
5. Robertson, C.; Mokaya, R. Microporous activated carbon aerogels via a simple subcritical drying route for CO_2 capture and hydrogen storage. *Microporous Mesoporous Mater.* **2013**, *179*, 151–156. [CrossRef]
6. Gross, A.F.; Vajo, J.J.; Van Atta, S.L.; Olson, G.L. Enhanced hydrogen storage kinetics of $LiBH_4$ in nanoporous carbon scaffolds. *J. Phys. Chem. C* **2008**, *112*, 5651–5657. [CrossRef]
7. Yamamoto, T.; Endo, A.; Ohmori, T.; Nakaiwa, M. Porous properties of carbon gel microspheres as adsorbents for gas separation. *Carbon* **2004**, *42*, 1671–1676. [CrossRef]
8. Dong, Y.-R.; Nakao, M.; Nishiyama, N.; Egashira, Y.; Ueyama, K. Gas permeation and pervaporation of water/alcohols through the microporous carbon membranes prepared from resorcinol/formaldehyde/quaternary ammonium compounds. *Sep. Purif. Technol.* **2010**, *73*, 2–7. [CrossRef]
9. Alcántara, R.; Lavela, P.; Ortiz, G.F.; Tirado, J.L. Carbon microspheres obtained from resorcinol-formaldehyde as high-capacity electrodes for sodium-ion batteries. *Electrochem. Solid-State Lett.* **2005**, *8*, A222–A225. [CrossRef]
10. Glora, M.; Wiener, M.; Petricevic, R.; Probstle, H.; Fricke, J. Integration of carbon aerogels in PEM fuel cells. *J. Non-Cryst. Solids* **2001**, *285*, 283–287. [CrossRef]
11. Lu, X.; Arduini-Schuster, M.; Kuhn, J.; Nilsson, O.; Fricke, J.; Pekala, R. Thermal conductivity of monolithic organic aerogels. *Science* **1992**, *255*, 971–972. [CrossRef] [PubMed]

12. Feng, J.; Zhang, C.; Feng, J. Carbon fiber reinforced carbon aerogel composites for thermal insulation prepared by soft reinforcement. *Mater. Lett.* **2012**, *67*, 266–268. [CrossRef]
13. Taylor, S.J.; Haw, M.D.; Sefcik, J.; Fletcher, A.J. Gelation mechanism of resorcinol-formaldehyde gels investigated by dynamic light scattering. *Langmuir* **2014**, *30*, 10231–10240. [CrossRef] [PubMed]
14. Taylor, S.J.; Haw, M.D.; Sefcik, J.; Fletcher, A.J. Effects of secondary metal carbonate addition on the porous character of resorcinol–formaldehyde xerogels. *Langmuir* **2015**, *31*, 13571–13580. [CrossRef] [PubMed]
15. Rey-Raap, N.; Angel Menéndez, J.; Arenillas, A. Simultaneous adjustment of the main chemical variables to fine-tune the porosity of carbon xerogels. *Carbon* **2014**, *78*, 490–499. [CrossRef]
16. Rey-Raap, N.; Angel Menéndez, J.; Arenillas, A. RF xerogels with tailored porosity over the entire nanoscale. *Microporous Mesoporous Mater.* **2014**, *195*, 266–275. [CrossRef]
17. Job, N.; Gommes, C.J.; Pirard, R.; Pirard, J.-P. Effect of the counter-ion of the basification agent on the pore texture of organic and carbon xerogels. *J. Non-Cryst. Solids* **2008**, *354*, 4698–4701. [CrossRef]
18. Fairen-Jimenez, D.; Carrasco-Marin, F.; Moreno-Castilla, C. Porosity and surface area of monolithic carbon aerogels prepared using alkaline carbonates and organic acids as polymerization catalysts. *Carbon* **2006**, *44*, 2301–2307. [CrossRef]
19. Laskowski, J.; Milow, B.; Ratke, L. Subcritically dried resorcinol-formaldehyde aerogels from a base-acid catalyzed synthesis route. *Microporous Mesoporous Mater.* **2014**, *197*, 308–315. [CrossRef]
20. Al-Muhtaseb, S.A.; Ritter, J.A. Preparation and properties of resorcinol–formaldehyde organic and carbon gels. *J. Adv. Mater.* **2003**, *15*, 101–114. [CrossRef]
21. El Khatat, A.M.; Al-Muhtaseb, S.A. Advances in tailoring resorcinol-formaldehyde organic and carbon gels. *Adv. Mater.* **2011**, *23*, 2887–2903. [CrossRef] [PubMed]
22. Tamon, H.; Ishizaka, H.; Mikami, M.; Okazaki, M. Porous structure of organic and carbon aerogels synthesized by sol-gel polycondensation of resorcinol with formaldehyde. *Carbon* **1997**, *35*, 791–796. [CrossRef]
23. Gaca, K.Z.; Parkinson, J.A.; Sefcik, J. Kinetics of early stages of resorcinol-formaldehyde polymerization investigated by solution-phase nuclear magnetic resonance spectroscopy. *Polymer* **2017**, *110*, 62–73. [CrossRef]
24. Rojas-Herrera, J.; Lozano, P.C. Mitigation of anomalous expansion of carbon xerogels and controllability of mean-pore-size by changes in mold geometry. *J. Non-Cryst. Solids* **2017**, *458*, 22–27. [CrossRef]
25. Pierre, A.C.; Pajonk, G.M. Chemistry of aerogels and their application. *Chem. Rev.* **2002**, *102*, 4243–4265. [CrossRef] [PubMed]
26. Lide, D.R. *CRC Handbook of Chemistry and Physics, Internet Version 2006*; Taylor and Francis: Boca Raton, FL, USA, 2006.
27. Barbieri, O.; Ehrburger-Dolle, F.; Rieker, T.P.; Pajonk, G.M.; Pinto, N.; Rao, A.V. Small-angle X-ray scattering of a new series of organic aerogels. In Proceedings of the 6th International Symposium on Aerogels (ISA-6), Albuquerque, NM, USA, 8–11 October 2000; pp. 109–115.
28. Fricke, J.; Tillotson, T. Aerogels: Production, characterization, and applications. *Thin Solid Films* **1997**, *297*, 212–223. [CrossRef]
29. Pekala, R.W.; Kong, F.M. A synthetic route to organic aerogels-mechanism, structure, and properties. *J. Phys. Colloq.* **1989**, *50*, 33–40. [CrossRef]
30. Job, N.; Pirard, R.; Marien, J.; Pirard, J.P. Porous carbon xerogels with texture tailored by pH control during sol-gel process. *Carbon* **2004**, *42*, 619–628. [CrossRef]
31. Tamon, H.; Ishizaka, H.; Yamamoto, T.; Suzuki, T. Preparation of mesoporous carbon by freeze drying. *Carbon* **1999**, *37*, 2049–2055. [CrossRef]
32. Czakkel, O.; Marthi, K.; Geissler, E.; Laszlo, K. Influence of drying on the morphology of resorcinol-formaldehyde-based carbon gels. *Microporous Mesoporous Mater.* **2005**, *86*, 124–133. [CrossRef]
33. Yamamoto, T.; Nishimura, T.; Suzuki, T.; Tamon, H. Control of mesoporosity of carbon gels prepared by sol-gel polycondensation and freeze drying. *J. Non-Cryst. Solids* **2001**, *288*, 46–55. [CrossRef]
34. Job, N.; Thery, A.; Pirard, R.; Marien, J.; Kocon, L.; Rouzaud, J.N.; Beguin, F.; Pirard, J.P. Carbon aerogels, cryogels and xerogels: Influence of the drying method on the textural properties of porous carbon materials. *Carbon* **2005**, *43*, 2481–2494. [CrossRef]
35. Jabeen, N.; Mardan, A. Effect of water removal on the textural properties of resorcinol/formaldehyde gels by azeotropic distillation. *J. Mater. Sci.* **1998**, *33*, 5451–5453. [CrossRef]

36. Schwertfeger, F.; Frank, D.; Schmidt, M. Hydrophobic waterglass based aerogels without solvent exchange or supercritical drying. *J. Non-Cryst. Solids* **1998**, *225*, 24–29. [CrossRef]
37. Vargaftik, N.; Volkov, B.; Voljak, L. International tables of the surface tension of water. *J. Phys. Chem. Ref. Data* **1983**, *12*, 817–820. [CrossRef]
38. Mukai, S.R.; Tamitsuji, C.; Nishihara, H.; Tamon, H. Preparation of mesoporous carbon gels from an inexpensive combination of phenol and formaldehyde. *Carbon* **2005**, *43*, 2628–2630. [CrossRef]
39. Jasper, J.J. The surface tension of pure liquid compounds. *J. Phys. Chem. Ref. Data* **1972**, *1*, 841–1010. [CrossRef]
40. Zanto, E.J.; Al-Muhtaseb, S.A.; Ritter, J.A. Sol-gel-derived carbon aerogels and xerogels: Design of experiments approach to materials synthesis. *Ind. Eng. Chem. Res.* **2002**, *41*, 3151–3162. [CrossRef]
41. Berthon, S.; Barbieri, O.; Ehrburger-Dolle, F.; Geissler, E.; Achard, P.; Bley, F.; Hecht, A.-M.; Livet, F.; Pajonk, G.M.; Pinto, N. DLS and SAXS investigations of organic gels and aerogels. *J. Non-Cryst. Solids* **2001**, *285*, 154–161. [CrossRef]
42. Thommes, M.; Kaneko, K.; Neimark, A.V.; Olivier, J.P.; Rodriguez-Reinoso, F.; Rouquerol, J.; Sing, K.S.W. Physisorption of gases, with special reference to the evaluation of surface area and pore size distribution (iupac technical report). *Pure Appl. Chem.* **2015**, *87*, 1051–1069. [CrossRef]
43. Calvo, E.; Menéndez, J.; Arenillas, A. Influence of alkaline compounds on the porosity of resorcinol-formaldehyde xerogels. *J. Non-Cryst. Solids* **2016**, *452*, 286–290. [CrossRef]
44. Lin, C.; Ritter, J.A. Effect of synthesis pH on the structure of carbon xerogels. *Carbon* **1997**, *35*, 1271–1278. [CrossRef]
45. Tamon, H.; Ishizaka, H. Influence of gelation temperature and catalysts on the mesoporous structure of resorcinol-formaldehyde aerogels. *J. Colloid Interface Sci.* **2000**, *223*, 305–307. [CrossRef] [PubMed]
46. GrenierLoustalot, M.F.; Larroque, S.; Grande, D.; Grenier, P.; Bedel, D. Phenolic resins: 2. Influence of catalyst type on reaction mechanisms and kinetics. *Polymer* **1996**, *37*, 1363–1369. [CrossRef]
47. Brunauer, S.; Emmett, P.H.; Teller, E. Adsorption of gases in multimolecular layers. *J. Am. Chem. Soc.* **1938**, *60*, 309–319. [CrossRef]
48. Lowell, S.; Shields, J.E.; Thomas, M.A.; Thommes, M. Micropore analysis. In *Characterization of Porous Solids and Powders: Surface Area, Pore Size and Density*; Springer: Berlin, Germany, 2004; pp. 129–156.
49. Barrett, E.P.; Joyner, L.G.; Halenda, P.P. The determination of pore volume and area distributions in porous substances. I. Computations from nitrogen isotherms. *J. Am. Chem. Soc.* **1951**, *73*, 373–380. [CrossRef]